Flow of Complex Fluids Past Confined Cylinders: from Macro to Micro Scale

Vera Maria Machado Ribeiro

Dissertation submitted to University of Porto for the Doctor Degree in Chemical and Biological Engineering

Supervisors:

Dr Manuel António Moreira Alves

Dr Paulo José da Silva Martins Coelho

Transport Phenomena Research Centre (CEFT)

Chemical Engineering Department

Faculty of Engineering of the University of Porto

Portugal

2013

UNIÃO EUROPEIA
Fundo Social Europeu

GOVERNO DE PORTUGAL

FCT
Fundação para a Ciência e a Tecnologia
MINISTÉRIO DA EDUCAÇÃO E CIÊNCIA

COMPETE
PROGRAMA OPERACIONAL FACTORES DE COMPETITIVIDADE

QREN
QUADRO DE REFERÊNCIA ESTRATÉGICO NACIONAL

POPH
PROGRAMA OPERACIONAL POTENCIAL HUMANO

Acknowledgements

Reached the end of this journey I would like to acknowledge and express my gratitude to all those, in their own way, gave me their enriching contribution and support:

To the Portuguese Foundation for Science and Technology (FCT) for the financial support through the scholarship SFRH/BD/44737/2008 and the project PTDC/EME-MFE/114322/2009.

To the Transport Phenomena Research Centre (CEFT) integrated in the Faculty of Engineering of University of Porto for the facilities and conditions granted to me to develop my work.

I would like also to express my deepest gratitude to my supervisors Professor Manuel Alves and Professor Paulo Coelho, who gave me the opportunity and the privilege to share with me their knowledge and experience, and who always gave me the liberty to express my doubts and my views.

To Professor Fernando Pinho for all the support and the discussions that usefully helped the development of my work.

To all my co-workers of CEFT who accompanied me in this journey, which would be much more difficult without their companionship, support and extraordinary amusing moments. In particular to Patrícia, I would like to express a deepest and special thanks for always being there with her friendship, support, always honest opinions, for everything.

To all my closest friends for their friendship, for the moments that they tried to show their interest in the topic of my thesis and for all moments that they didn't let me forget that there is much more life beyond the PhD.

To my family, to my father and my mother, for being always the greatest example in everything in my life and for always supporting me in my choices. To my sisters Raquel and Joana, and to Carlos for being always by my side, with their unconditional support. To my nephews Pedro and Inês, for being the sunshine of my days with their lovely smiles.

À minha familia, ao meu Pai e à minha Mãe por serem sempre o melhor exemplo em tudo na minha vida e por apoiarem sempre as minhas escolhas. Às minhas irmãs, Raquel e Joana, e ao Carlos por estarem sempre ao meu lado, com o seu apoio incondicional. Aos meus sobrinhos, Pedro e Inês, por serem como a luz do sol dos meus dias, com os seus adoráveis sorrisos.

Abstract

The main objective of the this thesis is to deepen our knowledge on the complex fluid flow around a confined cylinder centred at the mid plane of a rectangular duct, both at macro- and micro-scales, using Newtonian and viscoelastic fluids. In the experiments at the macro-scale, the effect of the aspect ratio (*AR*) was investigated in a symmetric geometry with 50% area blockage, to assess the influence of flow inertia and viscoelasticity in the complex three dimensional flows, from low flow rates up to the critical conditions for the onset of inertial and elastic instabilities, respectively for Newtonian and viscoelastic fluids. At the micro-scale, experiments were carried out to assess the effect of the aspect ratio (*AR*) and the blockage ratio (*BR*) on the flow around a confined cylinder and to investigate the elastic instabilities that arise at highly elastic flow conditions and low Reynolds number (*Re*) flows.

Both at macro- and micro-scales, the experiments were conducted from the creeping flow regime up to the onset of time-dependent flow, using Newtonian fluids, viscoelastic fluids with constant shear viscosity (so-called Boger fluids), and viscoelastic fluids with shear-thinning behaviour. The experiments included flow visualizations using long time exposure streak photography, detailed velocity measurements using particle image velocimetry (PIV) and pressure drop measurements.

The specificities of the complex fluid flows investigated in a three-dimensional benchmark geometry led to a compilation of valuable experimental data that can also be used for validation purposes of numerical methods. To establish a direct comparison with the experimental results, numerical calculations were successfully carried out using an in-house finite-volume code.

At the macro-scale, the Newtonian fluid flow is characterized by the onset of flow separation downstream of the cylinder at a critical *Re*, which is enhanced with increasing inertia, until the onset of a time-dependent flow at higher *Re*. The shear-thinning fluid flow shows the appearance of an elastic instability upstream of the cylinder, above a critical Deborah number (*De*). The elastic instability becomes more intense and the flow becomes progressively asymmetric and eventually time-dependent as *De* further increases. The critical conditions for the flow transitions were found to depend on the *AR*. Over the limited range of *De* studied, and for the Boger fluids, the flow patterns were always symmetric and steady.

As expected, for Newtonian fluids there are no dramatic changes as we move to smaller scales, although the opposite was found for the viscoelastic fluids due to the different elasticity numbers at different length scales. Over the wide range of *De* achieved to characterize the flow of Boger fluids at micro-scale, the Newtonian-like and the steady divergent streamlines flow regimes were observed. For the shear-thinning fluid, a wider range of *De* was investigated, and the following four flow regimes were identified with progressively increasing *De*: Newtonian-like flow; steady asymmetric flow; unsteady periodic flow; unstable chaotic-like flow. The critical conditions for the flow regime transitions depend on the aspect ratio and on the blockage ratio.

The study of the flow of Newtonian and viscoelastic fluids through a microfluidic array of cylinders, which can be considered as a simplified two-dimensional porous media analogue, is also a goal of the present work. Two different arrangements (staggered and aligned) were investigated with viscoelastic fluids, and different flow patterns were found with different levels of instability, which can be used to efficiently promote mixing at micro-scale.

Keywords: Confined cylinder flow; complex fluids; 3D flow; viscoelastic effects; flow visualization; particle image velocimetry; numerical simulations; elastic instabilities; 2D porous media analogue.

Resumo

O principal objetivo da presente tese é investigar, à escala macroscópica e à microescala, o escoamento de fluidos complexos em torno de um cilindro confinado numa secção retangular usando fluidos newtonianos e viscoelásticos. Nas experiências à escala macroscópica estudou-se o efeito da razão de forma (*AR*) para uma razão de bloqueio (*BR*) de 50%, com o objetivo de avaliar a influência da inércia e da viscoelasticidade no escoamento em torno de um cilindro confinado, que é caracterizado por conduzir a padrões de escoamento fortemente tridimensionais. Realizaram-se experiências partindo de caudais baixos, até às condições críticas para o aparecimento de instabilidades inerciais e elásticas para os fluidos newtonianos e viscoelásticos, respetivamente. Nas experiências à microescala avaliou-se o efeito da razão de forma e da razão de bloqueio no escoamento em torno de um cilindro confinado, com o objetivo de investigar as instabilidades elásticas que surgem para condições de elevada elasticidade e baixo número de Reynolds, que naturalmente se conseguem atingir no escoamento em microcanais.

Quer na escala macroscópica, quer na microescala, as experiências decorreram desde as condições de inércia desprezável até ao aparecimento de escoamento dependente do tempo, usando fluidos newtonianos, viscoelásticos com viscosidade constante (fluidos de Boger) e viscoelásticos com comportamento pseudoplástico. Para caracterizar o escoamento, realizaram-se visualizações dos padrões de escoamento usando uma técnica fotográfica de elevado tempo de exposição, mediu-se em detalhe o campo de velocidades usando a técnica de velocimetria por imagem de partículas, e mediram-se perdas de carga.

A caracterização do escoamento de fluidos complexos num escoamento de referência, como o escoamento tridimensional em torno de um cilindro, possibilitou a compilação de dados experimentais relevantes que podem ser usados na validação de métodos numéricos desenvolvidos para prever o escoamento de fluidos de reologia complexa. Com o objetivo de efetuar uma comparação direta com os resultados experimentais, fizeram-se simulações numéricas usando um código baseado no método dos volume-finitos.

O escoamento de fluidos newtonianos à escala macroscópica é caracterizado pela separação do escoamento a jusante do cilindro, que ocorre a um número de Reynolds (*Re*) crítico, verificando-se um aumento progressivo do comprimento da recirculação com o aumento de *Re*, até ao aparecimento de um escoamento dependente do tempo. O escoamento do fluido

viscoelástico com comportamento pseudoplástico é caracterizado pelo aparecimento de uma instabilidade elástica a montante do cilindro, acima de um número de Débora (*De*) crítico. Com o aumento de *De*, a instabilidade elástica torna-se mais intensa e o escoamento torna-se progressivamente assimétrico, tornando-se dependente do tempo para valores de *De* mais elevados. Verificou-se que as condições críticas para a transição de regime de escoamento é dependente da razão de forma. Na gama limitada de valores de *De* estudados com os fluidos de Boger, os padrões de escoamento mantiveram-se simétricos e estáveis.

Como expectável, para os fluidos newtonianos não se verificam alterações significativas quando se passa da escala macroscópica para a microescala. No entanto, o oposto verificou-se para os fluidos viscoelásticos, devido aos diferentes números de elasticidade observados na escala macroscópica e na microescala. Na gama limitada de valores de *De* obtidos para caracterizar o escoamento dos fluidos de Boger, observaram-se os seguintes regimes de escoamento estacionário: comportamento *quasi*-newtoniano; linhas de corrente divergentes. Para o fluido viscoelástico pseudoplástico, foi investigada uma gama mais ampla de *De* e identificaram-se quatro regimes de escoamento com o aumento progressivo de *De*: comportamento *quasi*-newtoniano; escoamento assimétrico estacionário; escoamento periódico não estacionário; escoamento caótico. As condições críticas para a transição de regime de escoamento dependem das razões de forma e de bloqueio.

O estudo do escoamento de fluidos newtonianos e viscoelásticos em microcanais com uma disposição matricial de cilindros é também um dos objetivos deste trabalho. Foram investigadas duas configurações de cilindros (desalinhados e alinhados) e foram observados diferentes padrões de escoamento bem como diferentes níveis de instabilidades, que podem ser usadas para promover mistura eficiente à microescala.

Palavras-chave: escoamento em torno de um cilindro confinado; fluidos complexos; escoamento 3D; efeitos viscoelásticos; visualização de escoamentos; velocimetria por imagens de particulas; simulações numéricas; instabilidades elásticas; análogos de meios porosos 2D.

Table of Contents

Nomenclature

Roman

AR	Aspect ratio
a_T	Shift factor (time-temperature superposition method)
BR	Blockage ratio
D	Diameter of the cylinder ; Diameter of the filament;
D_0	Diameter of the filament at time $t = 0$
$\mathbf{D}$	Deformation rate tensor
De	Deborah number
D_p	Diameter of the plates in the CaBER
d_e	Effective image diameter
d_p	Diameter of the particle
d_s	Diffraction-limited spot size of a point source of light
e	Interstitial space
El	Elasticity number
F	Normal force
G	Elastic modulus
G'	Loss modulus
G''	Storage modulus
H	Width
h	Depth
h_f	Final height
h_i	Initial height
k	Index
L	Characteristic length; Length of the filament
L_0	Length of the filament at time $t = 0$
L_v	Recirculation length
M	Magnification
n	Refractive index; Power law index
N_1	First normal stress difference
p	Pressure
p_{ref}	Reference pressure

R	Radius of the cylinder; Radius of the cone
Re	Reynolds number
$Re_{(s)}$	Reynolds for the onset of flow separation
$Re_{(vs)}$	Reynolds for the onset of vortex shedding
s_0	Objective working distance
T	Absolute temperature
T_0	Reference absolute temperature
t	Time
t_f	Characteristic time
t_c	Critical time
u	Velocity
U	Characteristic velocity
$\mathbf{u}$	Velocity vector
V	Particle visibility
V_{fr}	Volume fraction of particles
V_p	Volume of computational cells
Wi	Weissenberg number
x, y, z	Cartesian coordinates
u, v, w	Velocity components

Greek

β	Cut-off level of the edges of the particle image; Ratio of the solvent to total viscosities (Oldroyd-B model)
δ	Phase angle
ΔH	Activation energy
Δp	Pressure drop
Δt	Time interval between pulses; Time step
Δl, Δs, Δr	Cell dimensions
δz	Depth of field
δz_m	Total measurement depth
$\dot{\gamma}$	Shear rate
γ	Strain
γ_0	Strain amplitude

η	Shear viscosity
η_0	Shear viscosity at zero shear-rate
η_p	Polymer viscosity
η_s	Solvent viscosity
η'	Dynamic viscosity
λ	Relaxation time; Light wavelength
λ_0	Light wavelength in vacuum
Λ	Time parameter of the Carreau and Carreau-Yasuda models
μ_0	Dynamic viscosity at reference absolute temperature T_0
Ψ_1	First normal stress difference coefficient
Ψ_2	Second normal stress difference coefficient
ρ	Density
ρ_0	Density at the reference temperature
σ	Surface tension
τ_{xy}, τ_{xz}	Shear stress components
$\boldsymbol{\tau}$	Extra-stress tensor
τ_0	Stress amplitude
$\boldsymbol{\tau_p}$	Polymeric (solute) contribution to the extra-stress tensor
$\boldsymbol{\tau_s}$	Newtonian solvent contribution to the extra-stress tensor
θ	Angle
$\mathfrak{T}$	Torque
Ω	Angular velocity

Acronyms

2D	Two-dimensional
3D	Three-dimensional
CaBER	Capillary break-up extensional rheometer
CAD	Computer Aided Design
CUBISTA	Convergent and Universally Bounded Interpolation Scheme for Treatment of Advection
CFD	Computational fluid dynamics
CCD	Charge-coupled device

Em	Emission
Ex	Excitation
HWNP	High Weissenberg number problem
NA	Numerical aperture
PAA	Polyacrylamide
PDMS	Polydimethylsiloxane
PIV	Particle image velocimetry
SAOS	Small-amplitude oscillatory shear
SEM	Scanning electron microscope
SU-8	Designation of epoxi-bored photoresist used in the moulds
μPIV	Micro-particle image velocimetry
μTAS	Micro total analysis systems

Subscripts

k	Mode index of the linear viscoelastic spectra for the Boger fluid
p	Polymer
s	Solvent
c	Critical
x, y, z	Cartesian directions

Chapter 1

Introduction

This introductory chapter briefly describes the theoretical concepts and approaches inherent to the subject matter of this dissertation: it starts with the motivation in Section 1.1, defines the objectives of this research work in Section1.2 and ends with the outline of this thesis.

1.1. Introduction

1.1.1. Newtonian and non-Newtonian fluids

Inspired by the Greek quotation "panta rhei" (everything flows), taken from "Everything flows and nothing abides; everything gives way and nothing stays fixed" attributed to the Greek philosopher Heraclitus of Ephesus (536-470 BCE), Eugene Cook Bingham suggested the term Rheology to describe the science that studies the deformation and flow of matter, when the Society of Rheology was formally founded in the late 1920´s.

Despite this classical and formal definition, "Rheology" has also been defined by several scientists using different words to express the same scientific meaning. Morrison (2004) proposes a different definition useful for family and friends, and defined rheology as "the study of the flow of materials that behave in an interesting or unusual manner".

Any material within the range from fluid-like to the solid-like behaviour can be investigated in rheology (although some authors suggest that the classical limits of Newtonian fluids and Hookean solids are outside the scope of rheology) and this involves such materials as water, polymers, petroleum products, rubber, paints, printing inks, ceramics, food products (egg white, fruits, vegetal oils, among others), biological materials (blood, saliva, synovial fluid,

among others), pharmaceutical products, geological materials, over a wide range of practical applications such as extrusion, fibre spinning, injection moulding, heat exchangers, food processing, and coating processes (Malkin, 1994). At the same time this wide range of materials and applications is the subject of study and work of physicists, chemists, geologists, engineers, biologists and mathematicians, illustrating the wide range of applicability of rheology.

A fundamental difference between the fluid and solid states of matter is their response to an external force. Fluid-like materials are substances that move and deform continuously even when a vanishingly small shear stress is applied (yield stress fluids are an exception, despite some debate (Barnes, 1999)). If the relation between the applied shear stress and the resulting deformation rate is linear, and no normal stresses or memory effects exist in a simple shear (Couette) flow, those fluids are called Newtonian fluids, and are described by Newton's law of viscosity (Newton, 1687). The materials in the solid-like state have the capability to store energy and experience small deformations when a stress is applied. These deformations can be described in the linear regime by the Hookean elasticity law (Hooke, 1678). With these two extreme classical materials well established, the characterization of any material behaving in between these two limiting cases is in the realm of rheology, and the material is called a non-Newtonian fluid. Within this classification there is a wide range of possible behaviours, which differ in terms of the viscosity functions, the time and the space scales and their interplay and connection with their environment leading to all kinds of complex flow behaviour, as brilliantly shown in the rheological phenomena photo gallery of Boger and Walters (1993).

1.1.2. Dimensionless numbers

The flow of Newtonian and non-Newtonian fluids is usually characterised using dimensionless numbers to quantify the competing effects and forces acting on the fluid elements.

Stokes (1851) introduced the concept of the relative balance between inertial forces ($\propto \rho U^2/L$) and viscous forces ($\propto \eta U/L^2$) per unit volume which became more popular by Osborne Reynolds (1883), and for that reason become known as the Reynolds number (*Re*). The Reynolds number is the most famous and commonly used dimensionless number in fluid mechanics, and is defined as the ratio between inertial and viscous forces:

$$Re = \frac{\rho U L}{\eta} \ , \tag{1.1}$$

where ρ is the fluid density, U a characteristic velocity scale, L is a characteristic length scale and η is the shear viscosity of the fluid. The Reynolds number tends to be very small ($Re << 1$) when the viscous forces dominate and inertial effects can be neglected. In contrast, Re tends to be large ($Re >> 1$) when inertial effects dominate.

For non-Newtonian fluids with memory, known as viscoelastic fluids, in addition to the Reynolds number, it is useful to quantify the ratio between the relaxation time of the material (λ) and a characteristic time scale of the flow process (t_f), baptized by Reiner (1964) as the Deborah number (De):

$$De = \frac{\lambda}{t_f} \ . \tag{1.2}$$

The characteristic time scale of the flow can be estimated as $t_f = L / U$. The relaxation time of the fluid is the time necessary for the viscoelastic fluid to relax the stresses after flow/deformation is applied. In the flow of viscoelastic fluids, when De is very small ($De \rightarrow 0$) the fluid behaves as inelastic and often as Newtonian. In contrast, when De is large, elastic effects dominate.

The Weissenberg number quantifies the nonlinear response of the fluid and is defined as the ratio between elastic (normal) forces and viscous forces, and can be written as (Dealy, 2010; Poole, 2012):

$$Wi = \frac{\lambda U}{L} \ . \tag{1.3}$$

The Weissenberg number (Wi) is used often in viscoelastic flows in which there is an important elongation component of the flow, but is also applicable in shear-dominated flows.

The elasticity number (El) is also often used, and is a dimensionless parameter that quantifies the ratio between elastic and inertial forces $(El \propto L^{-2})$:

$$El = \frac{Wi}{Re} = \frac{\eta \lambda}{\rho L^2}, \tag{1.4}$$

being independent of the velocity, contrary to the previous dimensionless numbers. The elasticity number clearly shows that when the characteristic length scale is reduced, elastic effects become more important.

1.1.3. Complex fluid flow

A significant interest on complex fluids started in the 1940's, as a consequence of the Second World War, which promoted the development of important industrial products, such as plastics, glass and paints, among others. The study of the transport properties of these complex fluids, the so-called transport phenomena of non-Newtonian fluids, earned naturally its space. The transport phenomena include heat, mass and flow (momentum) transport, the latter being the focus of this thesis. The fluid dynamics of polymers is described in several textbooks, including Bird *et al.* (1987), which is a key reference in the literature and presents rigorously the analysis of the constitutive equations used to model the non-Newtonian behaviour of complex fluids.

The understanding of the flow dynamics of non-Newtonian fluids in different types of geometries used in industrial applications is very important in order to optimize the production processes and also to improve the products' quality. Such fluids, with large polymeric molecules, frequently exhibit viscoelastic behaviour due to the stretching and coiling of the polymeric chains which can partially store and release energy. The elasticity of the non-Newtonian fluids leads to anisotropic normal stresses, which are responsible for the onset of secondary flows, elastic instabilities and complex phenomena, as shown in Boger and Walters (1993).

Flow instabilities usually occur at higher *Re*, such as the transition from laminar to turbulent flow with Newtonian fluids (Reynolds, 1883). In viscoelastic fluid flow another type of flow instability can occur, even under creeping flow conditions, known as (purely) elastic instabilities. The appearance of elastic instabilities depends on the fluid rheology, flow geometry, flow rate and also depends on other properties such as temperature, concentration and surface tension gradients.

Instabilities in viscoelastic flows result either from a combination of inertial and elastic effects, or from purely elastic effects when inertia is negligible. Despite several studies on flow instabilities, it still remains an interesting and important topic of research. The identification of the critical conditions for the onset of flow instabilities is currently a major

challenge, recently stimulated by the identification of a new flow regime coined as elastic turbulence (Groisman and Steinberg, 2000), which corresponds to a turbulent-like flow, that arises under creeping flow conditions.

Concerning the topology and the complexity of the flow geometries, some simplifications were taken to reduce the degrees of freedom, by reducing the complexity of the geometries and a few benchmark flow problems have been proposed to be investigated independently, in order to obtain accurate solutions for benchmarking purposes (Brown and McKinley, 1994). Some of the more important benchmark flow problems are the flow in a 4:1 contraction, the flow around a confined cylinder and the die (or extrudate) swell flow. The ubiquity of cylinder flow in many industrial processes, combined with the absence of geometrical singularities and the specificities and complexity of its flow characteristics, especially for viscoelastic fluids, made it an established benchmark (Brown and McKinley, 1994), which will be the major topic of investigation in this thesis.

1.1.4. Flow around a cylinder

In the 19th century, Stokes (1851) investigated theoretically the Newtonian fluid flow around submerged bodies. The analytical solution for the Newtonian flow around a sphere and the corresponding solution for drag coefficient were determined under negligible inertial conditions (also denoted as creeping flow, or Stokes flow).

Oseen (1910) improved Stokes' description to higher *Re* by the partial inclusion of convective acceleration. Lamb (1911) obtained the solution for viscous flow past a sphere and the expression for the drag force coefficient. Later, Proudman and Pearson (1957) obtained a more complete analytical solution for the flow past a sphere and a cylinder, by matching Stokes' solution near the sphere with Oseen's solution which is valid far away from the sphere.

Even before the proposal as a benchmark flow problem (Brown and McKinley, 1994), experimental and analytical investigations concerning the Newtonian fluid flow around a confined cylinder were reported in the literature. Comprehensive reviews on the state-of-the-art of the Newtonian flow around a cylinder were published in several works (Strouhal, 1878; Hiemenz, 1911; Von Kármán, 1911; Cantwell and Coles, 1983; Telionis *et al.*, 1992; Williamson, 1996; Zdravkovich, 1997, 2003) highlighting the complexity of the flow as *Re* is increased with the appearance of a recirculation downstream of the cylinder and

the subsequent formation of a vortex sheet at higher *Re*. The flow becomes more complex as *Re* is further increased, with the occurrence of 3D effects and eventually the flow becomes turbulent. A more detailed description of the state-of-the-art of the Newtonian fluid flow around a cylinder can be found in Chapter 3.

The flow around a cylinder is an important industrial flow that can be found in several applications involving non-Newtonian fluids as in heat exchangers, textile coating processes or in waste water treatment (Nishimura, 1986). Given the complexity of the flow around a cylinder, the non-Newtonian fluid flow remains not completely resolved, particularly for viscoelastic fluids, and for that reason the two-dimensional (2D) flow around a confined cylinder with 50% blockage ratio remains an interesting case for investigation and an open benchmark flow problem. The studies concerning the numerical solution of non-Newtonian fluid flow past a confined cylinder are usually based on 2D calculations, due to the inherent expensive computational resources required for more realistic three-dimensional (3D) simulations. The classical high Weissenberg number problem (HWNP) has also been an important limitation to obtain accurate numerical simulations, above a modest critical Deborah number of order one.

A schematic overview of the 2D benchmark flow around a confined cylinder in a planar channel with a blockage ratio of 50% is shown in Figure 1.1. The ratio between the cylinder diameter ($D = 2R$) and the channel width (H) defines the blockage ratio, $BR = D/H$.

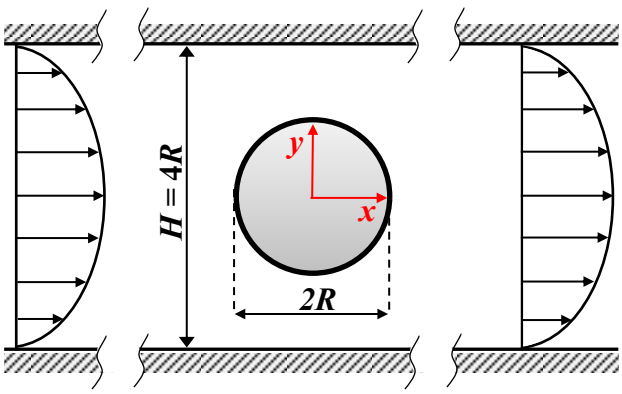

Figure 1.1. Schematic overview of the flow past a confined cylinder.

After the establishment as a benchmark case, the flow past a confined cylinder has been extensively studied experimentally and numerically from the steady symmetric creeping flow conditions up to the onset of flow instabilities. The experimental studies show that the practical implementation of the flow of viscoelastic fluids past a confined cylinder is

necessarily three-dimensional and it is clear that the characteristics can be significantly different from those predicted assuming 2D flow conditions.

McKinley *et al*. (1993) observed experimentally, for a cylinder with an aspect ratio (*AR* – ratio between the channel depth and the cylinder diameter) of 24, that at higher flow rates, when flow instabilities occur, the viscoelastic flow around the cylinder becomes highly 3D, with steady complex structures developing downstream of the cylinder along the spanwise direction. Increasing further the flow rate, led to the development of a second elastic instability with the occurrence of time-dependent flow. More recently, Verhelst and Nieuwstadt (2004) showed the appearance of 3D effects near the side walls in the flow past a confined cylinder in a rectangular duct with 50% blockage, for an aspect ratio of 16. Some studies concerning the viscoelastic fluid flow around a cylinder refer to the enhancement of mixing, dispersion, and effects upon the flow separation (Kim *et al.*, 2008). Recently Grilli *et al.* (2013) showed that the flow past a series of two or more cylinders at low *Re* could lead to the onset of elastic turbulence in the downstream straight channel for $Wi > 5.4$. The ability of using the flow past a cylinder to induce mixing is particularly relevant and is also a motivation for the research in this thesis. A more detailed description of the numerical and experimental works concerning the non-Newtonian fluid flow around a single cylinder in a channel can be found in Chapters 4 and 5.

1.1.5. Macro- versus micro-scale flows

Low Reynolds number flows of viscoelastic fluids in macro-scale geometries, with characteristic dimensions above ≈ 1 mm are difficult to achieve for low viscosity fluids. The reduction in the size of microfluidic devices, with characteristic dimensions on the order of 10 – 100's μm, leads to a reduction of the Reynolds number and for viscoelastic fluids it also strongly increases the Deborah number, which is inversely proportional to the length scale. Thus, flows of viscoelastic fluids at the micro-scale can be highly elastic, even for dilute polymer solutions, a flow condition that is impracticable to attain at the macro-scale. By scaling down flows to micro-scale, one can investigate non-Newtonian creeping flows, and the onset of purely elastic flow instabilities.

At the macro-scale the observed phenomena around the cylinder are less surprising than at the micro-scale, due to the weaker elastic conditions. However, the higher inertial conditions achieved at the macro-scale, which are less practical to attain at the micro-scale, allows the quantification of the inertial contribution in the non-Newtonian flow, and the analysis of

inertio-elastic instabilities. By looking at both macro- and micro-scale flows using the same fluid, the various flow characteristics can be achieved over a much wider range in the *De-Re* parameter space, as illustrated in Figure 1.2. A direct comparison between the macro- and micro-scale flows of a viscoelastic fluid can be found in Chapter 5.

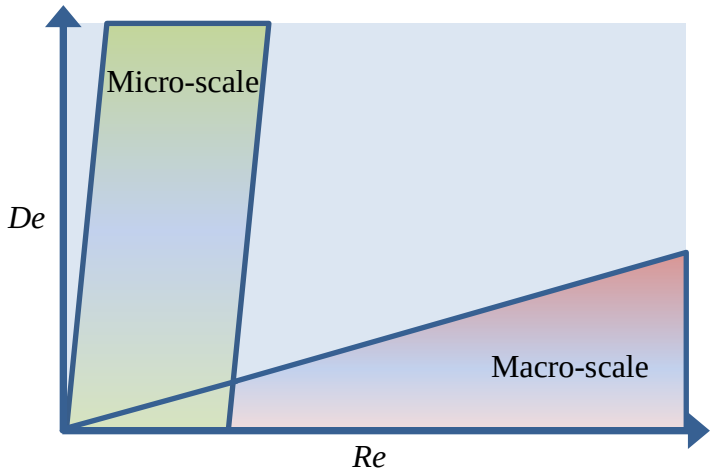

Figure 1.2. Operating space in a *De-Re* map typically observed at the macro- and micro-scales. Adapted from Oliveira *et al.* (2012).

1.1.6. Micro-scale flow

Progress in understanding microfluidic phenomena over the past decades has driven the development of lab-on-a-chip systems or micro total analysis systems (μTAS). The scale-down of laboratory functions and processes has found a range of applications in biological and chemical sciences, and in medicine, such as analysis of DNA molecules, cell sorting and manipulation, but also in engineering applications such as process intensification systems with increase heat or mass transfer rates, or inkjet printing heads.

Microfluidic devices have the advantages of a reduced consumption of materials and reagents, the reduction of the size of equipment, fast analysis, high sensitivity, and short reaction times (Oliveira *et al.*, 2012). Beyond the commercial and economic advantages, the use of microfluidic devices allows the development of real microenvironments, which are determinant in biological, medicine and chemical applications, and also allows the use of precisely controlled fluid flows (Kim *et al.*, 2008).

The developments in miniaturization allow the integration of several components in microfluidic devices such as pumps, valves, filters, separators and mixers (Kim *et al.*, 2008). Using complex fluids with viscoelastic behaviour, and given the highly elastic flow

conditions that naturally arise at the micro-scale, it is no surprise that purely elastic instabilities will occur, which can be used to promote passive mixing and enhance active mixing. Micromixing is only one aspect on the vast landscape of microfluidics applications, as the recent review of Suh and Kang (2010) shows, and the use of cylindrical obstacles in microfluidic devices has particular applications in the improvement of micromixing.

A more detailed description of the state-of-the-art of Newtonian and viscoelastic fluid flows in microfluidic devices is carried out in each of the results chapters of this thesis (Chapters 5 to 8), with particular focus on the use of cylindrical obstacles to induce elastic instabilities.

1.1.7. Computational rheology

Besides the experimental and purely analytical approaches to analyse fluid dynamics problems, numerical methods can also be employed in the so-called Computational Fluid Dynamics (CFD) approach. When the CFD techniques are used to model complex fluid flow behaviour, this field of research is known as computational rheology. Since the early developments, it was recognized that the numerical solutions obtained in computational rheology are strongly dependent on the adequacy of the rheological equations used to describe the non-Newtonian fluids. In classical Newtonian fluid mechanics, the rheological equation of state is exact, and using accurate numerical techniques one should be able to model adequately the flow of these fluids under laminar flow conditions. In the case of complex fluids, there are many constitutive equations that can be used, but unfortunately none of them is universally valid to model accurately the flow of complex fluids in complex flows.

In this thesis, numerical calculations were carried out using the numerical code developed in the host research group (CEFT – "Centro de Estudos de Fenómenos de Transporte") over the last two decades, with the aim to establish a direct comparison with the experimental results and explore additional characteristics of the flows which are difficult to measure.

The first developments in computational rheology occurred between the end of 1960's and the beginning of 1970's. The review published by Crochet and Walters (1983) and the book of Crochet *et al.* (1984) present the major developments since the early works on computational rheology. Later on, the review of Owens and Phillips (2002) presents the subsequent developments in computational rheology and remains an excellent bibliographic source for the most relevant works in computational rheology up to 2002. Since the early

numerical works using non-Newtonian fluids, the calculations showed problems of convergence and accuracy, even for low Deborah number (or Weissenberg number) flows. This problem to achieve convergence of the numerical solutions became known as the High Weissenberg Number Problem (HWNP) (Crochet and Walters, 1983; Keunings, 1986; Owens and Phillips, 2002). This numerical problem is related with the existence of a (modest) limit in the Weissenberg number above which the numerical calculations diverge. The limit Weissenberg number is more critical when there are geometric singularities in the flow, as happens in the re-entrant corner in contraction flows. Considering the limitations imposed by the HWNP, the field of computational rheology is very demanding and a motivation for several investigations.

The behaviour of non-Newtonian fluids in complex flows is intimately linked to the distribution of molecular conformations in the flow field. Macroscopic field variables such as the extra-stress and velocity are strongly coupled to microscopic quantities such as the stretch and orientation of polymer molecules, and they influence and determine the magnitude of each other. Recent advances in computational rheology led to the development of micro-macro methods that are capable of resolving information at various length and time scales. However, because of high computational cost, most numerical simulations are still based on a macroscopic approach of continuum mechanics, where the conservation laws of mass and momentum are solved with an adequate closed-form constitutive equation that relates the stress to the deformation history, without explicitly accounting for the microstructure variations.

Considering the isothermal laminar flow of an incompressible fluid, the governing equations are the mass conservation,

$$\nabla \cdot \mathbf{u} = 0, \tag{1.5}$$

and the momentum equation,

$$\rho\left(\frac{\partial \mathbf{u}}{\partial t} + \nabla \cdot \mathbf{uu}\right) = -\nabla p + \nabla \cdot \boldsymbol{\tau}, \tag{1.6}$$

where $\mathbf{u}$ represents the velocity vector, ρ the fluid density, t the time, p the pressure and $\boldsymbol{\tau}$ the extra-stress tensor, which is given as a sum of a Newtonian solvent and a polymeric contribution ($\boldsymbol{\tau} = \boldsymbol{\tau}_s + \boldsymbol{\tau}_p$). The solvent contribution is given by:

$$\boldsymbol{\tau}_s = \eta_s(\nabla\mathbf{u} + \nabla\mathbf{u}^T), \tag{1.7}$$

where η_s is the solvent viscosity.

The constitutive equation used in the numerical prediction of non-Newtonian fluid flows depends on the rheological properties of the fluid (Bird *et al.*, 1987). Despite the existence of several rheological models in the literature, the following models were used in this thesis to predict non-Newtonian flows: Carreau and Carreau-Yasuda Generalized Newtonian fluid models (GNF); Oldroyd-B model.

A detailed description of each constitutive equation used and the details of the meshes used in the numerical simulations can be found in Chapters 3 to 7.

1.2. Objectives

The main goal of this work is to advance our knowledge on the complex fluid flow around a confined cylinder, at macro- and micro-scales, using Newtonian and viscoelastic fluids.

To achieve the main goal of this research, the work plan was divided as follows:

(i) Study the macro-scale flow of Newtonian and viscoelastic fluids around a confined cylinder using different aspect ratios (*AR* – ratio between the channel depth and the cylinder diameter) at a blockage ratio of 50%;

(ii) Study the micro-scale flow of Newtonian and viscoelastic fluids around a confined cylinder using different aspect and blockage ratios.

Regarding objective (i), the effect of the aspect ratio (*AR*) on the Newtonian and on the viscoelastic fluid flow in a rectangular duct at macro-scale (width of duct 20 mm; depth of duct variable from 20 mm to 160 mm), where a cylinder is positioned at the mid plane to define a symmetric geometry with a 50% area blockage, was carried out to assess the influence of flow inertia and viscoelasticity in the complex three dimensional flow, from low flow rates up to the critical conditions for onset of inertial and elastic instabilities, respectively for Newtonian and viscoelastic fluids.

The proposed objective (ii) concerns the flow of Newtonian and viscoelastic fluids in microfluidic devices with channel width and depth in the range of 50 - 200 μm. The effect of the aspect ratio (*AR*) and the blockage ratio (*BR*) on the flow around a confined cylinder was

carried out to investigate the elastic instabilities that arise at highly elastic flow conditions, under creeping flow. As expected for Newtonian fluids there is no dramatic change as we move to smaller scales, although the opposite is expected for the complex viscoelastic fluids due to the different elasticity numbers at different length scales. Regarding the studies in microfluidic devices, it is also intended to explore the flow kinematics through an array of cylinders, which can be used to promote and enhance efficient mixing, or use as post arrays for collecting large molecules, such as DNA.

To achieve the proposed objectives, a combined experimental and numerical research work was carried out to investigate the Newtonian and viscoelastic fluid flows past a confined cylinder, from the creeping flow conditions ($Re \rightarrow 0$) up to the onset of time-dependent flow. The experiments were conducted with Newtonian fluids and with viscoelastic fluids, namely: constant viscosity fluids (so called Boger fluids), based on aqueous solutions of glycerine and polyacrylamide at different concentrations; shear-thinning viscoelastic fluids, based on aqueous solutions of polyacrylamide; wormlike micellar solution. The use of Boger fluids allows the isolation of viscoelastic effects, without the added complexity of shear-thinning effects.

The specificities of the complex fluid flows assessed in a complex three dimensional geometry lead to a compilation of valuable experimental data that can be used for validation purposes of numerical methods. The experiments rely on flow visualization studies using long time exposure streak photography, detailed velocity measurements using a particle image velocimetry (PIV) and pressure drop measurements.

Regardless of the dominant experimental component of this work, numerical calculations were also carried out using the numerical code developed in the host research group over the last two decades (Oliveira *et al.*, 1998; Alves *et al.*, 2003; Afonso *et al.*, 2009) for Newtonian and viscoelastic fluids, using the different viscoelastic models fitted to the measured rheology of the fluids.

1.3. Dissertation Outline

This dissertation is composed of three main parts:

Part I includes Chapter 1 – Introduction and Chapter 2 – Experimental.

The present section (included in Part I), summarizes the outline of this thesis and closes Chapter 1. This chapter described the theoretical concepts and important approaches inherent to the subject matter of this dissertation (1.1 Subjects) and present a description of the objectives of this research work (1.2. Objectives).

Chapter 2 describes the experimental set-ups used at the macro- and micro-scales, the experimental techniques used, detailing the inherent differences for each length scale, and the composition and the rheological characterization of the fluids used in the experiments.

Part II is composed of 6 chapters, each one based on a scientific paper. The papers either have been published, or are under final preparation, except chapter 8, and have all been prepared during the course of this work. These are Chapters 3 to 8, as described below:

Chapter 3: Three-dimensional effects in laminar flow past a confined cylinder (Ribeiro *et al.*, 2012).

Chapter 4: Viscoelastic fluid flow past a confined cylinder: three dimensional effects and stability.

Chapter 5: Viscoelastic fluid flow past a confined cylinder: a comparative study between macro- and micro-scales.

Chapter 6: Aspect ratio effect upon the viscoelastic fluid flow past a confined cylinder in microfluidic devices.

Chapter 7: Blockage ratio effect upon the viscoelastic fluid flow past a confined cylinder in a microfluidic channel.

Chapter 8: Viscoelastic fluid flow past an array of cylinders.

Finally, **Part III** summarizes the main conclusions of this thesis and highlights important topics for future research work in Chapter 9 – Conclusions and future work.

References

Afonso, A., Oliveira, P.J., Pinho, F.T., Alves, M.A., 2009. The log-conformation tensor approach in the finite-volume method framework. J Non-Newton Fluid Mech 157, 55-65.

Alves, M.A., Oliveira, P.J., Pinho, F.T., 2003. A convergent and universally bounded interpolation scheme for the treatment of advection. Int J Numer Meth Fl 41, 47-75.

Barnes, H.A., 1999. The yield stress - a review of "panta rhei" - everything flows? J. Non-Newton Fluid Mech 81, 133-178.

Bird, R.B., Armstrong, R.C., Hassanger, O., 1987. Dynamics of polymeric liquids. John Wiley and Sons, New York.

Boger, D.V., Walters, K., 1993. Rheological phenomena in focus. Elsevier, Amsterdam.

Brown, R.A., McKinley, G.H., 1994. Report on the VIIIth Int Workshop on numerical - methods in viscoelastic flows. J Non-Newton Fluid Mech 52, 407-413.

Cantwell, B., Coles, D., 1983. An experimental study of entrainment and transport in the turbulent near wake of a circular cylinder. J Fluid Mech 136, 321-374.

Crochet, M.J., Davies, A.R., Walters, K., 1984. Numerical simulation of non-Newtonian flow. Elsevier, Amsterdam.

Crochet, M.J., Walters, K., 1983. Numerical methods in non-Newtonian fluid mechanics. Annu Rev Fluid Mech 15, 241-260.

Dealy, J.M., 2010. Weissenberg and Deborah numbers - Their definition and use. Rheology Bulletin, 14-18.

Grilli, M., Vazquez-Quesada, A., Ellero, M., 2013. Transition to turbulence and mixing in a viscoelastic fluid flowing inside a channel with a periodic array of cylindrical obstacles. Phys Rev Lett 110, 174501.

Groisman, A., Steinberg, V., 2000. Elastic turbulence in a polymer solution flow. Nature 405, 53-55.

Hiemenz, K., 1911. Die Grenzschicht an einem in dem gleichförmigen Flüssigkeitsstrom eingetauchten geraden Kreiszylinder. University of Göttingen, Germany.

Hooke, R., 1678. De Potentia Restitutiva (or of Spring Explaining the Power of Springing Bodies). London.

Keunings, R., 1986. On the High Weissenberg Number Problem. J Non-Newton Fluid Mech 20, 209-226.

Kim, S.M., Lee, S.H., Suh, K.Y., 2008. Cell research with physically modified microfluidic channels: A review. Lab Chip 8, 1015-1023.

Lamb, H., 1911. On the Uniform Motion of a Sphere through a Viscous Fluid. Philos Mag 21, 112-121.

Malkin, A.Y., 1994. Rheology fundamentals. ChemTec Publishing, Canada.

McKinley, G.H., Armstrong, R.C., Brown, R.A., 1993. The Wake Instability in Viscoelastic Flow Past Confined Circular-Cylinders. Philos T Roy Soc A 344, 265-304.

Morrison, F.A., 2004. What is Rheology Anyway. Rheology Bulletin 73, 8-10.

Newton, S.I., 1687. Philosophiae Naturalis Principia Mathematica. London.

Nishimura, T., 1986. Flow across tube banks. In: Cheremisinoff, P. (Ed.), Encyclopedia of Fluid Mechanics. Gulf Publishing Company, pp. 763-785.

Oliveira, M.S.N., Alves, M.A., Pinho, F.T., 2012. Microfluidic flows of viscoelastic fluids. Chapter 6 in Transport and Mixing in Laminar Flows: From Microfluidics to Oceanic Currents. Wiley - VCH Verlag.

Oliveira, P.J., Pinho, F.T., Pinto, G.A., 1998. Numerical simulation of non-linear elastic flows with a general collocated finite-volume method. J Non-Newton Fluid Mech 79, 1-43.

Oseen, C.W., 1910. Über die Stokes'sche formel und über eine verwandte Aufgabe in der Hydrodynamik. Arkiv. Matem. Astron. Fysik, 1-20.

Owens, R.G., Phillips, T.N., 2002. Computational rheology. Imperial College Press, London.

Poole, R.J., 2012. The Deborah and Weissenberg numbers. Rheology Bulletin, 32-39.

Proudman, I., Pearson, J.R.A., 1957. Expansions at Small Reynolds Numbers for the Flow Past a Sphere and a Circular Cylinder. J Fluid Mech 2, 237-262.

Reiner, M., 1964. The Deborah Number. Phys Today 17, 62-62.

Reynolds, O., 1883. An experimental investigation of the circumstances which determine whether the motion of water shall be direct or sinuous and the law of resistance in parallel channels. Philosophical Transactions of the Royal Society 935-982.

Ribeiro, V.M., Coelho, P.M., Pinho, F.T., Alves, M.A., 2012. Three-dimensional effects in laminar flow past a confined cylinder. Chem Eng Sci 84, 155-169.

Stokes, G.G., 1851. On the effect of the internal friction of fluids on the motion of pendulums. Transactions of the Cambridge Philosophical Society 9, 8.

Strouhal, V., 1878. Ueber eine besondere Art der Tonerregung. Annalen der Physik 241, 216-251.

Suh, Y.K., Kang, S., 2010. A Review on Mixing in Microfluidics. Micromachines, 82-111.

Telionis, D.P., Gundappa, M., Diller, T.E., 1992. On the Organization of Flow and Heat Transfer in the Near Wake of a Circular Cylinder in Steady and Pulsed Flow. J Fluid Eng-Trans ASME 114, 348-355.

Verhelst, J.M., Nieuwstadt, E.M., 2004. Visco-elastic flow past circular cylinders mounted in a channel: experimental measurements of velocity and drag. J Non-Newton Fluid Mech 116, 301-328.

Von Kármán, T., 1911. Über den Mechanismus des Widerstandes, den ein bewegter Körper in einer Flüssigkeit erfährt. Göttingen Nachr. Math. Phys. Kl. 12, 509-517.

Williamson, C.H.K., 1996. Vortex Dynamics in the Cylinder Wake. Annu Rev Fluid Mech 28, 477-539.

Zdravkovich, M.M., 1997. Flow around circular cylinders. Vol 1: Fundamentals. Oxford University Press New York.

Zdravkovich, M.M., 2003. Flow around circular cylinders. Vol 2: Applications. Oxford Universtiy Press, New York.

Chapter 2

Experimental

The investigation of this thesis is essentially experimental and is described separately in chapters for each of the studies conducted. However, to better understand the scope of all the work developed, this chapter summarizes the design of the experimental set-up at the macro- and micro-scales, the techniques, principles and procedures, the selection of the test fluids, and their composition and rheological characterization.

2.1. Experimental set-ups

2.1.1. Macro-scale experimental set-up

The experimental set-up used at the macro-scale is shown in Figure 2.1. It is a closed system composed by a rectangular perspex test section and two reservoirs. The fluid flows through the rectangular test section by gravity (from reservoir R1 to reservoir R2) and a variable speed peristaltic pump (Pp) (ref. Lav 400 L/h, Dosim) is used to move the fluid back to the constant head reservoir R1, in order to maintain a constant liquid level (Lev) at the upper reservoir with the help of the overflow discharge pipe fitted with valve V3 (normally fully opened). During the measuring phase the pump is switched off, in order to be able to measure the flow rate by registering the change with time of the fluid weight in reservoir R2 using a digital balance (KERN DS 36k0.5; readout of 0.5g; maximum range of 36 kg) that is placed under reservoir R2 (during short time of the weighing, about 20 s, the liquid level variation in reservoirs R1 and R2 is small and the flow rate remains approximately constant). This balance is connected to a computer using a RS232 interface and the measured weight is monitored by LabView v7.1 software.

The flow rate in the test section is adjusted by changing the reservoir R1 height and through proper selection of the valves V1 and V2, with V1 fully opened for low flow rates and valve V2 or valves V1 and V2 fully opened for higher flow rates. All the valves are always fully opened (or closed) to minimize fluid degradation. The tubes connecting valves V1 and V2 to the test section have different diameters, which are selected according to the range of required flow rates.

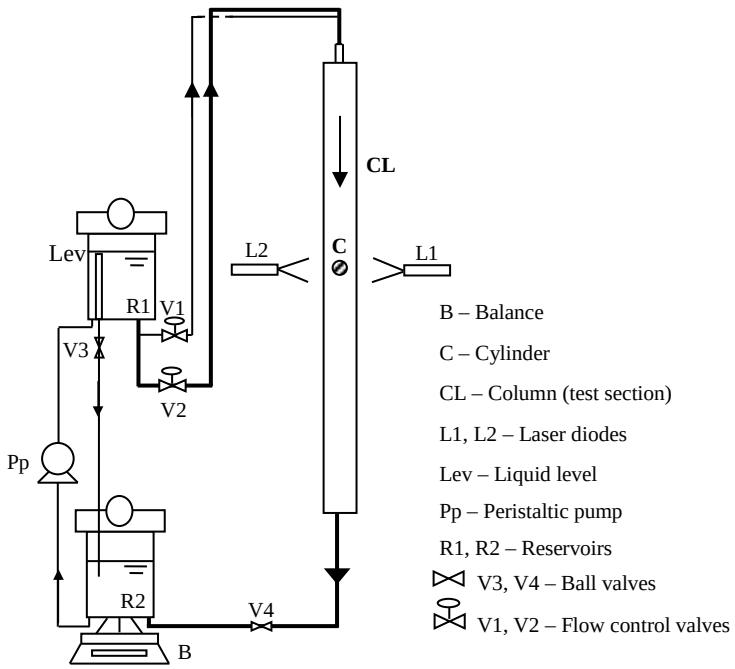

Figure 2.1. Schematic representation of the experimental set-up used at the macro-scale.

Figure 2.2 shows the test section, which is a 1700 mm long duct, machined in perspex, with a rectangular cross section having a width (H) of 20.0 mm and a variable depth (h), where the confined cylinder with D = 10.0 mm diameter is located. The cylinder is located 630 mm downstream of the duct inlet and is positioned at the mid plane to define a symmetric geometry with a 50% area blockage ($BR = D/H$). One of the end walls (parallel to the xy plane) can be moved along the spanwise direction (z) in order to change the depth (h), and consequently the aspect ratio ($AR = h/D$) of the geometry. The three different aspect ratios used, with the corresponding dimensions of the rectangular duct are listed in Table 2.1.

The coordinate system represented in Figure 2.2 has its origin at the centre of the cylinder, with the positive *x*-axis in the streamwise downstream direction, the *y*-axis in the cross-stream direction (normal to the side walls) and the *z*-axis along the spanwise direction (aligned with the cylinder axis).

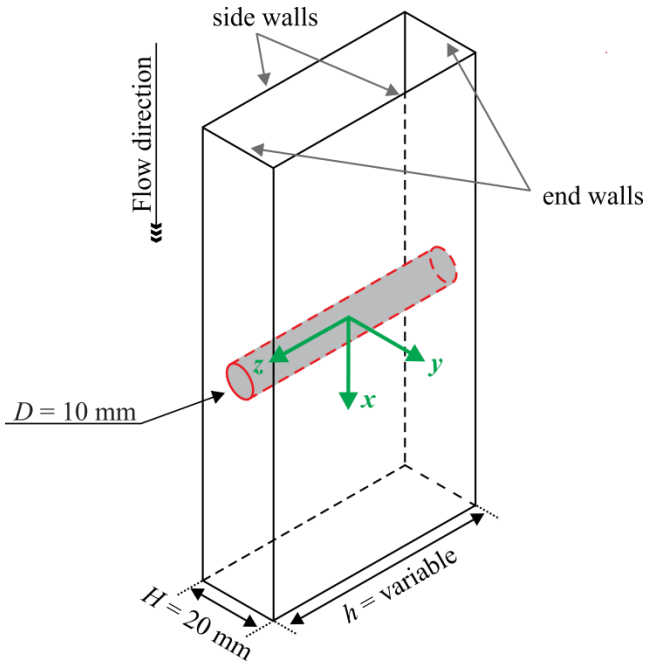

Figure 2.2. Test section with confined cylinder and coordinate system.

Table 2.1. Aspect ratios under study and corresponding duct dimensions.

	AR = 16	*AR* = 8	*AR* = 2
h (mm)	160.0	80.0	20.0
H (mm)	20.0	20.0	20.0

Figure 2.3 shows a photograph of the macro-scale experimental set-up, taken during the experiments. As can be observed, the duct inlet has a distributor with a maximum of six injectors (20 mm internal diameter) to ensure as much as possible a uniform velocity profile at the inlet of the rectangular duct. When is needed, spacers were used between the fixed and the moving end walls (cf. Figure 2.3), to ensure a constant width along the duct test section.

For the range of Reynolds number investigated, the distance between the distributor and the cylinder under study allows for a fully-developed velocity profile to be achieved well upstream of the cylinder. The exit is also sufficiently far away not to affect the flow dynamics in the vicinity of the cylinder.

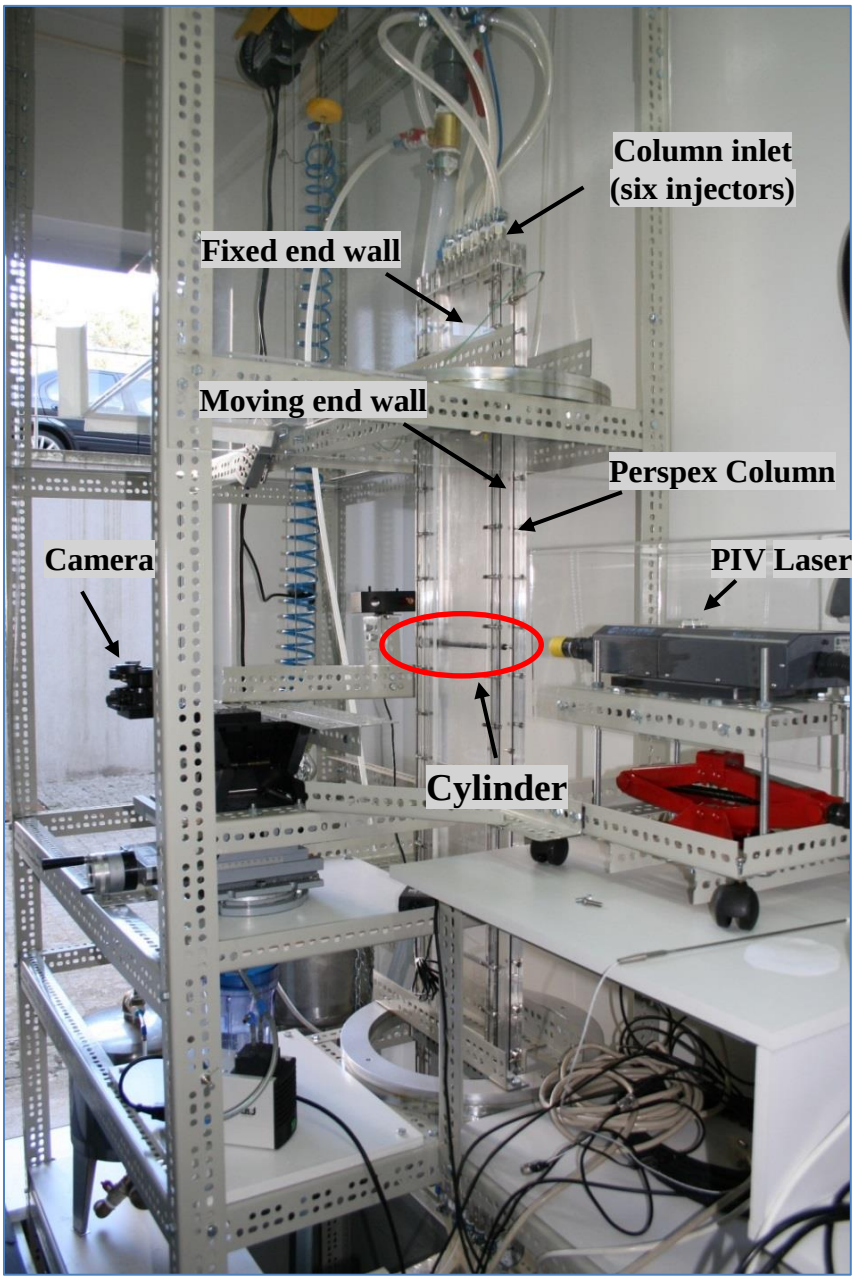

Figure 2.3. Experimental macro-scale set-up.

2.1.2. Micro-scale experimental set-up

The microgeometries used in this work were fabricated in polydimethylsiloxane (PDMS) (Sylgard 184, Dow Corning), from SU-8 reusable moulds, using the standard soft-lithography techniques (McDonald *et al.*, 2000). The final PDMS microchannels obtained by replication in the SU-8 mould were imaged in the inverted microscope set-up. A detailed description of the procedure used to fabricate the microchannels is presented in Appendix A.

Two types of micro-geometries were studied at the micro-scale. The first geometry was a confined cylinder placed right at the centreplane of the microchannels having a rectangular cross-section. The specific dimensions of the cylinder and of the channel are presented in Table 2.2. The second geometry consisted of an array of cylinders also placed inside microchannels of rectangular cross-section. The dimensions of the microchannels were measured by a scanning electron microscope (SEM) FEG-ESEM/EDS/EBSD (FEI Quanta 400FEG ESEM/EDAX Genesis X4M).

Regardless of the microfluidic devices used, a syringe pump (Nemesys, Cetoni GmbH) was used to inject the fluid and control the flow rate in the microchannels. Syringes (Hamilton) with different volumes (10 μl − 2 ml) were used, according to the desired flow rate, and were connected to the microgeometries using Tygon tubing with an internal diameter of 0.44 mm.

Confined cylinder

The microchannels width (H) is constant and equal to 212 μm but different depths (h) were used in order to obtain different aspect ratios. As shown in Figure 2.4, the cylinder diameter is also variable to obtain blockage ratios of 25%, 50% and 75%. The different blockage ratios and aspect ratios obtained with the corresponding dimensions of the microchannels are summarized in Table 2.2.

The cylinder is located at the same distance from the inlet and outlet of the microchannel, which is sufficient to allow a fully-developed velocity profile to occur well upstream of the cylinder and the outlet is also sufficiently far away not to affect the flow dynamics in the vicinity of the cylinder. The cylinder inside the channel is located at the centreplane of the channel, in all cases.

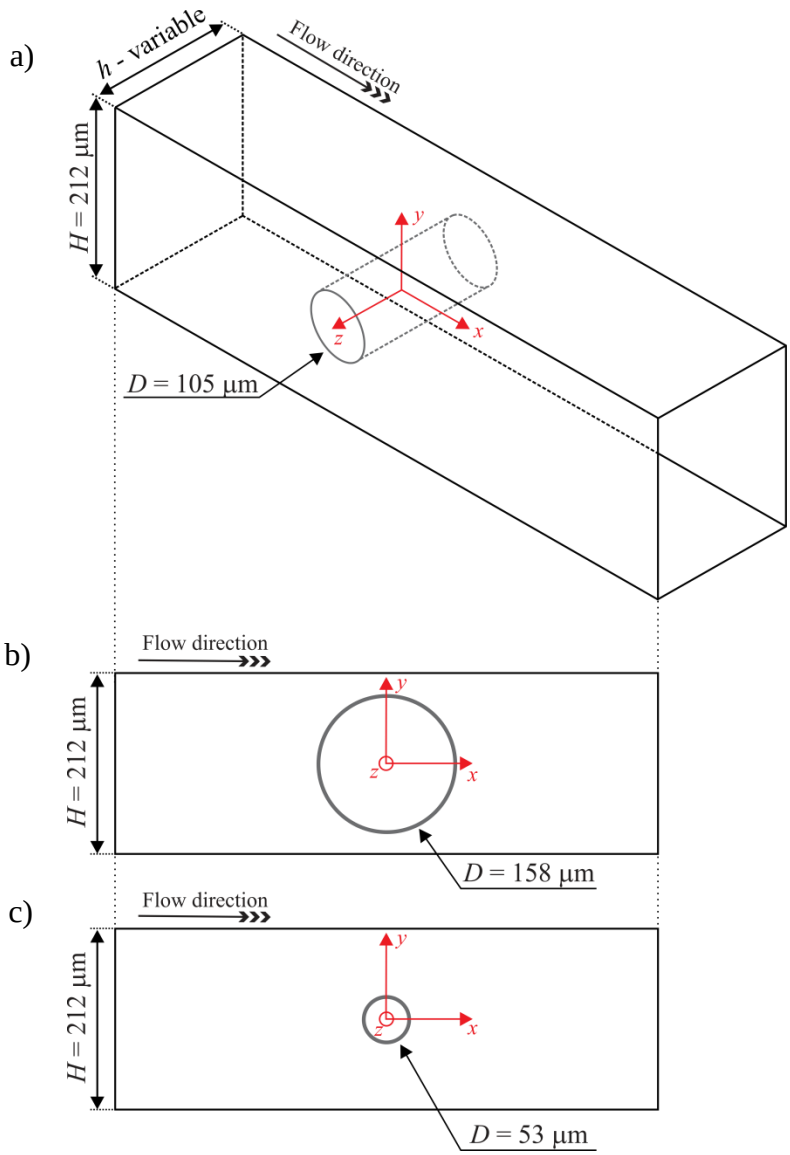

Figure 2.4. Schematic of the microfluidic devices with a confined cylinder: a) 3D view for *BR* = 50%; b) front view for *BR* = 75%; c) front view for *BR* = 25%.

Table 2.2. Dimensions of the microgeometries.

Width - *H* (μm)	Cylinder Diameter - *D* (μm)	*BR* = (*D*/*H*)	Depht – *h* (μm)	*AR* = (*h*/*D*)
212	53	25%	213	4.0
			105	2.0
			58	1.1
	105	50%	213	2.0
			105	1.0
			58	0.55
	158	75%	213	1.3
			105	0.66
			58	0.37

Figure 2.5 shows a photograph of a fabricated microfluidic device made of PDMS used in the experiments. The device shown was made from the mould with h = 105 μm and each of the three observable channels corresponds to a different *BR*. At this scale, the cylinder is not visible by the human eye.

Figure 2.6 shows SEM images of the microchannel used for AR = 0.55 and BR = 50%. The quality of the micro-manufacturing is good with well-defined vertical walls and a smooth well shaped cylinder.

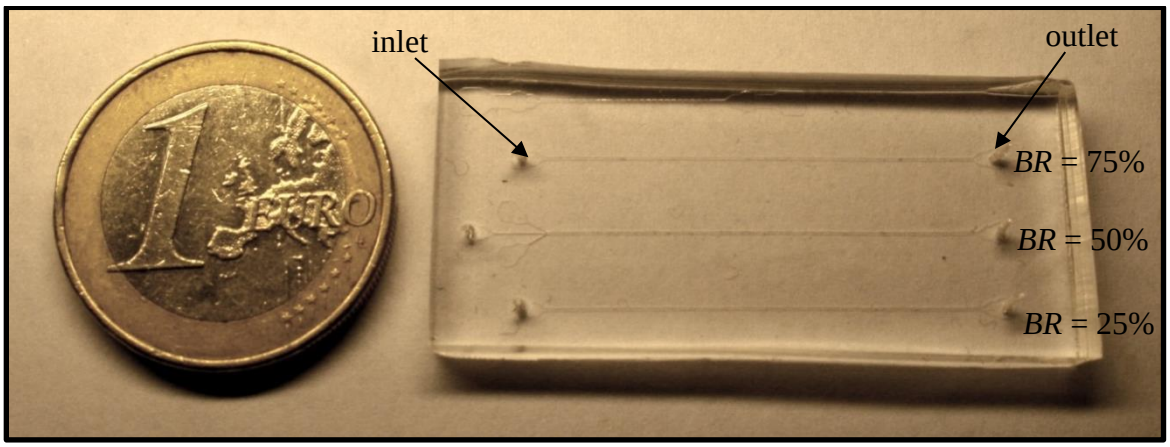

Figure 2.5. Microfluidic device fabricated in PDMS with h = 105 µm.

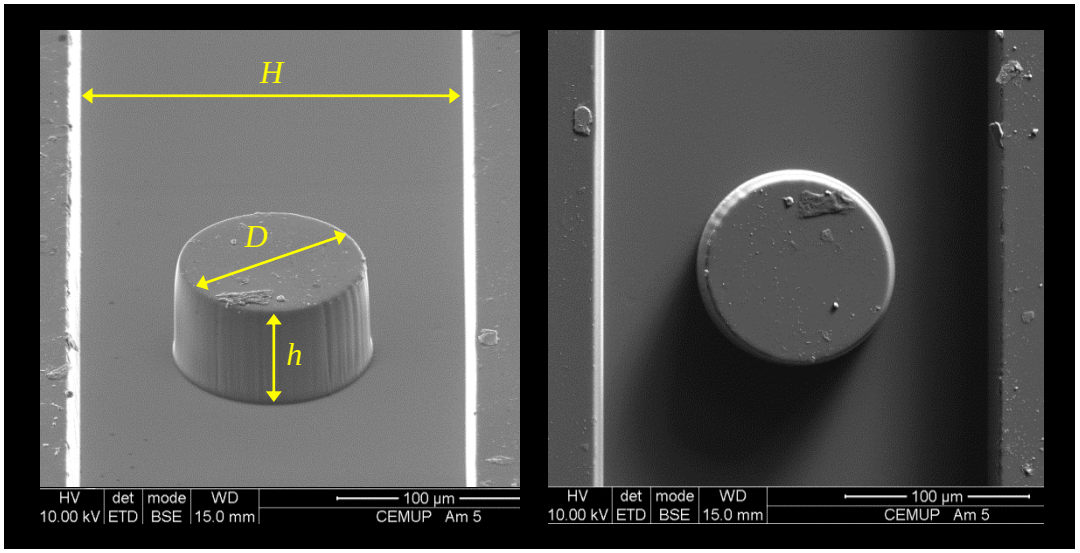

Figure 2.6. SEM image of the microfluidic device for AR = 0.55 and BR = 50%.

Arrays of cylinders

The microgeometries with arrays of cylinders were made with staggered and aligned configurations, to study their influence upon the flow characteristics. As can be observed in Figure 2.7, the width of the microchannels is H = 632 µm and 624 µm, depending on the configuration, and the depth (h) is 158 µm. The cylinders diameter (D) is constant and equal to 105 µm. The minimum interstitial space (e) between the cylinders is 50 µm for the staggered configuration and 14 µm for the aligned configuration.

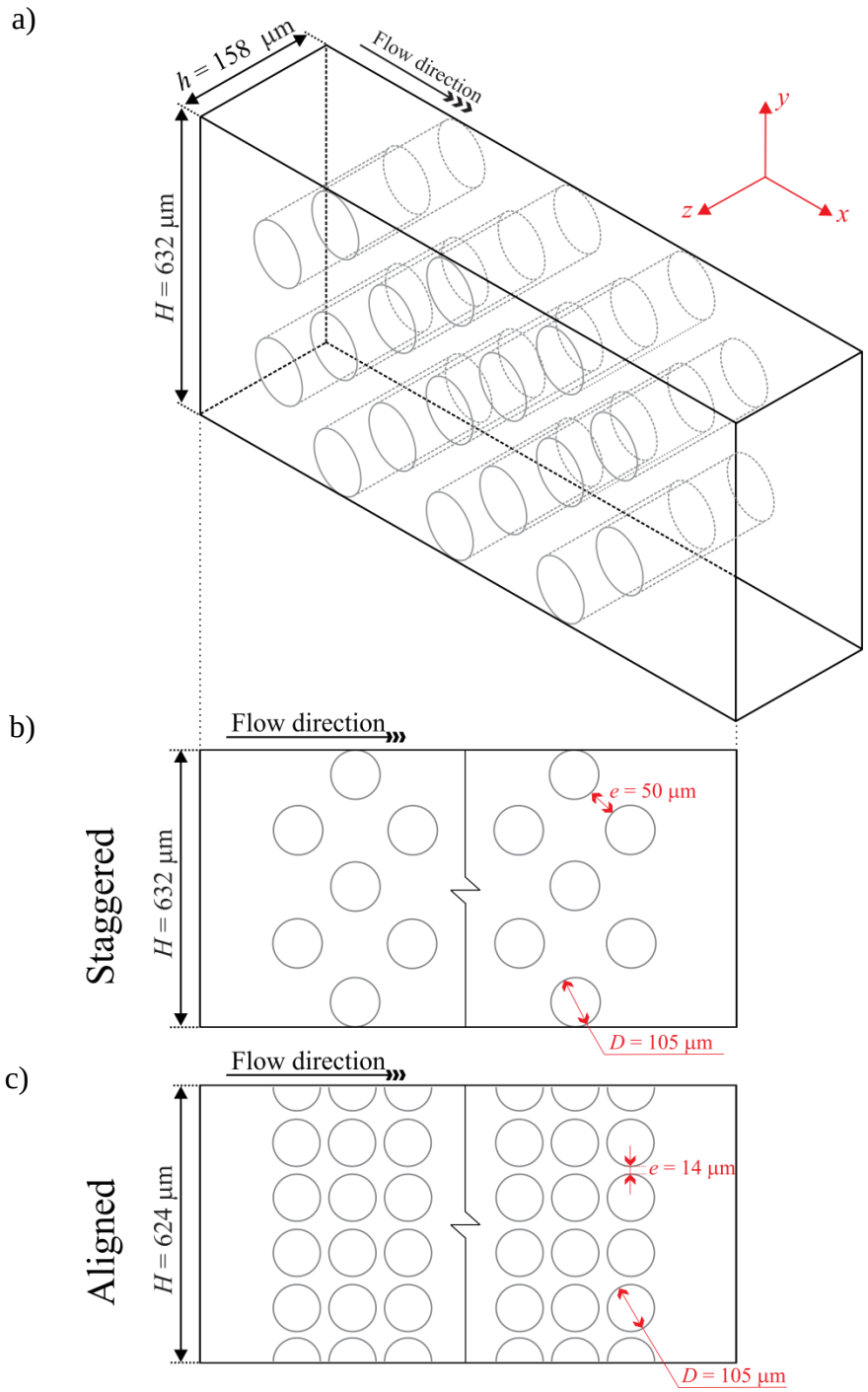

Figure 2.7. Schematic of the microfluidic arrays of cylinders: a) 3D view of the staggered configuration; b) front view of the staggered configuration; c) front view of the aligned configuration.

After the inlet and upstream of the outlet of the microchannels there are pressure taps to allow for the measurement of the pressure drop (Δp) across the cylinder arrays. The inlet port is sufficiently far upstream to achieve a fully-developed velocity profile well upstream of the region of interest.

Figure 2.8 shows SEM images of the microfluidic devices with arrays of cylinders in the staggered and aligned configurations, confirming the good manufacturing quality with well-defined walls and smooth well-shaped cylinders.

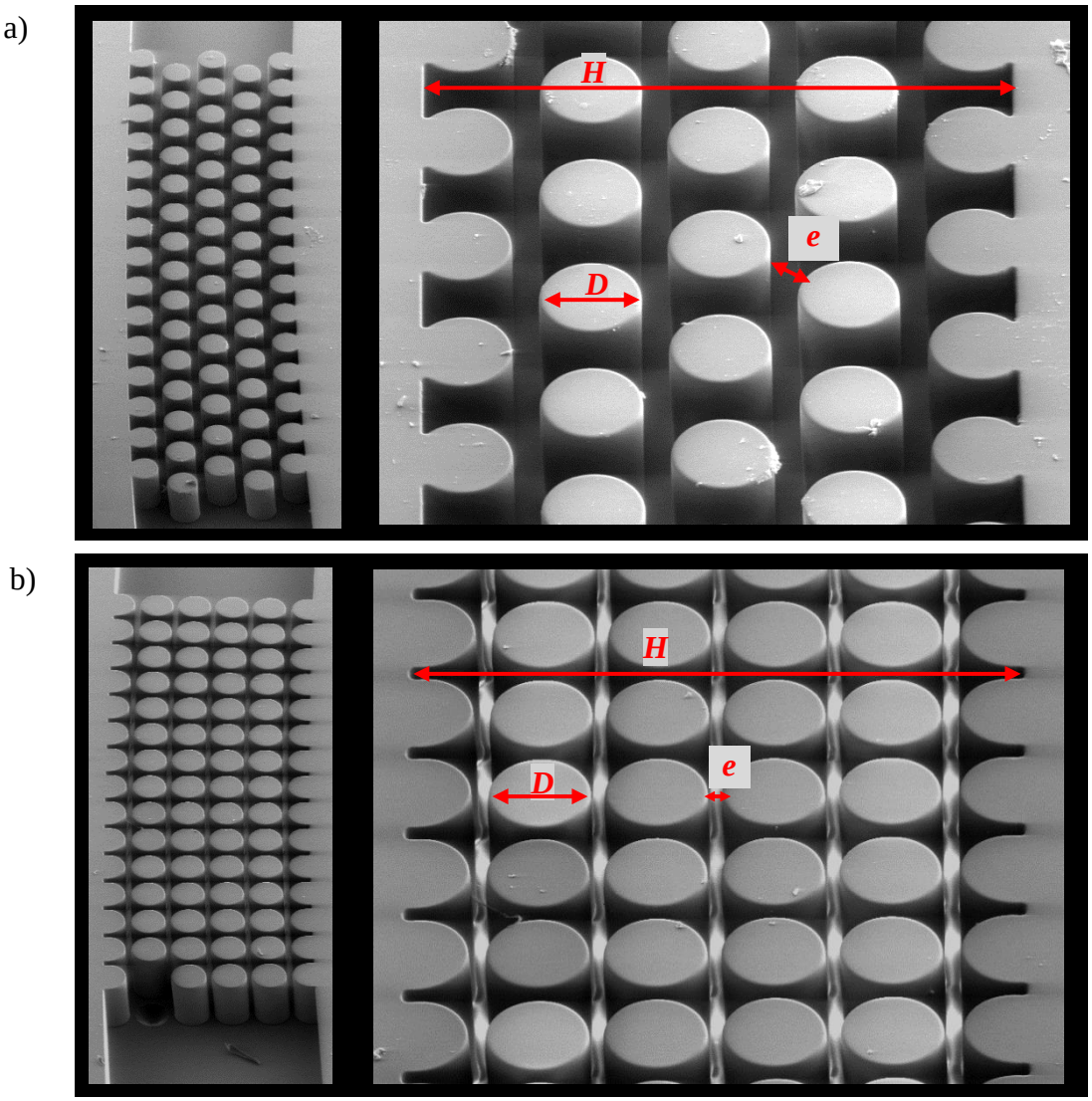

Figure 2.8. SEM images of the microfluidics devices with arrays of cylinders: a) staggered configuration; b) aligned configuration.

2.2. Experimental techniques

The dynamics of the fluid flow was characterised by imaging techniques, which provide qualitative and quantitative information. In this work, the flow field was characterised through flow visualizations (section 2.2.1) using long time exposure streak photography to obtain the pathlines, and particle image velocimetry, PIV, (section 2.2.2) to measure velocity fields. The flow rate control is done using a syringe pump and pressure drop measurements were done, as described below. In the following sections, each technique will be described in detail, considering the specific assumptions inherent to each length scale.

2.2.1. Flow visualization

The flow visualizations were taken using long time exposure streak photography to capture the path traveled by suspended tracer particles over a determined time, as described below.

2.2.1.1. *Macro-scale*

The flow was illuminated by two co-planar 635nm 5mW laser diodes L1 and L2 (Vector, model 5200-20), represented in Figure 2.1, equipped with a cylindrical lens to create a light sheet placed normal to the cylinder axis. The use of two laser diodes, instead of only one, was used to minimize shadows around the cylinder. The fluids were seeded with reflective tracer particles (hollow glass spheres with 10 μm diameter – HGS-10, Dantec Dynamics; ρ: 1100 kg/m^3) at a concentration of 30 ppm (w/w) and the reflected light was captured by a digital camera (CANON EOS 30D) equipped with a macro lens (EF100mm, f2.8). The exposure time in the visualizations was varied according to the flow rates of the experiments. The experimental apparatus included a manual *xy* traverse table to allow the simultaneous movement of the two laser diodes and the digital camera to minimize the required alignment adjustments for each plane under study.

2.2.1.2. *Micro-scale*

At the micro-scale, the flow visualizations were taken with an inverted epifluorescence microscope (DMI 5000M, Leica Microsystems GmbH), where the microgeometries were continuously illuminated by a 100 W mercury lamp. A filter cube (Leica Microsystems GmbH, excitation filter band pass BP 545/30 nm, short pass dichroic at 565 nm, and barrier filter 605/75 nm) was used to filter the multichromatic light into the excitation light which

reaches the microgeometries containing the seeded fluid via a microscope objective (Magnification M 20×, numerical aperture NA = 0.40). The light emitted by the fluorescent tracer particles was imaged through the same objective onto the camera (DFC350 FX, Leica Microsystems GmbH) in order to capture the particle trajectories. The fluids were seeded with 1.0 µm fluorescent polystyrene tracer particles at a concentration of 100 ppm (Nile Red, Molecular Probes, Invitrogen; Ex/Em: 535/575 nm; ρ: 1050 kg/m^3).

2.2.2. Particle image velocimetry

Particle image velocimetry is an optical technique used to measure the velocity field by determining the particle displacement over a known period of time (Δt) using a double-pulse laser technique in a defined interrogation area (Wereley and Meinhart, 2005). Despite the differences inherent to the length (and times) scales, the principles upon which standard and micro PIV are essentially the same. The flow is illuminated by a light source and the positions of illuminated particles at a certain plane are recorded using a digital camera. Two light pulses are used, where the second pulse is emitted a very short time after the first pulse. The analysis of the pairs of images by specialized cross-correlation algorithms extracts the particle displacements and the corresponding velocity fields (Stone *et al.*, 2002).

2.2.2.1. *Macro-scale - PIV*

In the macro-scale experiments, only the flow plane under investigation is illuminated by a double pulsed Nd:YAG (neodymium-doped yttrium aluminum garnet) laser (Solo PIV III, New Wave Research), which generates consecutive pairs of light sheets with a wavelength of 532 nm and a maximum energy of 50 mJ per pulse. The two consecutive pulses of light illuminate the suspended particles which reflect light allowing the determination of the corresponding velocities from the displacement of the imaged particles in the time interval between the laser pulses, as represented schematically in Figure 2.9. The fluids were seeded with reflective tracer particles (hollow glass spheres with 10 µm diameter – HGS-10, Dantec Dynamics; ρ: 1100 kg/m^3) and the particle concentration was chosen in order to satisfy the recommended criterion for PIV of having at least 5-10 particles per interrogation area (Adrian, 2005).

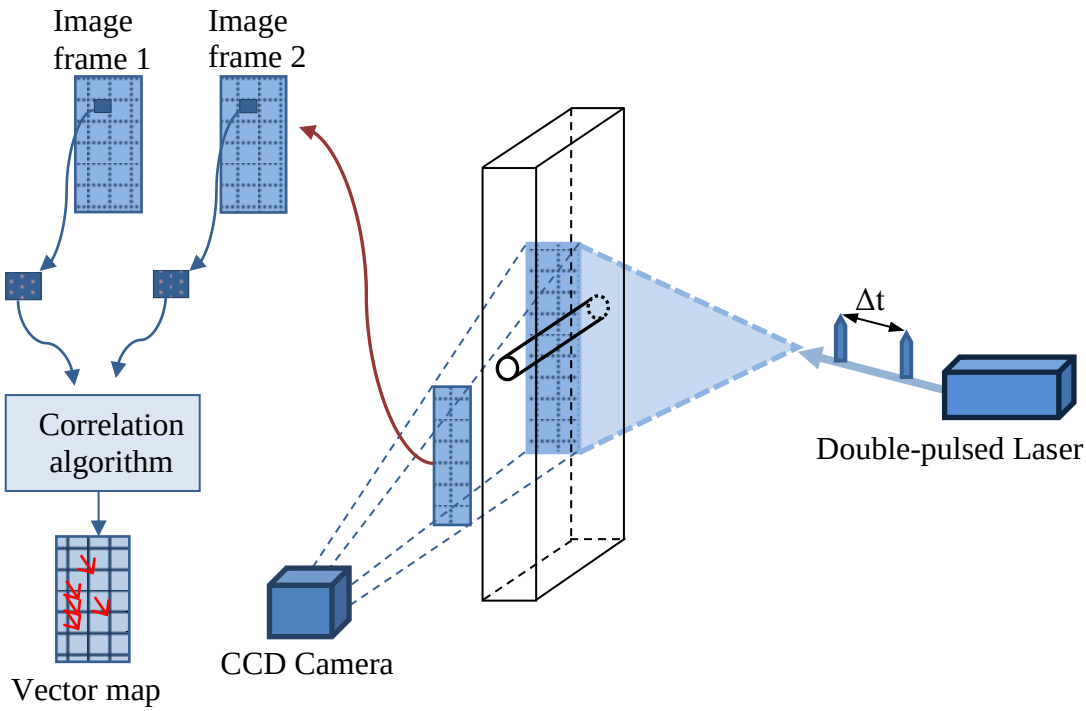

Figure 2.9. Schematic overview of the particle image velocimetry technique.

The images were acquired using a digital CCD camera (Flow Sense 2M, Dantec Dynamics) coupled with a Nikon AF Micro lens of 60 mm focal length. At least 50 pairs of images were acquired and used in ensemble-averaging and the velocity field was determined by processing the images with FlowManager v4.60 software (Dantec Dynamics), using an adaptive-correlation algorithm, to generate a two-dimensional velocity vector map for each image pair, on interrogation windows of 32 by 32 pixels, with 50% overlap. The adaptive-correlation is an iterative process in which the interrogation area is successively refined, to reduce the loss of particles in the interrogation areas that occurs between the light pulses. The average of the vector maps obtained from each pair of images provides the final vector map. The procedure performed in the PIV measurements is described in more detail in Appendix B.

The time between pulses (Δt) was adjusted according to the experimental flow conditions for each case, in order for the particles displacement between frames to be around 25% of the size of the interrogation area. To define the time between pulses the PIV system can be operated on double frame mode, with Δt up to 30 ms, or it can be operated on single frame mode for $\Delta t > 30$ ms. On single frame mode, the frequency between pulses was adjusted to created double frame images with the intended Δt.

2.2.2.2. *Micro-scale - µPIV*

The microgeometries were placed on an inverted epifluorescence microscope (DMI 5000M, Leica Microsystems GmbH) and were illuminated by a doubled pulsed Nd:YAG laser (Dual power 65-15, Dantec dynamics) with a wavelength (λ) of 532 nm, as shown in Figure 2.10. Instead of the use of a light sheet to illuminate the flow, as used in the macro-scale PIV system, volume illumination is used in the µPIV technique with focusing by the objective lens providing the discrimination of the measured plane. The volume illumination leads to a high background noise from out-of-focus particles, since the acquired images include the in-focus and out-of-focus particles due to the finite depth of field of the objective, which decreases with the increase of the objective numerical aperture.

The time interval between two consecutive pulses of light was adjusted according to the flow conditions. The µPIV system can operate on double frame mode, with a Δt of up to 66 ms, or on single frame mode for $\Delta t > 66$ ms. A minimum of 150 pairs of images were acquired for ensemble an average correlation, using a digital camera (Flow sense 4M, Dantec Dynamics). The velocity fields were determined by processing the pairs of images using an adaptive-correlation of the DYNAMIC STUDIO V2.3 software (Dantec Dynamics), which generates a two-dimensional velocity vector map from each image pair. A magnification of 20× (NA = 0.40) was used to capture the particle displacement over a wide field of the microchannel. The fluids were seeded with fluorescent polystyrene tracer particles with 0.5 µm in diameter at a concentration of 90 ppm (Nile Red, Molecular Probes, Invitrogen; Ex/Em: 535/575 nm; ρ: 1050 kg/m^3).

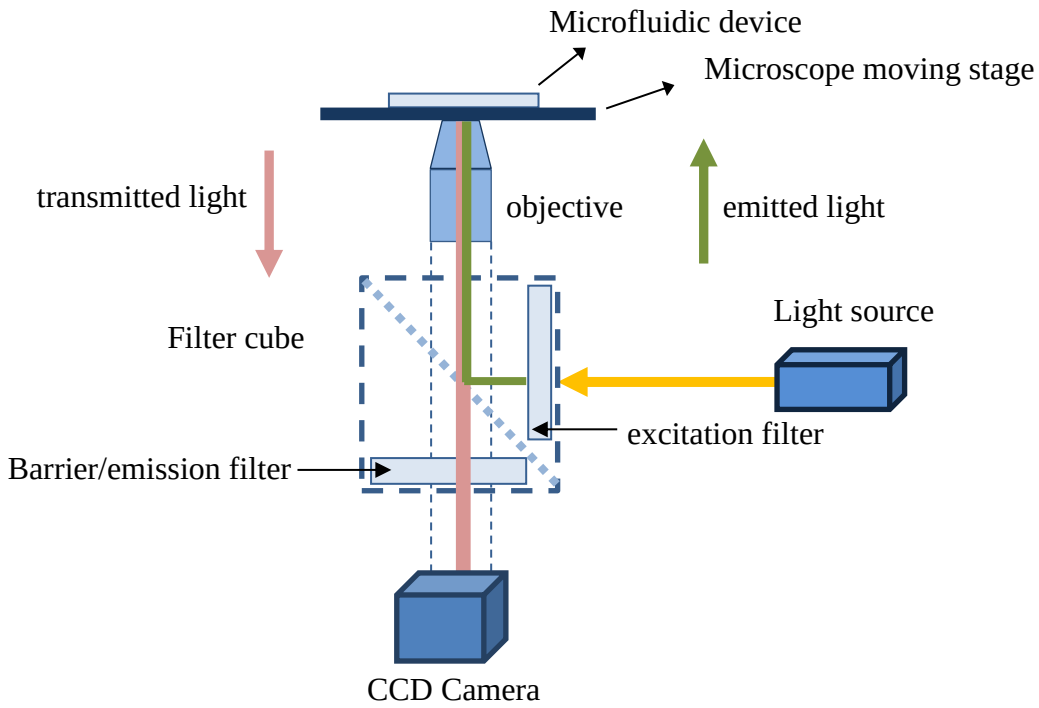

Figure 2.10. Schematic overview of the optical system for μPIV using an epi-fluorescence microscope.

To obtain velocity fields with high accuracy and high spatial resolution some considerations must be taken into account: particle visibility, in-focus spatial resolution and out-of-focus spatial resolution. To obtain a reasonable high quality particle image, an in-focus visibility (V) of at least 1.5 is necessary. The particle visibility is the ratio of the intensity of light from in-focus particles to the average intensity of the background light emitted by the out-of-focus particles (Olsen and Adrian, 2000). Moreover, the volume fraction of particles (V_{fr}) in solution allows the quantification of tracer particles necessary for the set-up under study and is given by (Wereley and Meinhart, 2005):

$$V_{fr} = \frac{2d_p^3 M^2 \beta^2 \left(s_0 - \frac{h}{2}\right)\left(s_0 - \frac{h}{2} + h\right)}{3V\,h\,s_0\left[M^2 d_p^2 + \frac{1.49\lambda^2}{\mathrm{NA}^2}(M+1)^2\right]} \times 100 \qquad (2.1)$$

where the parameter that defines the cut-off level of the edges of the particle image is β^2 = 3.67 (Adrian and Yao, 1985), d_p is the real diameter of the particles, s_0 is the objective working distance, M is the magnification and h is the depth of the microchannels. For a visibility of 1.5 and for the objective of 20×, a maximum particle concentration of 0.31%

(v/v), 0.17% (v/v) and 0.085% (v/v) is admissible for the microchannels depth of h = 58 μm, h = 105 μm and h = 213 μm, respectively.

The fluorescent tracer particles in the in-focus plane should be resolved in 3-4 pixels per particle diameter of the acquired images (Wereley and Meinhart, 2005) in order for the uncertainty of the correlation peak location to be ten times lower than the effective image diameter (d_e/M) (Prasad *et al.*, 1992). The effective image diameter, projected into the flow, is defined as (Wereley and Meinhart, 2005):

$$\frac{d_e}{M} = \frac{\left[d_s^2 + M^2 d_p^2\right]^{\frac{1}{2}}}{M} , \tag{2.2}$$

where d_s, which is the diffraction-limited spot size of a point source of light, is given by (Wereley and Meinhart, 2005):

$$d_s = 2.44(M+1)\frac{\lambda}{2\mathrm{NA}} . \tag{2.3}$$

In the experimental work an objective with a magnification of 20× (NA = 0.4) was used, obtaining d_s = 3.7 μm and d_e/M = 2.1 μm. Additionally, the relation between the uncertainty (d_e/10M) and the particle displacement should be lower than 2%, and for that condition the maximum particle displacement should be lower than 10.5 μm for the 20× objective used.

The out-of-focus spatial resolution can be determined by the measurement depth of field (δ_Z). The total measurement depth (δ_{Zm}) is the depth below which there is no significant contribution of out-of-focus particles. The measurement depth is determined as the sum of the effect due to the diffraction, the geometrical effect due to the optics and the effect due to the size of the particle, and is defined as:

$$\delta z_m = \frac{3n\lambda_0}{(\mathrm{NA})^2} + \frac{2.16 d_p}{\tan\theta} + d_p , \tag{2.4}$$

where n is the refractive index, λ_0 is the wavelength of the light in vacuum and $\tan\theta \approx \sin\theta$ = NA/n. With the 20× objective the measurement depth obtained in the experiments is δ_{Zm} = 14 μm.

2.2.3. Pressure drop measurements

Pressure drop measurements were performed in the microchannels with the cylinder arrays (cf. Figure 2.7) using differential pressure sensors (Honeywell 26PC). The pressure drop was measured between two ports, which are positioned upstream and downstream of the region of interest, as represented in Figure 2.11.

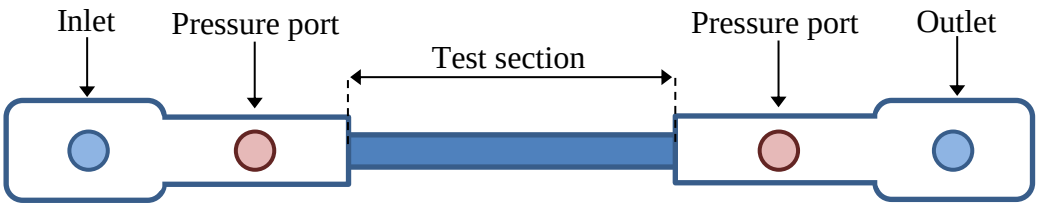

Figure 2.11. Top view of the microchannels with the location of the inlet/outlet and pressure ports.

The three pressure sensors used cover differential pressures up to 7 kPa, 34 kPa and 200 kPa and were selected according to estimates of the pressure drop to be measured, which depends on the flow rate and the geometrical arrangement under studied. The pressure sensors were previously calibrated using a static column of water for the 7 kPa and 34 kPa pressure sensors and using a compressed air line with a calibrated manometer (Wika Instrumental Corporation, model 332.50) for the 200 kPa pressure sensors.

The pressure sensors were powered using a 12 V power supply (Lascar electronics, PSU 206) and the output data was acquired using a data acquisition card (NI USB-6218, National Instruments), which was connected to the computer through a USB2 port. The output data was recorded and monitored using LabView v7.1 software.

2.3. Composition of the fluids

The experiments were conducted with two Newtonian fluids, four different viscoelastic fluids based on the polymer polyacrylamide (PAA) and one wormlike micellar solution based on cetyltrimethylammonium bromide (CTAB). The compositions of the fluids used are described in Tables 2.3 and 2.4. The Newtonian and the viscoelastic fluids based on PAA were used in the experiments at the macro- and micro-scales, in order to allow for a comparison between the two length scale experiments and especially to widen the range of flow conditions in the *De-Re* parameter space, as discussed in Chapter 1. Additionally, a

wormlike micellar solution was also used in the micro-scale experiments using the cylinder arrays.

Newtonian fluid flows have been extensively investigated at macro- and micro-scale, and it was also studied in this work in order to help in the cross-validation of the experimental results with numerical calculations. The numerical calculations were carried out with an in-house code which has been extensively verified for the Newtonian case (Oliveira *et al.*, 1998; Oliveira *et al.*, 2007) and at the same time validated by comparison with the experimental data of this work and previously by Oliveira *et al.* (2007) and Escudier *et al.* (2000; 2002a; 2002b). These sets of experimental data and of the corresponding numerical predictions also provide a reference scenario to compare with the viscoelastic fluid flow results. The Newtonian fluids used were de-ionized water and a 40% by weight aqueous solution of glycerine.

The non-Newtonian fluids used were based on polyacrylamide (PAA), added in different quantities and using different solvents to obtain two classes of fluids, one with shear-thinning behaviour and three Boger fluids (constant viscosity viscoelastic fluids). The shear-thinning fluid was an aqueous solution of PAA at a weight concentration of 1000 ppm. Two of the Boger fluids were 85% (w/w) aqueous solutions of glycerine with PAA at weight concentrations of 200 ppm and 400 ppm and with 1% of sodium chloride (NaCl) to stabilize the electrical charges of the polymer and consequently obtain a Boger fluid, as described by Stokes (1998). The third Boger fluid was an aqueous solution of PAA at a weight concentration of 125 ppm and with 1% of sodium chloride (NaCl). In order to minimize bacteriological growth in the fluid and prevent its degradation, a biocide (Kathon LXE, Rohm and Haas) was added at a weight concentration of 25 ppm in all fluids.

The polyacrylamide results from the polymerization reaction of the monomer acrylamide. The polyacrylamide molecule used in this work has a long chain of high molecular weight (14×10^6 g/mol), which confers to the non-Newtonian fluids a significant elasticity level. The scission of the chains, caused by specific flow conditions, degrades the polymer molecules leading to significant changes of the rheological properties. Therefore, in the preparation of the fluids, the polymer is dissolved in water and glycerine using very slow speed agitation, to avoid the scission of the molecular chains and consequently the degradation of the fluid.

Table 2.3. Compositions by weight of the Newtonian fluids and viscoelastic fluids based on polyacrylamide.

Fluid	PAA (ppm)	Glycerine (%)	Water (%)	NaCl (%)	Kathon (ppm)	ρ (T = 293.2 K) (kg/m^3)
Newtonian	-	40.0	60.0	-	25	1102.0
Newtonian	-	-	100.0	-	25	999.8
Shear-thinning - PAA1000	1000	-	99.90	-	25	1001.5
Boger - PAA200	200	85.05	13.91	1.02	25	1225.8
Boger - PAA400	400	85.06	13.89	1.01	25	1226.3
Boger - PAA125	125	-	98.98	1.01	25	1001.1

The wormlike micellar solution used was an aqueous solution of 30 mM cetyltrimethylammonium bromide (CTAB) and 240 mM sodium salicylate (NaSal).

The wormlike micellar solution displays many of the properties of polymer solutions, such as viscoelasticity, which generates complex flows. However, the wormlike micellar solutions are not covalently bonded along their backbone and consequently have the ability to break-up and reform dynamically during the flow, which in strong shear and extensional flows can lead to new and interesting phenomena and flow instabilities in addition to being extremely resistant to mechanical degradation. In recent works (Pathak and Hudson, 2006; Haward *et al.*, 2012), these wormlike micellar solutions have shown sharply-peaked bands of birefringence near stagnation points.

Table 2.4. Molar concentration of the wormlike micellar solution.

Fluid	CTAB (mM)	NaSal (mM)	ρ (T = 293.2 K) (kg/m^3)
CTAB	30	240	1001.0

2.4. Rheological characterization of the fluids

2.4.1 Shear rheology

In homogeneous shear flow conditions, the rheological properties of the fluids can be quantified through steady and dynamic measurements using a rotational rheometer, which can work either under controlled strain rate or under controlled stress. The rotational rheometers work with controllable and quasi-controllable flows, such as the flow between parallel plates, a cone and plate system and between concentric cylinders. In this thesis all fluids were characterised using a cone and plate system, which applies a constant shear rate over the entire sample and enables normal stress measurements. The theoretical considerations of the cone and plate system will be briefly described below and a detailed description of the others geometries can be found in Barnes *et al*. (1989) and Barnes (2000).

In the cone and plate geometry the plate remains static and the cone rotates with an angular velocity (Ω) (see Figure 2.12) and with an imposed torque ($\Im$) in controlled stress mode. The cone has a small angle, θ, in order to allow accurate normal stress measurements and ensure that the shear-rate remains constant in the entire sample.

In steady shear conditions the following material functions are defined: the shear viscosity (η), the coefficient of first normal stress difference (Ψ_1) and the coefficient of second normal stress difference (Ψ_2).

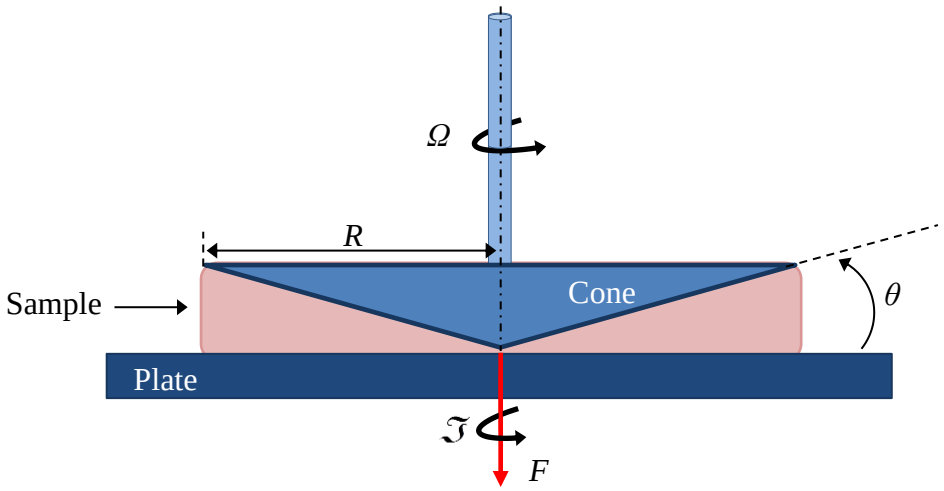

Figure 2.12. Schematic representation of the cone and plate system geometry.

For small values of θ, the shear-rate is defined as (Barnes *et al.*, 1989):

$$\dot{\gamma} = \frac{\Omega}{\theta}. \tag{2.5}$$

The shear stress can be determined from the torque necessary to apply on the cone and is defined as:

$$\tau_{xy} = \dot{\gamma}\,\eta(\dot{\gamma}) = \frac{3\Im}{2\pi R^3}. \tag{2.6}$$

For viscoelastic fluids a vertical normal force, F, arises which tries to separate the cone from the plate. The first normal stress difference (N_1) or the coefficient of the first normal stress difference (Ψ_1) can be calculated from the normal force F and are defined as:

$$N_1 = \Psi_1(\dot{\gamma})\,\dot{\gamma}^2 = \frac{2F}{\pi R^2}. \tag{2.7}$$

The shear viscosity represents the ratio between the shear stress and the corresponding shear rate and is defined as:

$$\eta(\dot{\gamma}) = \frac{\tau_{xy}}{\dot{\gamma}}. \tag{2.8}$$

The steady shear measurements were made using a rotational rheometer (Physica MCR 301, Anton Paar) with a 75 mm cone-plate system with 1º angle. Figure 2.13 shows the steady shear viscosity of the fluids used in this thesis, measured at the reference temperature T_0 = 293.2 K.

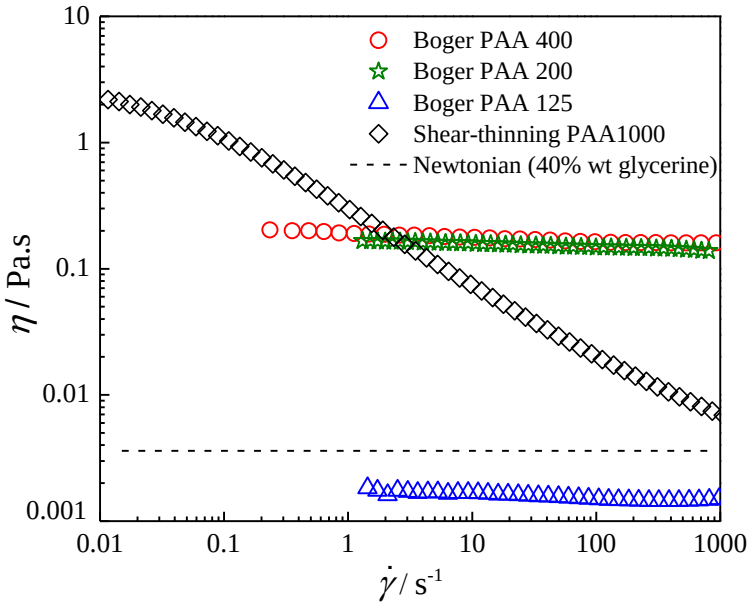

Figure 2.13. Steady shear viscosity of the fluids at the reference temperature T_0 = 293.2 K.

The cone and plate system geometry can also be employed to measure the response of a fluid sample to small amplitude oscillatory shear flow (SAOS) in what are called dynamic measurements. Here, oscillatory small amplitude shear stresses (or deformations) are applied to the fluid, to measure the corresponding material functions: the storage modulus (G'), proportional to the elastic behaviour of the sample, and the loss modulus (G'') proportional to the viscous behaviour of the sample. In dynamic measurements, the range of amplitude values in which the shear and elastic moduli are constant was measured, by applying an amplitude sweep for a fixed frequency of oscillation, followed by the measurement of a range of frequencies, a frequency sweep at constant amplitude, to measure the dynamic properties in the linear regime.

In dynamic measurements the sample is subject to a small sinusoidal oscillating strain (γ) or deformation as a function of time:

$$\gamma(t) = \gamma_0 \sin(\omega t), \tag{2.9}$$

where γ_0 is the strain amplitude and ω is the angular frequency.

Provided the amplitude of the oscillation is small, the resulting shear stress $\tau_{xy}(t)$ is also sinusoidal and shows a phase lag relative to the imposed strain as in:

$$\tau_{xy}(t) = \tau_0 \sin(\omega t + \delta), \tag{2.10}$$

where δ is the phase angle and τ_0 is the stress amplitude. The stress response to the applied strain is given as a sum of an elastic component in phase with the strain and a viscous component out of phase by $\pi/2$:

$$\tau_{xy}(t) = \tau_0 \left[\cos(\delta) \sin(\omega t) + \sin(\delta) \cos(\omega t) \right], \tag{2.11}$$

or,

$$\tau_{xy}(t) = \gamma_0 \left[G' \sin(\omega t) + G'' \cos(\omega t) \right], \tag{2.12}$$

where G' is the storage modulus and G'' is the loss modulus, which are defined respectively as:

$$G' = \frac{\tau_0}{\gamma_0} \cos\delta \tag{2.13}$$

and

$$G'' = \frac{\tau_0}{\gamma_0} \sin\delta . \tag{2.14}$$

The storage modulus, G', expresses the magnitude of the energy that is stored in the material and the loss modulus, G'', is the energy that is lost by viscous dissipation per cycle of deformation.

In this thesis, the steady shear measurements were performed using the rotational rheometer Physica MCR 301 and the dynamic shear measurements were performed using the rotational rheometer TA Instruments AR-G2.

2.4.2 Extensional rheology

An extensional flow can be generated by pulling out a piece of material in a defined direction, in order to obtain the material functions in extension, as illustrated in Figure 2.14. The material functions in extensional flow are difficult to measure, especially for low viscosity fluids, because it is difficult to generate a homogeneous extensional flow.

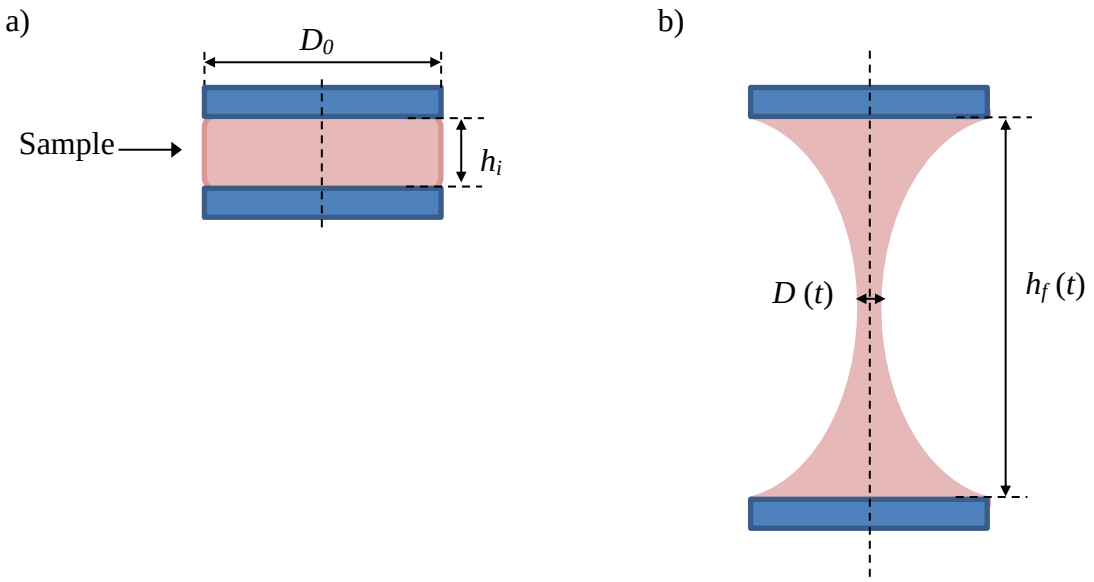

Figure 2.14. Schematic representation of an extensional flow: a) sample at the initial instant; b) sample being stretched in uniaxial elongational flow.

In this thesis the relaxation time in extensional flow was determined through the application of an uniaxial extensional flow using a capillary-breakup extensional rheometer, CaBER (Haake CaBER 1, Thermo Scientific).

In the CaBER measurements the sample is placed between two circular plates with a diameter, D_p (D_p = 6 mm was used), which are separated by an initial distance, h_i. At a given time, an axial step strain is imposed over a very short time (50 ms was used), until the final distance, h_f, is achieved. Subsequently, the time evolution of diameter of the filament $D\,(t)$ undergoing a capillary thinning process is monitored by a laser micrometer.

The variation of the filament diameter as a function of time of a Newtonian fluid follows a linear decrease with time (Entov and Hinch, 1997):

$$\frac{D(t)}{D_0} = \frac{\sigma}{6\eta D_0}(t_c - t), \tag{2.15}$$

where t_c is the critical time for the Newtonian fluid break and σ is the surface tension.

For a viscoelastic fluid an exponential decay is observed (Entov and Hinch, 1997):

$$\frac{D(t)}{D_0} = \left(\frac{GD_0}{\sigma}\right) e^{-\frac{t}{3\lambda}}, \tag{2.16}$$

where G is the elastic modulus of the viscoelastic fluid with relaxation time λ.

Equation (2.16) can be linearized as:

$$\ln[D(t)] = \ln\left(\frac{GD_0^{\,2}}{\sigma}\right) - \frac{t}{3\lambda}, \tag{2.17}$$

and the relaxation time can be determined from the slope of the experimental data in the linear region of log [D (t)] as a function of time t.

2.5. Outline of the experimental work

The experimental work was developed according to the established objectives and comprises experimental set-ups at macro- and micro-scales, different flow geometries, different measurement techniques to quantify the flow field, and various fluids. Table 2.5 summarizes the experimental set-ups, geometries, techniques and fluids used in the different chapters of this thesis.

Table 2.5. Experimental set-up, techniques and fluids used in each chapter.

Chapter	Experimental set-up	Geometry	Techniques	Fluids
3	Macro-scale	Confined cylinder *AR* = 16, 8, 2 *BR* = 50%	visualizations PIV	Newtonian
4	Macro-scale	Confined cylinder *AR* = 16, 8, 2 *BR* = 50%	visualizations PIV	Newtonian Shear-thinning PAA1000 Boger PAA200 Boger PAA400
5	Macro- and micro-scales	Confined cylinder *AR* = 2.0 *BR* = 50%	visualizations PIV μPIV	Newtonian Shear-thinning PAA1000
6	Micro-scale	Confined cylinder *AR* = 2.0, 1.0, 0.55 *BR* = 50%	visualizations μPIV	Newtonian Shear-thinning PAA1000 Boger PAA200
7	Micro-scale	Confined cylinder *BR* = 25%, 50%, 75%	visualizations μPIV	Newtonian Boger PAA200 Boger PAA125
8	Micro-scale	Array of cylinders Staggered, Aligned	visualizations pressure drop	Boger PAA125 CTAB:NaSal

References

Adrian, R.J., 2005. Twenty years of particle image velocimetry. Exp Fluids 39, 159-169.

Adrian, R.J., Yao, C.S., 1985. Pulsed Laser Technique Application to Liquid and Gaseous Flows and the Scattering Power of Seed Materials. Appl Optics 24, 44-52.

Barnes, H.A., 2000. A handbook of elementary rheology University of Wales, Institute of Non-Newtonian Fluid, Aberystwyth.

Barnes, H.A., Hutton, J.F., Walters, K., 1989. An introduction to rheology. Elsevier, Aberystwyth.

Entov, V.M., Hinch, E.J., 1997. Effect of a spectrum of relaxation times on the capillary thinning of a filament of elastic liquid. J Non-Newton Fluid Mech 72, 31-53.

Escudier, M.P., Gouldson, I.W., Oliveira, P.J., Pinho, F.T., 2000. Effects of inner cylinder rotation on laminar flow of a Newtonian fluid through an eccentric annulus. Int J Heat Fluid Fl 21, 92-103.

Escudier, M.P., Oliveira, P.J., Pinho, F.T., 2002a. Fully developed laminar flow of purely viscous non-Newtonian liquids through annuli, including the effects of eccentricity and inner-cylinder rotation. Int J Heat Fluid Fl 23, 52-73.

Escudier, M.P., Oliveira, P.J., Pinho, F.T., Smith, S., 2002b. Fully developed laminar flow of non-Newtonian liquids through annuli: comparison of numerical calculations with experiments. Exp Fluids 33, 101-111.

Haward, S.J., Ober, T.J., Oliveira, M.S.N., Alves, M.A., McKinley, G.H., 2012. Extensional rheology and elastic instabilities of a wormlike micellar solution in a microfluidic cross-slot device. Soft Matter 8, 536-555.

McDonald, J.C., Duffy, D.C., Anderson, J.R., Chiu, D.T., Wu, H.K., Schueller, O.J.A., Whitesides, G.M., 2000. Fabrication of microfluidic systems in poly(dimethylsiloxane). Electrophoresis 21, 27-40.

Oliveira, M.S.N., Alves, M.A., Pinho, F.T., McKinley, G.H., 2007. Viscous flow through microfabricated hyperbolic contractions. Exp Fluids 43, 437-451.

Oliveira, P.J., Pinho, F.T., Pinto, G.A., 1998. Numerical simulation of non-linear elastic flows with a general collocated finite-volume method. J Non-Newton Fluid Mech 79, 1-43.

Olsen, M.G., Adrian, R.J., 2000. Out-of-focus effects on particle image visibility and correlation in microscopic particle image velocimetry. Exp Fluids 29, S166-S174.

Pathak, J.A., Hudson, S.D., 2006. Rheo-optics of equilibrium polymer solutions: Wormlike micelles in elongational flow in a microfluidic cross-slot. Macromolecules 39, 8782-8792.

Prasad, A.K., Adrian, R.J., Landreth, C.C., Offutt, P.W., 1992. Effect of Resolution on the Speed and Accuracy of Particle Image Velocimetry Interrogation. Exp Fluids 13, 105-116.

Stokes, J.R., 1998. Swirling flow of viscoelastic fluids. Department of Chemical Engineering. The University of Melbourn.

Stone, S.W., Meinhart, C.D., Wereley, S.T., 2002. A microfluidic-based nanoscope. Exp Fluids 33, 613-619.

Wereley, S.T., Meinhart, C.D., 2005. Micron-Resolution Particle Image Velocimetry. In: Breuer, K. (Ed.), Microscale Diagnostic Techniques. Springer Berlin Heidelberg, pp. 51-112.

Chapter 3

Three-dimensional effects in laminar flow past a confined cylinder[1]

Abstract

An experimental and numerical study on the Newtonian fluid flow around a confined cylinder placed in a rectangular duct was undertaken in order to assess three-dimensional effects on the flow patterns. The cylinder was placed at the mid-plane to define a symmetric geometry with a 50% blockage ratio (BR, ratio between the cylinder diameter and the thickness of rectangular section). The flow visualizations by streak photography and the velocity measurements by particle image velocimetry were carried out for three different aspect ratios (AR, ratio between the depth and diameter of the cylinder) of 16, 8 and 2 and the Reynolds number varied between creeping flow conditions (Re → 0) up to the onset of time-dependent flow. The numerical calculations were performed in 3D meshes using an in-house finite volume code. They showed good agreement with experimental measurements and were also used to investigate the flow at very small and very large AR. For large values of AR, the results show unexpected velocity peaks near the cylinder end walls downstream of the cylinder for both inertia and diffusion controlled flow conditions. Increasing the aspect ratio of the cylinder does not reduce this local three-dimensional flow effect, which is found to occur near the ends of the cylinder at about one cylinder radius distance from the duct end walls. In contrast, reducing AR eliminated flow separation as expected for the Hele-Shaw type flows.

[1] The content of this chapter is adapted from: Ribeiro, V.M., Coelho, P.M., Pinho, F.T., Alves, M.A., 2012. Chemical Engineering Science 84, 155-169.

3.1. Introduction

Flows of Newtonian and non-Newtonian fluids around a confined circular cylinder are of relevance in a variety of industrial applications, the most typical case being the flow in heat exchangers, but including also other flows in food processing, flow through some porous media or in textile coating processes (Nishimura, 1986). The ubiquity of cylinder flow in addition to the absence of geometrical singularities and the specificities of some of its flow characteristics, especially for viscoelastic fluids, made it an established benchmark in the development of numerical methods for very low Reynolds number flows of non-Newtonian fluids (Brown and McKinley, 1994).

The flow around a finite length cylinder leads to three-dimensional (3D) effects, which are disregarded in traditional studies using two-dimensional (2D) geometries (Verhelst and Nieuwstadt, 2004); this is achieved experimentally by using long cylinders often with the help of end-plates. The impact of 3D effects on the overall flow characteristics depends essentially on the aspect ratio of the cylinder and the Reynolds number, but is also determined by the type of confinement and the rheology of the working fluid.

Before proceeding with a review of the state of the art, we note that throughout the literature the Reynolds number is defined both using the cylinder diameter, Re_D (Nieuwstadt and Keller, 1973; Williamson, 1996a, b; Leweke and Williamson, 1998; Coelho and Pinho, 2003; Chakraborty *et al.*, 2004) and the cylinder radius, *Re* (Thom, 1933; Kawaguti, 1953; Thompson *et al.*, 1996; Verhelst and Nieuwstadt, 2004; Ferreira, 2006) as characteristic length scale. In this work the cylinder radius will be used in the definition of the Reynolds number, but in this section both definitions will be referred.

Studies of Newtonian fluid flow around a cylinder started a long time ago, with important early contributions by Strouhal (1878), Hiemenz (1911), and von Kármán (1911). Comprehensive reviews on the state of the art were written by Cantwell and Coles (1983), Telionis et al. (1992), Williamson (1996b) and Zdravkovich (1997) . Most of the studies concerning Newtonian fluid flow around a cylinder focus on the vortex shedding phenomenon, the effect of blockage ratio (*BR*, defined as the ratio between the cylinder diameter and the thickness, *H*, of the rectangular section), the effect of aspect ratio (*AR*, defined as the ratio between the length and diameter of the cylinder) and the dynamics in various flow regimes (Sumer and Fredsoe, 1997). These investigations are limited in scope given the breadth of possibilities: they usually either concern flow at Reynolds numbers *Re*

below the critical value for the onset of vortex shedding ($Re < Re_{(vs)}$) or above this condition ($Re > Re_{(vs)}$), unbounded ($BR \approx 0$) or bounded flow and two-dimensional or three-dimensional flow.

Two-dimensional flows require cylinders of large AR, or at least intermediate values of AR with the observation being made far from the side walls. Flows under these conditions have been extensively studied and more than 40 years ago Gerrard (1966) proposed a mechanism to explain vortex shedding based on the formation and diffusion lengths, whereas Williamson (1996b) reviewed extensively the vortex dynamics in the cylinder wake and provided the main flow characteristics within each flow regime. More recently, the experiments of Coelho and Pinho (2003) on non-Newtonian fluid flows around cylinders with AR = 6 and 12 proceeded to the identification and demarcation of flow regimes for some viscoelastic fluids at $50 \leq Re_D \leq 9000$.

From the earlier studies, for 2D flow past an unbounded circular cylinder (i.e. $BR \approx 0$), the critical Reynolds number for the onset of the flow separation number, $Re_{D(s)}$, varied between $3.2 < Re_{D(s)} < 7$ (Sen *et al.*, 2009). Sen *et al.* (2009) concluded that the critical value for the onset of flow separation is $Re_{D(s)} \approx 6.29$ for $BR = 0.005$, i.e., for what is considered essentially an unbounded flow. The critical Reynolds number for the onset of laminar vortex shedding is $Re_{(vs)} \approx 23.5$ for aspect ratios above 45 (Lee and Budwig, 1991; Williamson, 1996b; Sahin and Owens, 2004). For aspect ratios below 45, the critical Reynolds number for the onset of vortex shedding increases, as the value of aspect ratio decreases (Nishioka and Sato, 1974). According to Lee and Budwig (1991), for $BR \approx 0$ and AR = 16, 8 and 2, i.e., for the values of aspect ratio under study in this work, the critical Reynolds numbers for the onset of laminar vortex shedding are $Re_{(vs)} \approx 30$, $Re_{(vs)} \approx 40$ and $Re_{(vs)} \geq 70$, respectively.

According to Payne (1958), early numerical calculations of the steady flow past a confined cylinder at $Re \approx 10$ and 20 were presented by Thom (1933), at $Re_D \approx 40$ by Kawaguti (1953) and at $1 \leq Re_D \leq 40$ by Nieuwstadt and Keller (1973).

More recently, Zdravkovich (2003) established a generic classification of the blockage effects. For $BR < 0.1$ the blockage effect is small and may be neglected; for $0.1 < BR < 0.6$ the blockage effect modifies the flow; for $BR > 0.6$ the flow is radically influenced by the blockage effect. Sen *et al*. (2009) investigated the effect of blockage ratio, in the range $0.000125 \leq BR \leq 0.8$ for $6 < Re_D < 40$, and concluded that the bubble length, separation angle and the critical Reynolds number for the onset of the flow separation $Re_{(s)}$, exhibit non-

monotonic variations with blockage ratio and that this effect is insignificant for $BR \leq 0.01$. The numerical study of the Newtonian fluid flow past a circular cylinder confined in a rectangular channel of Chakraborty *et al*. (2004) explored the interplay of flow parameters such as the length of the recirculation, the drag coefficient and the angle of flow separation in the range $Re_D \approx 0.1 - 200$. Sahin and Owens (2004) investigated numerically the effect of blockage ratio on the linear stability of confined cylinder flow and reported on the neutral curve and stability maps, but their analysis is restricted to 2D flow. The effect of the blockage ratio in the 2D flow past a cylinder in a channel was also investigated numerically by Rao *et al*. (2011), using Newtonian fluids and non-Newtonian fluids described by the power-law model, for the range of vortex shedding, $40 \leq Re \leq 140$.

Three-dimensional effects in the Newtonian circular cylinder flows at $Re \geq Re_{(vs)}$ were also extensively investigated. Gerich and Eckelmann (1982) looked at the effect of end-plates on the shedding frequency and Norberg (1994) studied experimentally the influence of aspect ratio at low blockage ratio in the range of Re_D from 50 up to $4x10^4$. Thompson *et al.* (1996) predicted numerically two shedding modes for different *Re* and the existence of the two modes for $Re \approx 250$. Williamson (1996a) and Leweke and Williamson (1998) explained the origin of the instabilities leading to the two modes of 3D vortex shedding in the wake transition regime, i.e., for Re_D from 190 to 240. The study of 3D effects and of the influence of aspect ratio on the characteristics of laminar flow around a confined cylinder at $Re \leq Re_{(vs)}$ has only been carried out recently by Ferreira(2006) , who considered the range $0 \leq Re \leq 40$ and also concluded that the Reynolds number marking the appearance of a steady separated flow in the rear region is $Re_{(s)} \approx 6$.

Since the establishment of the 2D creeping flow past a circular cylinder as a benchmark test case for non-Newtonian fluids there was an increased need to understand well the corresponding Newtonian fluid flows and consequently a variety of experimental and numerical studies for the flow around a confined cylinder at $Re \leq Re_{(vs)}$ were carried out. The experimental studies of Verhelst and Nieuwstadt (2004) for the Newtonian and non-Newtonian fluids flowing past a confined cylinder in a rectangular channel with a blockage ratio of 50% and aspect ratio of 16 showed the appearance of 3D effects near the end walls, but these were not described in detail. In a numerical investigation of laminar Newtonian and non-Newtonian flows around confined cylinders, Ferreira (2006) found the appearance of velocity peaks near the end walls in the range of $2 \leq AR \leq 16$ and $Re \leq 40$, but these predictions lacked experimental confirmation and an in depth analysis of the 3D effects, so it

is not yet clearly established when the low Reynolds number flow around a cylinder can be considered to be essentially 2D and what are the flow characteristics when the flow is markedly 3D.

Our long term objective is to investigate 3D flows of non-Newtonian fluids with viscoelastic behaviour, but an extensive investigation of this nature is necessarily long and expensive, because of the wide range of possible fluid properties and types. For a purely numerical investigation, the non-linear nature of the viscoelastic fluids also requires large computational resources. In any case, such endeavour must necessarily start with the investigation of the corresponding Newtonian fluid dynamics in detail and given the lack of information identified above, that is precisely the purpose of the present contribution. In this work, this is achieved both numerically and experimentally and we provide an extensive set of reference cases against which the results of the non-Newtonian fluids can be compared with in the future. Specifically, this is achieved experimentally by considering the Newtonian fluid flow across a single confined cylinder with a blockage ratio of 50% (the typical benchmark case in computational rheology) as a function of the Reynolds number and of the aspect ratio, which is varied between 2 and 16 (specifically for AR = 16, 8 and 2), under steady flow conditions (i.e. for $Re \leq Re_{(vs)}$), except for a few illustrative cases above $Re_{(vs)}$. All the experimental cases are numerically simulated and additionally computational results are also presented for other values of AR to better assess the influence of this geometrical parameter. According to the literature, for AR = 16 and BR of 50% the Reynolds number marking the appearance of a steady separated flow in the rear region is $Re_{(s)} \approx 6$ (Ferreira, 2006), whereas the Reynolds number for the onset of time-dependent vortex shedding is $Re_{(vs)} \approx 40$ for the limiting case of large AR (i.e. 2D flow) (Sahin and Owens, 2004; Ferreira, 2006); accordingly, the present study considers primarily this range of Re.

The remainder of this chapter is organized as follows: the experimental set-up and techniques are described in section 3.2 and section 3.3 presents the fluid characterization. The governing equations and a brief outline of the numerical method are described in section 3.4. Section 3.5 presents and discusses the experimental results and compares them with the numerical simulations. Section 3.6 summarizes the main conclusions of this work.

3.2. Experiments

3.2.1 Experimental set-up

The experimental set-up is a closed system shown in Figure 3.1a. The test section represented in Figure 3.1b is a 1700 mm long duct with a rectangular cross section with a width (H) of 20 mm and a variable depth (h), where the confined cylinder with 10 mm diameter is located. The cylinder is located 630 mm downstream of the duct inlet and is positioned at the mid plane to define a symmetric geometry with a 50% area blockage ($BR = D/H$).

As illustrated in Figure 3.1a**,** the fluid flows through the rectangular duct by gravity (from reservoir R1 to reservoir R2) and a variable speed peristaltic pump (Pp) (ref. Lav 400 l/h, Dosim) recirculates the fluid back to the constant head reservoir R1, in order to maintain a constant liquid level (Lev) at the upper reservoir with the help of the overflow discharge pipe fitted with valve V3 (normally fully opened). The pump is switched off to measure the flow rate using a digital balance (KERN DS 36k0.5; readout of 0.5g; maximum range of 36 kg) which is placed under reservoir R2 (during the measurement the liquid level variation in reservoir R1 is small). This balance is monitored by LabView v7.1 software to record time and weight of fluid. The flow rate in the test section is controlled by changing the vertical position of reservoir R1 using an electric winch (not illustrated in Figure 3.1a) and through proper regulation of valves V1 and V2, with V1 being used for low flow rates and V2 for higher flow rates. The tubes connecting valves V1 and V2 to the test section have different diameters, which are selected according to the range of flow rates required.

The origin of the coordinate system represented in Figure 3.1b is located at the centre of the cylinder, with the positive x-axis pointing in the streamwise downstream direction, the y-axis in the cross-stream direction (normal to the main rectangular duct walls) and the z-axis in the spanwise direction (along the cylinder axis).

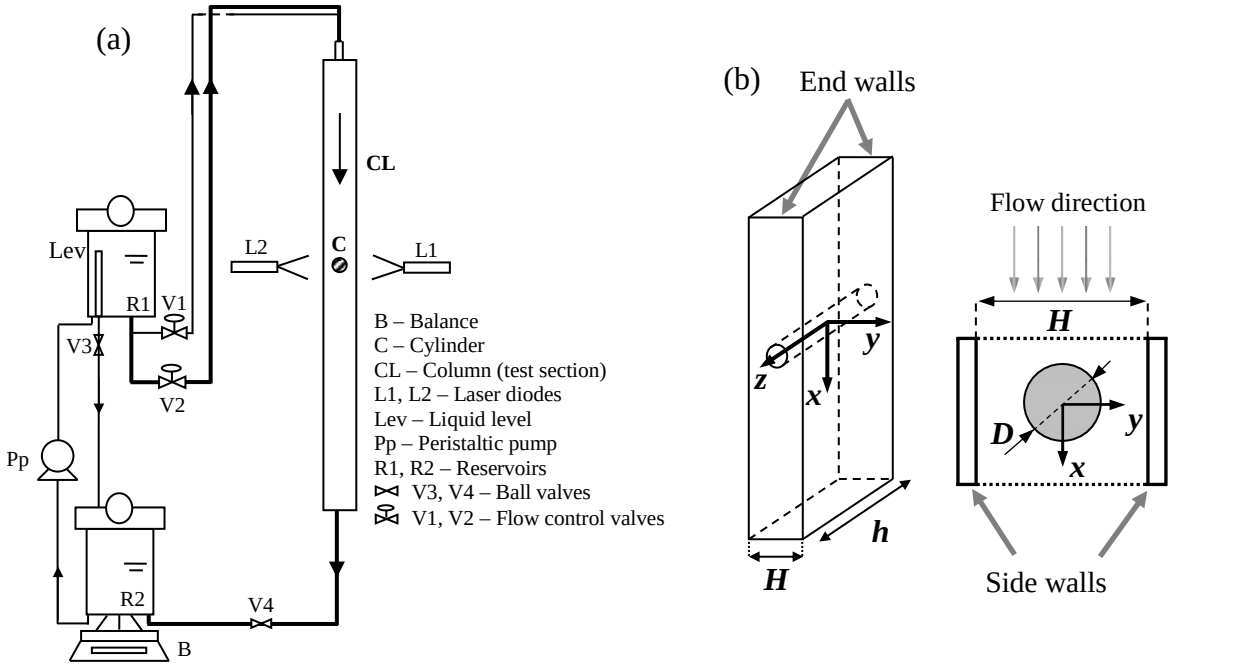

Figure 3.1. (a) Experimental set-up and (b) test section and the coordinate system.

One of the end walls can be moved along the spanwise direction (z) in order to change the depth (h), and consequently the aspect ratio ($AR = h/D$) of the geometry. Three different aspect ratios (AR = 16, 8 and 2) were used in the experiments with the corresponding dimensions of the rectangular duct described in Table 3.1. Spacers were also used to ensure that the duct dimensions were kept constant along the test section.

Table 3.1. Aspect ratios under study.

	AR = 16	AR = 8	AR = 2
h (mm)	160.0	80.0	20.0
D (mm)	10.0	10.0	10.0

The duct inlet has a distributor with a maximum of six injectors in order to obtain a velocity profile as uniform as possible at the inlet of the rectangular duct. The distance between the distributor and cylinder under study allows achieving a fully-developed velocity profile well upstream of the cylinder; the exit of the duct is also sufficiently far away not to affect the flow dynamics in the vicinity of the cylinder. Most of the experiments were carried out under

steady flow conditions, except for some flow visualizations conducted at higher *Re* to observe the vortex shedding phenomenon.

3.2.2 Experimental techniques

Flow visualizations using long time exposure streak photography and detailed velocity measurements using Particle Image Velocimetry (PIV) were carried out to characterize the flow field. Both techniques were used at various *xy* planes and in addition PIV measurements were taken at the symmetry plane $y/R = 0$. Figure 3.2 shows the planes where measurements were carried out for each *AR*.

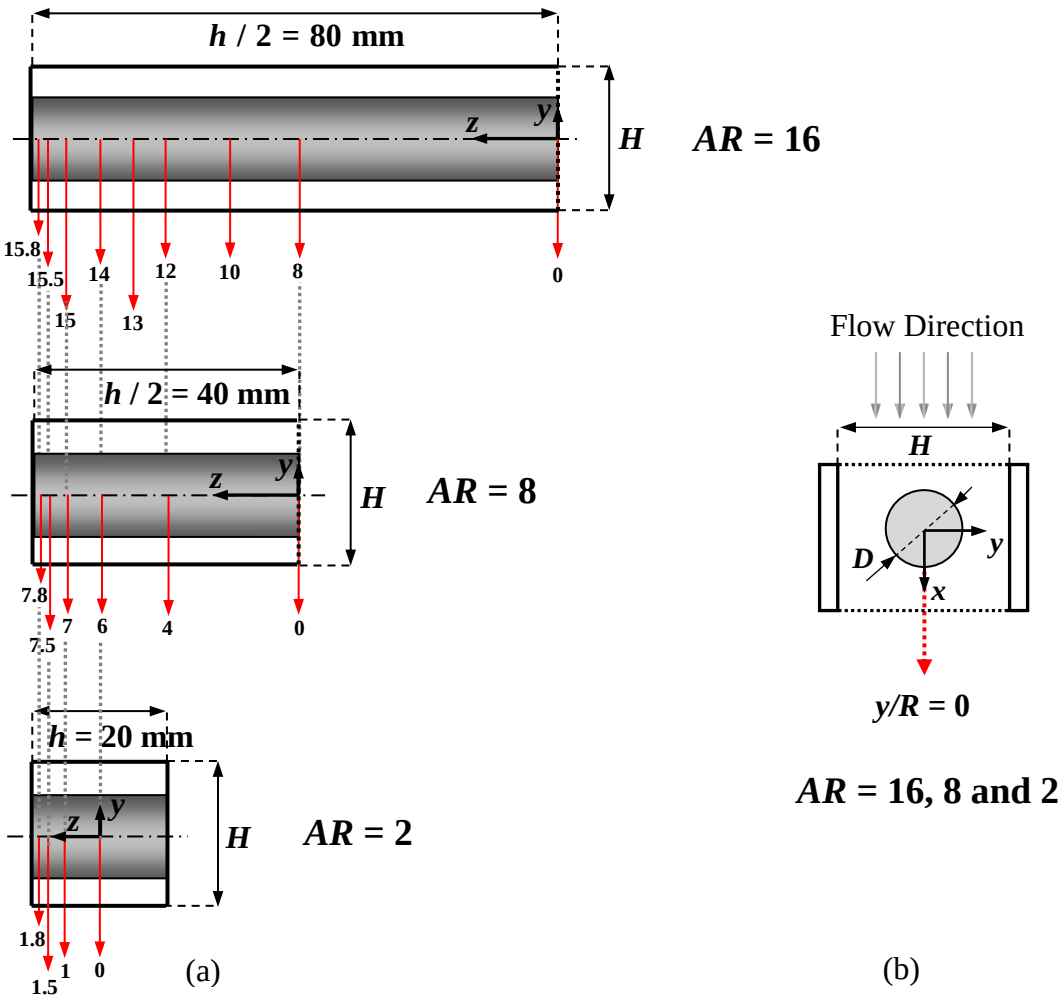

Figure 3.2. Planes under study for *AR* = 16, *AR* = 8 and *AR* = 2: (a) along the cylinder at different values of $|z/R|$; (b) symmetry plane, $y/R = 0$.

3.2.2.1. *Flow visualization*

In the study of flow patterns and recirculation length, using long time exposure streak photography, the flow was continuously illuminated using two co-planar 635nm 5mW laser diodes L1 and L2 (Vector, model 5200-20) equipped with cylindrical lenses to create a light sheet perpendicular to the cylinder axis (cf. Figure 3.1a). The fluid contained a suspension of reflective tracer particles (hollow glass spheres with 10 μm diameter – HGS-10, Dantec Dynamics) at a weight concentration of 30 ppm. The reflected light was captured by a digital camera (CANON EOS 30D) equipped with a macro lens (EF100 mm, f2.8) placed perpendicularly to the laser light sheet to record the flow pathlines. The exposure time was varied depending on the flow rate, ranging between 1 s and 30 s. The two laser diodes and the digital camera moved simultaneously, to simplify the adjustments for each plane under study (cf. Figure 3.2), using a manual traversing table with a relative positioning precision of ± 0.01 mm. The use of two laser diodes, instead of only one, minimized shadows around the cylinder.

3.2.2.2. *Particle image velocimetry – PIV*

The detailed measurements of velocity fields were carried out using a PIV system (Dantec Dynamics). The plane under investigation was illuminated by a double pulsed Nd:YAG laser (Solo PIV III, New Wave Research), which generates consecutive pairs of light sheets with a wavelength of 532 nm and a maximum energy of 50 mJ/pulse. The two consecutive pulses of light illuminated the suspended particles, which reflected light allowing the determination of the corresponding velocities from their displacement. The time between two consecutive pulses was short and was adjusted according to the flow conditions, and in particular to the average velocities being measured, and varied between 14 ms and 2.3 s. The images were acquired using a digital CCD camera (FlowSense 2M, Dantec Dynamics) coupled with a Nikon AF Micro lens of 60mm focal length. At least 50 pairs of images were acquired for each flow rate and the velocity field was determined by ensemble-averaging the corresponding velocity maps. FlowManager v4.60 software was used to process each image pair using an adaptive-correlation algorithm, in order to generate a two-dimensional velocity vector map on interrogation windows of 32 x 32 pixels, with 50% overlap. The velocity field is validated using a moving average criterion and the process were carried out for all the double images recorded, resulting in an averaged velocity field.

3.3. Fluid characterization

All experiments were carried out with a Newtonian fluid, a 40% by weight aqueous solution of glycerine, which was seeded with tracer particles, as described in section 3.2. The particle concentration satisfies the recommended criterion for PIV of having at least 5 - 10 particles per interrogation area (Adrian, 2005). In order to minimize bacteriological growth in the fluid and prevent its degradation, a biocide was added at a weight concentration of 25 ppm (Kathon LXE, Rohm and Haas).

To measure the dynamic viscosity of the Newtonian fluid at temperatures ranging from 288.2 K to 301.2 K a Physica MCR 301 shear rheometer was used with a 75 mm cone-plate system with 1º angle. The dependency of the dynamic viscosity (μ) on the absolute temperature (T) can be described by an Arrhenius equation in the form (Dealy and Plazek, 2009):

$$\ln\frac{\mu}{\mu_0}=\frac{\Delta H}{R}\left(\frac{1}{T}-\frac{1}{T_0}\right), \tag{3.1}$$

where μ_0 represents the dynamic viscosity at reference absolute temperature T_0 (293.2 K), ΔH represents the activation energy, and R is the universal gas constant.

The variation of dynamic viscosity with temperature is shown in Figure 3.3 and it is clear that this variation is well described by the Arrhenius equation. The viscosity at the reference temperature, T_0 = 293.2 K, is 0.00376 Pa s and $\Delta H/R$ = 2767 K. The density of the solution, measured at 293.2 K using a pycnometer, was 1102 kg/m^3.

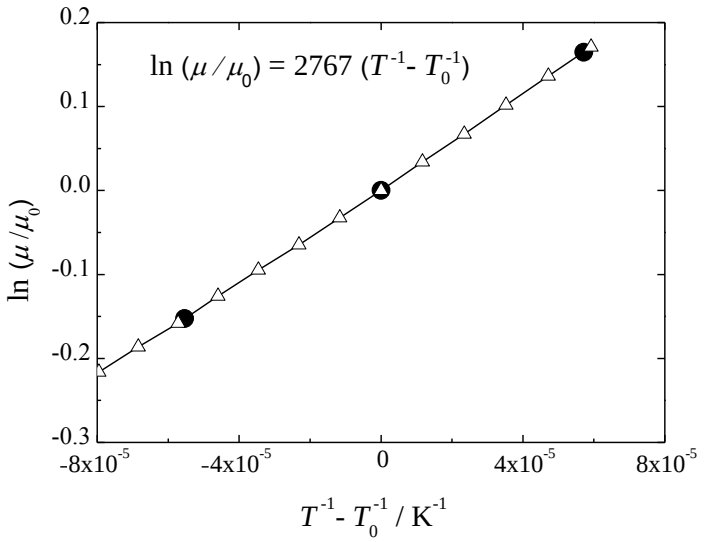

Figure 3.3. Influence of temperature on the dynamic viscosity of the Newtonian fluid used (Δ) and comparison with a 40 wt% glycerine aqueous solution (●) reported by Sheely (1932) (T_0 = 293.2 K).

3.4. Governing equations and the numerical method

The governing equations describing the isothermal laminar flow of an incompressible fluid are the mass conservation equation,

$$\nabla \cdot \mathbf{u} = 0\,, \tag{3.2}$$

and the momentum equation,

$$\rho\left(\frac{\partial \mathbf{u}}{\partial t} + \nabla \cdot \mathbf{uu}\right) = -\nabla p + \nabla \cdot \boldsymbol{\tau}\,, \tag{3.3}$$

where **u** represents the velocity vector, ρ the fluid density, t the time, p the pressure and $\boldsymbol{\tau}$ the extra-stress tensor. For the Newtonian fluids and through the application of Newton's law of viscosity, the extra-stress tensor can be written explicitly as:

$$\boldsymbol{\tau} = \mu\,(\nabla \mathbf{u} + \nabla \mathbf{u}^{\mathrm{T}})\,. \tag{3.4}$$

The conservation of mass and the momentum equations were solved numerically using an in-house finite-volume code, which has been extensively verified (Oliveira *et al.*, 1998; Oliveira *et al.*, 2007; Oliveira *et al.*, 2008b) and the implementation model validated against experimental data (Escudier *et al.*, 2000; Oliveira *et al.*, 2008a).

The numerical method is based on the time-marching version of the SIMPLEC pressure correction algorithm formulated for collocated variables (Oliveira *et al.*, 1998). The continuity and momentum equations for the Cartesian velocity vector written in non-orthogonal coordinates are integrated in space over each of the computational cells of volume V_P, and in time over a time step Δt, to form sets of linearized algebraic equations. The discretization of the governing equations is based on central differences for diffusion terms and for the convective terms the interpolating scheme employed is the CUBISTA high-resolution scheme (Alves *et al.*, 2003), formally of third-order accuracy in smooth fields. Regarding the boundary conditions, no-slip is assumed at the walls ($\mathbf{u} = 0$), while at inlet a uniform velocity field is assumed. Since the inlet channel is long, as in the experiments, the flow becomes fully-developed well upstream of the cylinder. At the outlet, vanishing gradients are assumed for the velocity while pressure is linearly extrapolated from the two upstream cells.

The full computational domain was mapped using block-structured meshes. The inlet and outlet were located 200 and 140 cylinder radii upstream and downstream of the origin of the coordinate system, respectively, to allow complete flow development upstream of the cylinder and to eliminate outlet boundary condition effects in the region of interest. To generate the mesh, the flow domain was divided into 24 blocks and within each block the cells were concentrated near the cylinder region, as illustrated in Figure 3.4.

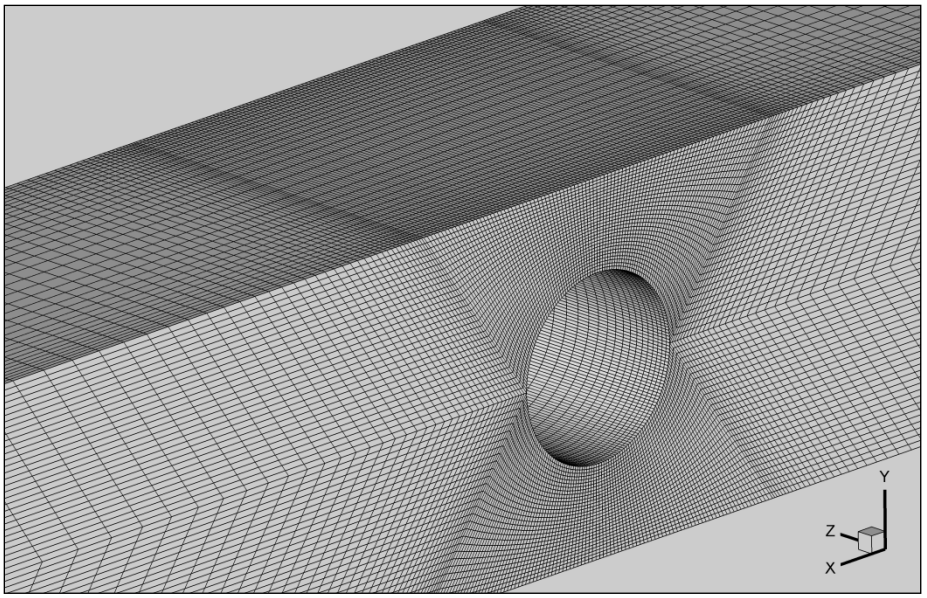

Figure 3.4. Zoomed view of the mesh used in the numerical simulations for $AR = 2$.

Extensive sets of calculations using meshes with different levels of refinement were carried out by Ferreira (2006) to estimate the numerical uncertainty and select an adequate mesh to provide mesh independent results. The characteristics of the meshes used in this work are presented in Table 3.2, where $(\Delta l/R)_{min}$ represents the minimum dimensionless cell size along the cylinder axis, $(\Delta r/R)_{min}$ the minimum cell size on the radial direction and $(\Delta s/R)_{min}$ the minimum cell size of the arc length over the cylinder surface.

Table 3.2. Minimum cell sizes of the computational meshes used.

AR	$(\Delta l/R)_{min}$	$(\Delta s/R)_{min}$	$(\Delta r/R)_{min}$
16	0.050	0.050	0.033
8	0.050	0.050	0.033
2	0.050	0.050	0.033
0.50	0.0125	0.050	0.033

3.5. Results and discussion

In addition to the geometric parameters previously defined (*AR* and *BR*) the flow characteristics depend also on the Reynolds number (*Re*), here defined as:

$$Re = \frac{\rho U R}{\mu} \ , \tag{3.5}$$

where *U* is the bulk upstream velocity and *R* is the radius of the cylinder.

The experiments were carried for three aspect ratios, *AR* = 16, 8 and 2 and for each case the results are reported for different planes along the cylinder (constant *z*/*R*) and for the symmetry plane *y*/*R* = 0, as shown in Figure 3.2. In the flow visualizations and PIV measurements the Reynolds number was varied between 2 and 40 for *AR* = 16 and 8 and between 2 and 70 for *AR* = 2, in order to maintain steady flow conditions. For comparison purposes numerical simulations were also carried out for the same steady flow conditions, and additionally the case *AR* = 0.5 was also numerically investigated. Additional flow visualizations were also done for unsteady conditions, and compared with numerical predictions. Both in the experiments and in the numerical simulations under steady flow conditions, the flow was found to be symmetric with respect to planes *y*/*R* = 0 and *z*/*R* = 0. In section 3.5.1 we present the flow visualization results, together with some numerical data, whereas the velocity fields obtained with the PIV technique and additional numerical data are reported in section 3.5.2.

3.5.1. Flow visualization - flow patterns and recirculation bubble length

Figure 3.5 compares the flow visualizations and numerical predictions at the symmetry plane (*z*/*R* = 0) for *AR* = 16, 8 and 2, in each case at two values of *Re* to illustrate the flow pattern within the separated flow region. For all values of *AR*, the recirculation length, L_v, increases with the increase of *Re*. A good agreement between the two sets is observed.

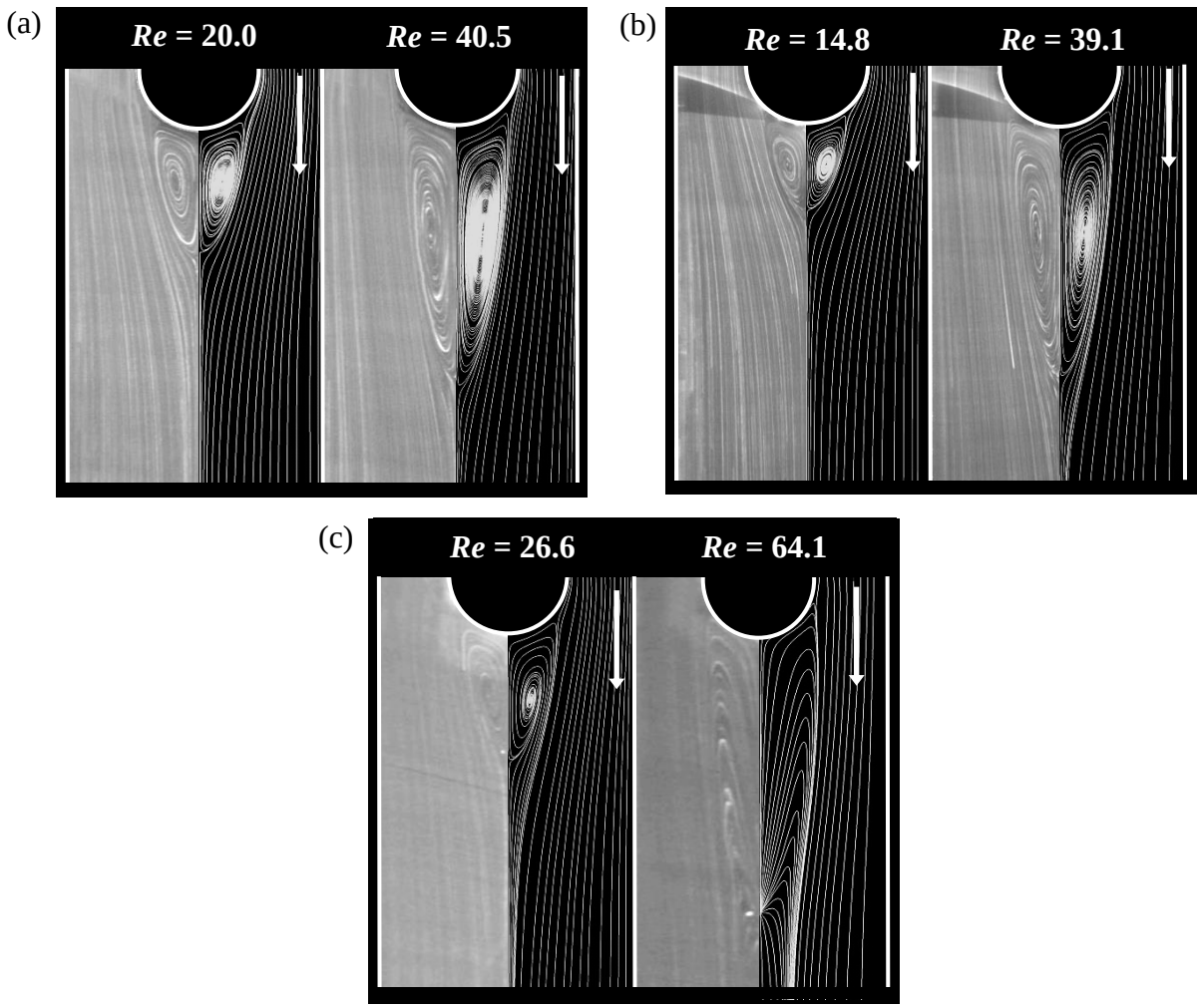

Figure 3.5. Experimental (left-hand side) and numerical (right-hand side) streamlines as a function of Reynolds number at the symmetry plane ($z/R = 0$) for (a) $AR = 16$, (b) $AR = 8$ and (c) $AR = 2$.

For the specific values of $AR = 8$ and $Re = 29.1$ the spanwise variation of the projected streamlines (i.e., at different values of z/R), is shown in Figure 3.6, containing again the corresponding numerical predictions. In this figure the recirculation length, L_v, is also marked at the various cross-section planes and again the comparison between the experimental and numerical data is remarkably good. Qualitatively, the pictures taken for $AR = 16$ and $AR = 2$, not shown, are similar and the agreement with the numerical results is as good as for $AR = 8$, hence no further comparison is shown for conciseness. However, from the whole set of fluid flow visualizations and the corresponding numerical simulations, we were able to construct plots showing the variation of L_v with Re, as explained next.

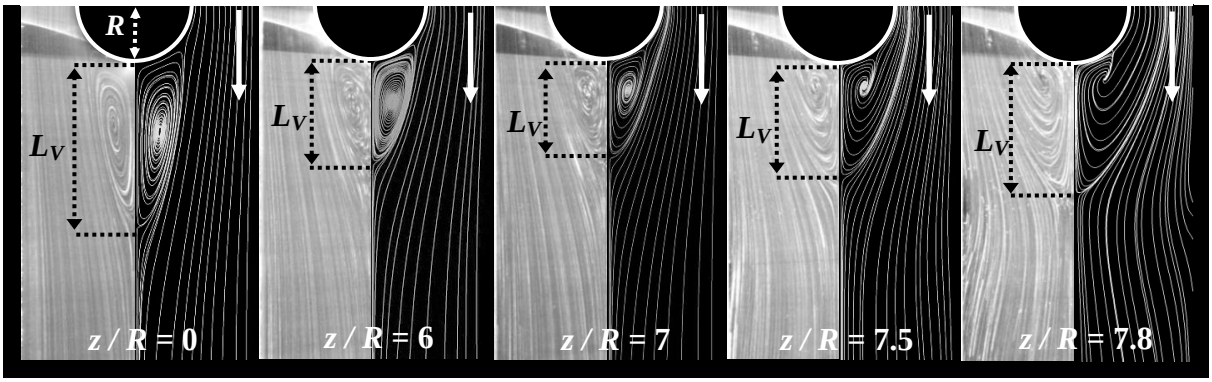

Figure 3.6. Experimental (left-hand side) and numerical (right-hand side) projected streamlines for AR = 8 and Re = 29.1 as a function of z/R.

Figure 3.7 shows the spanwise variation of the recirculation length for AR = 16, 8, 2 and 0.5 as a function of Re. The vortex length is measured at the symmetry plane (y/R = 0) and the plots show both the experimental (symbols) and numerical (lines) data. At all spanwise locations the recirculation length increases with Reynolds number (in agreement with the results presented in Figure 3.5) and the plots show a non-monotonic variation of L_v/R with z/R, for $AR \geq 2$. There is always a local maximum of L_v at the end wall, followed by an intense reduction in recirculation length with the minimum L_v occurring approximately at a distance of one cylinder radius from the wall for $AR \geq 2$, i.e., at $z/R \approx (AR - 1)$. Then, the length of the separated flow region increases again, except for AR = 0.5. The location of the second maximum depends on AR and Re. For AR = 0.5, a minimum value of L_v occurs at z/R = 0 for reasons to be explained below, and this also happens for $AR < 0.5$. In any case, for $AR < 0.5$ the width of the channel is already smaller than the cylinder radius.

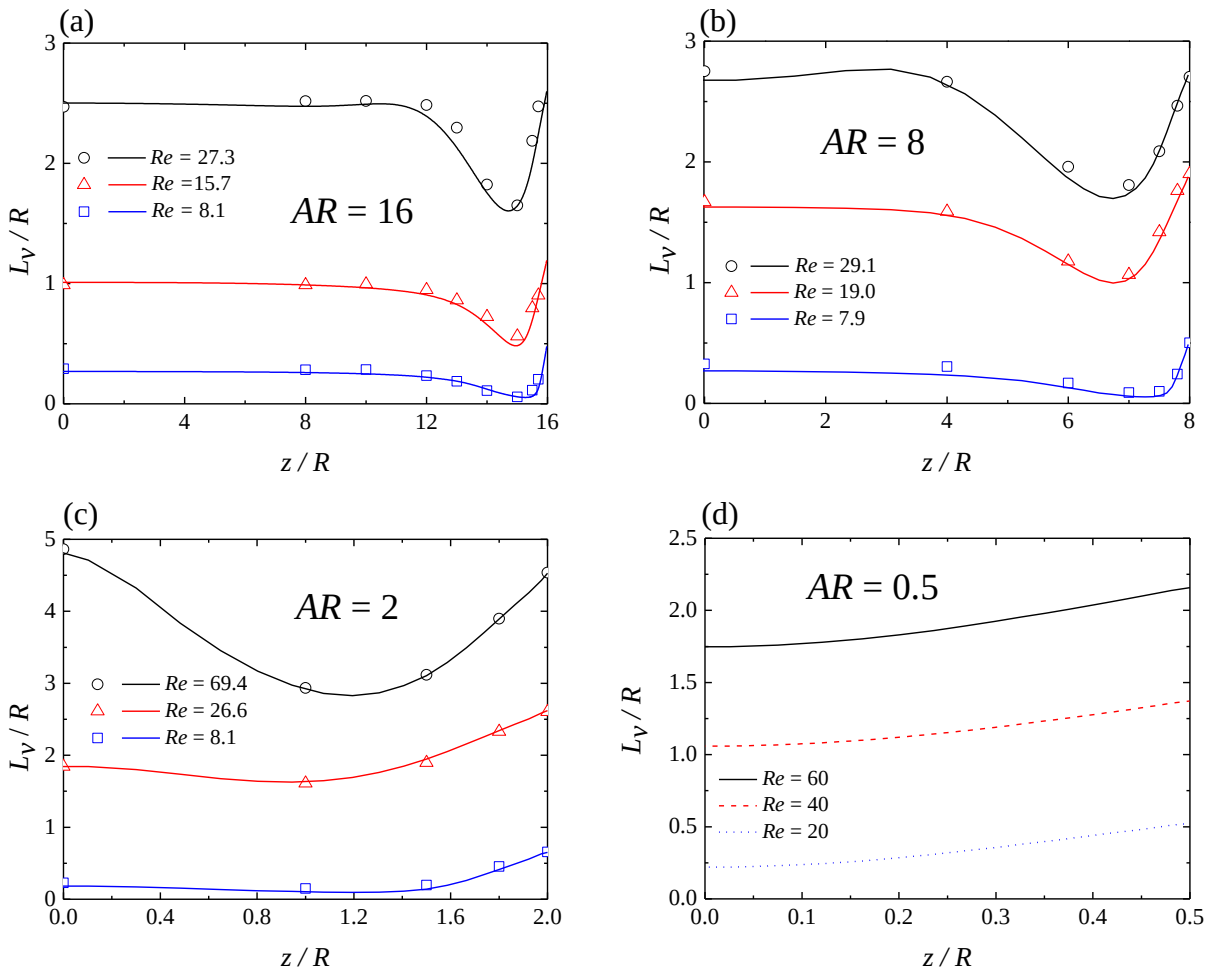

Figure 3.7. Spanwise variation of the length of the separated flow region as a function of the Reynolds number at the symmetry plane (y/R = 0): (a) AR = 16, (b) AR = 8, (c) AR = 2 and (d) AR = 0.5. Comparison between experiments (symbols) and numerical predictions (lines).

For large AR (e.g. AR = 16 and 8) the minimum L_v near the end wall is followed by an increase to a plateau value, as we move away from this wall, except at the higher Re where the recirculation length reaches a maximum value at about z/R = 11 for AR = 16 and at about z/R = 3 for AR = 8, before levelling to the plateau value. The differences are small and the detection of this is better seen in the numerical results, shown in Figures 3.7a and 3.7b. At low AR values, as for AR = 2, the second maximum of L_v occurs at z/R = 0 and this peak is actually larger than the peak L_v at the end wall, for the higher value of Re. For AR = 0.5, the channel span is so small that there is only one maximum of $L_{v,}$ located at the wall and a local minimum at z/R = 0. In all cases the experiments show the flow to be symmetric in relation to the z/R = 0 symmetry plane, therefore the previous discussion also holds for negative values of z/R.

The effect of the Reynolds number on the recirculation length at the $z/R = 0$ symmetry plane is shown in Figure 3.8a, where it is clear that L_v increases with Re. For $AR = 16$, 8 and 2 and for values of $Re < 6$ there is no flow separation. However, for $AR = 0.5$ the flow separation appears only for values of $Re \geq 14$, due to the stabilizing effect of the end walls, which approach each other as AR decreases. For large values of AR (e.g. $AR = 16$ and 8), the variation of L_v with Re at the $z/R = 0$ centreplane is quasi-linear and independent of AR, up to $Re \approx 30$, followed by a decrease in slope, which is stronger for higher values of AR. At $Re \geq 40$ the flow becomes unsteady for $AR = 16$ and 8. For $AR = 2$ the variation of L_v with Re is quasi-linear up to $Re \approx 45$ and a progressively slower increase of L_v with Re is observed for higher Re. The flow also becomes unsteady for $AR = 2$, but for $Re \approx 75$. Thus, as AR decreases there is a clear influence on L_v with smaller values being observed at constant Re and the variation of L_v with Re becoming non-linear at increasingly higher values of Re. The stabilizing effect of the end walls is clearly visible in the numerical results obtained with $AR = 0.5$, where now steady flow is observed at least up to $Re = 300$ (data for $Re > 80$ is not shown in Figure 3.8).

Figure 3.8b also plots the variation of L_v with Re, but now near the end walls, at the approximate location of the minimum recirculation length, i.e., at $z/R = (AR - 1)$. As for the $z/R = 0$ symmetry plane, for $AR = 16$, 8 and 2 there is no flow separation at $Re \leq 6$ and we observe a linear variation of L_v with Re up to $Re \approx 25$, but with a lower slope than at the symmetry plane. It is also interesting to observe the near collapse of the L_v versus Re curves for the various geometries at the $z/R = (AR - 1)$ planes and $Re \leq 25$, in contrast to what is seen at the symmetry plane. This shows that these near end wall flows have essentially the same characteristics and that they are determined by the proximity to the end wall, whereas at the symmetry plane the flow is independent of the end walls for large values of AR, but starts to be controlled by the end walls as AR decreases below a critical value (of order 1). Note that, when $AR << 1$ the flow becomes identical to that inside a Hele-Shaw flow cell, where the flow features are precisely controlled by the end wall and flow separation is no longer observed.

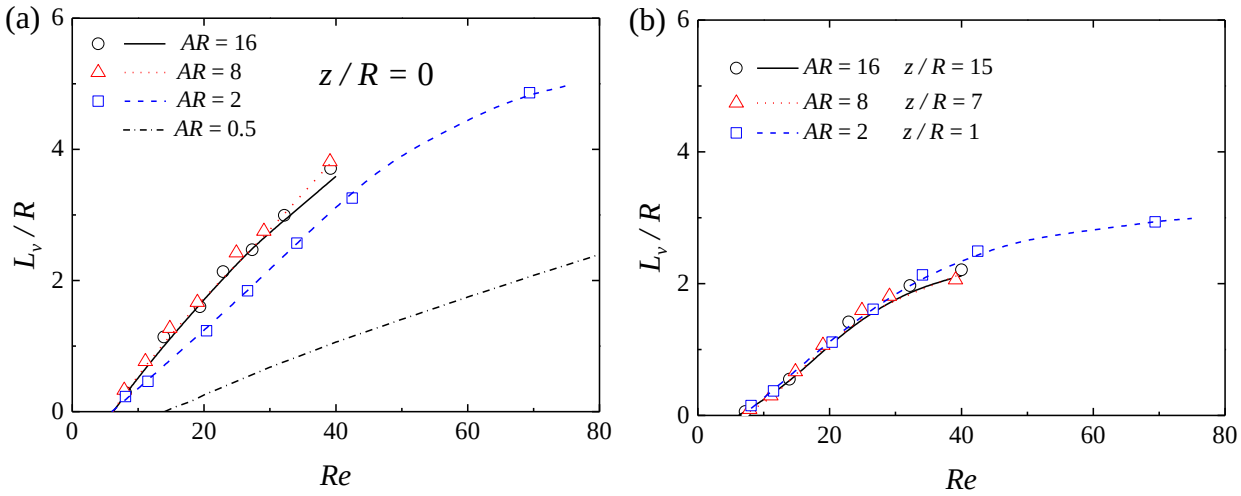

Figure 3.8. Variation of the separated flow region length with *Re*: (a) at the symmetry plane ($z/R = 0$) and (b) at near end wall planes, $z/R = AR - 1$ ($z/R = 15$ for $AR = 16$, $z/R = 7$ for $AR = 8$ and $z/R = 1$ for $AR = 2$). Comparison between experiments (symbols) and numerical predictions (lines).

At constant z/R planes, Figure 3.9a shows instantaneous pathlines obtained from flow visualizations and numerical predictions of instantaneous streamlines for $AR = 8$ (projected on the visualization plane), whereas Figure 3.9b only shows numerical data for $AR = 16$ and 2, taken at the symmetry plane and near the end walls. In all cases the flow patterns are unsteady with Figure 3.9a showing a fair agreement between numerical streamlines and experimental pathlines. Note that there was here no attempt to match the instant of time of experiments and predictions within the periodicity cycle. At these Reynolds numbers the free shear layers just started to interact with each other, as a sign of what will happen when the periodic vortex shedding is firmly established. For these Reynolds numbers this interaction only produces a moderate oscillation of the flow patterns on the wake of the cylinder. The same phenomenon can be seen at this stage in the flow around a cylinder with smaller blockage ratio as in the experiments of Coelho and Pinho (2003).

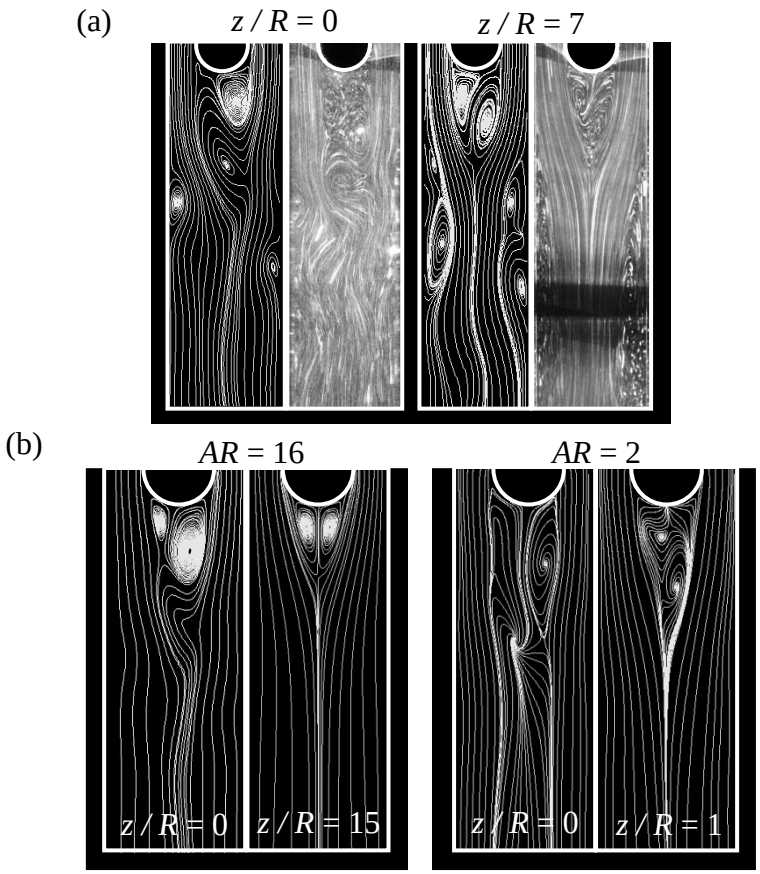

Figure 3.9. (a) Experimental pathlines (right-hand side) and numerical predictions of instantaneous projected streamlines (left-hand side) for AR = 8 and Re = 130.2; (b) numerical predictions for AR = 16 (Re = 45) and AR = 2 (Re = 80).

3.5.2. Velocity field

Figure 3.10 shows the influence of Re on the normalized streamwise velocity along the centreline (y/R = 0 and z/R = 0) for AR = 16, 8, 2 and 0.5. These profiles were obtained using both the PIV technique (symbols) and numerical simulation (lines); the agreement between both sets of data is again good. Qualitatively, all velocity profiles are similar upstream of the cylinder and for each value of AR they are essentially independent of the Reynolds number. The upstream influence of the cylinder on the centreline velocity profile is restricted to about four cylinder radii. The value of the normalized velocity at the centreline exceeds 1.5, the centreline normalized velocity for fully-developed flow between two infinite parallel plates, precisely because of the influence of the end walls, which is larger for the smaller the value of AR.

Indeed, the normalized centreline velocity for fully-developed flow conditions in a rectangular duct is maximum for a square channel ($AR = 2$; $u/U = 2.096$) and minimum for $AR \rightarrow 0$ or $AR \rightarrow \infty$ ($u/U = 1.5$) as can be easily obtained from the analytical solution for laminar flow in rectangular ducts (White, 1991). Downstream of the cylinder, the influence of the Reynolds number is obviously strong and the recirculation length is seen to increase with the Reynolds number, as previously observed in the flow visualizations. We remind that the end of recirculation corresponds to the location downstream of the cylinder where $u = 0$.

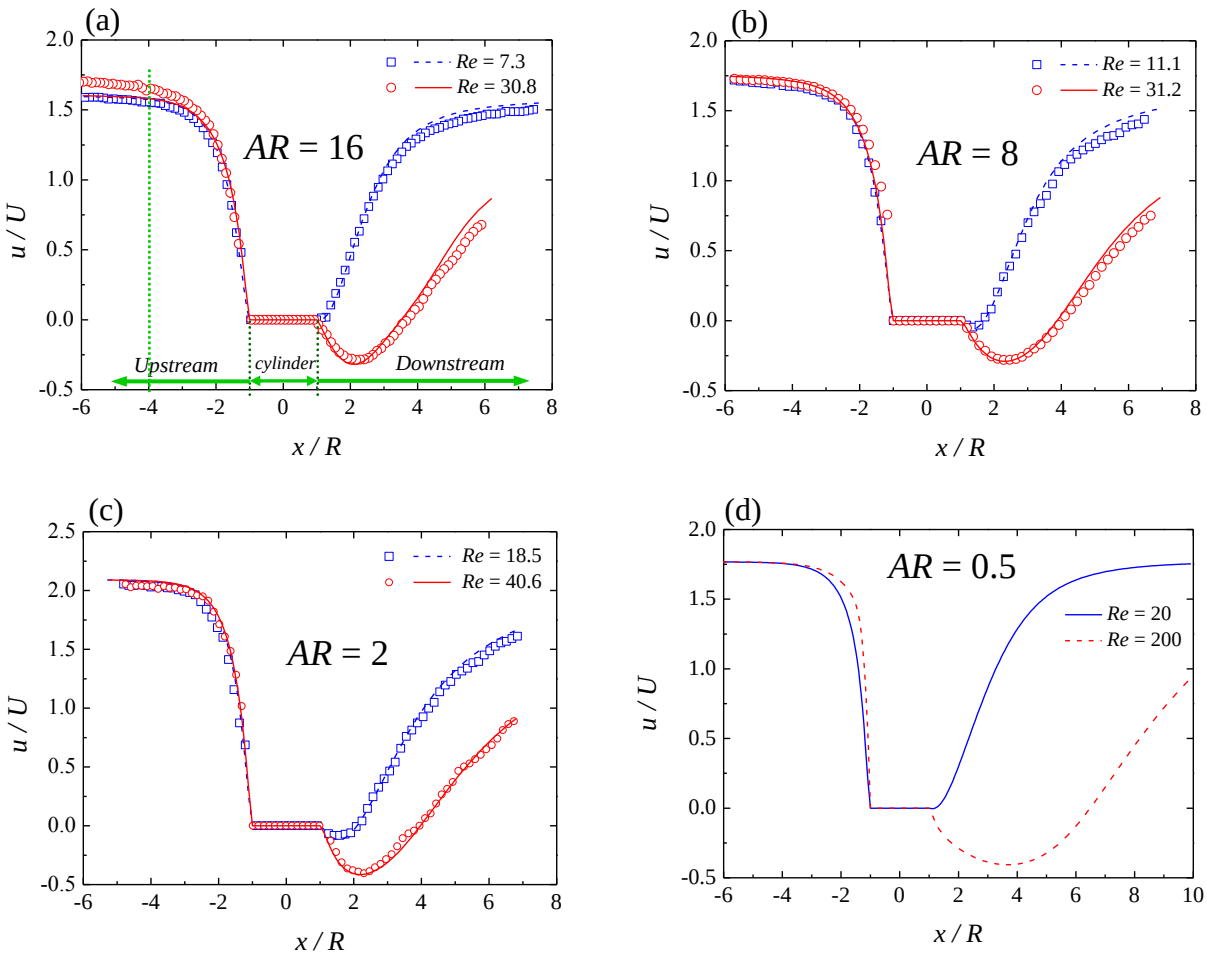

Figure 3.10. Streamwise velocity profile along the centreline ($y/R = 0$, $z/R = 0$) for two values of Re: (a) $AR = 16$, (b) $AR = 8$, (c) $AR = 2$ and (d) $AR = 0.5$. Comparison between experiments (symbols) and numerical predictions (lines).

Similar normalized profiles of the streamwise velocity are shown in Figure 3.11, but now at different spanwise planes, including the centreline for reference. Specifically, the profiles plotted are all at the symmetry plane, $y/R = 0$, and comparison is made between the profiles at the centreline ($y/R = 0$ and $z/R = 0$) and at the line near the end walls where the minimum recirculation length was seen in the flow visualizations, namely at $y/R = 0$ and $z/R = (AR - 1)$.

For all values of *AR*, the velocity upstream of the cylinder is higher on the centreline than on the line near the end walls as expected and the upstream flow is affected by the presence of the cylinder only in the region $-4 \leq x/R \leq -1$. Along the central region of the geometry the approaching flow decelerates continuously due to the blockage imposed by the cylinder, but in contrast, near the end walls a small flow acceleration is initially observed to occur prior to the deceleration for the geometries with larger aspect ratio (*AR* = 16 and 8). This suggests the local appearance of a small spanwise velocity component towards the end wall and that there is a fundamental difference between the flow characteristics at high and low *AR*.

Downstream of the cylinder, and for all *AR*, flow recovery starts earlier in the near-wall plane than on the centreline, because of the shorter recirculation length (cf. Figure 3.7), leading to higher velocities there and in spite of the retarding effect of the end walls. Further downstream, however, the ever present retarding effect of the end walls takes over and the near-wall velocities stabilize to lower values than at the symmetry plane as already observed far upstream under fully developed flow conditions. At the higher Reynolds numbers the cross-over of the two velocity profiles take place at increasingly longer distances from the rear stagnation point.

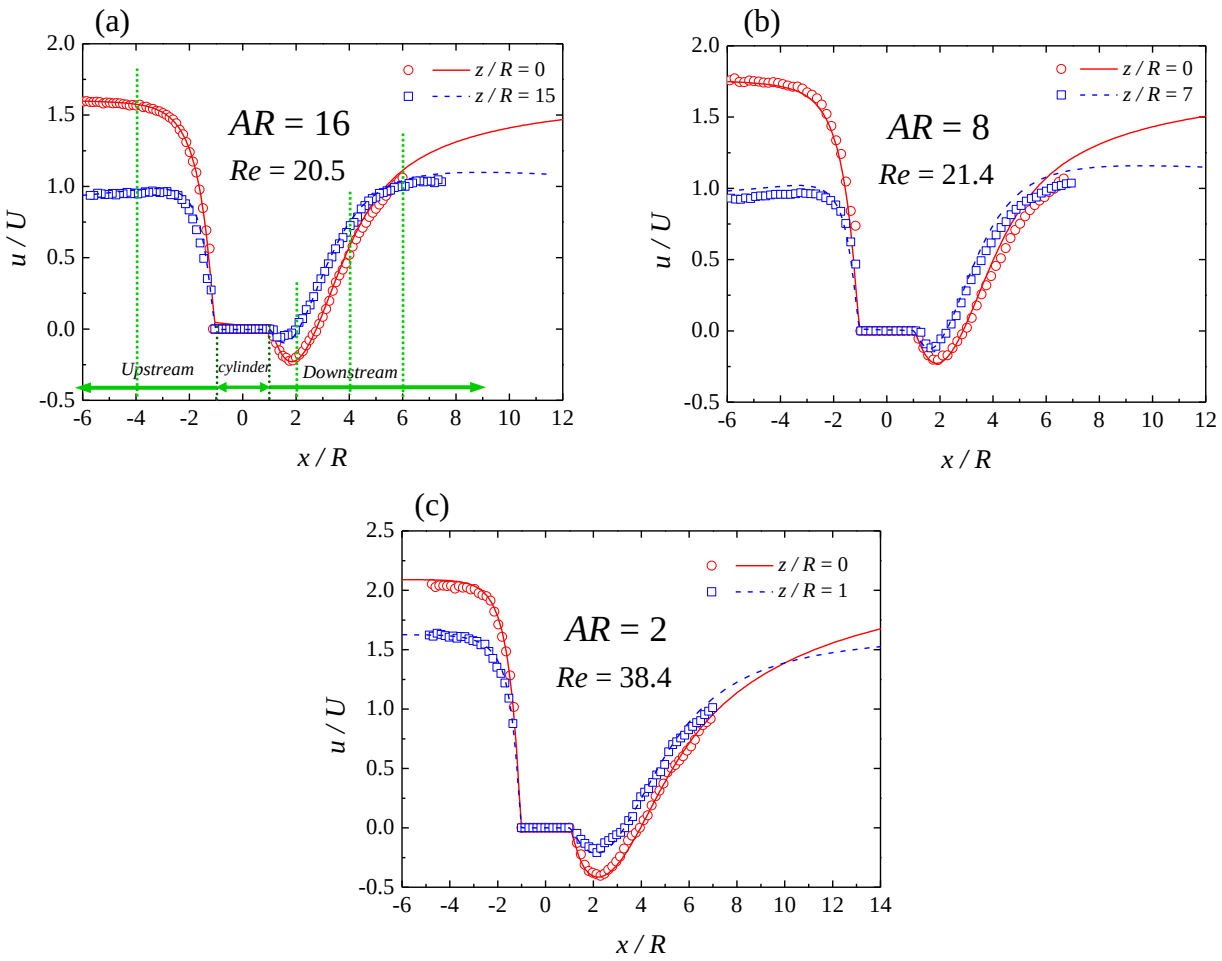

Figure 3.11. Streamwise variation of streamwise velocity for $y/R = 0$. Comparison between the profiles on the centreline ($z/R = 0$) and near the end walls ($z/R = AR - 1$): (a) $AR = 16$, $Re = 20.5$; (b) $AR = 8$, $Re = 21.4$ and (c) $AR = 2$, $Re = 38.4$. Comparison between experiments (symbols) and numerical predictions (lines).

In order to understand the flow characteristics and in particular the effect of the end walls, we present in Figures 3.12 - 3.14 transverse profiles of the normalized velocity at the symmetry ($z/R = 0$) and near end wall planes ($z/R = AR - 1$) at one upstream and three downstream locations. Figures 3.12 - 3.14 pertain to $AR = 16$, 8 and 2, respectively, the Reynolds number is approximately the same ($Re \approx 26$) and for each case the upstream location is $x/R = -4$ and the downstream profiles are at $x/R = 2$, 4 and 6. These locations are also marked in Figure 3.11a. Since all flows are symmetric only half the profiles are shown. The figures contain experimental data obtained by PIV (symbols) and the corresponding numerical data (lines) and the agreement is good. In all cases, and as shown in Figures 3.12a, 3.13a and 3.14a, the upstream profiles at $x/R = -4$ approach the analytical solution (lines) for fully-developed laminar flow in a rectangular duct (White, 1991), especially for the smaller AR, since the

influence of the cylinder is negligible for $x/R < -4$, and so the velocities are always higher on the symmetry plane than on the near end wall plane.

The downstream profiles (Figures 3.12b-d, 3.13b-d and 3.14b-d) are in agreement with the previous observations that the recirculation length is shorter near the end walls and consequently the flow there develops faster. Thus, at $x/R = 2$ (Figures 3.12b, 3.13b and 3.14b) the velocities are higher near the end walls than at the symmetry plane region from $y/R = 0$ to a location that varies with AR ($|y/R| \approx 0.9$ for $AR = 16$ and $|y/R| \approx 1$ for $AR = 8$; for $AR = 2$ the numerical simulations indicate a value of $|y/R| < 0.7$, whereas for the experiments the difference between the two profiles are within experimental uncertainty). This non-monotonic variation of the cross-over point is related to the change of type of the flow: for small AR the flow characteristics are everywhere determined by the end walls, whereas for large AR the flow in the central region of the domain is essentially independent of the end wall effects and depends primarily on the Reynolds number. In the gap between the cylinder and the side walls (at $|y/R| = 2$) the velocities will be higher in the symmetry plane region than near the end walls as a consequence of the larger approach flow velocities, cf. Figures 3.12a, 3.13a and 3.14a. However, these differences are not proportional to the corresponding upstream flow velocities, and the actual velocity difference between both velocity profiles in the gap is smaller than in the approach flow (for all values of AR the velocity profiles in Figures 3.12b, 3.13b and 3.14b are not too different), on account of a secondary flow developing along the cylinder, in the spanwise direction, which brings fluid from the central region to the near end wall region. It is this secondary flow that induces the velocity peaks in the y-direction, which are strongly enhanced by the increasing flow inertia. Indeed the loci of the velocity peaks are also dependent on the Reynolds number.

Moving further downstream to $x/R = 4$ (cf. Figures 3.12c, 3.13c and 3.14c for $AR = 16$, 8 and 2, respectively) and then to $x/R = 6$ (Figures 3.12d, 3.13d and 3.14d) a similar behaviour to that found at $x/R = 2$ is also observed, but with the cross-over point at a different location with lower peak velocities and located closer to the $y/R = 0$ symmetry plane as expected. At $x/R = 6$ there are no longer cross-over points for the $AR = 2$ case since the separated flow regions end earlier and the flow redevelopment process is consequently in a more advanced stage than at larger AR.

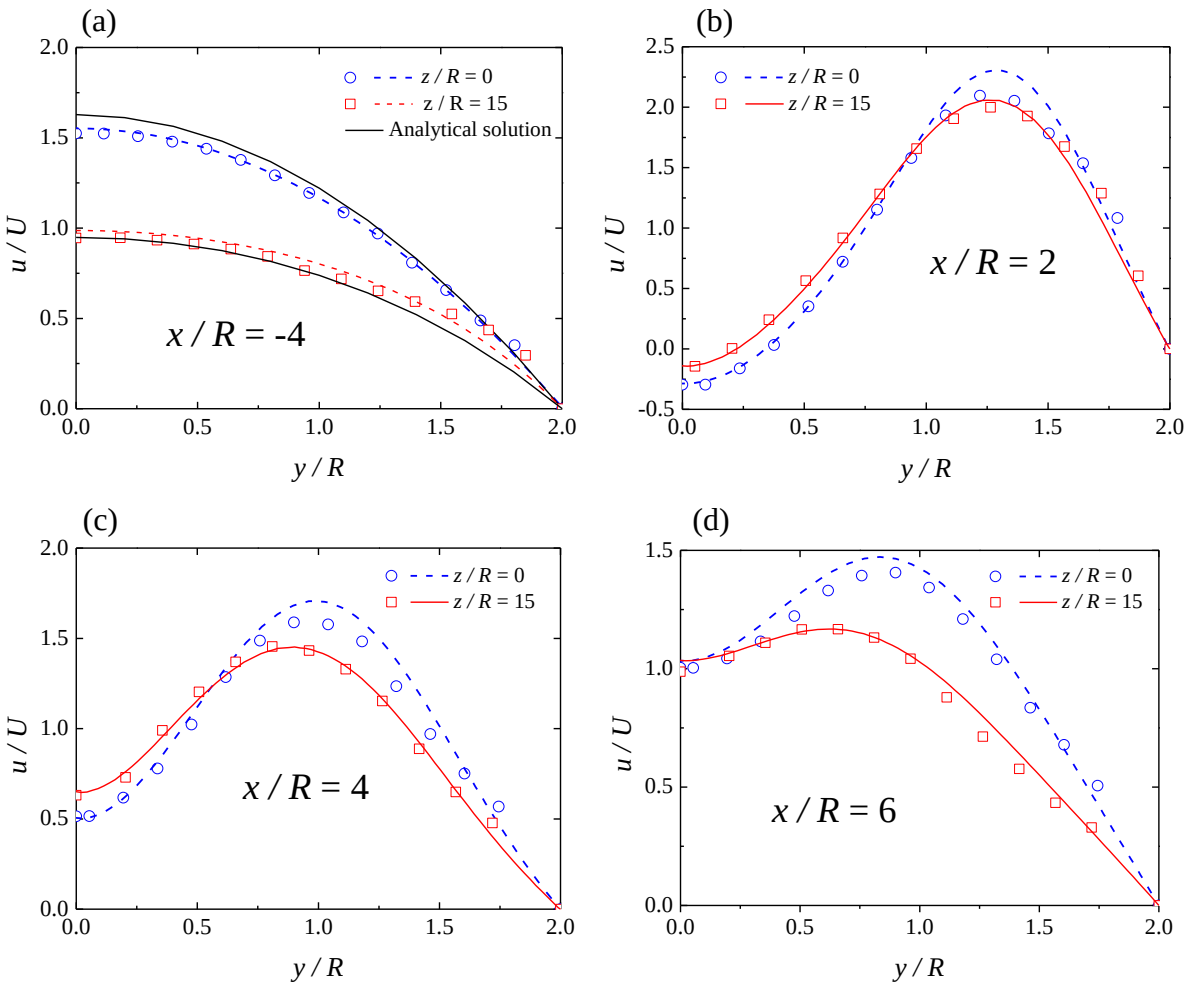

Figure 3.12. Transverse variation of streamwise velocity at the symmetry plane (z/R = 0) and near the end wall (z/R = 15) for AR = 16 and Re = 25.3: (a) x/R = -4, (b) x/R = 2, (c) x/R = 4 and (d) x/R = 6. Comparison between experiments (symbols) and numerical predictions (lines).

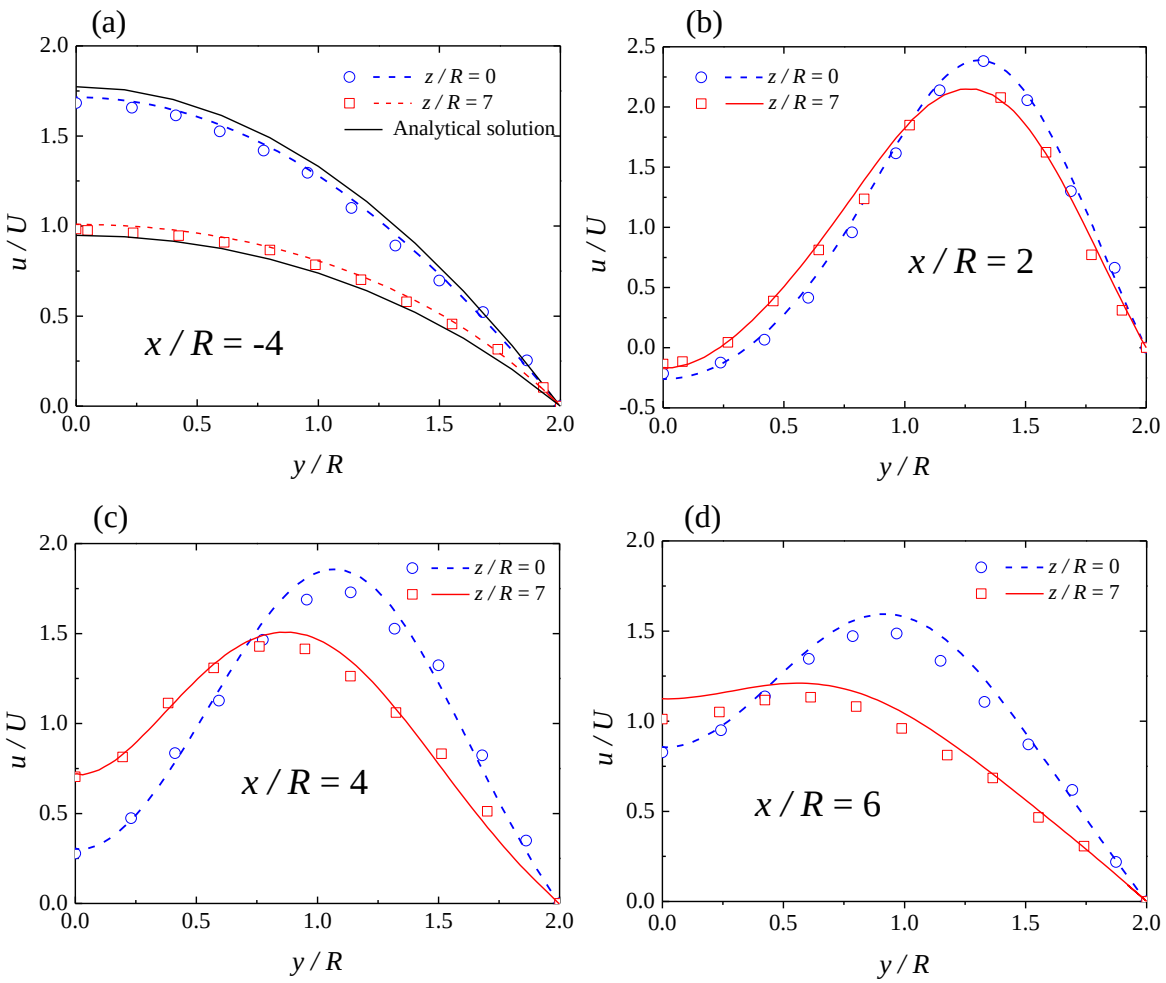

Figure 3.13. Transverse variation of streamwise velocity at the symmetry plane (z/R = 0) and near the end wall (z/R = 7) for AR = 8 and Re = 25.6 (a) x/R = -4, (b) x/R = 2, (c) x/R = 4 and (d) x/R = 6. Comparison between experiments (symbols) and numerical predictions (lines).

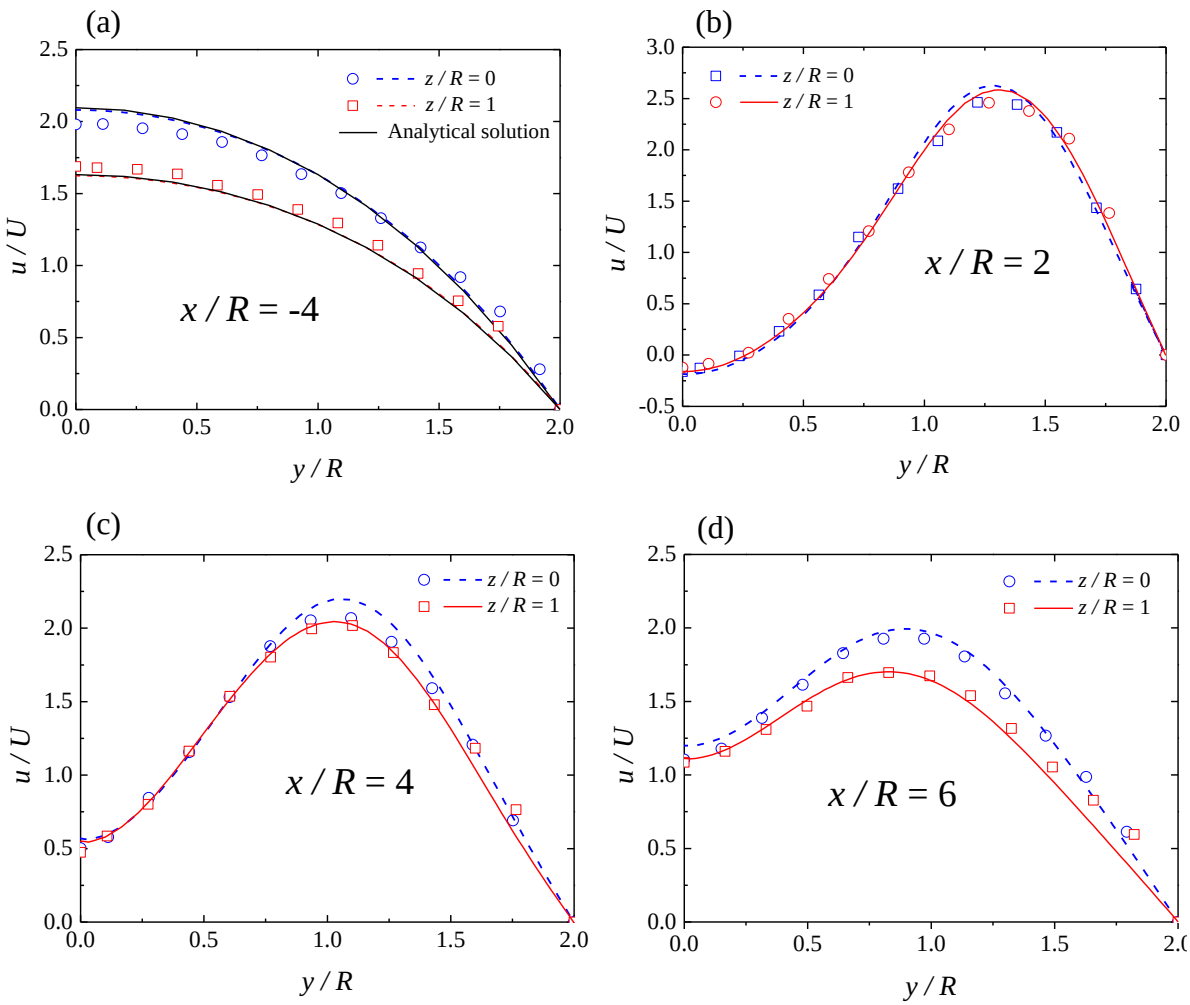

Figure 3.14. Transverse variation of streamwise velocity at the symmetry plane (z/R = 0) and near the end wall (z/R = 1) for AR = 2 and Re = 26.1: (a) x/R = -4, (b) x/R = 2, (c) x/R = 4 and (d) x/R = 6. Comparison between experiments (symbols) and numerical predictions (lines).

Spanwise profiles of normalized streamwise velocity at the symmetry plane y/R = 0 and at the downstream location x/R = 4 are shown in Figure 3.15 for different values of Re. The shape of these profiles is inverse to those of the corresponding profiles of recirculation length shown in Figure 3.7, i.e., where there is a local maximum in recirculation length, a local velocity minimum is observed and vice versa. These results confirm the existence of velocity peaks near the end walls, which are enhanced by flow inertia. The curves corresponding to cases with a large separated flow region (higher Re), Figures 3.15a and 3.15b, show that next to the strong positive velocity peak there is a region of minimum velocity. This local velocity deficit is possibly due to fluid that feeds into the nearby near-wall jet.

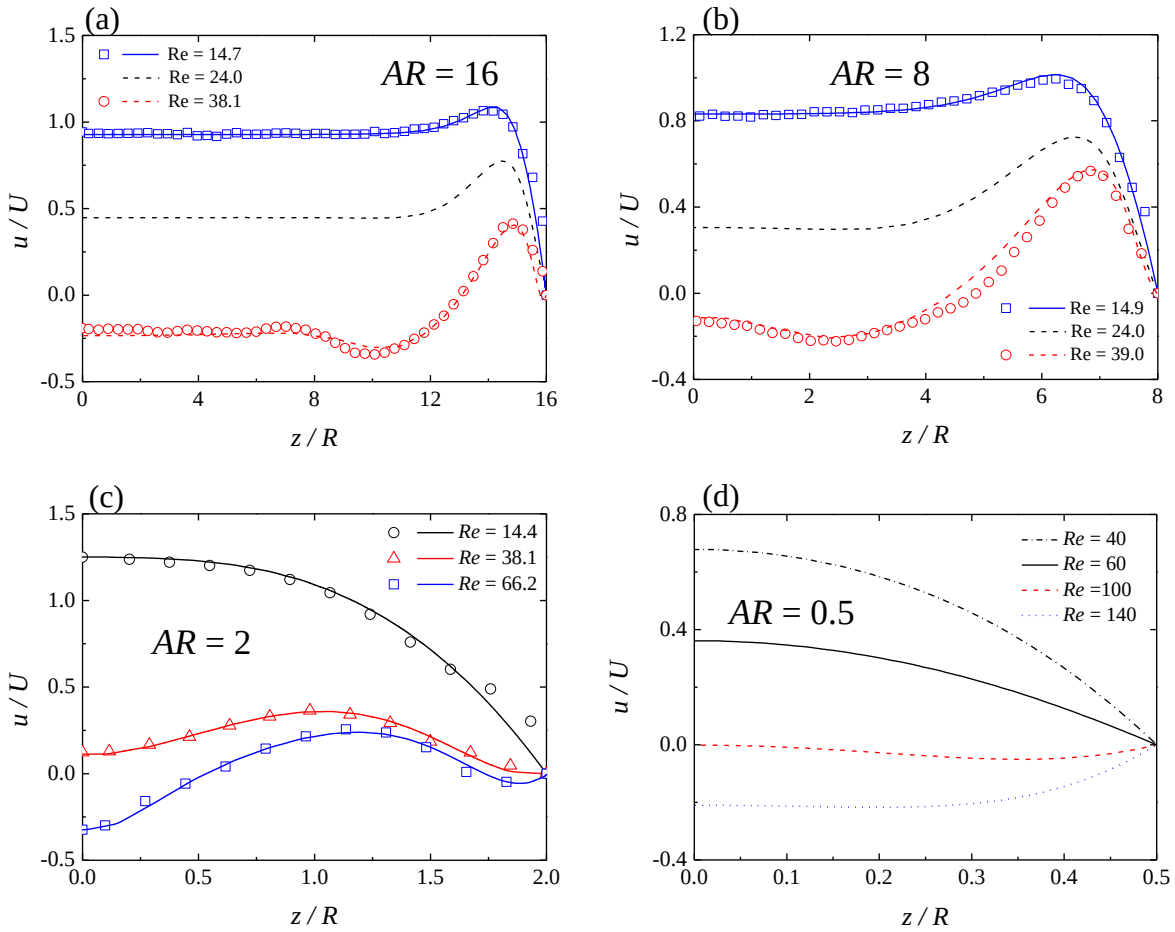

Figure 3.15. Spanwise variation of the normalized streamwise velocity downstream of the cylinder (x/R = 4) and on the symmetry plane y/R= 0 as a function of Re: (a) AR = 16, (b) AR = 8, (c) AR = 2 and (d) AR = 0.5 Comparison between experiments (symbols) and numerical predictions (lines).

The difference in the behaviours at AR = 16, 8 and 2, even at the high Reynolds number flow, is a consequence of the qualitative differences imposed by the end walls upon the flow at the core of the duct. The downstream profiles at the lower Reynolds number ($Re \approx 15$) develop fast especially for lower AR. For AR = 16 and 8 the influence of the end walls is confined to a region near those walls and does not propagate to the centre of the duct, where the flow is essentially controlled by the vicinity of the side walls of the duct, parallel to the cylinder axis. In contrast, for AR = 2 the end walls are as important as the side walls and affect significantly the flow at the symmetry plane, z/R = 0, because even though its region of influence may be of similar physical size it corresponds to a proportionally larger volume of the flow domain than at larger values of AR.

3.5.3. Numerical results and mechanism for the velocity peaks

Considering that the comparison between experimental and numerical data of Figures 3.5 - 3.15 showed a good agreement, in what follows only numerical data are used to explore in detail the flow dynamics and help interpret the causes for the velocity peaks. The main issues that we aim to address with this study are to determine the value of *AR* below which the effects of the end walls dominate the whole flow and what are the causes of the appearance of the velocity peaks in its various forms.

According to the results shown in sections 3.5.1 and 3.5.2 the velocity peaks are located at $z/R \approx (AR - 1)$. For higher *AR* this location is near the end walls and far away from the centreplane (i.e. $z/R >> 0$), while for lower *AR* this location is in the centreplane (i.e. $z/R = 0$) and the velocity profiles show a parabolic shape. The velocity peaks near the end walls tend to disappear for $AR \lesssim 6$, when the influence of the end walls becomes as important as the influence of the side walls.

Velocity peaks are not exclusive of high Reynolds number flows and have been reported at low *Re* flow conditions with viscoelastic fluids by Verhelst and Nieuwstadt (2004) (cf. their Figure 31 at a Deborah number of 2.72). Interestingly, in Figures 3.16a and 3.16b we show, based on numerical simulations, that velocity peaks are also observed in the spanwise profiles of streamwise velocity at $y/R = 0$ and downstream locations (e.g. at $x/R = 4$), even under creeping flow conditions (i.e. in the limit $Re \rightarrow 0$) for Newtonian fluids. These profiles pertain to aspect ratios of 2, 8, 16, 32 and 128 and clearly illustrate the existence of local velocity peaks near the end walls at $Re = 0$ and increasing as *AR* is raised. Note that in these creeping flow cases there is no flow separation. The shapes of the velocity profiles and of the velocity peaks at $Re = 0$ in Figure 3.16 are different from those at the large Reynolds number flows with separation in Figure 3.15, but not too different from the shape of the profile at $Re \approx 15$ in the same Figure 3.15 despite the existence of flow separation.

Creeping flow is simulated numerically deleting the convective term in the momentum equation. The transient term is retained since a time marching algorithm is used. When steady flow is achieved the transient term cancels out, and the Stokes equations are solved corresponding exactly to creeping flow conditions.

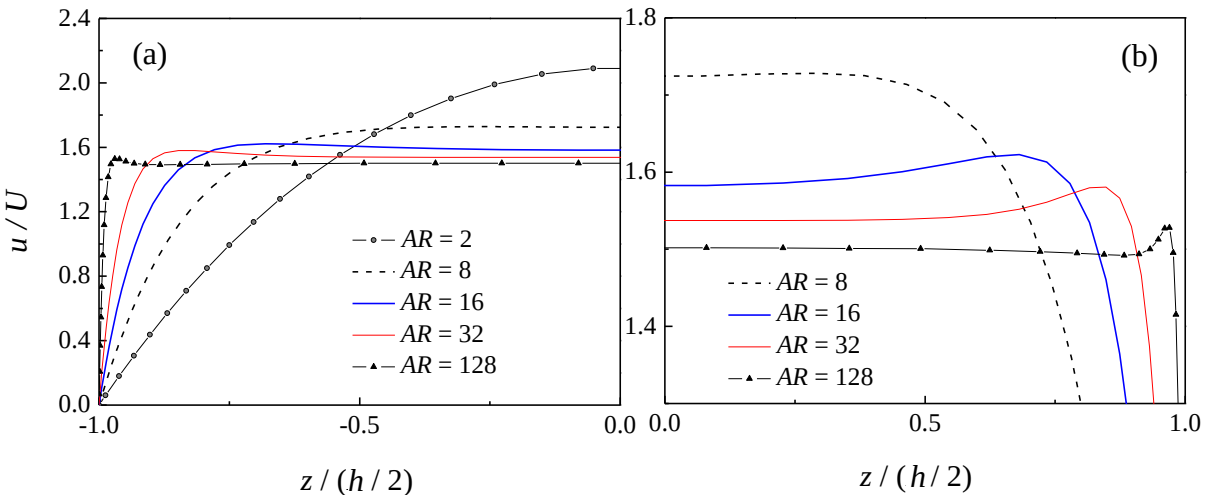

Figure 3.16. Axial velocity profiles at $y/R = 0$ and $x/R = 4$ as a function of spanwise coordinate for various aspect ratios and $Re = 0$. A smaller range of u/U is shown in part (b) in order to better illustrate the existence of small velocity overshoots under creeping flow conditions for large values of AR. Only numerical results are shown.

The behaviour of the flow around a confined cylinder and in particular the causes for the appearance of the velocity peaks in its various forms are discussed next. It is appropriate to start with a limiting case, such as creeping flow ($Re \approx 0$), which is dominated by viscous forces that generate the pressure contours shown in Figure 3.17a. At large aspect ratios and upstream of the cylinder, the fluid will have to accelerate to circumvent the obstacle, with the corresponding pressure reduction being higher near the end-wall than in the centre. Hence a negative spanwise pressure gradient (in the coordinate system used) appears and the upstream fluid acquires a spanwise velocity from the centre to the end wall region as is shown in the contour plots of Figure 3.17c and in the corresponding contours of streamwise velocity of Figure 3.17b. This effect starts to be observed at about four cylinder diameters upstream of the obstacle and by pushing fluid towards the near-wall region, the upstream region with a peak velocity shown in Figures 3.16 and 3.17b is formed.

In spite of the locally increased flow near the end-wall, the pressure decrease of the flow around the cylinder is less here than in the centre, so that the flow downstream of the cylinder has now a higher pressure near the end-wall than in the centre (cf. Figure 3.17a) thus creating a positive spanwise pressure gradient that moves the fluid from the near-wall region into the centre. This is seen both as contours of negative spanwise velocity in Figure 3.17c as well as in the symmetric orientation of contours of streamwise velocity in Figure 3.17b. This fore-aft symmetry of the velocity field is precisely a major characteristic of creeping flows of purely viscous fluids around symmetric obstacles. Note also that the $\Delta z/h$ distance of the peaks to the end wall increases in inverse proportion to AR, but this corresponds to the same distance $\Delta z/R$.

This picture is only changed by inertia, which reduces the time available for τ_{xz} to act and for this reason the peak velocity at $Re \approx 15$ in Figure 3.15a is found closer to the end wall than the peak at $Re = 0$ in Figure 3.16, for the same value of AR. Needless to say further downstream of $x/R \approx 4$ this diffusive flux continues to act and the velocity peaks will be smoothed out and the velocity profile becomes that of the fully-developed rectangular duct flow.

Under creeping flow conditions, as AR decreases, the τ_{xz} stresses increase and this smoothes the localized peaks and the velocity profiles acquire the parabolic shape typical of Hele-Shaw flow, where the flow is now totally dominated by the large gradients of τ_{xz}. Inertia counteracts this effect and this is well shown in Figure 3.15c (or in Figure 3.7c for the corresponding profiles of L_v), where we see the velocity peak moving away from the centreline at $Re = 15$ to $z/R > 1$ as the Reynolds number further increases. Therefore, as the Re increases the flow is perturbed by inertial effects, which become superimposed and eventually dominate the above diffusion mechanism.

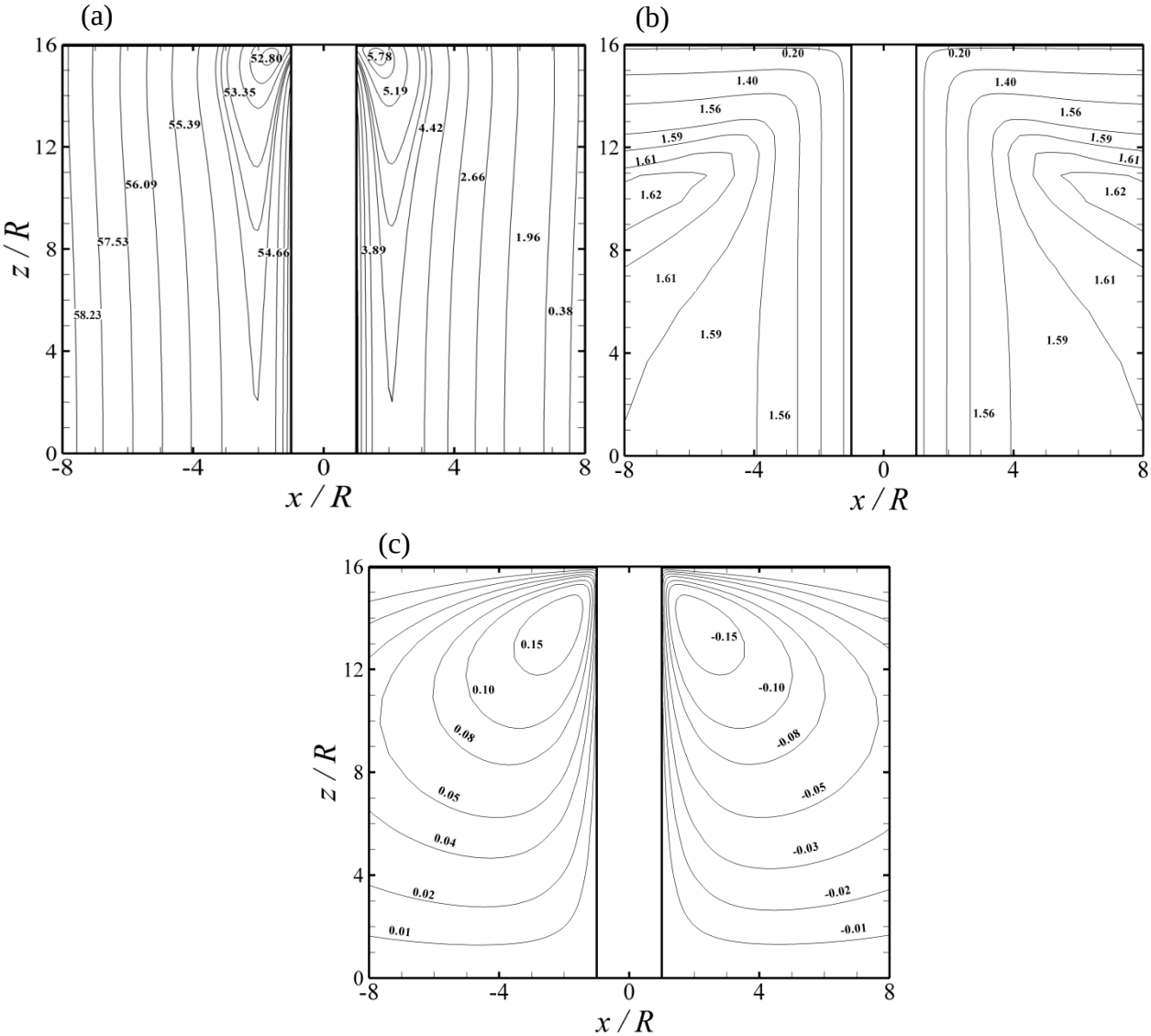

Figure 3.17. Contours of normalized pressure and velocity predicted numerically at $y/R = 0$ for $AR = 16$ and $Re = 0$: (a) pressure, $(p - p_{ref}) / (\eta U/R)$; (b) streamwise velocity, u/U; and (c) spanwise velocity, w/U.

For large aspect ratios, such as $AR = 16$, we have essentially the flow picture explained above, except that the increase in the Reynolds number leads to the formation of a separated flow region all along the cylinder span, whose length is affected by the proximity of the end wall, since the strong streamwise adverse pressure gradient downstream of the cylinder also varies in the spanwise direction. Consequently, a region of minimum recirculation length appears at the same location of the velocity peaks, where the adverse pressure gradient is weaker, and this is especially noticeable for flows with strong separation (cf. Figure 3.7a). At large Re the flow in the region of small L_v is able to negotiate the cylinder with minimum pressure loss, i.e., it separates later and consequently is able to recover pressure more

efficiently than fluid farther from the wall, as is confirmed in Figure 3.18 which shows a later flow separation and a shorter recirculation near the end wall. There are two main causes for this behaviour. The slowdown imposed by the wall to the fluid as it approaches the cylinder is not very strong, but it is sufficient to reduce locally the *Re* and this leads to a smaller recirculation length very much as the effect of *Re* on L_v depicted in Figure 3.8. Additionally, there is a secondary flow in the spanwise direction that appears within the separated flow helping the fluid in the region of minimum L_v to better sustain the local adverse pressure gradient. Note that this fluid came from the upstream region along the end-wall as depicted in Figure 3.19. This fluid, which had been pushed toward the cylinder edges upstream of the obstacle, flows now towards the centre on the downstream side of the cylinder.

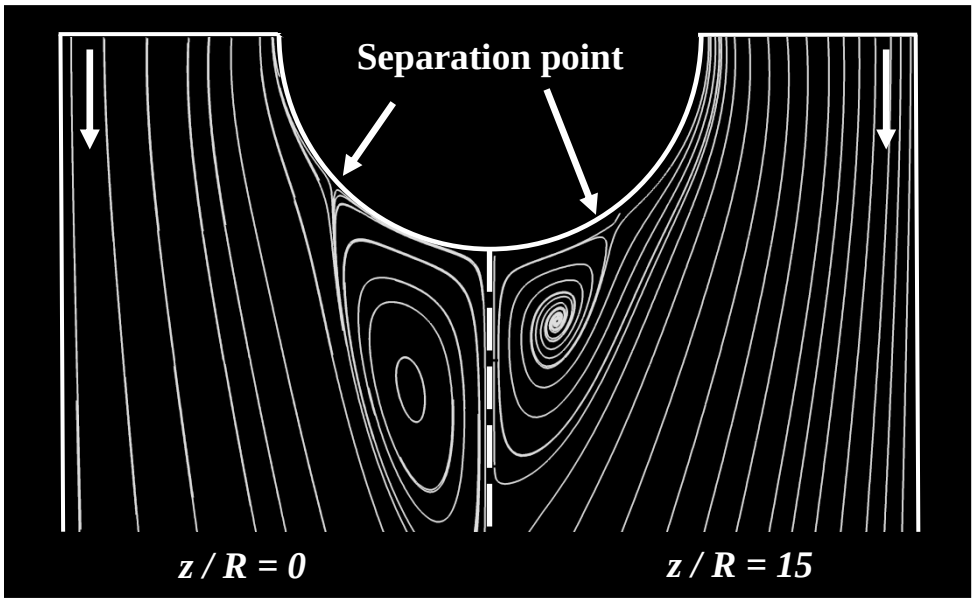

Figure 3.18. Numerical predictions for *AR* = 16 and *Re* = 20 to illustrate the location of the separation point for *z/R* = 0 and *z/R* = 15 (projected streamlines).

The better pressure recovery in the region of minimum L_v leads to a higher pressure there than further away from the wall, where pressure recovery is poorer. Additionally a spanwise pressure gradient is seen to exist behind the cylinder, which is consistent with the spiralling secondary flow inside the open separated flow region from the end walls to the symmetry plane, a mechanism enhanced by flow inertia and illustrated in Figure 3.19. This secondary flow takes fluid out of the minimum L_v near end wall region and into the symmetry plane region, while simultaneously fluid must enter the separated flow region at the near wall region. These near end wall features are also confirmed in the spiralling stream traces on the right-half of Figure 3.18. In contrast, upstream of the cylinder a spanwise pressure variation

is also seen to exist (cf. Figure 3.20) but now with lower pressures near the end wall and higher pressure in the centre, which is consistent with the slight deviation of the upstream streamlines from the centre toward the end-wall observed in Figure 3.19 that seems to constitute the feeding mechanism of the secondary flow. At large *Re* these inertial boundary layer mechanisms far outweigh the acceleration mechanism described earlier and the velocity peaks acquire their special sharp forms. Reducing aspect ratio brings into action the discussed smoothing effect of the shear stress τ_{xz}.

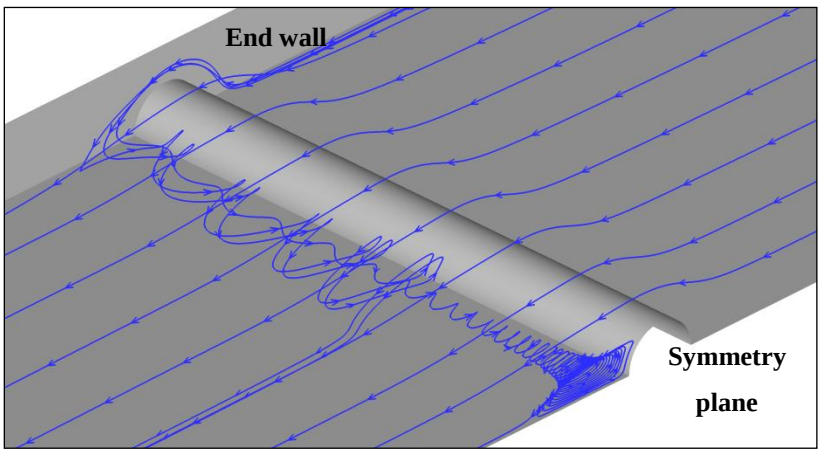

Figure 3.19. Illustration of some particle pathlines predicted numerically near the cylinder for *AR* = 16 and *Re* = 39.2.

A final observation is needed in regard to the increase in L_v at the end wall itself. The boundary layer arguments invoked above for the near wall region, that a low velocity fluid is able to negotiate better the cylinder and recover pressure more efficiently are only valid if the region is not being constantly drained of momentum by viscous forces as happens at the end wall. At this location flow energy is being drained by viscosity simultaneously at the cylinder wall and at the end-wall hindering the capability of the fluid to negotiate the cylinder in spite of the lower local Reynolds number, so the outcome is an early flow separation and a sharp increase in L_v.

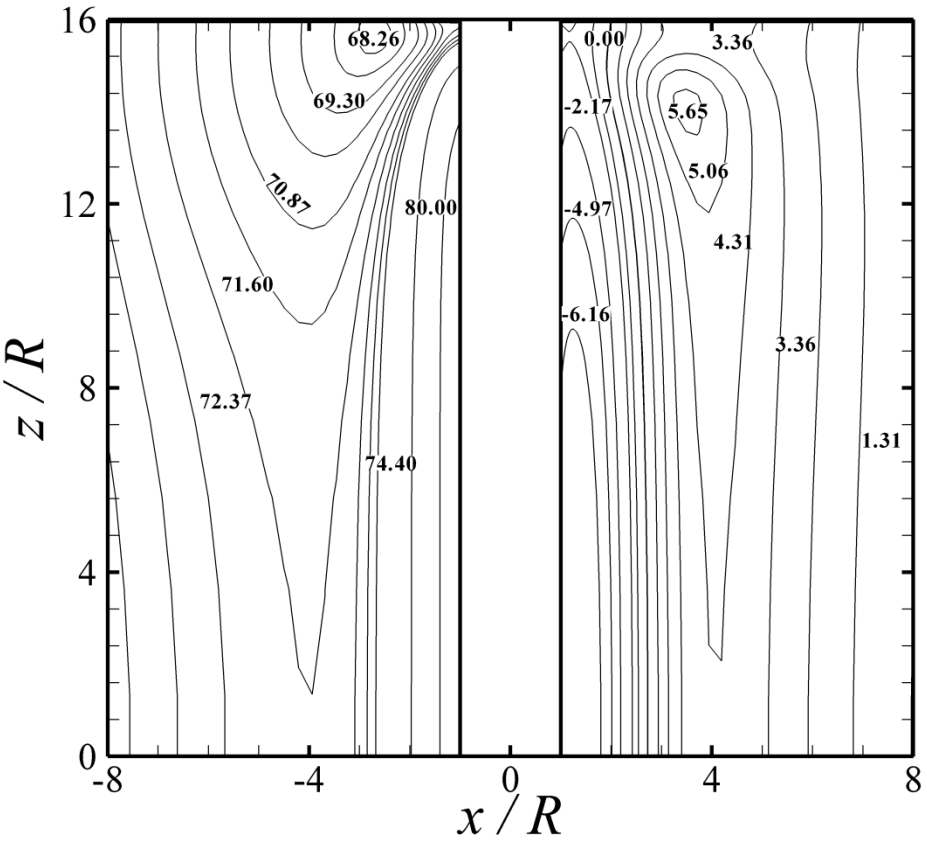

Figure 3.20. Contours of normalized pressure, $(p - p_{ref}) / (\eta U/R)$, predicted numerically at centreplane $y/R = 0$ for $AR = 16$ and $Re = 20$.

3.6. Conclusions

An experimental and numerical investigation was carried out on the laminar steady flow around a confined cylinder placed in a rectangular duct with a 50% blockage ratio duct to assess the effects of the channel aspect ratio. The aspect ratio of the duct varied between $AR = 0.5$ and $AR = 32$ (in the experiments $AR = 2$, 8 and 16 were considered) and the Reynolds number varied between creeping flow conditions ($Re \rightarrow 0$) up to the onset of time-dependent flow. The experiments relied on flow visualizations, using streak photography, and detailed velocity measurements by PIV, both taken in various planes around the cylinder.

The numerical calculations were carried out with a finite volume numerical method and the predictions compare very well with the experimental results. The good agreement between numerical and experimental results indicated that a more detailed study could be carried out numerically to explore flow conditions not studied experimentally and to help to interpret the results. Both the experimental and numerical results always showed symmetry with respect to planes $y/R = 0$ and $z/R = 0$ under the steady flow conditions investigated.

For all values of *AR*, the upstream influence of the cylinder occurs up to $x/R \approx -4$. Downstream of the cylinder the velocity fields have an inverse shape to the corresponding profiles of recirculation length, i.e., where there is a local minimum in recirculation length (near the end walls), we find a local velocity maximum and vice versa. The results showed that the recirculation length increases with *Re* regardless of the *AR*, and also varies along the neutral *z*-direction. A maximum recirculation length is observed at the end walls and for high *AR* a local minimum recirculation length is found near these end walls at about one cylinder radius distance, i.e., at $z/R \approx (AR - 1)$. This local minimum in L_v coincides with the location of a maximum value of streamwise velocity. The fluid in this region is able to sustain better the adverse streamwise pressure gradient than on the centreplane, as shown by a later separation angle and consequently it is able to recover more pressure as it flows around the cylinder. At large values of *AR* the separated flow region is open, i.e., there is also a spiralling spanwise secondary flow inside the separated flow region, from the end wall towards the symmetry plane.

At very low *Re* there is no longer flow separation and the maximum velocity peaks are all due to the excessive braking role of the end wall, which forces a local fluid acceleration for mass conservation which the very small diffusive spanwise-streamwise momentum flux (τ_{xz}) is unable to smooth out. These peaks disappear when the aspect ratio is reduced (for $AR < 6$) and by implication the τ_{xz} stress increases strongly. Then, the influence of the end walls becomes as important as that of the side walls, and as the flow tends to that of a Hele-Shaw apparatus ($AR \rightarrow 0$) the velocity variations become parabolic and the end walls dominate the flow. However, inertia counteracts the role of this diffusive momentum flux even at small values of *AR* so much that at $AR = 2$ and $Re = 38$ there are still velocity peaks. This emphasizes the importance of inertial effects in this flow.

References

Adrian, R.J., 2005. Twenty years of particle image velocimetry. Exp Fluids 39, 159-169.

Alves, M.A., Oliveira, P.J., Pinho, F.T., 2003. A convergent and universally bounded interpolation scheme for the treatment of advection. Int J Numer Meth Fl 41, 47-75.

Brown, R.A., McKinley, G.H., 1994. Report on the VIIIth Int Workshop on numerical - methods in viscoelastic flows. J Non-Newton Fluid Mech 52, 407-413.

Cantwell, B., Coles, D., 1983. An Experimental-Study of Entrainment and Transport in the Turbulent near Wake of a Circular-Cylinder. J Fluid Mech 136, 321-374.

Chakraborty, J., Verma, N., Chhabra, R.P., 2004. Wall effects in flow past a circular cylinder in a plane channel: a numerical study. Chem Eng Process 43, 1529-1537.

Coelho, P.M., Pinho, F.T., 2003. Vortex shedding in cylinder flow of shear-thinning fluids I. Identification and demarcation of flow regimes. J Non-Newton Fluid 110, 143-176.

Dealy, J., Plazek, D., 2009. Time-temperature superposition. Rheology Bulletin 18, 16-31.

Escudier, M.P., Gouldson, I.W., Oliveira, P.J., Pinho, F.T., 2000. Effects of inner cylinder rotation on laminar flow of a Newtonian fluid through an eccentric annulus. Int J Heat Fluid Fl 21, 92-103.

Ferreira, H.H., 2006. Escoamento de fluidos newtonianos e viscoelásticos em torno de um cilindro: estudo numérico de efeitos tridimensionais. MSc thesis. MSc on Fundamentals and Applications of Fluid Mechanics. Faculdade de Engenharia da Universidade do Porto.

Gerich, D., Eckelmann, H., 1982. Influence of End Plates and Free Ends on the Shedding Frequency of Circular-Cylinders. J Fluid Mech 122, 109-121.

Gerrard, J.H., 1966. Mechanics O Formation Region of Vortices Behind Bluff Bodies. J Fluid Mech 25, 401-413.

Hiemenz, K., 1911. Die Grenzschicht an einem in dem gleichförmigen Flüssigkeitsstrom eingetauchten geraden Kreiszylinder. University of Göttingen, Germany.

Kawaguti, M., 1953. Numerical Solution of the Navier-Stokes Equations for the Flow around a Circular Cylinder at Reynolds Number-40. Journal of the Physical Society of Japan 8, 747-757.

Lee, T., Budwig, R., 1991. A study of the effect of aspect ratio on vortex shedding behind circular cylinders. Physics Fluids 3.

Leweke, T., Williamson, C.H.K., 1998. Three-dimensional instabilities in wake transition. European Journal of Mechanics B-Fluids 17, 571-586.

Nieuwstadt, F., Keller, H.B., 1973. Viscous flow past circular cylinders. Computers and Fluids 1, 59-71.

Nishimura, T., 1986. Flow across tube banks. In: Cheremisinoff, P. (Ed.), Encyclopedia of Fluid Mechanics. Gulf Publishing Company, pp. 763-785.

Nishioka, M., Sato, H., 1974. Measurements of Velocity Distributions in Wake of a Circular-Cylinder at Low Reynolds-Numbers. J Fluid Mech 65, 97-112.

Norberg, C., 1994. An Experimental Investigation of the Flow around a Circular-Cylinder - Influence of Aspect Ratio. J Fluid Mech 258, 287-316.

Oliveira, M.S.N., Alves, M.A., Pinho, F.T., McKinley, G.H., 2007. Viscous flow through microfabricated hyperbolic contractions. Exp Fluids 43, 437-451.

Oliveira, M.S.N., Alves, M.A., Pinho, F.T., McKinley, G.H., 2008a. Newtonian fluid flow through microfabricated hyperbolic contractions. Exp Fluids 3, 437-457.

Oliveira, M.S.N., Rodd, L.E., McKinley, G.H., Alves, M.A., 2008b. Simulations of extensional flow in microrheometric devices. Microfluid Nanofluid 5, 809-826.

Oliveira, P.J., Pinho, F.T., Pinto, G.A., 1998. Numerical simulation of non-linear elastic flows with a general collocated finite-volume method. J Non-Newton Fluid 79, 1-43.

Payne, R.B., 1958. Calculations of Unsteady Viscous Flow Past a Circular Cylinder. J Fluid Mech 4, 81-86.

Rao, M.K., Sahu, A.K., Chhabra, R.P., 2011. Effect of Confinement on Power-Law Fluid Flow Past a Circular Cylinder. Polym Eng Sci 51, 2044-2065.

Sahin, M., Owens, R.G., 2004. A numerical investigation of wall effects up to high blockage ratios on two-dimensional flow past a confined circular cylinder. Phys Fluids 16, 1305-1320.

Sen, S., Mittal, S., Biswas, G., 2009. Steady separated flow past a circular cylinder at low Reynolds numbers. J Fluid Mech 620, 89-119.

Sheely, M.L., 1932. Glycerol viscosity tables. Ind Eng Chem 24, 1060-1064.

Strouhal, V., 1878. Ueber eine besondere Art der Tonerregung. Annalen der Physik 241, 216-251.

Sumer, B.M., Fredsoe, J., 1997. Hydrodynamics around cylindrical structures. World Scientific, London.

Telionis, D.P., Gundappa, M., Diller, T.E., 1992. On the Organization of Flow and Heat-Transfer in the near Wake of a Circular-Cylinder in Steady and Pulsed Flow. J Fluid Eng-T Asme 114, 348-355.

Thom, A., 1933. The flow past circular cylinders at low speeds. Proceedings of the Royal Society of London Series a-Containing Papers of a Mathematical and Physical Character 141, 651-669.

Thompson, M., Hourigan, K., Sheridan, J., 1996. Three-dimensional instabilities in the wake of a circular cylinder. Experimental Thermal and Fluid Science 122, 190-196.

Verhelst, J.M., Nieuwstadt, E.M., 2004. Visco-elastic flow past circular cylinders mounted in a channel: experimental measurements of velocity and drag. J Non-Newton Fluid Mech 116, 301-328.

von Kármán, T., 1911. Über den Mechanismus des Widerstandes, den ein bewegter Körper in einer Flüssigkeit erfärt. Göttinger Nachrichten mathematisch-physikalische Klasse 509.

White, F.M., 1991. Viscous Fluid Flow. McGraw-Hll.

Williamson, C.H.K., 1996a. Three-dimensional wake transition. J Fluid Mech 328, 345-407.

Williamson, C.H.K., 1996b. Vortex dynamics in the cylinder wake. Annu Rev Fluid Mech 28, 477-539.

Zdravkovich, M.M., 1997. Flow around circular cylinders. Vol 1: Fundamentals. Oxford University Press New York.

Zdravkovich, M.M., 2003. Flow around circular cylinders. Vol 2: Applications. Oxford Universtiy Press, New York.

Chapter 4

Viscoelastic fluid flow past a confined cylinder: three dimensional effects and stability

Abstract

The flow of viscoelastic fluids past a confined cylinder in a rectangular duct was investigated experimentally and numerically in order to assess the three-dimensional effects associated with the fluid rheology and cylinder aspect ratio (AR). The blockage ratio (BR) was 50%, the cylinder aspect ratios were AR = 16, 8 and 2, and the flow conditions tested varied from creeping flow conditions up to the onset of time-dependent flow. Three viscoelastic fluids were tested, namely a shear-thinning and two Boger fluids, and the results were compared against the numerical and experimental data for Newtonian fluids.

For the shear-thinning fluid, and in the range of Deborah numbers (De) studied ($0.025 < De < 0.99$), elastic instabilities appear upstream of the cylinder at a critical Deborah number (De_c), that depends on the aspect ratio. In contrast, for the Boger fluids the flow remained symmetric both upstream and downstream of the cylinder in the range of Deborah numbers studied ($De < 1.3$). For all non-Newtonian fluids studied, the streamwise velocity profiles show that the length required to achieve the fully-developed velocity downstream of the cylinder increases with De and with AR.

4.1. Introduction

The flow past circular cylinders is of relevance for industrial flows and can be found in structural design and in the process industry. It is in the latter that typical applications involve fluids with non-Newtonian characteristics, as in heat exchangers, textile coating processes or in waste water treatment, among others (Nishimura, 1986). In addition, the two-dimensional (2D) flow around a confined cylinder with 50% blockage ratio is a classical benchmark problem in computational rheology (Brown and McKinley, 1994).

There is a wealth of investigations on Newtonian fluid flow past an unconfined cylinder, which are summarized in the reviews of Telionis *et al*. (1992), Williamson (1996) and in the books of Zdravkovich (Zdravkovich, 1997, 2003). The interplay between the far flow field and the cylinder allows the study of the vortex shedding phenomenon, and the effects upon the flow around the cylinder of the aspect ratio (*AR*, defined as the ratio between the cylinder length and diameter), of the blockage ratio (*BR*, defined as the ratio between the cylinder diameter and the width of the channel) and also of the rheology of the working fluid.

The flow of Newtonian fluids past a cylinder in a rectangular channel is characterized by two geometrical ratios (eg. *AR* and *BR*) and by the Reynolds number, which represents the relative importance of inertial relative to viscous forces. Sen *et al*. (2009) indicate the range $3.2 < Re < 7$ for the onset of downstream flow separation. The critical Reynolds number for the onset of laminar vortex shedding is found to be $Re \approx 47$ for high aspect ratios and increases when the aspect ratio decreases (Williamson, 1996; Sahin and Owens, 2004; Kumar and Mittal, 2006; Ribeiro *et al.*, 2012). Ribeiro *et al.* (2012) investigated the 3D effects on the laminar flow of a Newtonian fluid past a confined circular cylinder with *BR* = 50% and showed good agreement between experimental results and numerical predictions. An unusual phenomenon was observed experimentally and confirmed numerically, consisting of intense velocity peaks downstream of the cylinder in the vicinity of the cylinder end walls, which are not reduced even when the aspect ratio of the cylinder increases. For the largest aspect ratios investigated (*AR* = 16 and 8) the influence of the end walls on the local velocity peaks was predominant while for $AR < 6$ the flow was found to be also influenced by the side walls, due to geometric confinement.

For viscoelastic fluids, the flow past a confined cylinder has also been thoroughly studied experimentally and numerically. Some of the experimental studies of non-Newtonian fluids

around a confined cylinder refer only to steady creeping flow conditions (Manero and Mena, 1981; Shiang *et al.*, 1997). Nevertheless, at higher flow rates (or Deborah numbers) when elastic instabilities occur, the flow becomes highly three-dimensional, with steady complex structures developing upstream and downstream of the cylinder. At further higher flow rates, a second elastic instability develops and the flow becomes time-dependent (McKinley *et al.*, 1993). McKinley (1991) investigated purely elastic instabilities in viscoelastic flow past a circular cylinder using a Boger fluid. The cylinder used in the experiments had a high aspect ratio (AR = 24), thus the flow in the middle plane could be assumed as quasi-2D at low Deborah numbers. Above De = 1.30 a cellular structure was observed in the spanwise direction, thus significant 3D effects were found for such high AR geometry. More recently, the experiments of Verhelst and Nieuwstadt (2004) showed the appearance of three-dimensional (3D) effects near the walls in the flow past a confined cylinder in a rectangular duct with 50% blockage ratio and an aspect ratio AR = 16.

Numerical investigations of non-Newtonian fluid flow past a cylinder are usually based on two-dimensional calculations, due to the expensive computational resources required for 3D simulations. For some viscoelastic fluids, such simulations showed the steady flow behind the cylinder to be characterized by the appearance of velocity overshoots, which depend significantly on the rheology of the fluid (Phan-Thien and Dou, 1999). The studies of the viscoelastic flow past a gradual contraction, which can be qualitatively compared with the upstream flow around a cylinder, also show the appearance of velocity overshoots, along the centreline and near the end walls upstream the contraction for 3D geometries (Poole *et al.*, 2007b; Poole and Alves, 2009). These velocity overshoots near the walls, which were called "cat's ears" phenomenon (Poole *et al.*, 2007a), are a manifestation of fluid elasticity and were qualitatively captured in the 3D numerical simulations of Poole and Alves (2009).

Despite the smaller number of works reporting 3D simulations, some studies regarding the viscoelastic flow around a 3D cylinder have also been reported in the literature. Sahin and Wilson (2007) performed 2D and 3D viscoelastic fluid flow simulations around a confined circular cylinder in a channel with 50% blockage ratio, and analysed the flow patterns up to a Weissenberg number (Wi) of 1.2. The converged 2D numerical results beyond Wi = 0.7 indicate that the solutions are mesh dependent, at least in a small region in the near wake of the cylinder, whereas for the 3D calculations the results at high Weissenberg numbers did not converge, due to the classical high Weissenberg number problem (HWNP) (Fattal and Kupferman, 2004). More recently, Sahin (2011) simulated numerically the 2D and 3D flow

of an Oldrody-B fluid past a confined cylinder and concluded that at Wi = 0.7 mesh convergence is still achieved in his calculations, even in the wake of the cylinder. However, no steady-state solution was possible for an Oldroyd-B fluid beyond Wi = 0.8. Richter *et al*. (2010) studied numerically the 3D viscoelastic flow past a circular cylinder at moderate Reynolds numbers to assess the influence of viscoelasticity on the flow. More recently, Tenchev *et al.* (2011) compared 2D and 3D flow simulations of an Oldroyd-B fluid around a confined cylinder and of a Rolie-Poly fluid flowing through a sudden contraction. In both cases, the results for 2D and 3D flows show significant differences, thus emphasizing the need for 3D computations for reliable simulations.

The practical implementation of the flow of viscoelastic fluids past a confined cylinder is necessarily three-dimensional and it is clear from the previous works that their characteristics can be significantly different from those observed in a simplified two-dimensional geometry. Therefore, the goal of this work is the characterization of three-dimensional effects of the flow of viscoelastic fluids past a confined cylinder centred in a rectangular channel with 50% blockage ratio. This is achieved by considering the flows of a viscoelastic fluid with shear-thinning behaviour and of two Boger fluids in three different geometries having aspect ratios of AR = 16, 8 and 2. The flows analysed varied from creeping flow conditions (very low Reynolds number) up to the onset of time-dependent flow, i.e., which corresponds to the range of the Reynolds numbers between $0.008 < Re < 3.25$ and Deborah numbers between $0.025 < De < 0.99$. This work was preceded by a similar investigation involving the laminar flow of Newtonian fluids at low Reynolds numbers (Ribeiro *et al.*, 2012) – Chapter 3. Numerical predictions were also carried out in order to predict the Newtonian and non-Newtonian fluid flow. These numerical predictions, together with the results of Chapter 3 will be used here to assess and separate the effects of elasticity from those of shear-thinning viscosity.

The remainder of this chapter is organized as follows: the experimental set-up and techniques are described in section 4.2, while section 4.3 presents the rheological characterization of the fluids used. The governing equations and a brief outline of the numerical method are described in section 4.4. Section 4.5 presents and discusses the experimental results and compares them with the corresponding Newtonian fluid flow. In section 4.6 the main conclusions are summarized.

4.2. Experiments

4.2.1. Experimental set-up

The measurements were carried out in the test section schematically represented in Figure 4.1, which is made of transparent perspex. The whole closed loop rig, described in detail in Chapter 3 (Ribeiro *et al.*, 2012) (cf. Figure 3.1), is here only briefly described. The 1700 mm long test section has a rectangular cross section with a width (H) of 20.0 mm and a variable depth (h) in order to assess the effect of the aspect ratio ($AR = h/D$) of the geometry. This is achieved by moving one of the end walls (parallel to the xy plane), allowing the depth (h) of the cross section to be 160.0 mm, 80.0 mm or 20.0 mm, resulting in AR = 16, 8 or 2, respectively. The 10.0 mm diameter cylinder is located 630 mm downstream of the duct inlet and is positioned at the mid plane to define a symmetric geometry with a 50% blockage ratio ($BR = D/H$). The origin of the coordinate system represented in Figure 4.1 is located at the centre of the cylinder, with the x-axis pointing in the streamwise direction, the y-axis in the cross-stream direction (normal to the main rectangular duct walls, i.e., the side walls) and z-axis in the spanwise direction (along the cylinder axis).

The duct inlet has a distributor with six injectors (20 mm internal diameter) to obtain a nearly uniform velocity profile at the inlet of the rectangular duct. The distance between the distributor and the cylinder allows a fully-developed velocity profile to be achieved well upstream of the cylinder, and the exit is sufficiently far away to minimize perturbation of the flow dynamics in the vicinity of the cylinder.

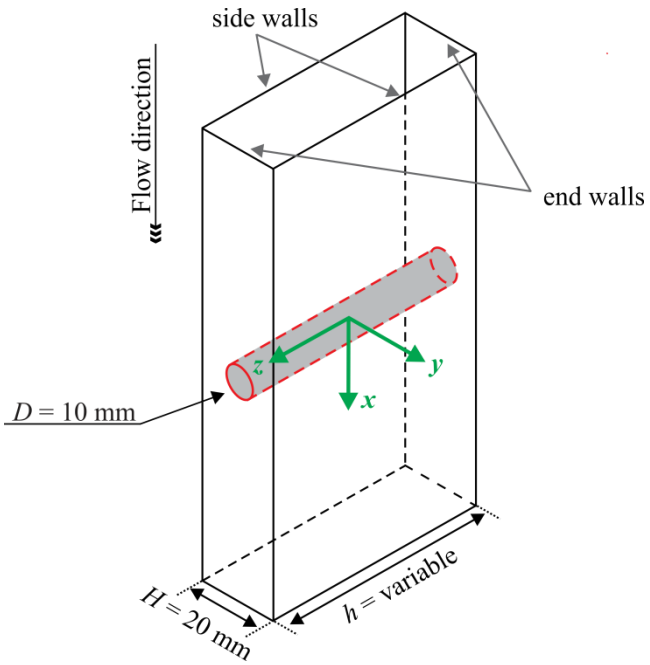

Figure 4.1. Test section and coordinate system.

4.2.2. Experimental techniques

Experiments rely on flow visualization using long time exposure streak photography and detailed velocity measurements using Particle Image Velocimetry (PIV). Both techniques were used at the various *xy* planes marked in Figure 4.2 to assess the spanwise variation of the flow field. The planes under study for each *AR* are at the same absolute distance of the end-wall. However, most experiments focus on the centreplane, $z/R = 0$.

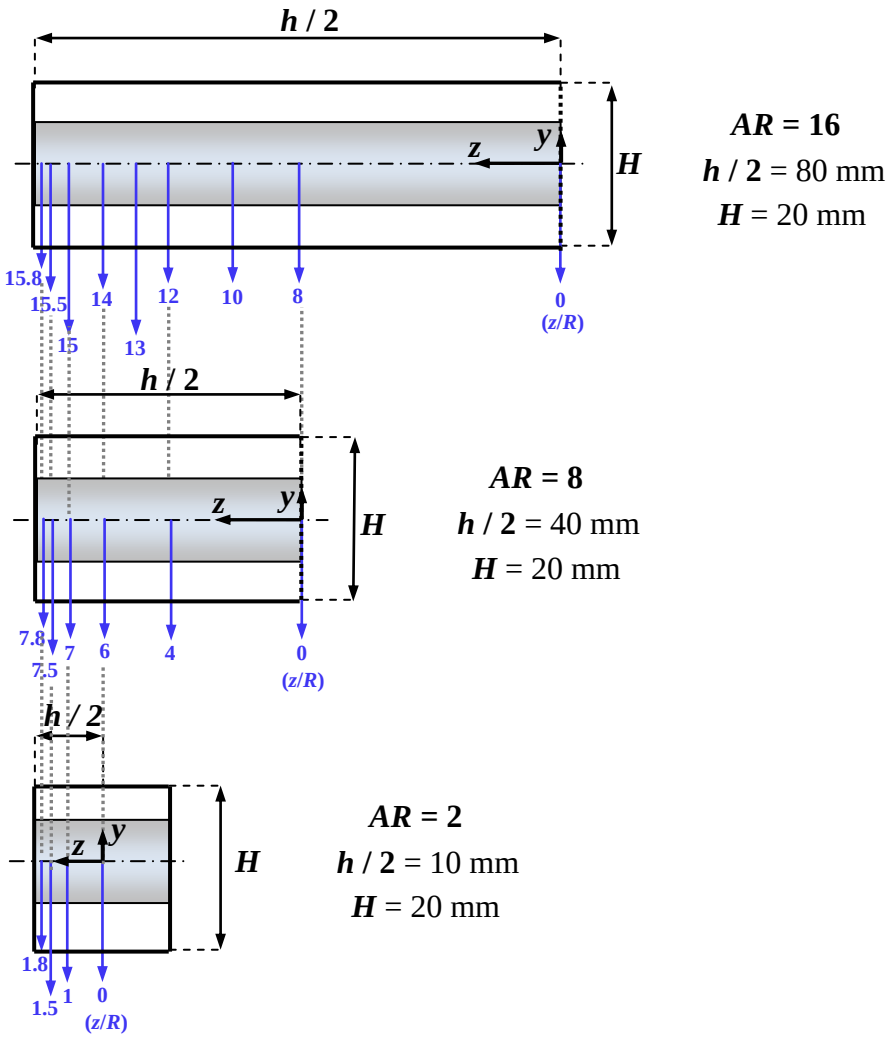

Figure 4.2. Planes under study for *AR* = 16, 8 and 2 along the cylinder axis at different values of |*z*/*R*|. Adapted from Ribeiro *et al*. (2012).

4.2.2.1. *Flow visualization*

In the visualization of flow patterns using long time exposure streak photography, the flow was continuously illuminated with two co-planar 635nm 5mW laser diodes (Vector, model 5200-20), both equipped with a cylindrical lens to create a light sheet that is directed perpendicularly to the cylinder axis. The use of two opposed laser diodes minimizes the shadows around the cylinder. The light reflected from the illuminated suspended tracer particles (30 ppm w/w of hollow glass spheres with 10 μm diameter – HGS-10, Dantec Dynamics) was captured by a digital camera (CANON EOS 30D), equipped with a macro lens (EF100mm, f2.8), which was placed perpendicularly to the laser light sheet. The exposure time was adjusted according to the flow rate and varied between 1 and 30 s. The

laser diodes and digital camera moved together using a *xy* traversing table to simplify the adjustments in each plane under study.

4.2.2.2. *Particle image velocimetry*

The detailed measurements of the velocity fields were carried out using a PIV system supplied from Dantec Dynamics. The flow plane under investigation was illuminated by a double pulsed Nd:YAG laser (Solo PIV III, New Wave Research), which generates consecutive pairs of light sheets with a wavelength of 532 nm and a maximum energy of 50 mJ per pulse. The two consecutive pulses of light illuminated the suspended particles (same as those used for flow visualization), which reflected the light allowing the determination of the corresponding velocities from the displacement of the imaged particles in the time interval between the laser pulses. The particle concentration was chosen in order to follow the recommendations for PIV of having at least 5-10 particles per interrogation area (Adrian, 2005). The time between two consecutive pulses varied between 1.0 ms and 2.0 s, depending on the flow rate, the plane of measurement and the aspect ratio under study. The images were acquired using a double frame digital CCD camera (Flow Sense 2M, Dantec Dynamics) coupled with a Nikon AF Micro lens of 60 mm focal length. For all flow rates, at least 50 pairs of images were acquired and the velocity field was determined by processing the images with FlowManager v4.60 software (Dantec Dynamics), using an adaptive-correlation algorithm, to obtain a two-dimensional velocity vector map for each image pair, on interrogation windows of 32 × 32 pixels, with 50% overlap.

4.3. Fluid characterization

The fluids used were a shear-thinning viscoelastic fluid and two Boger fluids, all prepared with different concentrations of polyacrylamide (PAA). In addition, flow data for a Newtonian fluid (Ribeiro *et al.*, 2012) is also used for comparison purposes. The shear-thinning fluid was an aqueous solution of PAA at a weight concentration of 1000 ppm and the Boger fluids were aqueous solutions of glycerine (85% w/w) with PAA at weight concentrations of 200 ppm and 400 ppm, with 1% NaCl. All fluids were seeded with tracer particles, as described in section 4.2. In order to minimize bacteriological growth in the fluids and minimize their inherent degradation, a biocide was added at a concentration of 25 ppm (kathon LXE, Rohm and Haas). The density (ρ) of the fluids was measured at 293.2 K using a pycnometer. The composition and the density of the fluids are presented in Table 4.1.

Table 4.1. Fluid composition (mass concentration) and density measured at 293.2 K.

Fluid	PAA (ppm)	Glycerine (%)	Water (%)	NaCl (%)	Kathon (ppm)	ρ (kg/m^3)
Newtonian	-	40	60	-	25	1102.0
Shear-thinning - PAA1000	1000	-	99.90	-	25	1001.5
Boger - PAA200	200	85.05	13.91	1.02	25	1225.8
Boger - PAA400	400	85.06	13.89	1.01	25	1226.3

The rheological characterization of the fluids was carried out in shear and extensional flow. The shear measurements were made using two rotational rheometers: Physica MCR 301 with a 75 mm cone-plate system with 1º angle; TA Instruments AR-G2 with a 40 mm cone-plate system with 2º angle (Boger fluids only). The data are represented in Figures as hollow and filled symbols for the Physica MCR 301 and for TA Instruments AR-G2, respectively.

In the steady shear measurements for the viscoelastic shear-thinning fluid (PAA1000), the flow curve was measured at different temperatures (283.5 - 303.2 K). The time-temperature superposition principle was used in order to obtain the master curve at the reference temperature (T_0 = 293.2 K). The corresponding shift factor is defined as (Dealy and Plazek, 2009):

$$a_T = \frac{\eta(T)}{\eta(T_0)} \frac{T_0}{T} \frac{\rho_0}{\rho}, \tag{4.1}$$

where η (T_0) is the shear viscosity at the reference temperature T_0, η (T) is the shear viscosity at a given temperature T, ρ_0 is the density at the reference temperature T_0 and ρ is the density at temperature T. Since the temperature variation for the rheological measurements is small, the fluid density does not change significantly and the shift factor simplifies to (Dealy and Plazek, 2009):

$$a_T = \frac{\eta(T)}{\eta(T_0)}. \tag{4.2}$$

Figure 4.3 shows the steady-state shear viscosity master curve, together with the corresponding fit to a generalized Newtonian fluid (GNF). The Carreau model (Carreau, 1972) was used for the viscosity function, which is defined as:

$$\eta = \eta_s + \frac{\eta_0 - \eta_s}{\left[1 + (\Lambda\dot{\gamma})^2\right]^{(1-n)/2}} \quad . \tag{4.3}$$

The parameters of this fitted model were: η_0 = 2.0 Pa.s; η_s = 0.004 Pa.s, Λ = 28 s, n = 0.38.

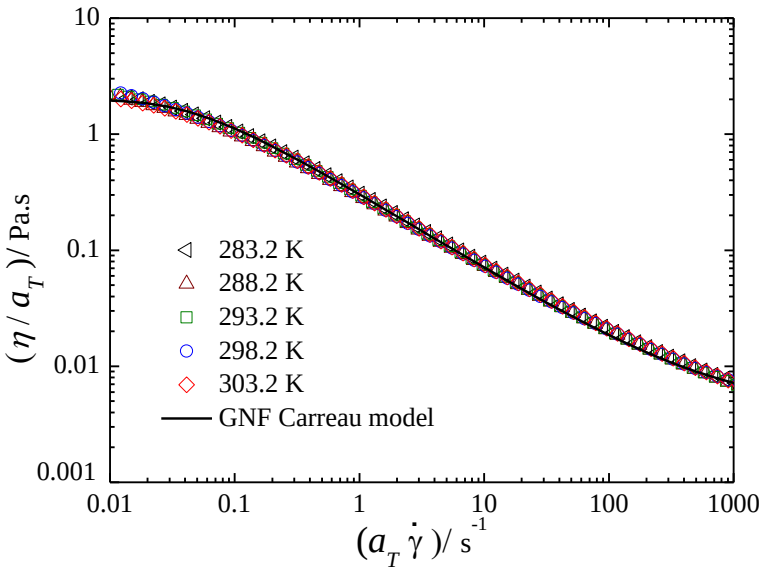

Figure 4.3. Steady shear viscosity of the shear-thinning fluid (PAA1000). The symbols represent the experimental data measured at different temperatures and the solid line the fit by a GNF Carreau model.

In the steady shear measurements for the Boger fluids (PAA200 and PAA400) the flow curve was measured at different temperatures (288.5 – 298.5 K). As for the shear-thinning fluid, the time-temperature superposition principle was used in order to obtain the master curve at the reference temperature (T_0 = 293.2 K). Figure 4.4a shows nearly constant viscosities of 0.152 Pa.s and 0.174 Pa.s for the PAA200 and PAA400, respectively in the shear rate range of 1 < $\dot{\gamma}$ / s^{-1} < 1000. The shear viscosities of these diluted polymer solutions are similar since these are essentially determined by the viscous solvent. Figure 4.4b shows the dynamic shear viscosity (η') and G'/ω^2 vs. ω. A two-mode model was used to fit G' and η' and the details of the linear viscoelastic spectrum determined at T_0 = 293.2 K are shown in Table 4.2. The predictions using the two-mode model (solid lines) are overlapped with the experiments.

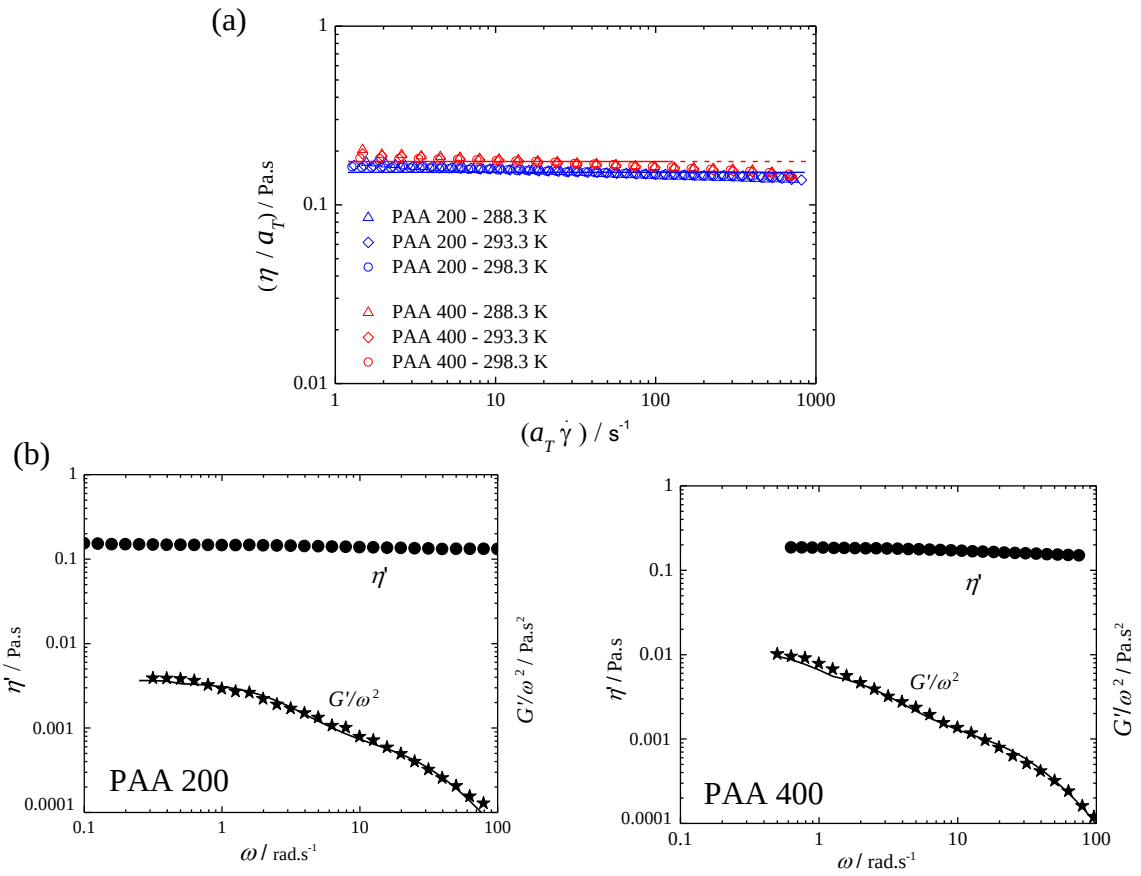

Figure 4.4. Material functions of Boger fluids PAA200 and PAA400 in: a) steady shear flow (the symbols represent the experimental data measured at different temperatures); b) small amplitude oscillatory shear flow. The solid lines represent the fits by the two-mode Oldroyd-B model.

Table 4.2. Linear viscoelastic spectra for the Boger fluids.

Mode k	**PAA 200**		**PAA 400**	
	λ_k (s)	η_k (Pa.s)	λ_k (s)	η_k (Pa.s)
1	0.030	0.020	0.031	0.034
2	0.38	0.0075	0.40	0.014
Solvent	-	0.126	-	0.126

The fitted two-mode model (solid lines) overlaps the rheological measurements shown in Figure 4.4b and it is clear that, within the measured frequency range, a two-mode Oldroyd-B

model is adequate to represent the linear viscoelastic behaviour of the Boger fluids. The solvent viscosity, η_s = 0.126 Pa.s, corresponds to the dynamic viscosity of the Newtonian solvent used in the preparation of the fluids. Using the parameters of the two-mode model presented in Table 4.2, an average relaxation time can be calculated as:

$$\lambda = \frac{1}{\eta_p} \sum_{k=1}^{2} \eta_k \lambda_k , \tag{4.4}$$

where $\eta_p = \sum_{k \neq solvent} \eta_k$, leading to λ = 125 ms for the Boger fluid PAA200 and λ = 139 ms for the Boger fluid PAA400.

The extensional behaviour of the solution was measured at the reference temperature (T_0 = 293.2 K) using a capillary break-up extensional rheometer (Haake CaBER 1, Thermo Scientific). The characteristic relaxation time in extensional flow was determined by fitting the experimental data of log [*D(t)*] *vs* time in the region of elasto-capillary balance which obeys the following equation (Entov and Hinch, 1997):

$$\frac{D}{D_0} = e^{-\frac{t}{3\lambda}}, \tag{4.5}$$

where D_0 is the diameter of the filament at the reference time t = 0 and D is the diameter at the time t. These measurements were performed using two circular plates with a diameter of 6 mm.

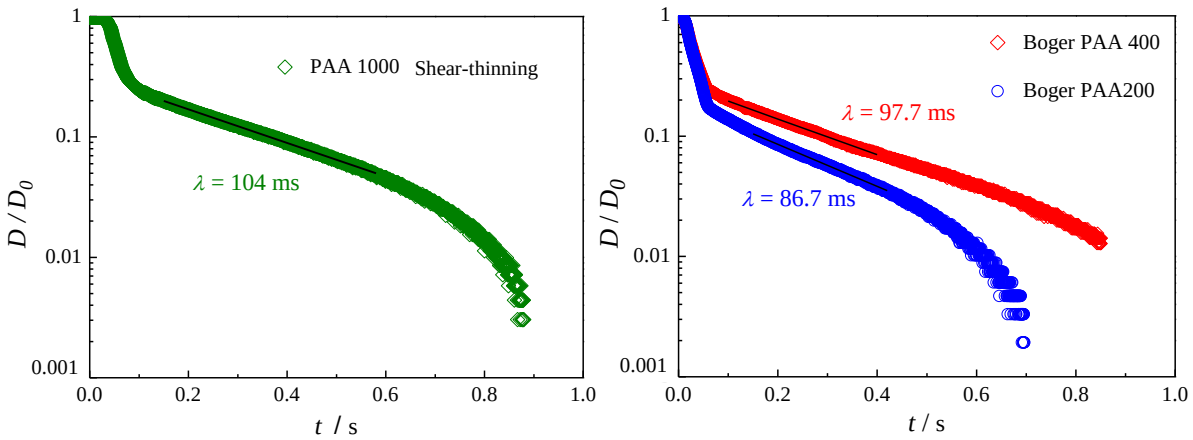

Figure 4.5. Diameter of the filament measured as a function of time using Haake CaBER 1 for: a) shear-thinning fluid PAA1000; b) Boger fluids PAA200 and PAA400.

As shown in Figure 4.5 the experimental data were fitted and the relaxation time was found to be λ = 104 ms for the shear-thinning fluid (PAA1000), λ = 86.7 ms for the PAA200 Boger fluid and λ = 97.7 ms for the PAA400 Boger fluid.

The two methods used to determine λ lead to slightly different values, as expected. However, since the values obtained are of the same order of magnitude, this gives some reliability to the results obtained with the Boger fluids. The relaxation time determined in extensional flow is thought to be the more appropriate for the flow under study, since the flow around the cylinder is strongly dominated by the extensional stresses on the wake of the cylinder. Therefore, in the remaining of this chapter, the relaxation time determined using the CaBER rheometer will be used in the calculations. We note, however, that the relaxation time obtained for the semi-diluted shear-thinning fluid is much smaller that the value that can be estimated from the flow curve (Figure 4.3). The onset of shear-thinning usually occurs at a shear rate which is approximately the inverse of the relaxation time. From Figure 4.3 we would estimate a relaxation time in shear of the order of 20 s, which is more than two orders of magnitude above the relaxation time in extension. Therefore, for the shear-thinning fluid, the relaxation time used in the remaining calculations of this chapter should be viewed as a rough estimated, and the *De* values calculated are, most probably too small.

4.4. Governing equations and numerical method

The experimental results were simulated using an implicit finite-volume method with a time marching pressure-correction algorithm (Oliveira *et al.*, 1998). The governing equations describing the isothermal laminar flow of an incompressible fluid are the mass conservation,

$$\nabla \cdot \mathbf{u} = 0, \tag{4.6}$$

and the momentum equation,

$$\rho\left(\frac{\partial \mathbf{u}}{\partial t} + \nabla \cdot \mathbf{uu}\right) = -\nabla p + \nabla \cdot \boldsymbol{\tau}, \tag{4.7}$$

where $\mathbf{u}$ represents the velocity vector, ρ the fluid density, t the time, p the pressure and $\boldsymbol{\tau}$ the extra-stress tensor, which is given as a sum of a Newtonian solvent and a polymeric

contribution $(\boldsymbol{\tau} = \boldsymbol{\tau}_s + \boldsymbol{\tau}_p)$. For Newtonian fluids, the polymeric contribution is null, $\boldsymbol{\tau}_p = \mathbf{0}$, and the Newtonian solvent component $\boldsymbol{\tau}_s$ is defined as:

$$\boldsymbol{\tau}_s = \eta_s \, (\nabla \mathbf{u} + \nabla \mathbf{u}^T) = 2\eta_s \, \mathbf{D} \, , \tag{4.8}$$

where η_S is the constant solvent viscosity and **D** is the deformation rate tensor.

For the numerical calculations of the shear-thinning viscoelastic fluid, a generalized Newtonian fluid (GNF) was used based on the Carreau model. The numerical calculations with this GNF model do not describe accurately the flow near the cylinder, where the elastic effects are more relevant, but are able to predict with good accuracy the flow far from the cylinder under fully-developed flow conditions, where the shear viscosity is more relevant.

In the numerical predictions using the Carreau model the polymeric contribution to the extra-stress tensor is neglected, $\boldsymbol{\tau}_p = \mathbf{0}$, and the shear-thinning viscosity function is introduced via the $\boldsymbol{\tau}_s$ term:

$$\boldsymbol{\tau}_s = 2\eta(\dot{\gamma})\mathbf{D}, \tag{4.9}$$

with the function $\eta(\dot{\gamma})$ given by the Carreau model.

For the numerical calculations of the Boger fluid flow, the polymeric contribution is included and is described using the Oldroyd-B model, given by:

$$\boldsymbol{\tau}_p + \lambda\left(\frac{\partial \boldsymbol{\tau}_p}{\partial t} + \nabla \cdot \mathbf{u}\boldsymbol{\tau}\right) = \eta_p(\nabla \mathbf{u} + \nabla \mathbf{u}^T) + \lambda(\boldsymbol{\tau}_p \cdot \nabla \mathbf{u} + \nabla \mathbf{u}^T \cdot \boldsymbol{\tau}_p), \tag{4.10}$$

where η_p is the shear viscosity of the polymer.

The fitted parameters of the Carreau and the Oldroyd-B models were described in section 4.3.

The numerical method is based on a time-marching version of the SIMPLEC pressure correction algorithm formulated for collocated variables (Oliveira *et al.*, 1998). The discretization of the governing equations is based on central differences for diffusion terms and is based on the CUBISTA high-resolution scheme (Alves *et al.*, 2003) for the convective

terms both in the momentum and constitutive equations. The computational domain was mapped using non-orthogonal block-structured meshes. Extensive sets of calculations were carried out by Ferreira (2006) to estimate the numerical uncertainty and select an adequate mesh to provide mesh independent results. To generate the mesh the flow domain was divided into 24 blocks and within each block the cells were concentrated near the cylinder region and channel walls, as illustrated in Figure 4.6 for AR = 8.

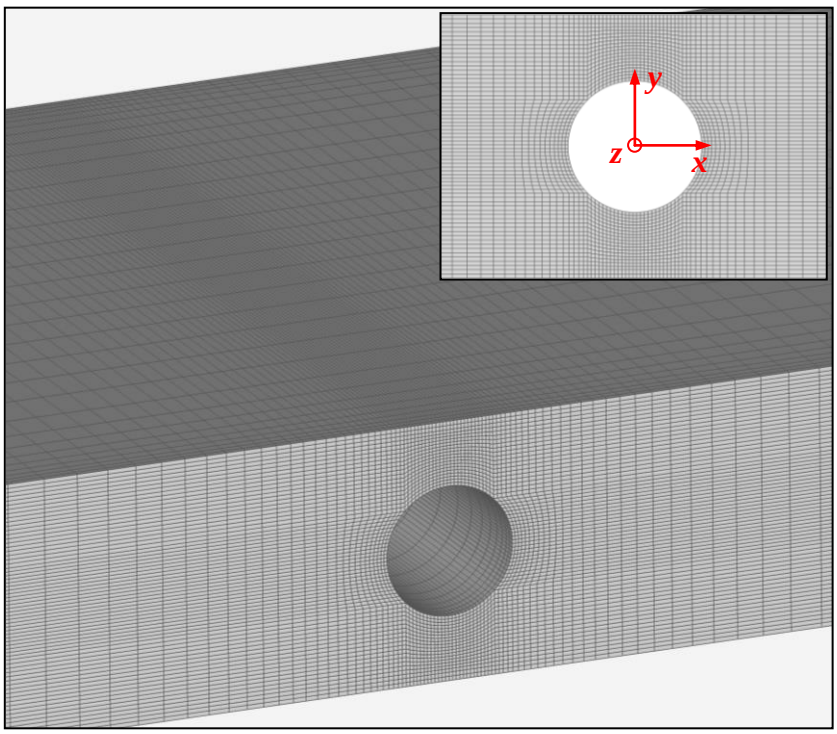

Figure 4.6. Zoomed view of the mesh used in the numerical simulations for AR = 8.

4.5. Results and discussion

The viscoelastic fluid flow around a confined cylinder was characterized using flow visualizations and detailed velocity field measurements using PIV. The experiments were carried out at an average temperature of 293 K, and ranged between 291.7 K and 294.7 K. The experimental work was conducted with the three viscoelastic fluids previously described: shear-thinning PAA1000, Boger PAA200 and Boger PAA400. The experiments were carried out for AR = 16, 8 and 2 using the shear-thinning fluid, whereas for the Boger fluids the experiments were restricted to the AR = 16 case. The selection of the Boger fluids, i.e., constant viscosity elastic fluids, allows the isolation of viscoelastic effects, without the added complexity of shear-thinning effects.

A thorough experimental and numerical investigation of Newtonian fluid flow around a confined cylinder for *AR* = 16, 8 and 2 was presented in Chapter 3 (Ribeiro *et al.*, 2012). In the present chapter, some of the previous results are used to provide a reference scenario to compare with the viscoelastic fluid flow.

The flow characteristics of Newtonian fluids depend on two geometrical ratios (*AR* and *BR*) and on the Reynolds number (*Re*), here defined as:

$$Re = \frac{\rho U R}{\eta}, \tag{4.11}$$

where U is the bulk upstream velocity, R is the radius of the cylinder and η is the shear viscosity of the fluid. For the shear-thinning fluid the viscosity in Eq. (4.11) is evaluated at the characteristic shear rate $\dot{\gamma} = U/R$.

The flow of viscoelastic fluids is also characterized using the Deborah number, which represents the ratio of a characteristic time of the fluid (λ) and a characteristic flow time scale (R/U):

$$De = \frac{\lambda U}{R}. \tag{4.12}$$

The Deborah numbers calculated were based on the relaxation time of the fluid measured in the CaBER, since the flow around the cylinder has a strong extensional component.

4.5.1. Shear-thinning fluid – PAA1000

4.5.1.1. *Flow Patterns*

The effect of *De* on the flow patterns at the symmetry plane ($z/R = 0$) is illustrated in some representative photographs shown in Figures 4.7, 4.8 and 4.9 for *AR* = 16, 8 and 2, respectively, obtained using long time exposure streak photography. The vertical and horizontal lines inside the cylinder are a guide to the eye to highlight possible flow asymmetry. For all *AR* at low *De*, symmetric flow patterns are observed upstream and downstream of the cylinder (cf. Figures 4.7a, 4.8a and 4.9a). Beyond a critical Deborah number, De_c, which depends on *AR*, an elastic instability occurs upstream of the cylinder, near the forward stagnation point, as seen in Figures 4.7b-d, 4.8b-d and 4.9b. At these critical

flow conditions, we observe the onset of steady upstream asymmetric flow instability, which is particularly noticeable on the right side of the figures. For AR = 16 and 8, the instability appears at $De_c \approx 0.04$, whereas $De_c \approx 0.4$ for AR = 2, suggesting that the end walls have a stabilizing effect. Note that the inherent uncertainties of the experimental technique based on the visual inspection of the flow pathlines only provide an estimate value of De_c. In all cases the flow asymmetry magnitude increases with De. Far upstream of the cylinder, the flow is symmetric, which highlights the influence of the cylinder on the onset of the elastic instability. Then, as De is increased further, the steady asymmetry intensifies and the flow eventually becomes time-dependent. Again, we remark that the relaxation time used in the calculation of De for the shear-thinning fluid is probably too much small, therefore it comes as no surprise that the values of De_c for the shear-thinning fluid are so small.

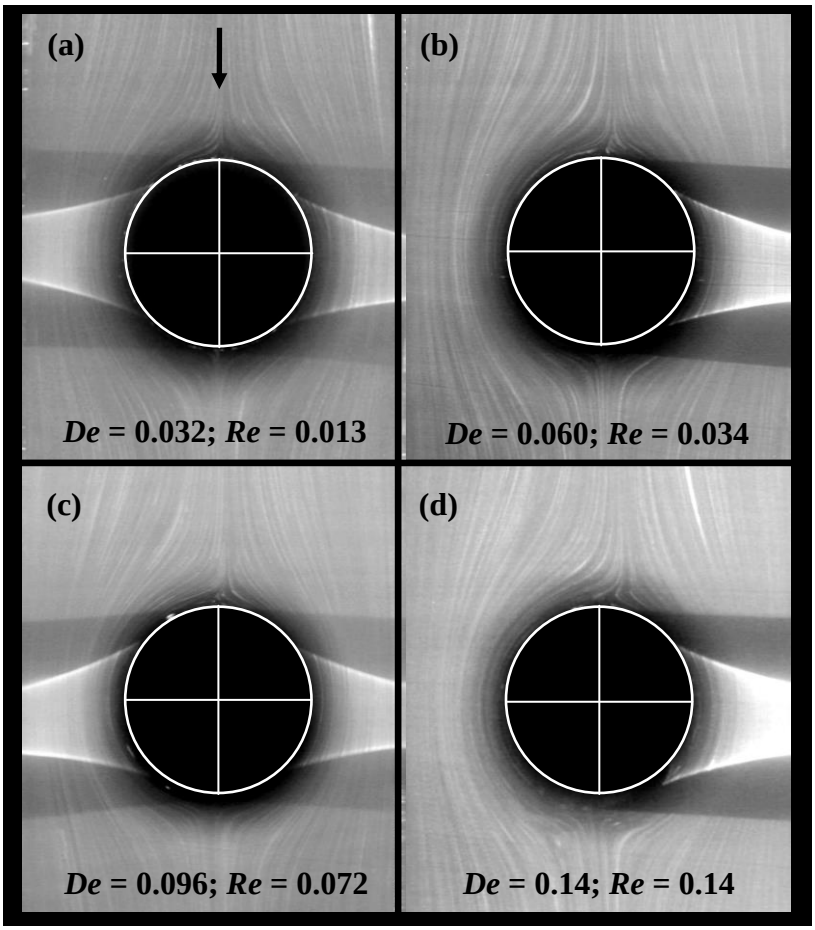

Figure 4.7. Long-time exposure streak photography: effect of elasticity on the flow patterns at the symmetry plane (z/R = 0) for AR = 16, using the PAA1000 shear-thinning fluid.

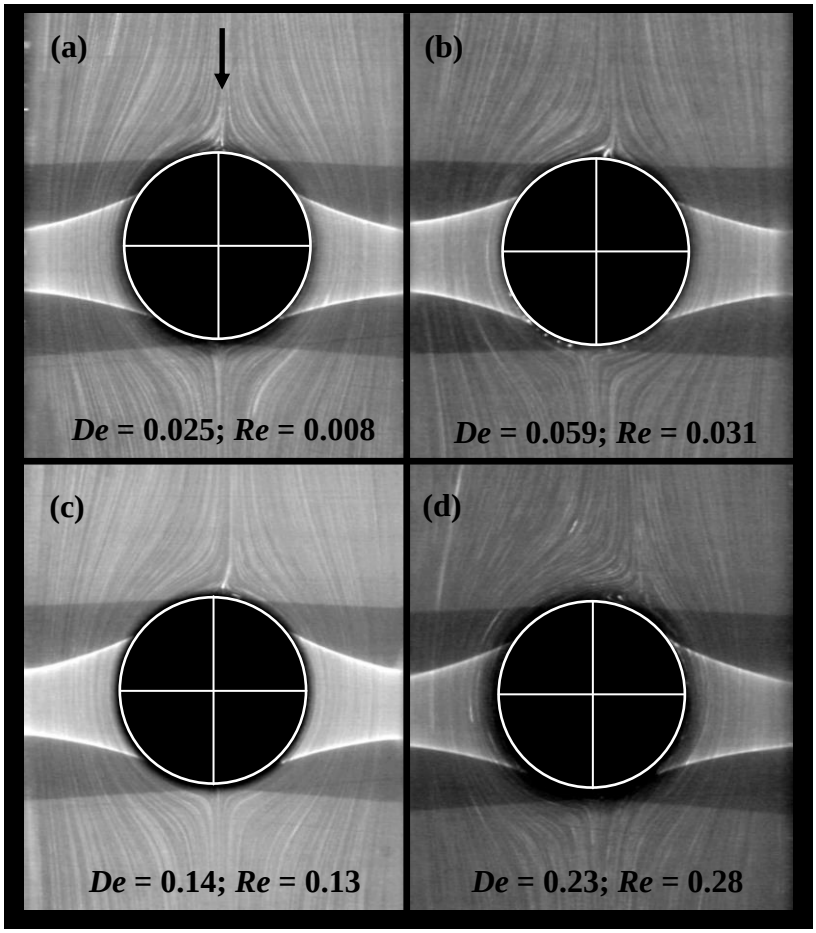

Figure 4.8. Long-time exposure streak photography: effect of elasticity on the flow patterns at the symmetry plane ($z/R = 0$) for $AR = 8$, using the PAA1000 shear-thinning fluid.

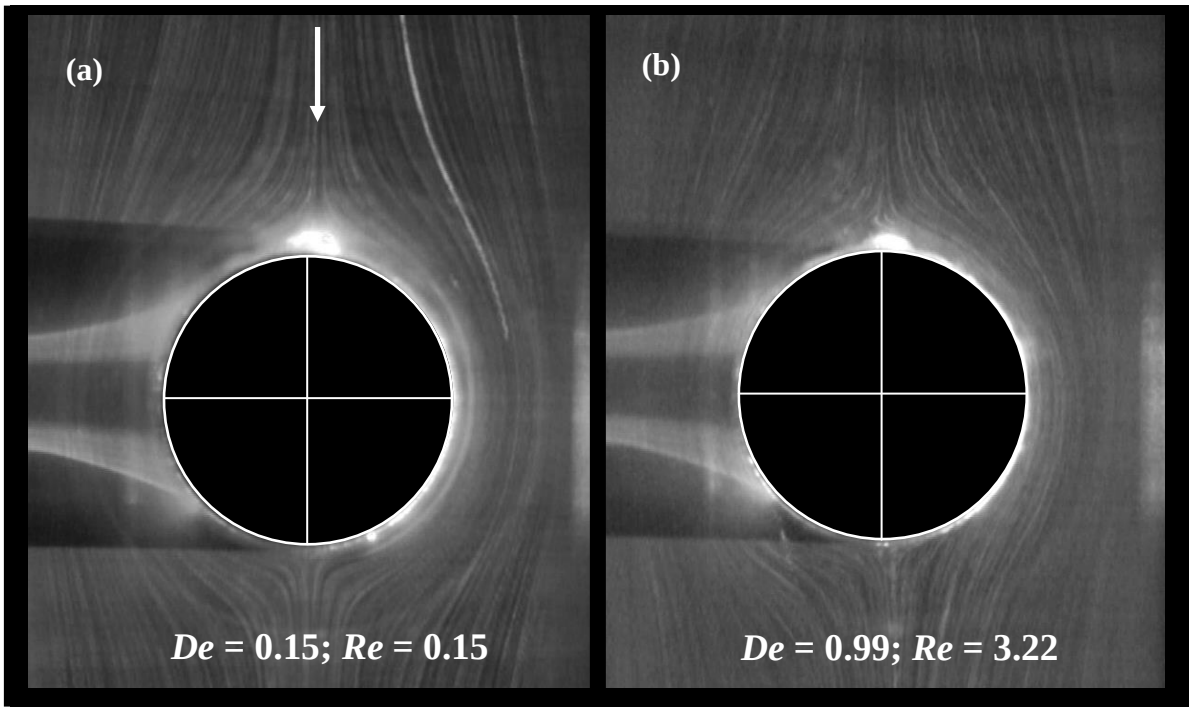

Figure 4.9. Long-time exposure streak photography: effect of elasticity on the flow patterns at the symmetry plane ($z/R = 0$) for $AR = 2$, using the PAA1000 shear-thinning fluid.

In order to illustrate the extension of the elastic instability along the spanwise direction, Figure 4.10 shows the projected pathlines at different z - planes along the cylinder axis for $De = 0.31$, $Re = 0.47$ and $AR = 8$, which corresponds to a flow condition under the steady asymmetric regime. In the middle plane ($z/R = 0$), the flow is distorted towards one side of the cylinder in the cross-stream direction (here to the right side), but as we approach the end wall ($z/R \rightarrow 8$), the flow asymmetry progressively spans to both sides of the cylinder. This spanning of the asymmetry seems to coincide with a detachment from the wall of the forward stagnation point and the upstream formation of an asymmetric region of separated flow, which also grows with De. The same pattern also occurs for $AR = 16$ and 2, but the corresponding plots are not shown for conciseness.

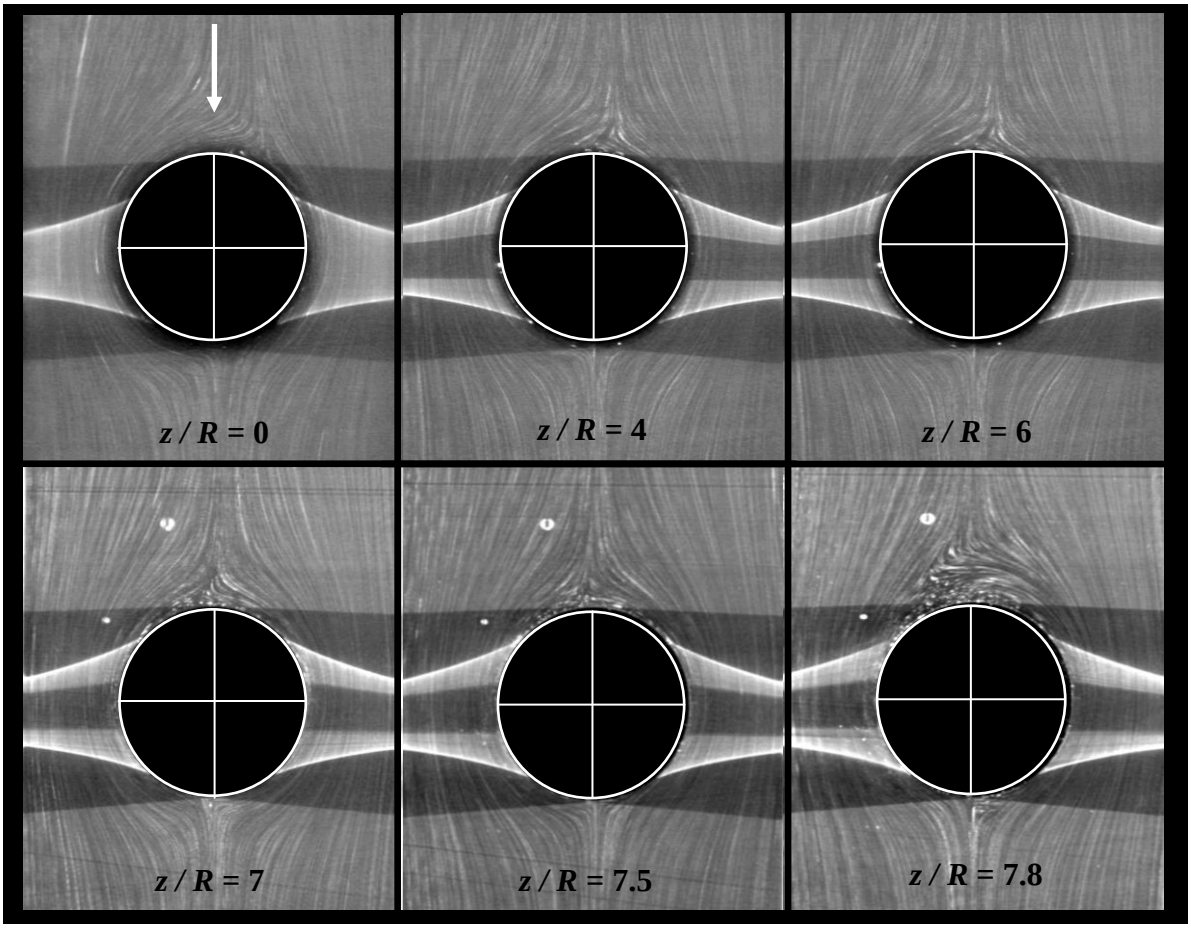

Figure 4.10. Long-time exposure streak photography: flow patterns obtained with the PAA1000 shear-thinning fluid at different planes along the *z*-direction for *De* = 0.31, *Re* = 0.47 and *AR* = 8.

Figure 4.11 shows the influence of *AR* on the extent of the elastic instability at constant *De*. For *De* ≈ 0.14 and *Re* = 0.14, the elastic instability is clearly visible for *AR* = 16 (and similarly for *AR* = 8 – not shown), but for *AR* = 2 the flow is still symmetric. Therefore, for the same flow conditions the elastic instability is enhanced as *AR* increases, although for large *AR* there is no significant influence, as demonstrated by the similar De_c values for *AR* = 16 and 8.

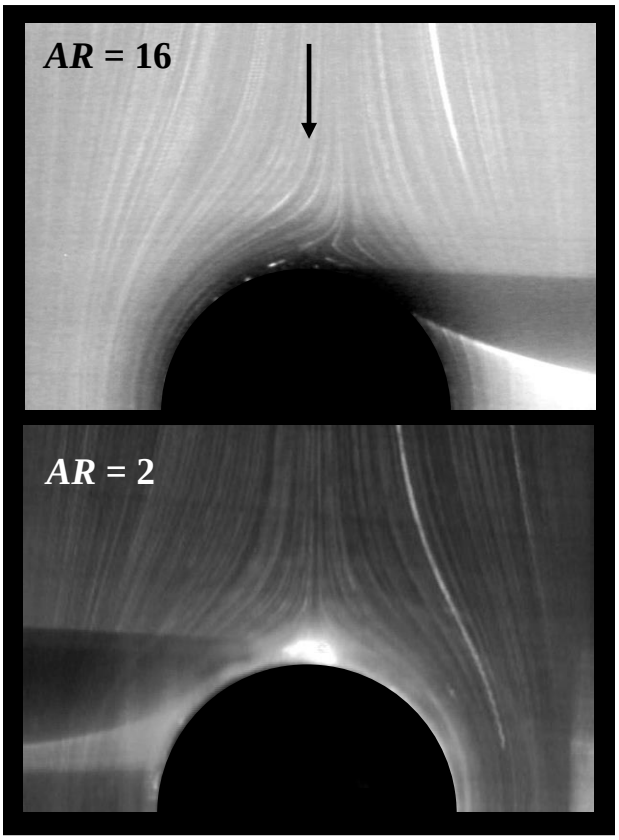

Figure 4.11. Long-time exposure streak photography: flow patterns obtained at the symmetry plane (z/R = 0) as a function of AR using the PAA1000 shear-thinning fluid $De \approx 0.14$ and $Re \approx 0.14$

When the flow rate is increased further, leading to higher Deborah numbers, but still at relatively low Reynolds numbers (Re < 1) the flow asymmetry intensifies until the flow eventually becomes time-dependent, with a periodic behaviour. Figure 4.12 shows a sequence of *instantaneous* pathlines visualized for AR = 8 at De = 0.39 and Re = 0.72, where we can clearly observe the flow unsteadiness. The same phenomenon is also observed for AR = 16 and AR = 2 at high De. We note that for small values of Re, as those reported in this section, the Newtonian flow was shown in the previous chapter (Ribeiro *et al.*, 2012) to be perfectly symmetric and steady, and thus the steady asymmetric flow and the unsteady flow at higher De reported here are due to the elasticity of the fluid.

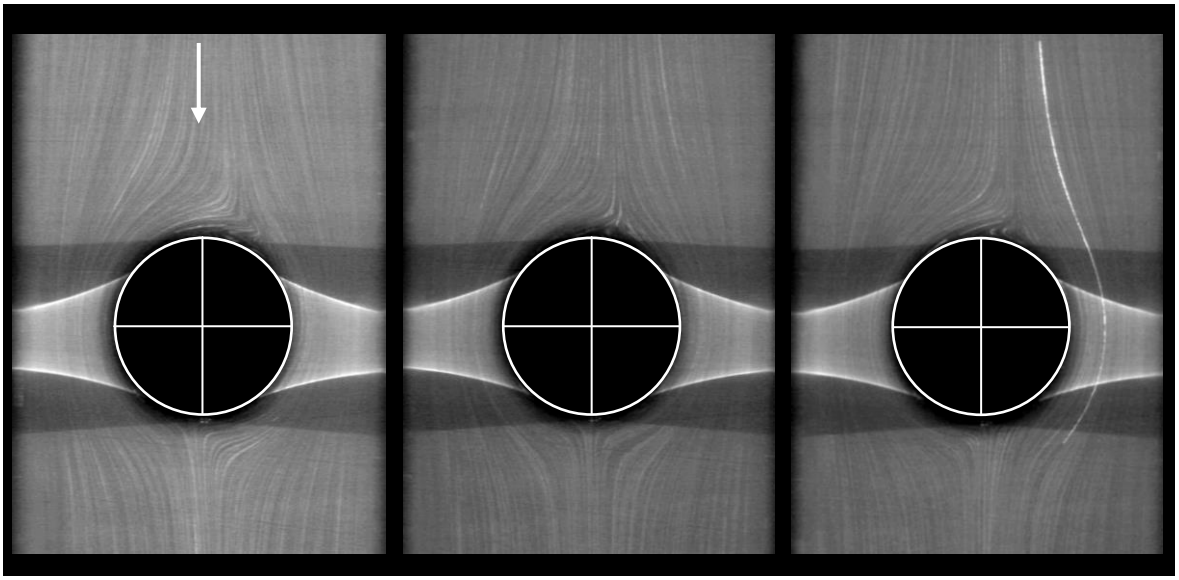

Figure 4.12. Long-time exposure streak photography showing the flow patterns obtained with the PAA100 shear-thinning fluid for AR = 8, De = 0.39 and Re = 0.72, at the symmetry plane (z/R = 0) and at three instants along the flow oscillation.

4.5.1.2. *Velocity field*

Figure 4.13 shows the influence of AR upon the streamwise dimensionless velocity component, u/U, measured along the centreline (y/R = 0 and z/R = 0) for the shear-thinning fluid at various De. We also compare the results with the corresponding velocity profile of a Newtonian fluid under creeping flow conditions, predicted from numerical simulations, to highlight the influence of viscoelasticity and shear-thinning effects.

Numerical simulations were also obtained for the Carreau generalized Newtonian fluid to assess the influence of shear-thinning on the velocity profiles. The numerical results obtained with the GNF model at the same Re, also represented in Figure 4.13, are not able to predict accurately the velocity profile near the cylinder, where the elastic effects are dominant, but are able to predict adequately the fully-developed velocity far from the cylinder, where the shear flow and viscous shear stresses are dominant.

Far from the cylinder, the measured velocity profiles are fully-developed and the shear-thinning behaviour of the viscoelastic fluid is clear from the lower centreline velocities (plug like behaviour), when compared to the Newtonian velocity profiles.

The experimental results show that as the flow approaches the cylinder the velocity decreases up to the forward stagnation point and this effect occurs earlier for the higher *AR* and *De*. Comparing the experimental results with the GNF predictions for the fully-developed velocity, for the two highest *AR* (*AR* = 16 and 8) the deceleration starts upstream of *x/R* = -15 (not shown) whereas for *AR* = 2 the deceleration starts at *x/R* ≈ -8 (cf. Figure 4.13). The development lengths required for the downstream flow redevelopment increase with *De*, for all *AR* under study, in agreement with the results obtained by McKinley *et al*. (1993). For similar values of *De*, for example *De* ≈ 0.26 - 0.3 and for *AR* = 16 and 8 the flow redevelopment only occurs at *x/R* > 15, while for *AR* = 2 the velocity redevelopment occurs at *x/R* ≈ 10 (cf. Figure 4.13). Thus, the length required for velocity recovery downstream of the cylinder is influenced by *De*, increasing progressively as elasticity increases, and is also influenced by *AR*, decreasing as the degree of confinement increases, which suggests that the end walls have a stabilizing effect, as already observed in the flow visualizations.

As *AR* decreases down to *AR* = 2, the fully-developed centreline velocity increases, due to geometric confinement. A similar effect also happens with Newtonian fluids, with the maximum fully-developed dimensionless velocity occurring for a square channel (*AR* = 2), for which a dimensionless velocity *u/U* = 2.096 is obtained (cf. Figure 4.13c), in agreement with the analytical solution for Newtonian fluid flow in a rectangular channel (White, 1991).

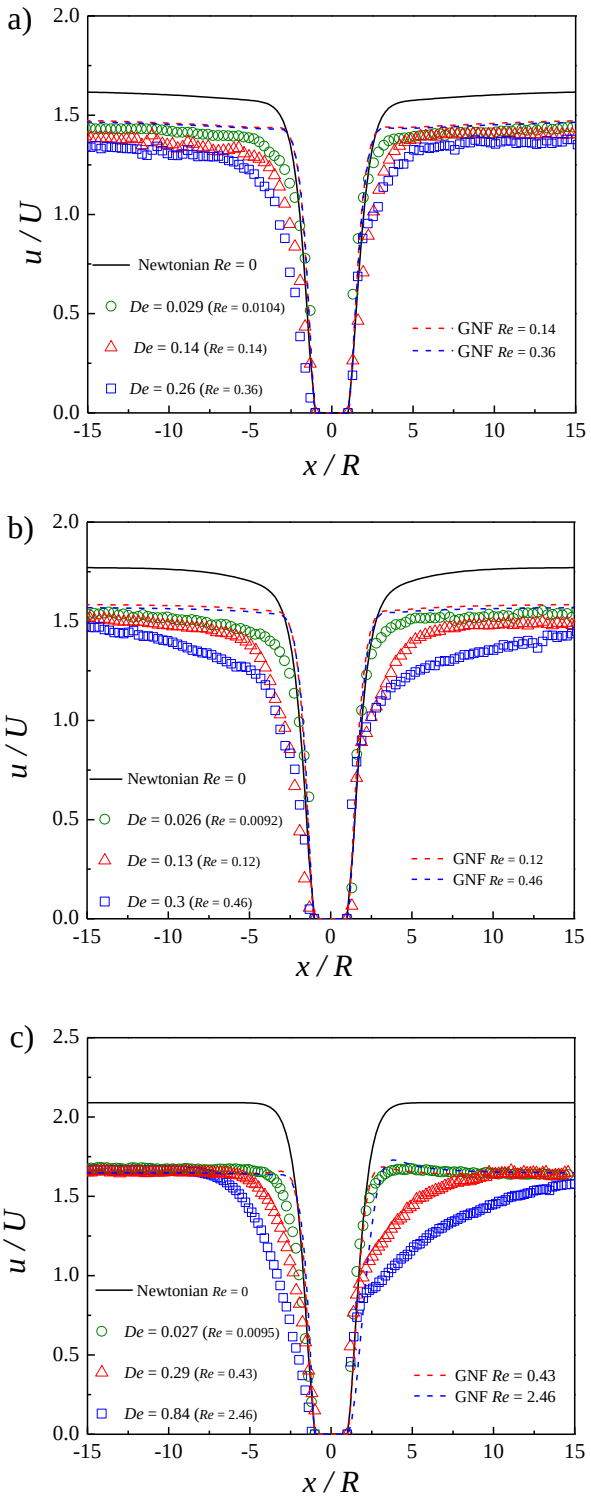

Figure 4.13. Streamwise velocity profiles along the centreline (z/R = 0, y/R = 0) for the shear-thinning fluid as a function of *De* (symbols) and comparison with numerical predictions with the GNF model (dashed lines) and inertialess Newtonian flow: (a) AR = 16, (b) AR = 8, (c) AR = 2.

The velocity profiles measured near the end walls, along the line at $z/R = (AR - 1)$ and $y/R = 0$, are presented in Figure 4.14. The chosen plane, $z/R = (AR - 1)$, corresponds to the location of a local maximum velocity for Newtonian fluids (Ribeiro *et al.*, 2012). Figure 4.14 also includes numerical predictions for the corresponding Newtonian fluid under creeping flow conditions ($Re \rightarrow 0$) and for the Carreau model at the same Re as in the experiments.

For the higher AR investigated (AR = 16 and 8) and upstream of the cylinder, in this near end-wall region the flow accelerates until a maximum velocity is reached, between $-5 \leq x/R \leq -3$, followed by a significant reduction of the velocity, due to the approaching cylinder. The acceleration starts well upstream of the cylinder, upstream at $x/R \approx -15$. A similar effect also occurs for Newtonian fluids under creeping flow conditions as shown by the full lines corresponding to the numerical predictions. Downstream of the cylinder there is also a velocity overshoot, before the fully-developed velocity profile is asymptotically approached (for Newtonian creeping flow there is flow symmetry upstream and downstream of the cylinder, due to the flow reversibility) at $x/R > 15$. In contrast, for $AR = 2$ the velocity decreases (upstream of the cylinder) and increases (downstream of the cylinder) monotonically until the fully-developed velocity is approached. As for the centreplane $z/R = 0$, and in contrast to what happens for AR = 16 and AR = 8, the deceleration upstream of the cylinder starts closer to the cylinder at $x/R \approx -8$ and the downstream fully-developed velocity is already achieved at $x/R \approx 10$.

Comparing the velocity profiles near the end walls with those at the centreplane, and for all AR, the fully-developed velocity decreases as expected. It is important at this stage to remind the reader that the higher De cases plotted in Figures 4.13 and 4.14 are asymmetric close and upstream of the cylinder ($De > De_c$).

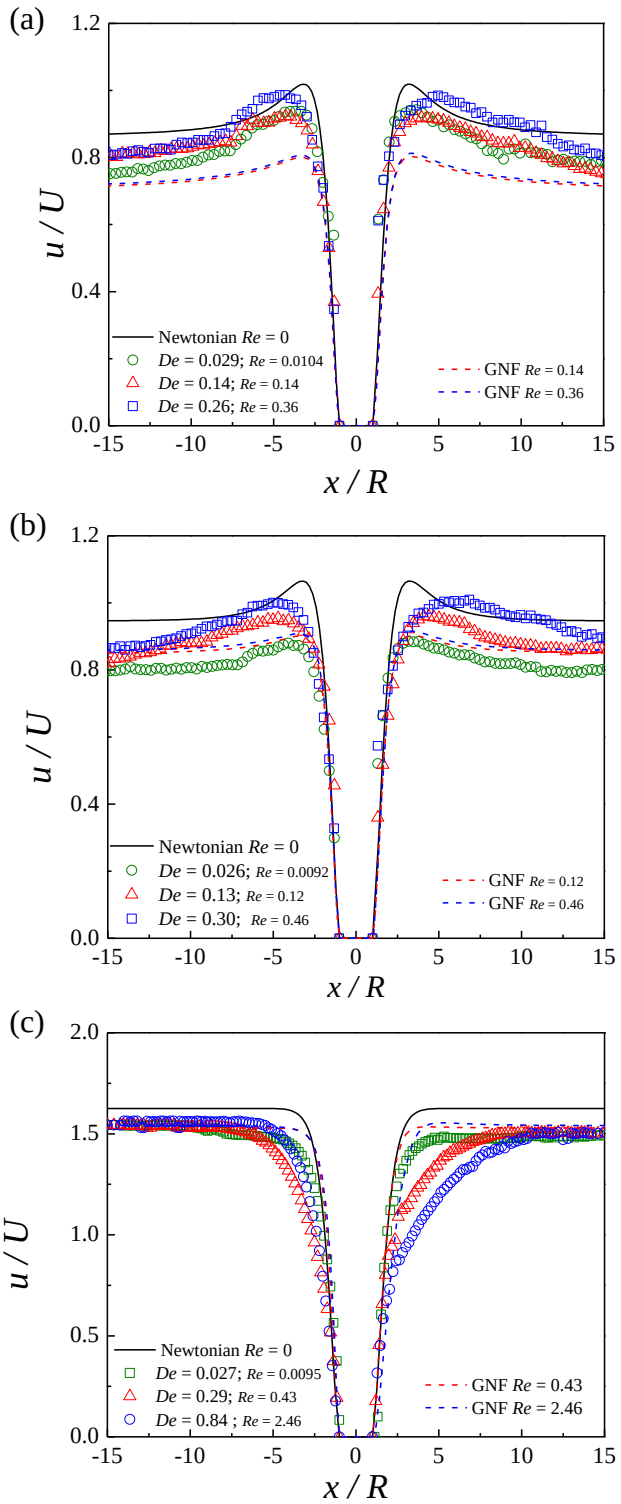

Figure 4.14. Streamwise velocity profiles along the line $z/R = AR - 1$ and $y/R = 0$, obtained for the shear-thinning fluid as a function of *De* (symbols). Comparison with numerical predictions with the GNF model (dashed lines) and inertialess Newtonian flow: (a) $AR = 16$, (b) $AR = 8$, (c) $AR = 2$.

Figure 4.15 shows the spanwise evolution of the measured profiles of the streamwise velocity for several values of z/R (cf. Figure 4.2) taken on the $y/R = 0$ centreplane for all AR and at $De \approx 0.12$, corresponding to symmetric flow for $AR = 2$ and asymmetric for $AR = 16$ and $AR = 8$. As for the Newtonian fluids, the fully-developed velocity is higher on the centreline and decreases as the flow approaches the end walls for all AR.

For $AR = 16$ and 8, in the profiles closer to the centreplane (up to $z/R = 12$ for $AR = 16$ and to $z/R = 4$ for $AR = 8$) the velocity profiles are similar to that at $z/R = 0$, except for a slight decrease of the fully-developed velocity. Near the end walls ($z/R \geq 13$ for $AR = 16$ and $z/R \geq 6$ for $AR = 8$), for both upstream and downstream of the cylinder, a velocity peak is observed at $x/R \approx -4$ and $x/R \approx 4$. The exact locations of the velocity maximum upstream and downstream of the cylinder depend on De. The changes observed in the velocity profiles behaviour closer to the end walls are related to the influence created by the presence of the walls, which is similar to that seen for Newtonian fluids (Ribeiro *et al.*, 2012). However, for viscoelastic fluids it is enhanced by fluid elasticity, which is also responsible for flow asymmetry absent from the corresponding Newtonian creeping flow case. For $AR = 2$ the velocity profiles upstream and downstream of the cylinder are monotonic, in agreement with the observations at the centreplane.

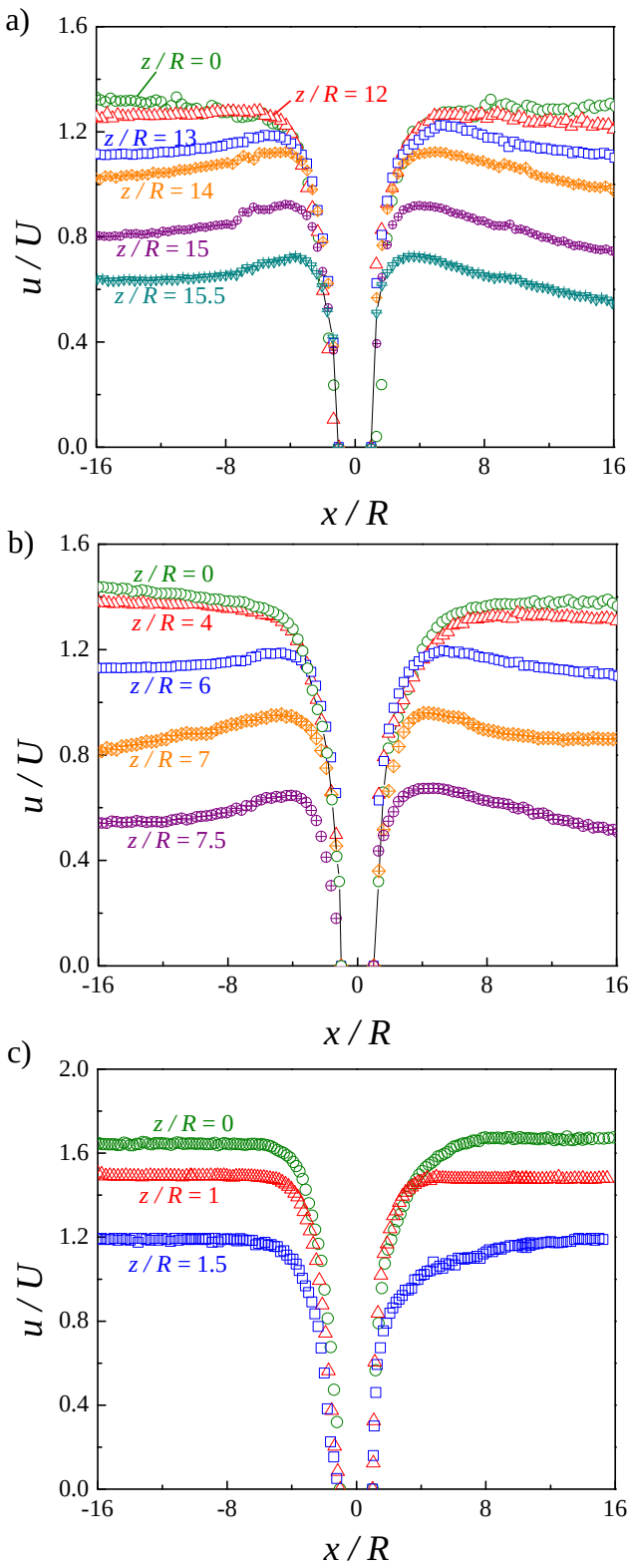

Figure 4.15. Streamwise profiles of the streamwise velocity component at the symmetry plane (y = 0) along the cylinder axis for the shear-thinning fluid at De = 0.12 and Re = 0.10: (a) AR = 16, (b) AR = 8, (c) AR = 2.

Figures 4.16 and 4.17 show transverse profiles of the normalized streamwise velocity at two upstream (x/R = -6 and -2) and two downstream locations (x/R = 2 and 6) at the symmetry plane (z/R = 0), $De \approx 0.03$ and 0.3. These figures pertain to AR = 8 and 2, respectively, thus representing the high and low AR cases (the results for AR = 16 and AR = 8 are similar). It is important to remind the reader that the flow for the highest De ($De \approx 0.3$) in Figure 4.16 is asymmetric, since $De > De_c$. However these asymmetries are not visible in Figure 4.16 because the upstream location under study closer to the cylinder is x/R = -2 and at this distance of the cylinder the local steady instability does not influence significantly the velocity profiles.

For AR = 8 and far upstream of the cylinder, at x/R = -6, the flow is slightly influenced by the presence of the cylinder (Figure 4.16a), due to the flow deceleration already reported in Figure 4.13 in the symmetry plane (y/R = 0). At this same location (x/R = -6) and for AR = 2 (Figure 4.17a) the influence of the cylinder is nearly negligible, as shown previously in Figure 4.13c. At x/R = -6 the velocities are always higher on the symmetry plane than near the side walls. For AR = 8 the effect of the approaching cylinder occurs earlier with the increase of De. This also happens for AR = 2, but still closer to the cylinder, i.e., at $|x/R| < 6$. Thus the effect of the cylinder is shown again to occur earlier as AR increases.

Closer to the cylinder, e.g. at x/R = -2 (Figure 4.16b, 4.17b), the flow is now significantly influenced by the presence of the cylinder for all AR investigated and the velocities are higher at $y/R \approx 1 - 1.5$ than at the symmetry plane as the former corresponds to the gap between the cylinder and the side walls. As can be observed in Figures 4.16b and 4.17b for $De \approx 0.3$ the velocity peaks occur at $|y/R| \approx 1.5$ while for De = 0.03 the velocity peaks occur at $|y/R| \approx 1.3$, regardless of AR. Thus, at x/R = -2 the location of the velocity peaks depends on De, and is found to be closer to the side walls as well as more pronounced when De increases.

Figures 4.16c, d and 4.17c, d show that the redevelopment of the velocity profile downstream of the cylinder occurs further downstream for the higher De, in agreement with the profiles show earlier in Figure 4.13b, c for the streamwise velocity along the centreline. Downstream of the cylinder, at x/R = 2, the flow is still influenced by the bluff body for AR = 8, regardless of De, and the streamwise velocities are higher near the side walls than at the symmetry plane. At this location, the velocity peak occurs at $|y/R| \approx 1.2$, regardless of De. For AR = 2 the velocity is higher on the symmetry plane for lower De, (cf. Figure 4.17c for De = 0.027),

but when *De* increases further, the velocities become higher near the side walls. Thus, at this streamwise location (*x/R* = 2) and at lower *De*, the effect of the duct confinement overlaps the effect of the presence of the cylinder. Moving downstream to *x/R* = 6 (Figure 4.16d and 4.17d) the flow is still dependent of *De*, and the velocity field is still developing, in agreement with Figure 4.13.

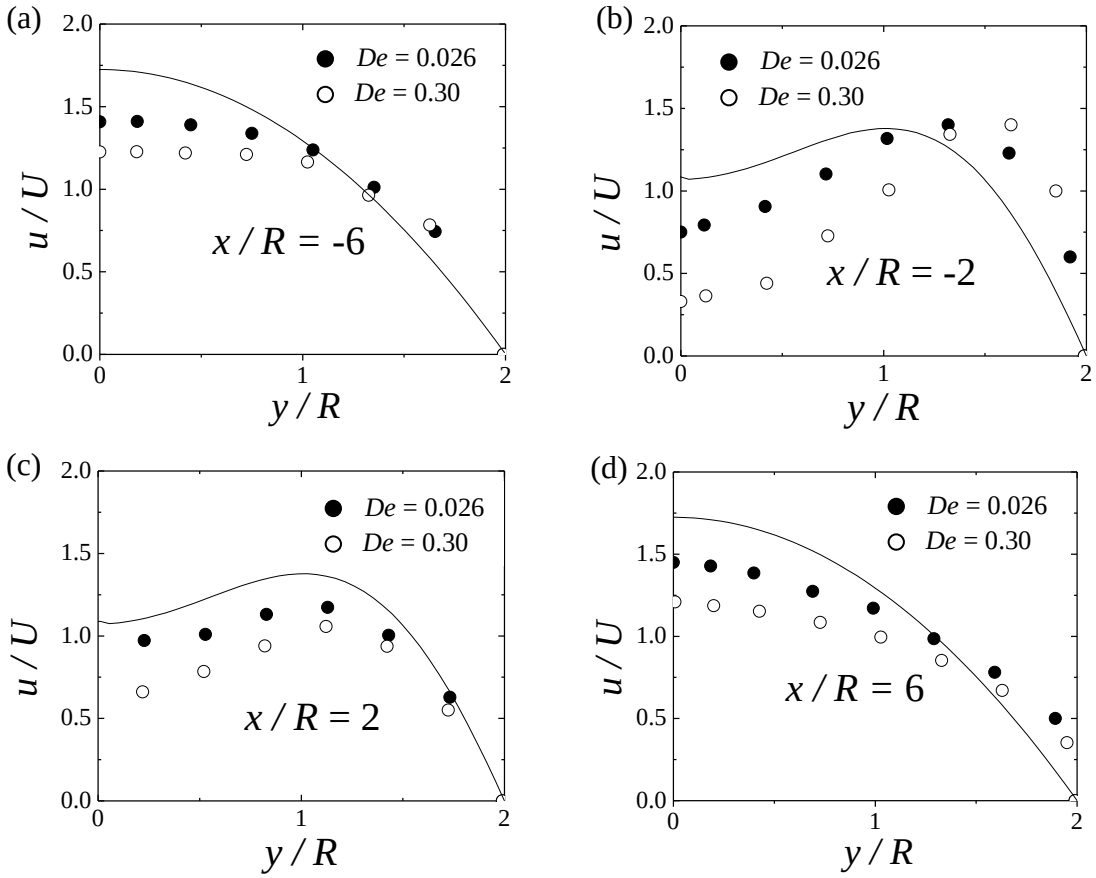

Figure 4.16. Streamwise variation of the transverse profiles of the streamwise velocity component at the *z/R* = 0 symmetry plane for the flow of the PAA1000 shear-thinning fluid at *AR* = 8 for *De* = 0.026, *Re* = 0.009 and *De* = 0.30, *Re* = 0.46: (a) *x/R* = -6; (b) *x/R* = -2; (c) *x/R* = 2; (d) *x/R* = 6. The lines represent the numerical predictions for the corresponding Newtonian fluid under creeping flow conditions (*Re* → 0).

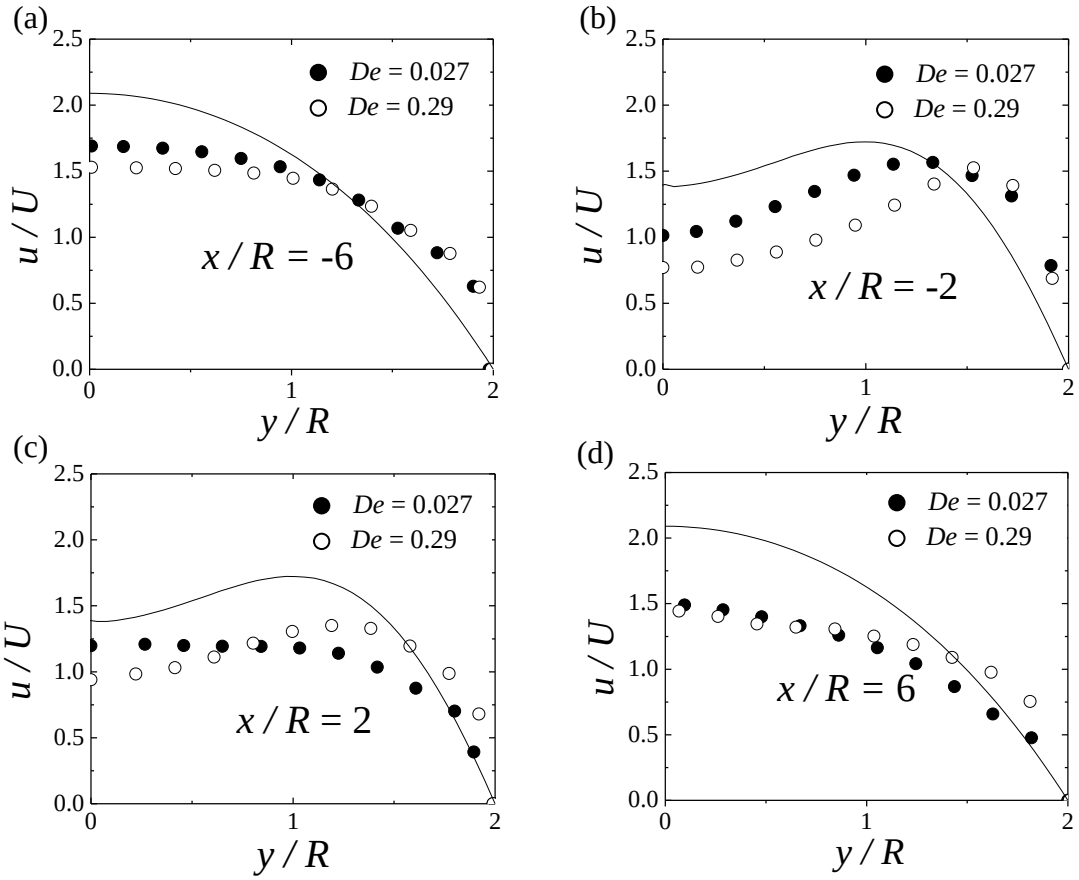

Figure 4.17. Streamwise variation of the transverse profiles of the streamwise velocity component at the $z/R = 0$ symmetry plane for the flow of the PAA1000 shear-thinning fluid at $AR = 2$ for $De = 0.027$, $Re = 0.0095$ and $De = 0.29$, $Re = 0.43$): (a) $x/R = -6$; (b) $x/R = -2$; (c) $x/R = 2$; (d) $x/R = 6$. The lines represent the numerical predictions for the corresponding Newtonian fluid under creeping flow conditions ($Re \rightarrow 0$).

4.5.2. Boger fluids

4.5.2.1. *Flow patterns*

Figure 4.18 shows the effect of *De* on the flow patterns observed for the Boger fluids at the central plane ($z/R = 0$) for $AR = 16$ (PAA200 in Figure 4.18a and PAA400 in Figure 4.18b). The range of *De* studied with these fluids ($0.01 < De < 0.14$), is below that for the shear-thinning fluids and the flow remains symmetric upstream and downstream of the cylinder. The high viscosities of the Boger fluids reduce the maximum (achievable) flow rates in the rig, thus limiting here the values of *De*.

Symmetric flow upstream and downstream of the cylinder was also observed in the spanwise direction, as shown in Figure 4.19 for PAA200 Boger fluid at De = 0.13, including the corresponding streamlines predicted numerically using the Oldroyd-B model. The comparison with the experimental data shows good agreement, and it is found that in this range of flow conditions the influence of fluid elasticity is not significant in qualitative terms. However, at higher flow rates the elastic effects are enhanced and the onset of elastic-driven flow instabilities is expected to occur.

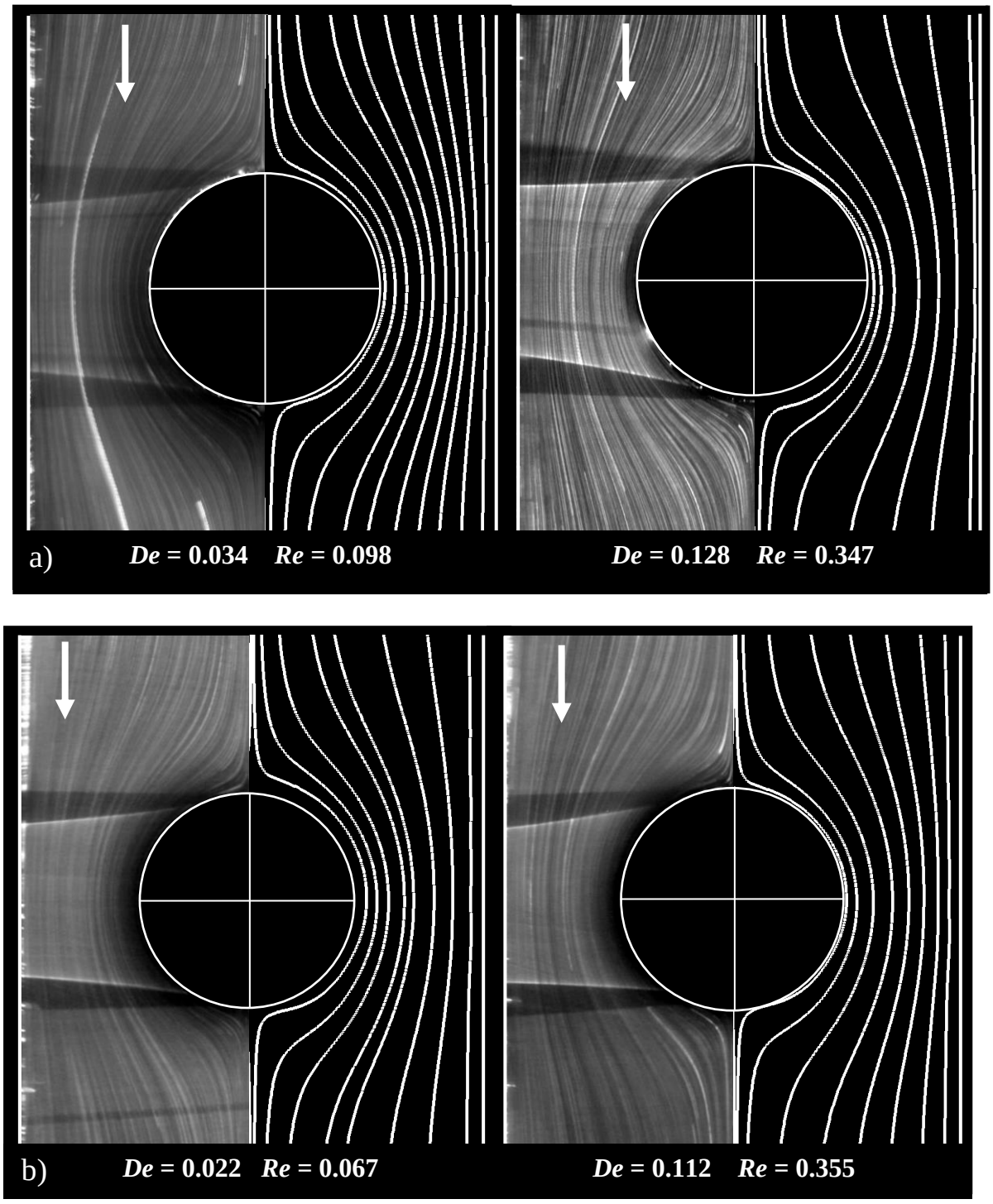

Figure 4.18. Experimental (left) and numerical (right) flow patterns at the symmetry plane ($z/R = 0$) for $AR = 16$: a) PAA200 fluid; b) PAA400 fluid.

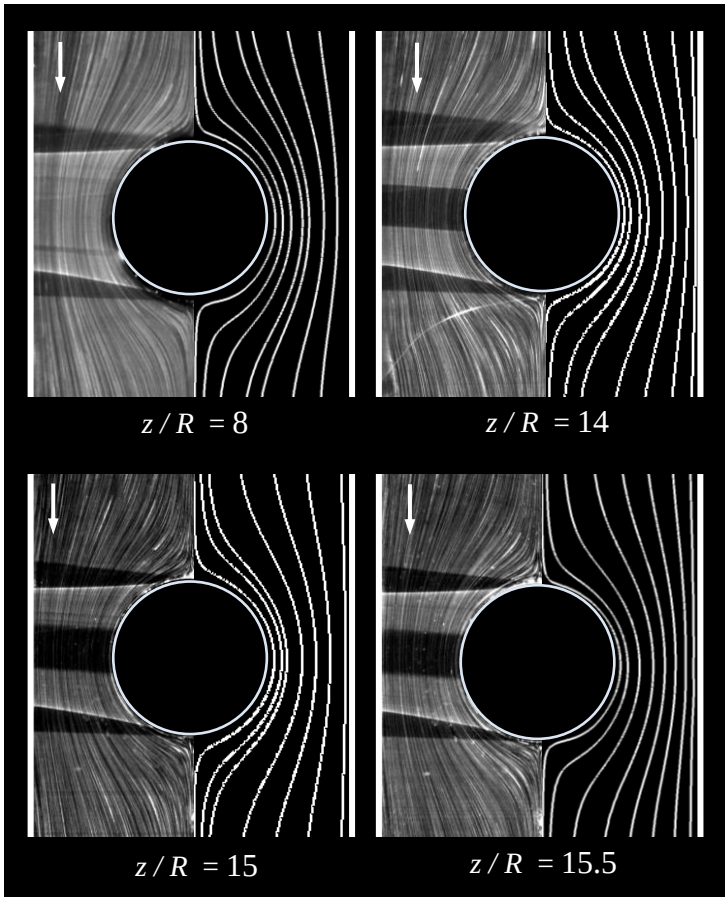

Figure 4.19. Experimental (left) and numerical (right) flow patterns at different *xy*-planes along the cylinder axis for *AR* = 16, *De* = 0.13 and *Re* = 0.35 using the PAA200 Boger fluid.

4.5.2.2. *Velocity field*

Figure 4.20 shows the profiles along the centreline (y/R = 0, z/R = 0) of the streamwise dimensionless velocity for *AR* = 16, using both PAA200 and PAA400 Boger fluids. The symbols represent the experimental data and lines represent the corresponding numerical predictions obtained with the Oldroyd-B model. Careful inspection shows that the experimental velocity profiles for both Boger fluids are similar, even for the higher *De* achieved numerically, and for that reason the results presented below only refer to the Boger fluid PAA200. The differences observed between the results of Boger fluids PAA200 and PAA400 are primarily due to the difference between their viscosity ratios (β, ratio of the solvent to total viscosities) and similarly for the two fitted Oldroyd-B models used in the simulations. The good agreement between the experimental results and the numerical predictions validates the numerical calculations for *AR* = 16. Consequently, to further explore

the influences of *AR* and elasticity, numerical computations using the Oldroyd-B model were carried out for *AR* = 8 and 2, as discussed next.

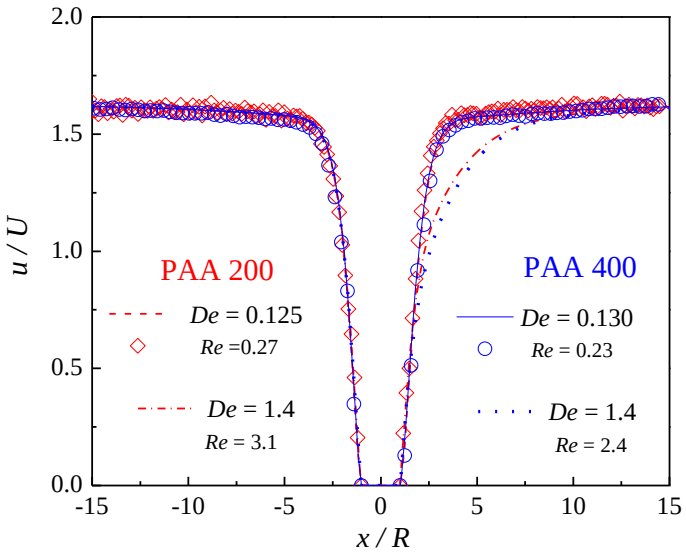

Figure 4.20. Streamwise velocity profiles along the centreline (*y/R* = 0, *z/R* = 0) of the streamwise velocity component for the flow of Boger fluids PAA200 and PAA400 for *AR* = 16. Comparison between experimental (symbols) and numerical predictions (lines).

Figure 4.21 shows the influence of *AR* upon the dimensionless streamwise velocity along the centreline (*y/R* = 0, *z/R* = 0) for the PAA200 Boger fluid, as a function of *De*. Figure 4.21a includes experimental results (symbols) and numerical predictions obtained with the Oldroyd-B model fitted to the PAA200 Boger fluid (full lines) for *AR* = 16, whereas Figures 4.21b-c only show numerical predictions for *AR* = 8 and *AR* = 2, respectively. Figure 4.21 also includes numerical computations for Newtonian fluid flows (dashes lines) at the same flow conditions as for the PAA200 Boger fluid, i.e., with the same density, shear viscosity and for the same mean velocity (i.e. same *Re*) in order to isolate the influence of elasticity on the velocity field.

For all *AR*, the fully-developed dimensionless velocity profile upstream of the cylinder is independent of flow rate (or *De*) since the fluid has a constant shear viscosity and the shape of such velocity profile is exclusively determined by the shear stress (if the second normal stress difference is small). However, the flow upstream is influenced by the presence of the cylinder, due to the necessary flow deceleration up to the forward stagnation point, and this effect depends on *AR*. The deceleration starts at $|x/R| \approx 13$ for *AR* = 16 and 8, while for *AR* = 2 it starts at $|x/R| \approx 5$. Downstream of the cylinder, the required length to achieve the fully-

developed velocity (indicated as dash-dot lines) increases with *De* and also depends on the *AR*. The fully-developed velocity is achieved at $x/R > 15$ for $AR = 16$ and 8 and reduces to $x/R \approx 12$ for $AR = 2$, because of geometric confinement. Note that the fully-developed velocity on the centreline is the same for all these constant shear viscosity fluids and agree with the analytical solutions for Newtonian fluids in rectangular ducts, as shown previously by Ribeiro *et al.* (2012).

For $AR = 16$ and $De = 0.09$ (cf. Figure 4.21a), the comparison between the experimental data and the numerical predictions obtained with the Oldroyd-B model shows a good agreement. Comparing the Newtonian simulations (dashed line) with the viscoelastic simulations for $De = 1.25$ at the same $Re = 2.7$ (solid line) we conclude that the viscoelasticity leads to an increase in the required development length. For $AR = 8$ and 2, Figures 4.21b and c also show an increase of the development length with *De*. We can also conclude from the various comparisons in Figure 4.21 that in these conditions of low inertia, the influence of inertia upon flow development length is significantly weaker than that viscoelasticity. In addition, the observed increase of the development length with *De* agrees with the numerical study of Alves *et al.* (2001) for 2D cylinder flow of an Oldroyd-B fluid.

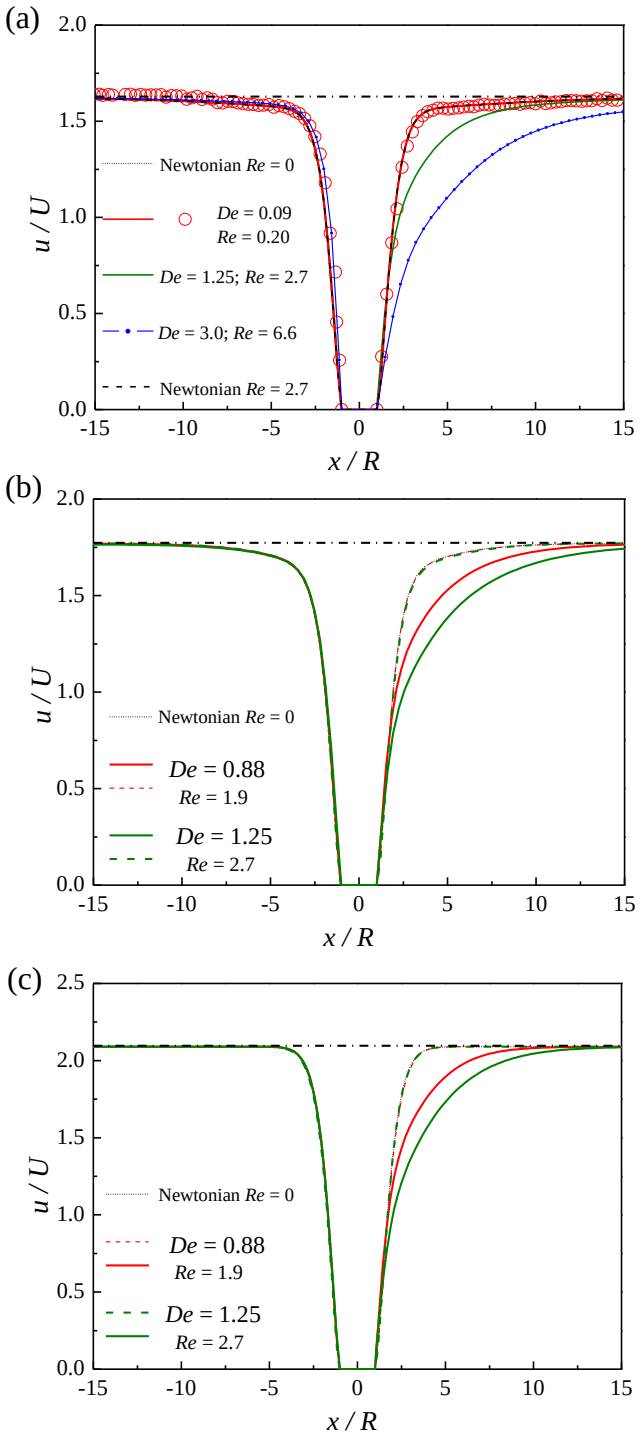

Figure 4.21. Streamwise velocity component along the centreline ($y/R = 0$, $z/R = 0$) for the PAA200 Boger fluid flow as function of *De*: (a) *AR* = 16; (b) *AR* = 8; (c) *AR* = 2. Comparison between experimental (symbols), numerical predictions using the Oldroyd-B model (full lines) and numerical predictions for a Newtonian fluid at the same *Re* (dashed lines). The dash-dot lines are a guide to the eye and represent the fully-developed velocity in the rectangular duct.

Figures 4.22 and 4.23 show the evolution along the cylinder of the streamwise profiles of the streamwise velocity component at the $y/R = 0$ centreplane for $AR = 16$ and 2, respectively. The figures show curves at different values of *De* and include both experimental and numerical data. For both *AR* cases, the fully-developed velocity is higher on the centreline and decreases as the flow approaches to the end walls, as also happens for the Newtonian fluid flow (Ribeiro *et al.*, 2012) and the fully-developed velocity is the same upstream and downstream the cylinder, as expected.

For the $AR = 16$ geometry (Figure 4.22) the velocity profiles are essentially similar for $z/R \leq 8$ and no velocity overshoots are observed. At the near end-wall planes ($z/R = 12$, 14, 15 and 15.5), the streamwise velocity profiles display a significant overshoot, localized at $x/R \approx -3$, followed by a reduction of the velocity, due to the approach of the cylinder. A fore-aft quasi-symmetric velocity profile is observed around the cylinder for the lower *De* flow case. The flow upstream of the cylinder is essentially independent of the *De* for all planes along the cylinder, in agreement with Figure 4.21. However, downstream of the cylinder the location of the velocity peaks strongly depends on *De*, being less pronounced and occurring farther downstream from the cylinder as *De* increases, thus breaking the fore-aft symmetry.

In Figure 4.23, corresponding to $AR = 2$, a slight velocity overshoot is only observed in the plane closer to the end wall ($z/R = 1.5$ and $z/R = 1.8$) for the lower *De* near $x/R \approx 3$. For all planes illustrated, the length required for the flow redevelopment downstream of the cylinder increases with *De*, as also observed for $AR = 16$, and the velocity profiles are quasi-symmetric relative to $x/R = 0$ for the lower *De*.

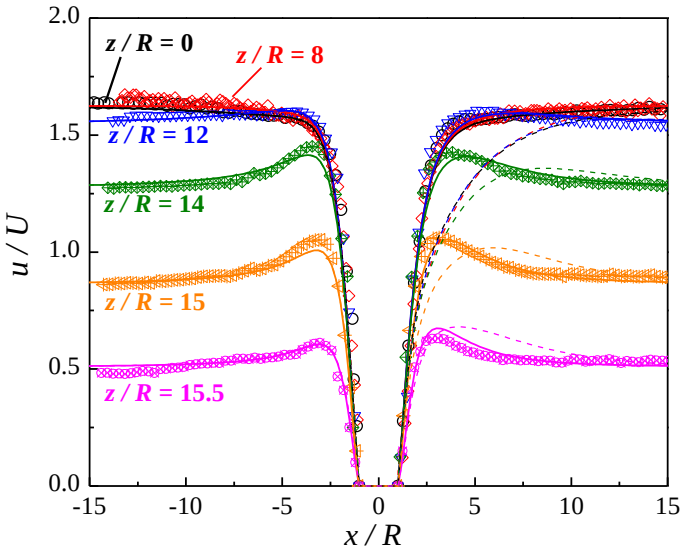

Figure 4.22. Streamwise profiles of the normalized streamwise velocity taken at the $y = 0$ centreplane as a function of the spanwise coordinate for $AR = 16$ and for PAA 200 Boger fluid: $De = 0.09$, $Re = 0.20$ - experimental (symbols) and numerical (full lines); $De = 1.25$, $Re = 2.7$ - numerical (dashed lines).

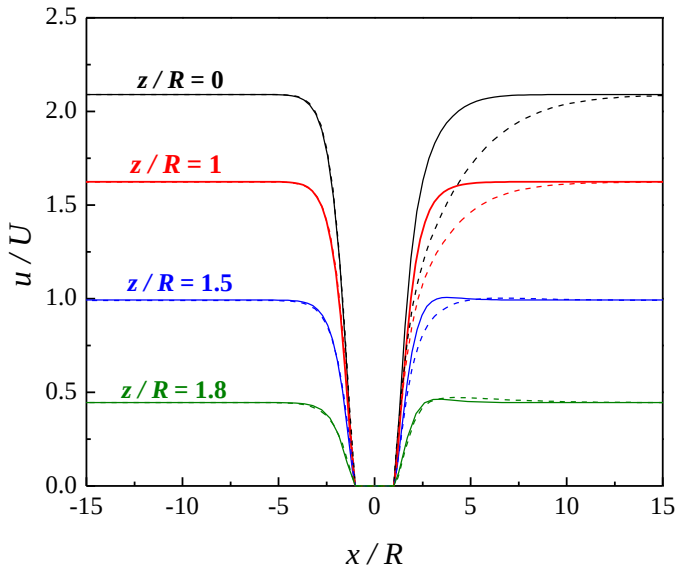

Figure 4.23. Streamwise profiles of the normalized streamwise velocity taken at the $y = 0$ centreplane as a function of the spanwise coordinate for $AR = 2$ and for PAA 200 Boger fluid: $De = 0.5$, $Re = 1.1$ (full lines) and $De = 1.25$, $Re = 2.7$ (dashed lines).

4.6. Conclusions

An experimental and numerical study was carried out on the flow past a confined cylinder placed in a rectangular duct with a 50% blockage ratio using a Newtonian, a shear-thinning and two Boger fluids. The flow was characterized experimentally using streak photography and PIV to quantify the complex flow field. The flow conditions investigated ranged from inertialess and low *De* flow up to the onset of time-dependent flow, for aspect ratios of 16, 8 and 2.

The measurements for the shear-thinning fluid show the appearance of an elastic instability upstream the cylinder, at a critical Deborah number, De_c. For low *De*, the flow is symmetric relative to the planes $y = 0$ and $z = 0$ (for creeping flow of Newtonian fluids is also symmetric relative to the $x = 0$ plane). When *De* exceeds a critical value, De_c, an elastic instability arises and becomes more intense with the increase in *De,* and the flow becomes progressively asymmetric and eventually time-dependent at higher *De*. At a constant *De*, the intensity of the asymmetry decreases when *AR* decreases, due to the increasing relevance of viscous effects of the end walls. The deceleration upstream of the cylinder and the subsequent velocity recovery downstream of the cylinder depend also on *AR* and *De*. As expected, the shear-thinning viscoelastic fluid shows a decrease of the fully-developed nondimensional velocity at the duct axis, compared with the corresponding fully-developed velocity for the constant shear viscosity fluids (Newtonian and Boger fluids).

The results for the Boger fluids are particularly useful to isolate the elastic effects. Over the range of *De* studied for the Boger fluids, the flow patterns are symmetric and steady and the numerical predictions using the Oldroyd-B model fitted to their rheology matched very well with the experimental data. The velocity measurements with the Boger fluids show that for lower *De* elastic effects are negligible, but as *De* increases the elasticity of the fluid leads to an increase of the required development length downstream of the cylinder, in agreement with the numerical simulations using the Oldroyd-B model. The velocity development length is found to increase with an increase of *AR*.

References

Adrian, R.J., 2005. Twenty years of particle image velocimetry. Exp Fluids 39, 159-169.

Alves, M.A., Oliveira, P.J., Pinho, F.T., 2003. A convergent and universally bounded interpolation scheme for the treatment of advection. Int J Numer Meth Fl 41, 47-75.

Alves, M.A., Pinho, F.T., Oliveira, P.J., 2001. The flow of viscoelastic fluids past a cylinder: finite-volume high-resolution methods. J Non-Newton Fluid Mech 97, 207-232.

Brown, R.A., McKinley, G.H., 1994. Report on the VIIIth Int Workshop on numerical - methods in viscoelastic flows. J Non-Newton Fluid Mech 52, 407-413.

Carreau, P.J., 1972. Rheological Equations from Molecular Network Theories. Trans. Soc Rheol 16, 99-127.

Dealy, J., Plazek, D., 2009. Time-temperature superposition - a user guide. Rheology Bulletin 78, 16-31.

Entov, V.M., Hinch, E.J., 1997. Effect of a spectrum of relaxation times on the capillary thinning of a filament of elastic liquid. J Non-Newton Fluid Mech 72, 31-53.

Fattal, R., Kupferman, R., 2004. Constitutive laws for the matrix-logarithm of the conformation tensor. J Non-Newton Fluid Mech 123, 281-285.

Ferreira, H.H., 2006. Escoamento de fluidos newtonianos e viscoelásticos em torno de um cilindro: estudo numérico de efeitos tridimensionais. MSc thesis. MSc on Fundamentals and Applications of Fluid Mechanics. Faculdade de Engenharia da Universidade do Porto.

Kumar, B., Mittal, S., 2006. Prediction of the critical Reynolds number for flow past a circular cylinder. Comput Method in Appl Mech and Engng 195, 6046-6058.

Manero, O., Mena, B., 1981. On the Slow Flow of Viscoelastic Liquids Past a Circular-Cylinder. J Non-Newton Fluid Mech 9, 379-387.

McKinley, G.H., 1991. Nonlinear dynamics of viscoelastic flows in complex geometries, PhD Thesis. Department of Chemical Engineering. Massachusetts Institute of Technology, Cambridge.

McKinley, G.H., Armstrong, R.C., Brown, R.A., 1993. The Wake Instability in Viscoelastic Flow Past Confined Circular-Cylinders. Philos T Roy Soc A 344, 265-304.

Nishimura, T., 1986. Flow across tube banks. In: Cheremisinoff, P. (Ed.), Encyclopedia of Fluid Mechanics. Gulf Publishing Company, pp. 763-785.

Oliveira, P.J., Pinho, F.T., Pinto, G.A., 1998. Numerical simulation of non-linear elastic flows with a general collocated finite-volume method. J Non-Newton Fluid Mech 79, 1-43.

Phan-Thien, N., Dou, H.S., 1999. Viscoelastic flow past a cylinder: drag coefficient. Comput Method in Appl Mech and Engng 180, 243-266.

Poole, R.J., Alves, M.A., 2009. Velocity overshoots in gradual contraction flows. J Non-Newton Fluid Mech 160, 47-54.

Poole, R.J., Alves, M.A., Oliveira, P.J., 2007a. Purely elastic flow asymmetries. Phys Rev Lett 99, 164503.

Poole, R.J., Escudier, M.P., Afonso, A., Pinho, F.T., 2007b. Laminar flow of a viscoelastic shear-thinning liquid over a backward-facing step preceded by a gradual contraction. Phys Fluids 19, 093101.

Ribeiro, V.M., Coelho, P.M., Pinho, F.T., Alves, M.A., 2012. Three-dimensional effects in laminar flow past a confined cylinder. Chem Eng Sci 84, 155-169.

Richter, D., Iaccarino, G., Shaqfeh, E.S.G., 2010. Simulations of three-dimensional viscoelastic flows past a circular cylinder at moderate Reynolds numbers. J Fluid Mech 651, 415-442.

Sahin, M., 2011. A stable unstructured finite volume method for parallel large-scale viscoelastic fluid flow calculations. J Non-Newton Fluid Mech 166, 779-791.

Sahin, M., Owens, R.G., 2004. A numerical investigation of wall effects up to high blockage ratios on two-dimensional flow past a confined circular cylinder. Phys Fluids 16, 1305-1320.

Sahin, M., Wilson, H.J., 2007. A semi-staggered dilation-free finite volume method for the numerical solution of viscoelastic fluid flows on all-hexahedral elements. J Non-Newton Fluid Mech 147, 79-91.

Sen, S., Mittal, S., Biswas, G., 2009. Steady separated flow past a circular cylinder at low Reynolds numbers. J Fluid Mech 620, 89-119.

Shiang, A.H., Lin, J.C., Öztekin, A., Rockwell, D., 1997. Viscoelastic flow around a confined circular cylinder: measurements using high-image-density particle image velocimetry. J Non-Newton Fluid Mech 73, 29-49.

Telionis, D.P., Gundappa, M., Diller, T.E., 1992. On the Organization of Flow and Heat-Transfer in the near Wake of a Circular-Cylinder in Steady and Pulsed Flow. J Fluid Eng-T Asme 114, 348-355.

Tenchev, R., Gough, T., Harlen, O.G., Jimack, P.K., Klein, D.H., Walkley, M.A., 2011. Three dimensional finite element analysis of the flow of polymer melts. J Non-Newton Fluid Mech 166, 307-320.

Verhelst, J.M., Nieuwstadt, E.M., 2004. Visco-elastic flow past circular cylinders mounted in a channel: experimental measurements of velocity and drag. J Non-Newton Fluid Mech 116, 301-328.

White, F.M., 1991. Viscous fluid flow. McGraw-Hill, New York.

Williamson, C.H.K., 1996. Vortex dynamics in the cylinder wake. Annu Rev Fluid Mech 28, 477-539.

Zdravkovich, M.M., 1997. Flow around circular cylinders. Vol 1: Fundamentals. Oxford University Press New York.

Zdravkovich, M.M., 2003. Flow around circular cylinders. Vol 2: Applications. Oxford Universtiy Press, New York.

Chapter 5

Viscoelastic fluid flow past a confined cylinder: a comparative study between macro- and micro-scales

Abstract

The Newtonian and viscoelastic fluid flow around a confined cylinder at both macro- and micro-scales was investigated for comparison purposes and in order to access a wide range in the Deborah number (De) - Reynolds number (Re) parameter space. The flows are geometrically similar with the channels having an aspect ratio (AR - ratio between the channel depth and the cylinder diameter) of 2.0 and a blockage ratio (BR – ratio between the cylinder diameter and the channel width) of 50%. The cylinder diameters are 10.0 mm and 105 μm, respectively at the macro- and micro-scales, thus defining a scale factor between length scales of 95. Experimental flow visualizations, using long-time exposure streak photography and detailed velocity measurements, using (micro-) particle image velocimetry (PIV), are compared with numerical simulations. For the Newtonian fluid flow there are no considerable differences changing from the macro-scale to the micro-scale, as expected when we compare the same Reynolds number flows in both geometries. However, that is not the case for viscoelastic fluid flow where the elasticity number also plays an important role. The measurements over a wide range of Deborah and Reynolds numbers identified four flow regimes of distinct flow behavior. More detailed information is provided regarding the low De Newtonian-like regime in an attempt to assess the causes of the first elastic transition.

5.1. Introduction

Many engineering processes involve flows in large scale systems, and even the down scaling implemented in laboratory experiments often have typical length scales of the order of tens of millimetres. This length scale is still two to three orders of magnitude larger than found in a new wave of engineering systems operating at the micro-scale, thus strongly changing the ratio of relevant forces in the processes and in particular enhancing the role of surface forces over those of volumetric forces (Oliveira *et al.*, 2012). Progress in microfluidics has been swift over the last fifteen years leading to the development of a variety of lab-on-chip or micro total analysis systems (μTAS) for applications in biological and chemical sciences, medicine and engineering. This miniaturization allows the implementation and integration of microfluidic devices with specific applications in controlled heat or mass transfer, immobilization and manipulation of systems (such as pumps, valves, filters, separators and mixers) (Kim *et al.*, 2008), detection of substances, micro-scale chemical reactions, analysis of DNA molecules, cell sorting and manipulation, or development of inkjet printing heads (deMello, 2006).

With their typical dimensions of the order of ten to hundreds of microns, microfluidic devices have the advantage of the reduced consumption of materials and reagents, the reduction of the size of equipment and waste produced, fast analysis, high sensitivity and short reaction times, among other characteristics (Fiorini and Chiu, 2005). Beyond the economic advantages, the use of microfluidic devices allows the development of real microenvironments, which can be useful in biological and chemical applications, and also allows the use of precisely controlled laminar fluid flows (Kim *et al.*, 2008).

The flow around cylinders is an important industrial flow and can be found in many applications involving non-Newtonian fluid flow characteristics as in heat exchangers and in waste water treatment systems (Nishimura, 1986) at the macro-scale and in textile coating processes at the micro-scale, among others. Conscious of its importance and several applications, and due to the geometrical simplicity, Brown and McKinley (1994) reported the selection of the flow around a cylinder with blockage ratio of 50% as a benchmark flow problem in computational rheology, during the VIIIth International workshop on numerical methods for non-Newtonian fluids. At the macro-scale, the viscoelastic flow around a cylinder has been studied experimentally and numerically, from Newtonian-like creeping flow conditions up to the onset of elastic instabilities, where the flow becomes highly three-

dimensional and time-dependent (Manero and Mena, 1981; McKinley *et al.*, 1993; Shiang *et al.*, 1997). Sahin and Wilson (2007) performed 2D and 3D numerical simulations of viscoelastic fluid flow around a confined circular cylinder in a channel with 50% blockage ratio, and were able to capture the nature of the flow patterns up to a Weissenberg number of 1.2. Purely elastic instabilities in viscoelastic fluid flow past a cylinder, hence with negligible inertia, were observed by McKinley (1991) using a constant-viscosity viscoelastic fluid (Boger fluid). More recently, Moss and Rothstein (2010) investigated the flow around a confined cylinder using viscoelastic wormlike micellar solutions, also observed the onset of elastic instabilities. A more detailed review of the research concerning the viscoelastic flow around a confined cylinder at the macro-scale was presented in Chapter 4 (Ribeiro *et al.*, 2013), with a focus on the complex three-dimensionality of the flow patterns.

At the micro-scale, with typical characteristic dimensions below 1 mm, studies concerning the viscoelastic fluid flow around a cylinder are still scarce, and refer to the enhancement of mixing, dispersion and separation processes (Kim *et al.*, 2008) and more recently explore the onset and development of instabilities (Kenney *et al.*, 2013). Microfluidic devices with bluff bodies can be used to promote mixing via chaotic advection (Lynn and Dandy, 2007) provided flows are three-dimensional and advection is sufficiently strong. According to Jayaraj *et al*. (2007) chaotic advection is one of the best methods for efficient mixing in low Reynolds number flows. The curved flow trajectories resulting from the placement of solid obstacles in the microchannel lead to secondary flows which can drive chaotic motion induced by the inertial nonlinearities. This disorganization of ordered flow increases the contact area between different fluid elements, thus enhancing mixing (Kumar *et al.*, 2011). The use of cylindrical obstacles in a properly designed channel (layout and number of obstacles) can increase the mixing performance in microfluidic devices without significantly increasing the pressure drop (Wang, 2004) . For viscoelastic fluids this arrangement may also be advantageous and additional nonlinearities induced by the fluid rheology can become relevant.

The decrease in the size of microfluidic devices reduces significantly the Reynolds number, which scales linearly with the characteristics length scale. For viscoelastic fluids the Deborah number is enhanced, which represents a measure of the elasticity of the flow and scales inversely with the length scale. Clearly, by scaling down the geometry size facilitates achieving very high Deborah number flows, and consequently the investigation of purely

elastic flow instabilities, which require inertialess flow conditions, and are also useful for improving the mixing quality. Recent works on elastic instabilities have shown that a turbulent-like flow arises at arbitrarily small Reynolds numbers, with the chaotic behaviour being induced by the nonlinearities of the fluid, a phenomena that was coined as elastic turbulence (Groisman and Steinberg, 2000; Li *et al.*, 2010; Li *et al.*, 2012).

At the macro-scale the observed phenomena in the flow around cylinders are poorer and less surprising than at the micro-scale, due to the corresponding lower values of the elasticity number that can be achieved. However, the higher Reynolds numbers at the macro-scale introduces inertial effects, thus making the contributions of macro- and micro-scales complementary.

Investigating both macro- and micro-scale versions of the same flow arrangement allow us to access a wider range in the *De-Re* parameter space. Specifically, in this investigation of viscoelastic fluid flow around a confined cylinder at the macro- and micro-scales, the following main objectives are set:

- Perform a direct comparison between the results obtained at the macro- and micro-scales in order to properly assess the contributions of inertia and elasticity in the flow field;
- Explore a wider range of the *De* - *Re* parameter space. At the macro-scale, the results show the combination of inertial and elastic effects and *De* tends to be fairly low, whereas at the micro-scale inertial effects can be nearly eliminated, elastic effects enhanced and the identification of the critical conditions for the onset of purely elastic instabilities directly observed;
- Characterize the viscoelastic fluid flow around a confined cylinder at conditions beyond the onset of purely elastic instabilities;
- Assess the validity of the *continuum* hypothesis at the micro-scale.

To achieve these goals, the complex three-dimensional fluid flow past a confined cylinder centred in a channel is characterized both at the macro- and micro-scales using experimental and numerical methods. On the experimental side, flow visualization, using long time exposure streak photography, and detailed velocity measurements using particle image velocimetry are carried out and compared with results from numerical simulations carried out

using an in-house viscoelastic fluid flow solver (Oliveira *et al.*, 1998; Alves *et al.*, 2003), but here restricted to computations of generalized Newtonian fluids (GNF).

The highly elastic flow conditions achieved at the micro-scale imply that the numerical calculations for viscoelastic fluids are extremely difficult and require robust and accurate time-dependent flow solvers, such as those developed within the host research group (Alves *et al.*, 2003; Afonso *et al.*, 2009). Recent success in predicting numerically a purely elastic instability in a cross-slot flow (Poole *et al.*, 2007) is promising for the future numerical analysis we foresee regarding the time-dependent complex flow past a confined cylinder.

Regardless of the length scale, the fluids flow inside geometrically similar channels with an aspect ratio (*AR* - ratio between the channel depth and the cylinder diameter) of 2.0 and 50% blockage ratio (*BR* – ratio between the cylinder diameter and the channel width), which is one of the typical benchmark problems in computational rheology (Brown and McKinley, 1994). For this work we consider the flows of one Newtonian fluid and one viscoelastic fluid with shear-thinning behaviour, and in all cases the flows were investigated from the Newtonian-like creeping flow conditions (small Reynolds number) up to the onset of time-dependent flow.

Regarding the numerical predictions, for the Newtonian fluid all the experimental data were compared with the corresponding numerical predictions and additional computational results are also presented to analyse flow conditions and details that were not studied experimentally. The non-linear nature of the viscoelastic fluids hinders the achievement of numerical calculations at highly elastic flow conditions, due to the large computational resources required to deal with 3D time-dependent flows as in here. Hence, the numerical investigation was restricted to the use of the Carreau model to assess the effect of shear-thinning, without including elasticity into the analysis.

The remainder of this chapter is organized as follows: the experimental set-up and techniques are described in section 5.2, while section 5.3 presents the rheological characterization of the fluids used in the experiments. The governing equations and a brief outline of the numerical method are described in section 5.4. Section 5.5 presents and discusses the experimental results and provides a comparison with the corresponding numerical simulations. In section 5.6 the main conclusions are summarized.

5.2. Experimental

5.2.1. Experimental set-up

5.2.1.1. *Macro-scale*

The test section made in transparent acrylic is the key element of a closed loop rig, described in detail in Chapter 3 (Ribeiro *et al.*, 2012). The test section, shown in Figure 5.1, has a square cross section with a depth (h) and a width (H) of 20.0 mm. The 10.0 mm diameter cylinder (D) is positioned at the mid plane to define a symmetric geometry with a 50% blockage ratio ($BR = D/H$) and an aspect ratio of 2.0 ($AR = h/D$). The origin of the coordinate system is located at the centre of the cylinder, with the x-axis in the streamwise direction, as illustrated in Figure 5.1.

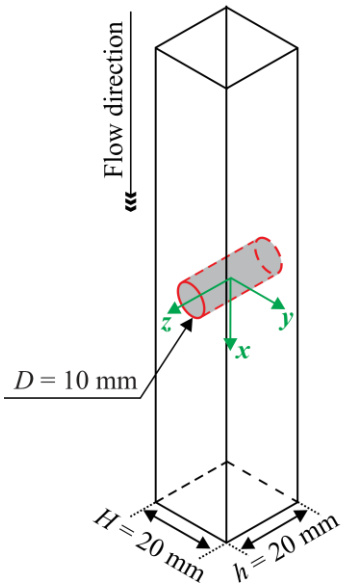

Figure 5.1. Test section at the macro-scale and coordinate system.

The flow is driven by gravity, which limits the maximum allowable flow rate, but efficiently promotes steady and smooth flow conditions, and minimizes the fluid degradation (for polymeric fluids) as described in detail in Chapter 3.

5.2.1.2. *Micro-scale*

The microchannels used in this study were fabricated in polydimethylsiloxane (PDMS) (Sylgard 184, Dow Corning), from a reusable SU-8 mould using standard soft-lithography techniques (McDonald *et al.*, 2000). The final PDMS microchannels were obtained by replication in the SU-8 mould. The cylinder is located at the centre of the microchannel as shown in Figure 5.2. There is one inlet and one outlet located at the ends of the microchannel. The width (H) and depth (h) of the microchannel are similar, H = 212 µm and h = 213 µm, and the cylinder diameter (D) is 105 µm thus providing a microchannel with 50% of blockage ratio and a cylinder aspect ratio of 2.0. Some additional measurements were made using another microchannel with a smaller microfluidic device for the same BR = 50% and aspect ratio of 2.0, and with H = 106 µm, h = 104 µm and D = 53 µm, to widen the explored region on the *De* - *Re* parameter space.

The origin of the coordinate system represented in Figure 5.2 is located at the centre of the cylinder with the same orientation of axes of the macro-scale. A syringe pump (Nemesys, Cetoni GmbH) was used to inject the fluid at constant flow rate in the microchannels. Hamilton syringes with different volumes (10 µl − 1 ml) were used, according to the required flow rate, and were connected to the microgeometries using Tygon tubing with an internal diameter of 0.44 mm.

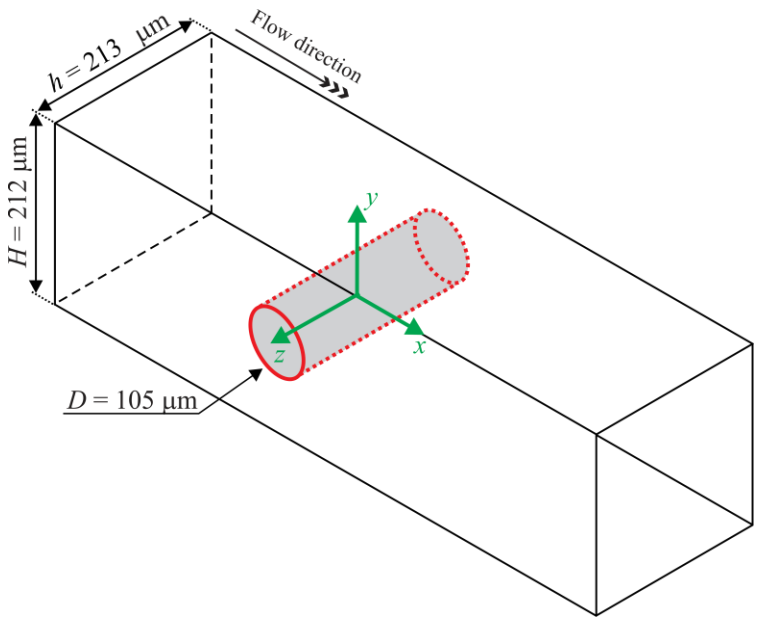

Figure 5.2. Microchannel (micro-scale) and coordinate system.

5.2.2. Experimental techniques

The macro- and micro-scale Newtonian and viscoelastic fluid flows around a confined cylinder were characterized experimentally through flow visualizations and detailed measurements of velocity fields. The flow visualizations used long time exposure streak photography and the velocity fields were measured using Particle Image Velocimetry (PIV) at the macro-scale and using micro-Particle Image Velocimetry (μPIV) at the micro-scale.

5.2.1.1. *Flow visualizations – Macro-scale*

In the visualizations at the macro-scale, the flow was continuously illuminated with two co-planar 635nm 5mW laser diodes (Vector, model 5200-20), both equipped with a cylindrical lens to create a light sheet normal to the cylinder axis. The use of two opposed laser sources minimizes shadows around the cylinder. The reflected light from the illuminated suspended tracer particles (30 ppm w/w of hollow glass spheres with 10 μm diameter – HGS-10, Dantec Dynamics) was captured by a digital camera (CANON EOS 30D), equipped with a macro lens (CANON EF100mm, f2.8), which was placed perpendicularly to the laser light sheets. The exposure time was adjusted depending on the flow rate and varied typically between 1 and 30 s.

5.2.1.2. *Flow visualizations – Micro-scale*

The flow in the microgeometries was visualized using an inverted epifluorescence microscope (DMI 5000M, Leica Microsystems GmbH) and were continuously illuminated by a 100 W mercury lamp. A filter cube (Leica Microsystems GmbH, excitation filter band pass BP 545/30 nm, short pass dichroic at 565 nm, and barrier filter BP 605/75 nm) was used to filter the polychromatic light allowing the excitation light to reach the microgeometries containing the fluid seeded with tracer particles via a 20× microscope objective with numerical aperture NA = 0.4 (Leica Microsystems GmbH). The light emitted by the fluorescent tracer particles was imaged through the same objective onto the CCD of the camera (DFC350 FX, Leica Microsystems GmbH) and the pathlines of the fluid particle were captured using *long* time exposure times. The fluids were seeded with 1.0 μm fluorescent polystyrene tracer particles at a concentration of 100 ppm (Nile Red, Molecular Probes, Invitrogen; Ex/Em: 535/575 nm; ρ: 1050 kg/m^3).

5.2.1.3. *Velocity measurements (particle image velocimetry) – Macro-scale*

The flow plane under investigation was illuminated by a double pulsed Nd:YAG laser (Solo PIV III, New Wave Research), which generates consecutive pairs of light sheets with a wavelength of 532 nm and a maximum energy of 50 mJ per pulse. The two consecutive pulses of light illuminated the suspended particles (same used for flow visualization at the macro-scale), which reflected light allowing the determination of the corresponding velocities from the displacement of the imaged particles in the time interval between the laser pulses. The particle concentration was chosen in order to satisfy the recommended criterion for PIV of having at least 5-10 particles per interrogation area (Adrian, 2005). The time between the two pulses was short and varied between 1.0 ms and 2.0 s, depending on the flow rate. The images were acquired using a digital PIV double frame CCD camera (Flow Sense 2M, Dantec Dynamics) coupled with a Nikon AF Micro lens of 60 mm focal length. A minimum of 50 pairs of images were acquired and used in the ensemble-averaging to determine the velocity field using FlowManager v4.60 software (Dantec Dynamics), using an adaptive-correlation algorithm. The two-dimensional velocity vector map for each image pair was determined, on interrogation windows of 32×32 pixels, with 50% overlap.

5.2.1.1. *Velocity measurements (microparticle image velocimetry) – Micro-scale*

For the μPIV measurements, the microgeometries were placed on the inverted epifluorescence microscope stage and were illuminated using a doubled pulsed Nd:YAG laser (Dual power 65-15, Dantec Dynamics) operating at a wavelength of 532 nm. The time between the two consecutive pulses of light was adjusted according the flow conditions in a range between 50 μs and 6.7 ms. A minimum of 150 pairs of images were acquired for ensemble - averaging using a PIV digital camera (Flow sense 4M, Dantec Dynamics) with a resolution of 2048×2048 pixels operating in double frame mode. The velocity fields were determined by processing the images using the Dynamic Studio V2.3 software (Dantec Dynamics). A $20\times$ microscope objective (NA = 0.4) was used to capture the particle displacement over a wide field of the microchannel. The fluids were seeded with fluorescent polystyrene tracer particles with 0.5 μm in diameter at a concentration of 90 ppm (Nile Red, Molecular Probes, Invitrogen; Ex/Em: 535/575 nm; ρ: 1050 kg/m^3).

5.3. Fluid characterization

A Newtonian fluid and a shear-thinning viscoelastic fluid were used in this work. The Newtonian fluid was an aqueous solution of glycerine (40% w/w) and the shear-thinning fluid was an aqueous solution of polyacrylamide (PAA, M_w = 14x10^6 g/mol) at a weight concentration of 1000 ppm. The fluids were seeded with tracer particles at low concentration (as described in section 5.2) and a biocide was added at a concentration of 25 ppm (kathon LXE, Rohm and Haas) in order to reduce bacteriological growth in the fluids and minimize its degradation. The density (ρ) of the fluids was measured at 293.2 K using a pycnometer and was found to be 1102 kg/m^3 and 1001.5 kg/m^3 for the Newtonian and the shear-thinning fluids, respectively. The rheological characterization of the fluids was made using a rotational shear rheometer (Physica MCR 301, Anton Paar) with a 75 mm cone-plate system with 1º angle to measure in shear flow conditions and using a capillary break-up extensional rheometer (CaBER, Haake CaBER 1, Thermo Scientific) to measure the relaxation time of the fluid in extensional flow.

For the Newtonian fluid, the steady shear viscosity was measured at the reference temperature (T_0 = 293.2 K) and other temperatures in the range between 291.7 K and 294.7 K. The dependency of the shear viscosity on the temperature can be described using an Arrhenius-type equation (Bird *et al.*, 1987). The shear viscosity at the reference temperature is 3.76 mPa.s and is represented in Figure 5.3 as a dashed line.

For the viscoelastic fluid (PAA1000), the flow curve was measured at different temperatures in the range between 283.2 and 303.2 K. The time-temperature superposition principle was used in order to obtain the master curve at the reference temperature (T_0 = 293.2 K). The corresponding shift factor is defined as (Dealy and Plazek, 2009):

$$a_T = \frac{\eta(T)}{\eta(T_0)} \frac{T_0}{T} \frac{\rho_0}{\rho}, \tag{5.1}$$

where η (T_0) is the shear viscosity at the reference temperature T_0, η (T) is the shear viscosity at a temperature T, ρ_0 is the density at the reference temperature and ρ is the density at temperature T. The temperature variation relative to the reference temperature is small for the range of measurements, thus the fluid density does not change significantly, and the shift factor further simplifies to (Dealy and Plazek, 2009):

$$a_T = \frac{\eta(T)}{\eta(T_0)}. \tag{5.2}$$

Figure 5.3 shows the steady shear viscosity master curve, and includes the corresponding fit to a generalized Newtonian fluid (GNF) model. The Carreau model (Carreau, 1972) was used for the viscosity function, which is given by (Bird *et al.*, 1987):

$$\eta = \eta_s + \frac{\eta_0 - \eta_s}{\left[1 + (\Lambda\dot{\gamma})^2\right]^{(1-n)/2}}, \tag{5.3}$$

where the fitted parameters are η_0 = 2.0 Pa.s, η_s = 0.004 Pa.s, Λ = 28 s and n = 0.38.

Note that the cylinder flow experiments at the micro- and macro-scales were carried out at temperatures in the range between 291.7 K and 294.7 K, and the average temperature of the measurements was 293 K.

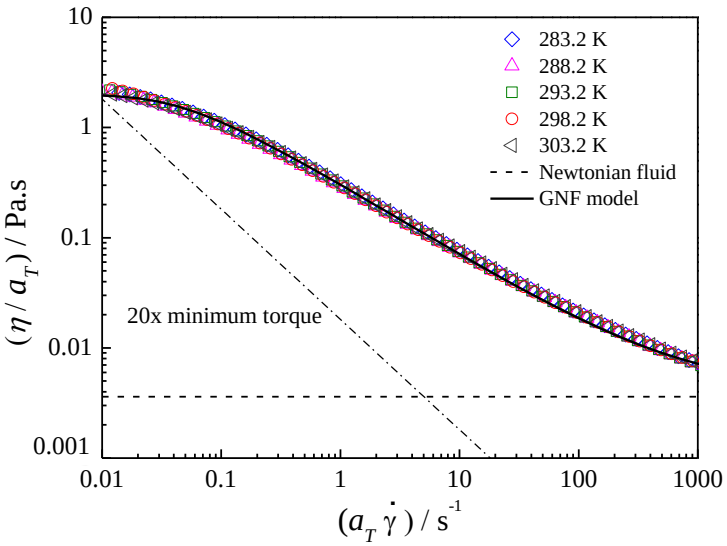

Figure 5.3. Steady shear viscosity of the shear-thinning fluid. The symbols represent the experimental data measured at different temperatures and the solid line the GNF model fit. The minimum measurable shear viscosity, based on 20x the rheometer torque resolution is represented by the dash-dot line.

The relaxation time in extensional flow was measured at the reference temperature (T_0 = 293.2 K) using the CaBER rheometer by fitting the experimental data of the filament thinning in the elasto-capillary regime to the following expression (Entov and Hinch, 1997):

$$\frac{D}{D_0} = e^{-\frac{t}{3\lambda}}, \tag{5.4}$$

where D_0 is the diameter of the filament at the reference time t = 0 and D is the diameter at the time t. These measurements were performed using two circular plates with a diameter of 6 mm, and an initial spacing of 3.0 mm. A final distance of 9.0 mm between the plates was imposed after the step strain which was done within 50 ms.

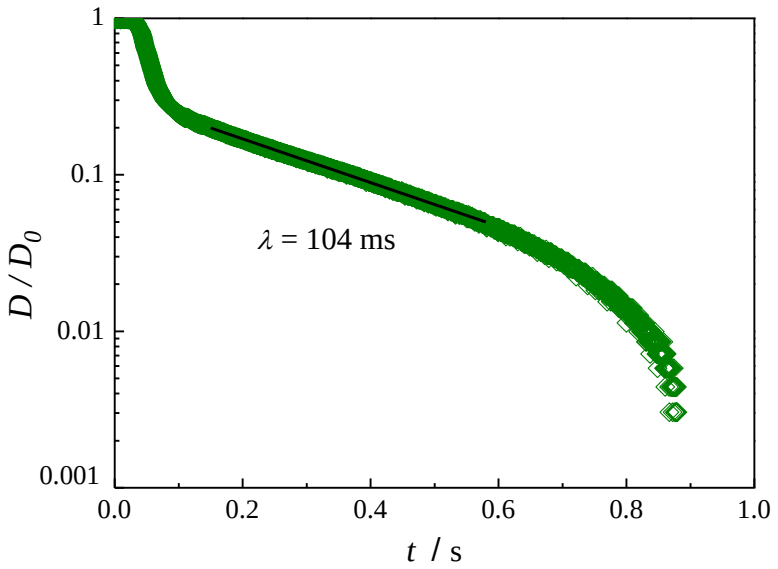

Figure 5.4. Normalized diameter of the filament measured as a function of time using the CaBER rheometer for the shear-thinning fluid PAA1000.

As shown in Figure 5.4 the experimental data of log (D/D_0) vs t was fitted according to Eq. (5.4), and the relaxation time λ = 104 ms was determined for the shear-thinning fluid PAA1000.

The relaxation time determined in extensional flow is thought to be the more appropriate for the flow under study, since the flow in the forward and backward stagnation points is extensionally dominated and therefore will be used on the remaining of this work to quantify the flow elastic behaviour. We note, however, that this relaxation time is probably too small and the *De* values reported in this chapter will also be small. From Figure 5.3 we observe that shear-thinning behaviour starts to occur at $\dot{\gamma} \approx 0.05\ \mathrm{s}^{-1}$, thus an estimate of the relaxation time is shear would be $\lambda \approx 20\,\mathrm{s}$ (typically shear-thinning starts at a shear rate which is approximately the inverse of λ).

5.4. Governing equations and numerical method

The governing equations describing the isothermal laminar flow of an incompressible fluid are the mass conservation,

$$\nabla \cdot \mathbf{u} = 0\,, \tag{5.5}$$

and the momentum equations,

$$\rho\left(\frac{\partial \mathbf{u}}{\partial t} + \nabla \cdot \mathbf{uu}\right) = -\nabla p + \nabla \cdot \boldsymbol{\tau}\,, \tag{5.6}$$

where **u** represents the velocity vector, $\boldsymbol{\tau}$ the extra-stress tensor, t the time and p the pressure. The extra stress tensor is calculated as:

$$\boldsymbol{\tau} = \eta(\dot{\gamma})\,(\nabla \mathbf{u} + \nabla \mathbf{u}^{\mathrm{T}}) = 2\,\eta(\dot{\gamma})\,\mathbf{D}\,, \tag{5.7}$$

where $\eta(\dot{\gamma})$ is the shear viscosity and **D** is the deformation rate tensor. For Newtonian fluids $\eta(\dot{\gamma}) = \eta_s$ is constant.

For the shear-thinning fluid, a generalized Newtonian fluid (GNF) model was used to perform the numerical predictions in all steady flow conditions. The numerical calculations with the GNF model do not describe adequately the flow near the cylinder, where the elastic effects are more relevant, but are able to predict the fully-developed velocity profiles far from the cylinder, where the shear rheology is more relevant. However, since the channels have a square cross section, weak secondary flows can be developed due to the fluid normal stresses (Yue *et al.*, 2008), and this behaviour is not reproduced by the GNF model. The Carreau model was used with the fitted parameters shown in section 5.3.

The numerical method is based on the time-marching version of the SIMPLEC pressure correction algorithm formulated for collocated variables (Oliveira *et al.*, 1998). The discretization of the governing equations is based on central differences for the diffusion terms and on the CUBISTA high-resolution scheme (Alves *et al.*, 2003) for the convective terms. The computational domain was mapped using block-structured meshes with a total number of cells NC = 255200. To generate the mesh the flow domain was divided into 24

blocks and within each block the cells were concentrated near the cylinder region. A zoomed view of the mesh is show in Figure 5.5.

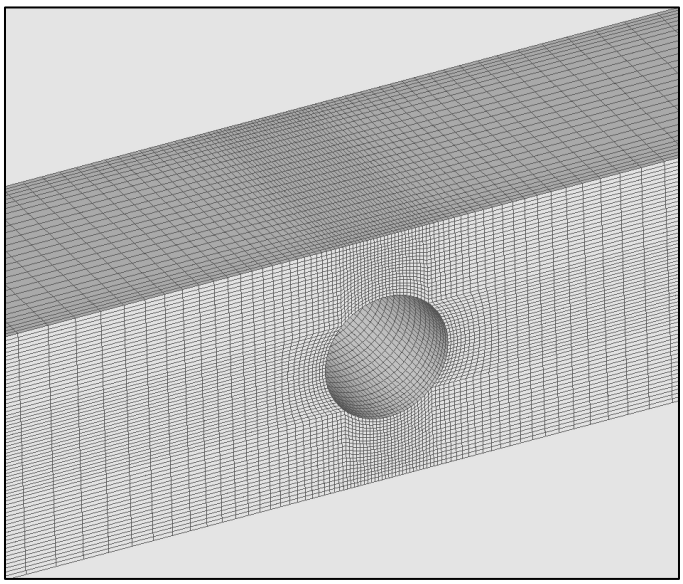

Figure 5.5. Zoomed view of the mesh used in the numerical simulations.

5.5. Results

The fluid flow around a confined cylinder was investigated using flow visualization and detailed velocity measurements using PIV. The measurements were conducted at the symmetry plane $z/R = 0$ at both macro- and micro-scales using the Newtonian fluid and the shear-thinning viscoelastic fluid. In addition to the geometrical parameters previously defined (*AR* and *BR*) the Newtonian fluid flow depends also on the Reynolds number:

$$Re = \frac{\rho U R}{\eta}, \tag{5.8}$$

where U is the bulk velocity away from the cylinder, R is the radius of the cylinder and ρ and η are the density and shear viscosity of the fluid, respectively. For the shear-thinning viscoelastic fluid the shear viscosity is evaluated at a characteristic shear rate, $\dot{\gamma}_c = U / R$.

The flow of viscoelastic fluids also depends on the Deborah number (*De*), which represents the ratio between the characteristic times of the fluid (λ) and of the flow (R/U):

$$De = \frac{\lambda U}{R}. \tag{5.9}$$

For the Newtonian fluid, the Reynolds number varied in the range $2 < Re < 75$, which includes the onset of time-dependent flow due to inertia. For the viscoelastic fluid the studied flows varied in the range $0.02 \leq De \leq 1.0$ at the macro-scale. At the micro-scale the Deborah number varied in the range $0.03 \leq De \leq 9.7$, with the 105 μm cylinder diameter microchannel (Figure 5.2). Additional flow visualizations were carried out in the smaller microfluidic channel (D = 53 μm), where the Deborah number varied in the range $0.35 \leq De \leq 40$. Considering both micro-scale geometries, the Reynolds number for the viscoelastic fluid experiments varied in the range $7\times10^{-6} \leq Re \leq 3\times10^{-2}$. At the micro-scale it was possible to achieve unstable flow conditions while at the macro-scale the flow remained steady at the maximum Deborah number that could be achieved using the gravity-driven experimental set-up described in section 5.2.1.

5.5.1. Flow visualizations

Newtonian fluid

Figure 5.6 compares the experimental and numerical flow patterns in the downstream wake of the cylinder for Newtonian fluid flows at both the macro- and micro-scales for Re = 17.5. At this Reynolds number flow separation occurs downstream of the cylinder, and the recirculation length (L_v) was measured at the symmetry plane (z/R = 0) and its value normalized with the cylinder radius. Comparing the macro- and micro-scale sets at the same Re, we observe that there are no noticeable differences in the recirculation length and flow patterns, as expected. The comparisons between the experimental and numerical results show also good agreement for both sets of data. Note the open nature of the recirculation, which is characteristic of 3D flows. The fluid inside the recirculation moves away from the centre leaving the vortex at the periphery towards downstream.

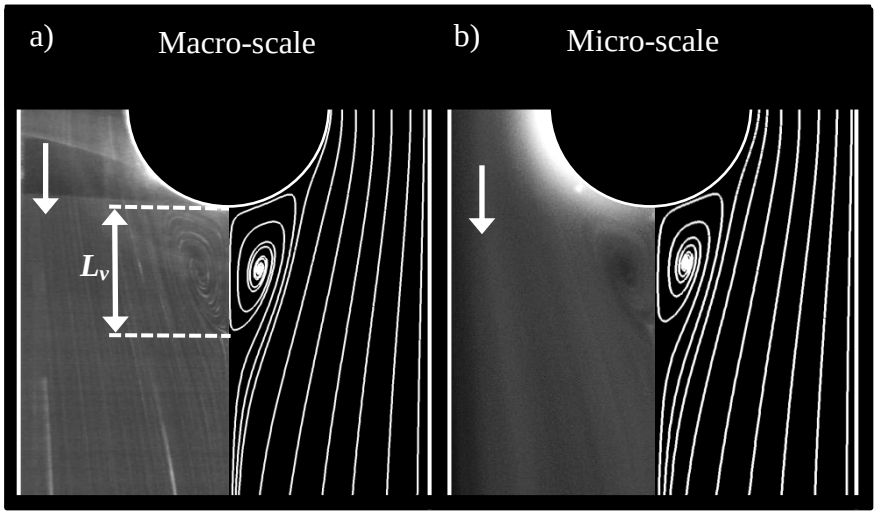

Figure 5.6. Experimental (left hand side) and numerical (right hand side) flow patterns at the symmetry plane ($z/R = 0$) for Newtonian fluid flow at $Re = 17.5$: a) macro-scale; b) micro-scale. The arrow indicates the flow direction.

Based on the whole set of experimental flow visualizations and the corresponding numerical simulations, we plot in Figure 5.7 the variation of the dimensionless recirculation length (L_v/R) with Re for both the macro- and micro-scales, where the symbols represent the experimental data and the line represents the numerical predictions (obviously, the numerical predictions show no differences between computations at both scales because a *continuum* approach is assumed). It is clear that L_v increases with Re and there is a good agreement between the experimental results at the macro- and micro-scales and also with the corresponding numerical predictions. Comparing the macro- and micro-scale results, we can also conclude that there are no differences in the critical Re for the onset of flow separation and for the onset of vortex shedding, which take place at $Re \approx 6$ and $Re \approx 75$, respectively. The variation of L_v with Re is nearly linear up to $Re \approx 40$ and a progressively slower increase of L_v with Re is observed for $Re > 40$. The agreement between both sets of data allows us to conclude that the *continuum* hypothesis is valid, for Newtonian fluid flow, at the length scales used in these experiments.

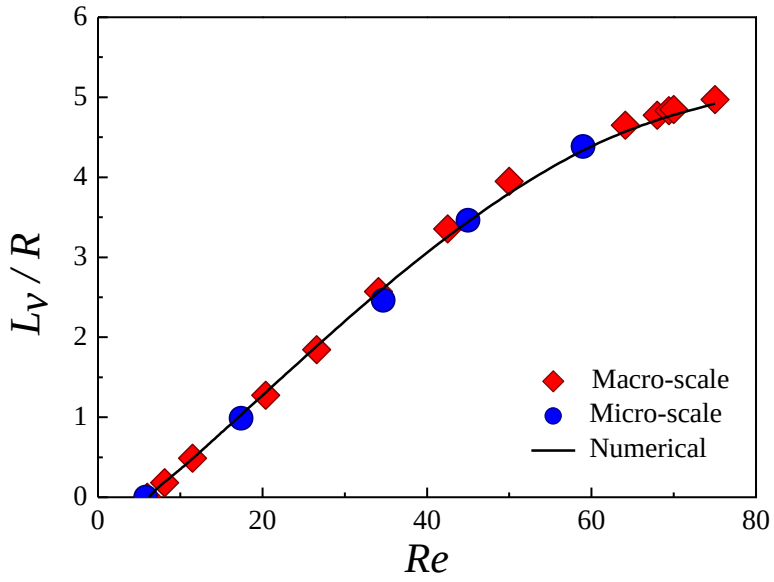

Figure 5.7. Dimensionless vortex length measured downstream of the cylinder at the centreplane (z/R = 0), as a function of the Reynolds number. Comparison between experiments at macro-scale and micro-scale (symbols) and numerical predictions (lines).

Viscoelastic fluid

The influence of the Deborah number on the flow patterns at the symmetry plane (z/R = 0) is illustrated in Figure 5.8 for the shear-thinning viscoelastic fluid at the macro-scale. At low *De* the flow is symmetric upstream and downstream of the cylinder (cf. Figure 5.8a) as for the corresponding Newtonian flow at the low *Re*. However, as *De* increases the flow patterns change progressively and above a critical value of the Deborah number (De_c) an elastic instability arises upstream of the cylinder, near the forward stagnation point and the flow loses symmetry but remains steady (cf. Figure 5.8b). At the macro-scale, the critical Deborah number for the onset of this elastic instability was found to be in the range at $De_c \approx 0.4$ and $Re \approx 0.8$, i.e. although, the Reynolds number is small its value is not negligible. Slight changes on the flow patterns can be also observed downstream of the cylinder as *De* increases (cf. Figure 5.8b). Note that these values of De_c are approximate, because their determination is based on the visual inspection of the experimental pathlines.

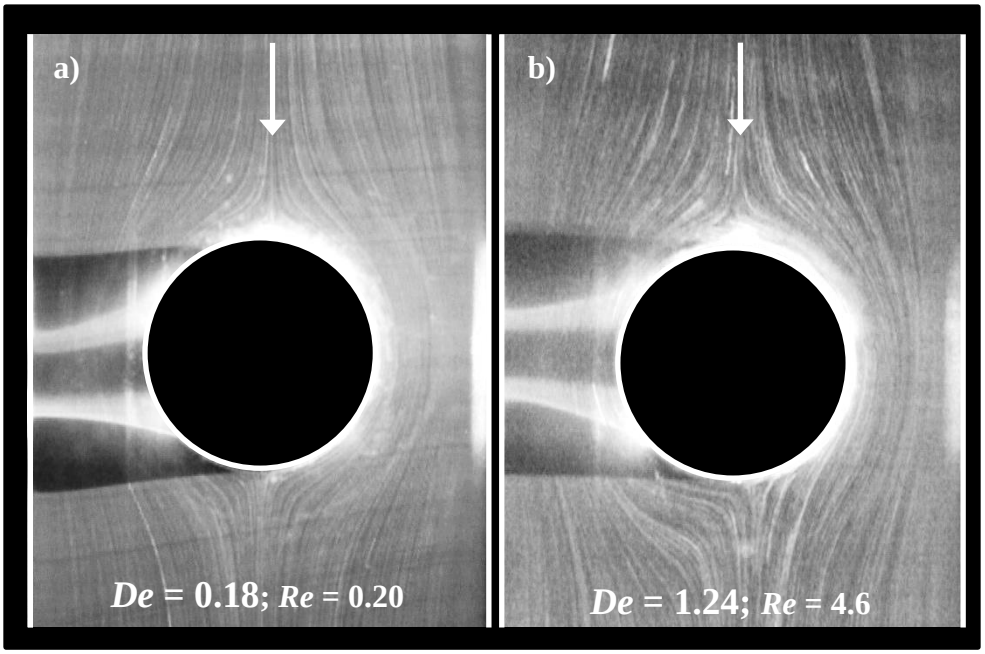

Figure 5.8. Effect of Deborah and Reynolds numbers on the flow patterns observed with the viscoelastic fluid at the symmetry plane ($z/R = 0$) at the macro-scale.

At the micro-scale it was possible to achieve significantly higher Deborah numbers while keeping *Re* small. The influence of *De* on the flow patterns at the symmetry plane ($z/R = 0$) is shown in Figure 5.9. For low *De* the flow is symmetric upstream and downstream of the cylinder (cf. Figure 5.9a), as also observed at the macro-scale. As *De* increases an elastic instability also arises upstream of the cylinder, near the forward stagnation point (cf. Figure 5.9b-d) at a critical value of Deborah number in the range $De_c \approx 0.5$, which is similar to the values found at the macro-scale (but slightly higher), but now the Reynolds number is negligible, of the order of 10^{-4}, suggesting that at the macro-scale the Reynolds number effect was not yet significant, within the uncertainties inherent to the visual technique used to determine the onset of instabilities from the flow pathlines. Although the elastic instability was observed to occur initially upstream of the cylinder, slight changes on the flow patterns can also be observed downstream of the cylinder when *De* increases further, but in all cases the flow remains stable.

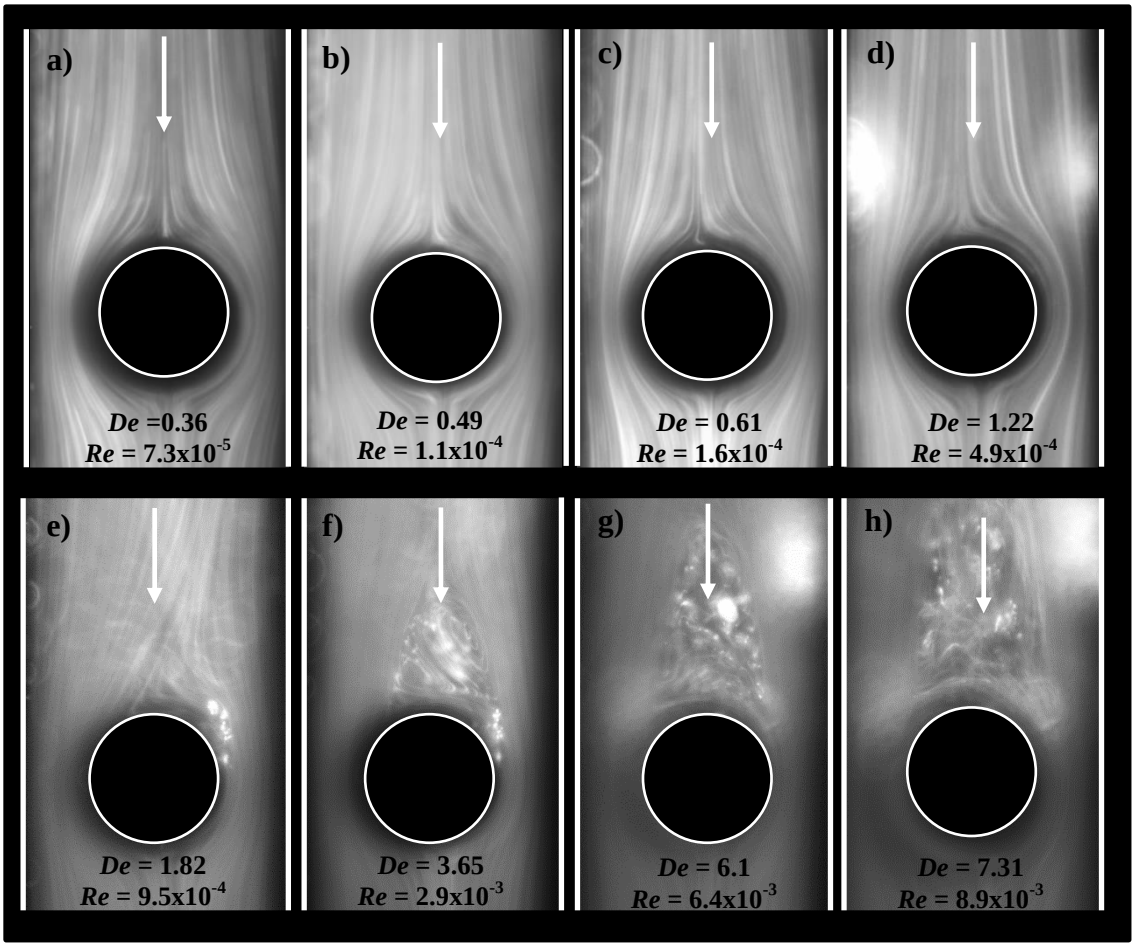

Figure 5.9. Effect of Deborah number on the flow patterns observed with the viscoelastic fluid at the symmetry plane (z/R = 0) at the micro-scale. In d) – h) the flow is unsteady, and the images correspond to the one *instant* of the oscillation cycle.

When the Deborah number is further increased, the steady flow asymmetry intensifies, and eventually the flow becomes unsteady above a second critical *De*. Initially this unsteadiness is characterized by a periodic behaviour. The pictures illustrated in Figure 5.10 pertain to two instants of that cycle of periodicity. As *De* increases further the time-dependent flow loses periodicity and becomes significantly more complex, and eventually chaotic.

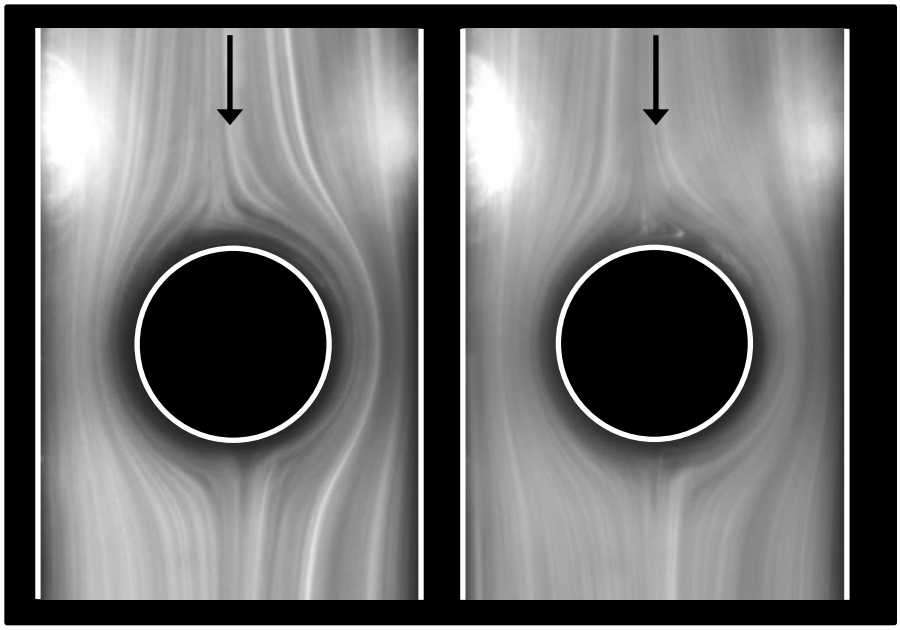

Figure 5.10. Flow patterns observed with the viscoelastic fluid at De = 1.22 (Re = 4.9x10^{-4}) at two *instants* along the flow oscillation at the symmetry plane (z/R = 0) at the micro-scale.

Combining the experiments at the macro- and micro-scales, a wider range in the *De-Re* parameter space can be accessed, allowing the characterization of the viscoelastic fluid flow past a confined cylinder with AR = 2, as illustrated in Figure 5.11. At the micro-scale, curve A represents the results obtained in the larger of the two microchannels, in which most of the experiments were carried out (cf. Figure 5.2) and curve B pertains to the smaller microchannel with cylinder diameter of D = 53 μm and curve C contains the macro-scale data.

At the macro-scale only two regimes were observed for the viscoelastic fluid flow and were categorized as follows: Newtonian-like flow at low *De*; steady asymmetric flow, following the first instability at higher *De*. At the micro-scale, a wider range of *De* was investigated and the different types of flow were categorized in the following flow regimes for increasing *De*: Newtonian-like flow; steady asymmetric flow; unsteady periodic flow; unsteady chaotic-like flow. In the Newtonian-like flow, the flow patterns are symmetric upstream and downstream of the cylinder, the elastic effects are negligible and the flow is reversible (at low *Re* and very low *De* – Stokes flow regime). In the subsequent three regimes the flow is influenced by some elastic instability. First, in the steady asymmetric flow regime, steady elastic flow

instability is observed upstream of the cylinder. As *De* further increases the elastic instability intensifies and the flow becomes unsteady, but periodic in nature until eventually the flow loses periodicity at even higher *De*. Similar flow transitions were observed by Kenney *et al.* (2013) in a microfluidic channel with a cylinder with a larger blockage ratio (*BR* = 65%) and smaller aspect ratio (*AR* = 0.54).

The *De-Re* map shows that the transition from Newtonian-like flow to the steady asymmetric flows occurs at similar critical conditions for both microchannels studied and also for both macro- and micro-scales. The similar behaviour showed both at micro- and macro-scales show that the *continuum* hypothesis is still valid for polymer flow at micro-scale, an important result since the *continuum* hypothesis at the micro-scale has been questioned particularly for flows with long flexible molecules (Oliveira *et al.*, 2012), as those used here.

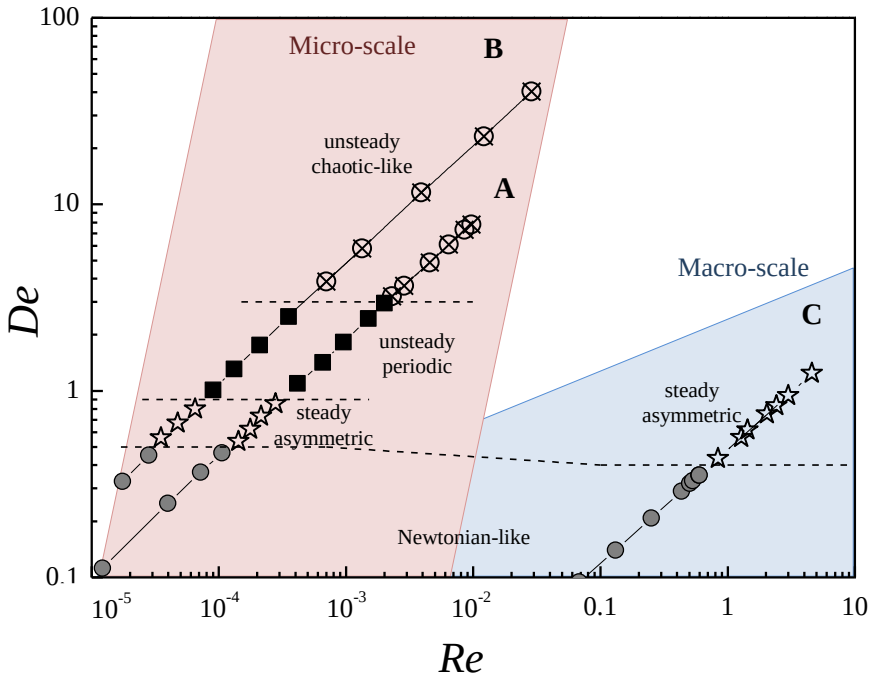

Figure 5.11. *De-Re* flow map for the shear-thinning fluid flowing past a confined cylinder in a square channel (*AR* = 2), with *BR* = 50%. Identification of different flow regimes observed at micro- and macro-scales. The diameter of the cylinder varies 190 times from macro- to micro-scales: (A) *D* = 105 μm; (B) *D* = 53 μm; (C) *D* = 10.0 mm.

5.2.3. Velocity fields

In order to analyse quantitatively the influence of elastic effects upon the viscoelastic fluid flow, the velocity field was measured using PIV. Figures 5.12a and 5.12b plot the streamwise velocity component along the centreline ($y/R = 0$; $z/R = 0$) measured at the macro- and micro-scales, respectively. The numerical results shown in the same figure as solid lines correspond to a Newtonian fluid under creeping flow conditions ($Re \rightarrow 0$) and to the Carreau model flowing at the same flow rate used in the experiments.

The experimental results in Figure 5.12 (symbols) confirm that the flows far upstream and far downstream of the cylinder are fully-developed and agree well with the predictions of the inelastic GNF model. As the fluid approaches the cylinder, the velocity decreases up to the forward stagnation point and this deceleration starts occurring farther away from the cylinder for the higher *De*. For both macro- and micro-scales the deceleration starts at $x / R \approx -8$ (cf. Figure 5.12) for the larger *De* and the dimensionless velocity profiles are qualitatively similar in the upstream region. Downstream of the cylinder, the length required for the flow redevelopment increases with *De*, in agreement with the findings of McKinley *et al*. (1993) and as expected for viscoelastic flows. In contrast to the upstream events, the length required for the flow redevelopment downstream of the cylinder is also significantly influenced by the length scale via the Reynolds number. In the range of *De* represented in Figure 5.12, the velocity profiles are different at the macro- and micro-scale for the same *De*, illustrating that the non-negligible Reynolds number at the macro-scale, leads to longer development lengths downstream of the cylinder.

Comparing the velocity fields of the Newtonian fluid under creeping flow conditions ($Re \rightarrow 0$) with the similar velocity profiles for the viscoelastic fluid, shows that shear-thinning decreases the value of the fully-developed velocity at the centreline. Moreover, we observe a good agreement between the experimental of the fully-developed velocities far from the cylinder, where the steady shear flow conditions are dominant, and the corresponding numerical predictions obtained with the GNF model. This purely viscous GNF model is not able to predict accurately the flow near the cylinder, where the streamwise velocity gradients induce significant extensional effects and the elastic forces become very important, which are not captured by the inelastic GNF model.

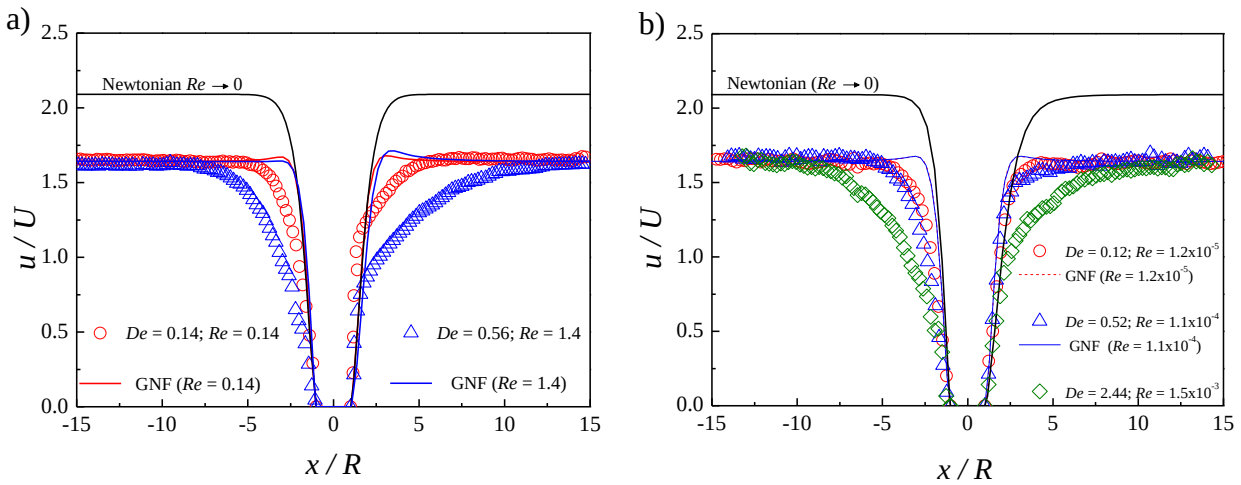

Figure 5.12. Streamwise velocity profile along the centreline (y/R = 0; z/R = 0) for the shear-thinning fluid (symbols) as a function of *De* and comparison with numerical predictions obtained with the GNF model and a Newtonian fluid under creeping flow conditions: a) macro-scale; b) micro-scale.

The influence of the length scale on the flow field upstream and downstream of the cylinder can be better observed in Figure 5.13 which shows the streamwise velocity profile along the centreline (y/R = 0, z/R = 0) at macro- and micro-scales for *De* = 0.027 and *De* = 0.29, respectively. The numerical results (lines) were obtained with the purely-viscous Carreau model.

As also observed in Figure 5.12, the comparison between the experimental and the GNF model numerical results show that far upstream and far downstream of the cylinder the velocity profiles are clearly fully-developed and nearly independent of *De* and on the length scale under study. We note that for fully-developed flow the Reynolds number has no influence, thus the results at the macro- and micro-scale should coincide for the same *De*. We also note that the fully developed velocity profiles depend on the shear rheology of the fluid and can be dependent on *De*, but for the range of shear rates under study the slope of d[log $\eta(\dot{\gamma})$] *vs*. d[log $(\dot{\gamma})$] is nearly constant and thus the dimensionless velocity is nearly independent on *De*.

Upstream of the cylinder, the velocity profiles are found to be nearly independent on the length scale, as was also observed in Figure 5.12. The differences observed upstream of the cylinder between the GNF model numerical predictions and the experimental results in the

region near the cylinder show the influence of the elasticity of the fluid, which is not captured by the GNF model. However, downstream of the cylinder it is clear that the velocity profiles depend significantly on *De* and also on the length scale. For *De* = 0.027, there are no dramatic changes between both scales, which shows that at these flow conditions (or *De*), the inertial effects are not significant for both scales. Given the low elasticity flow conditions in this case, the GNF reproduces reasonably well the complete velocity field. For *De* = 0.29, the required length for the flow redevelopment increases on going from the micro- to the macro-scale but *Re* also increases from 4.3×10^{-5} to 4.3×10^{-1}. For the micro-scale, the higher elasticity of the fluid and the inertialess flow conditions indicate that the required length for the fully-developed velocity is the result of the elasticity of the fluid. The increase in the development length required for the velocity recovery observed at the macro-scale is due to the combined inertial and elastic contributions. The differences observed between the GNF model numerical predictions and the experimental results in the region near the cylinder show again the influence of the elastic contribution of the fluid in the flow which is not captured in the GNF simulations. In fact, the small *Re* in all cases does not influence significantly the predictions of the GNF model, in contrast with the experimental results that are significantly influenced by *Re* for *De* = 0.29, as the comparison between micro- and macro-scales shown in Figure 5.13b suggests.

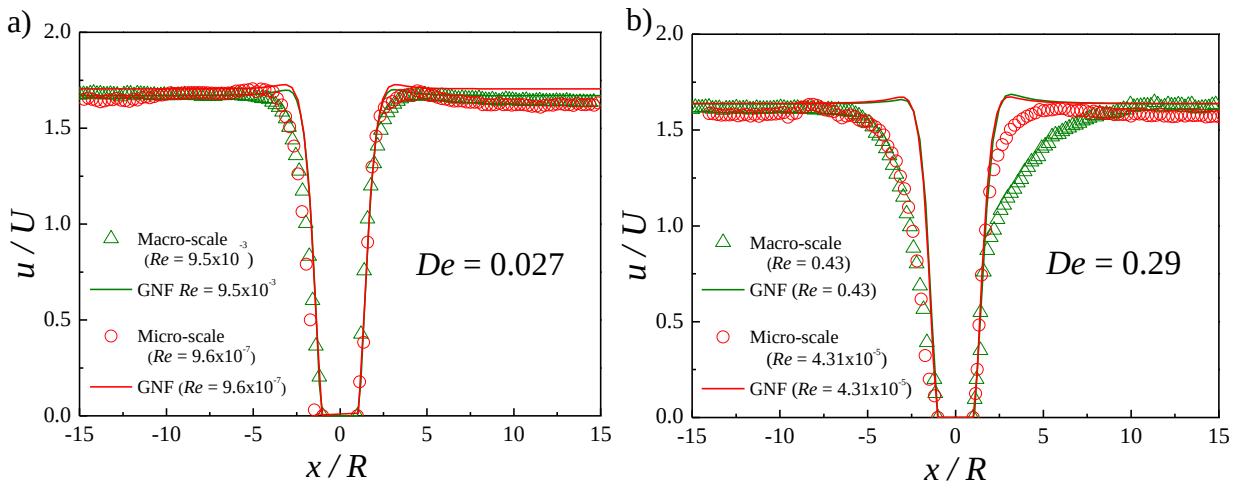

Figure 5.13. Streamwise velocity profile along the centreline (*y/R* = 0, *z/R* = 0) for macro- and micro-scales for the shear-thinning fluid (symbols) and comparison with numerical predictions obtained with the GNF model (lines) for: a) *De* = 0.027; b) *De* = 0.29.

The transverse profiles of the normalized streamwise velocity component were analysed at two upstream (x/R = -6 and -2) and two downstream locations (x/R = 2 and 6) at the symmetry plane (z/R = 0), and are represented in Figure 5.14, both at macro- and micro-scales, considering two *De* flow conditions.

Far upstream of the cylinder, at x/R = -6, both at macro- and micro-scales the flow is only slightly influenced by the presence of the cylinder, but this effect increases with *De*. At x/R = -6 the velocities are always higher on the symmetry plane than near the walls. As we approach the cylinder, the flow becomes significantly influenced by the presence of the cylinder. At x/R = -2 the velocities are significantly higher in the region $|y/R| \approx 1$ - 1.5 than at the symmetry plane. The position of velocity peaks is nearly independent of the length-scale but depends on *De*, approaching the walls as *De* increases while at the same time the peaks becomes more pronounced. At the micro-scale and *De* = 1.03 (Figure 5.14c1) the flow is already slightly asymmetric upstream of the cylinder (cf. Figure 5.11) and very close to the onset of the flow unsteadiness, but in Figure 5.14c1, at x/R = -2 the velocity profiles are still symmetric, showing that at *De* = 1.03 the asymmetry is limited to a small region close to the upstream stagnation point.

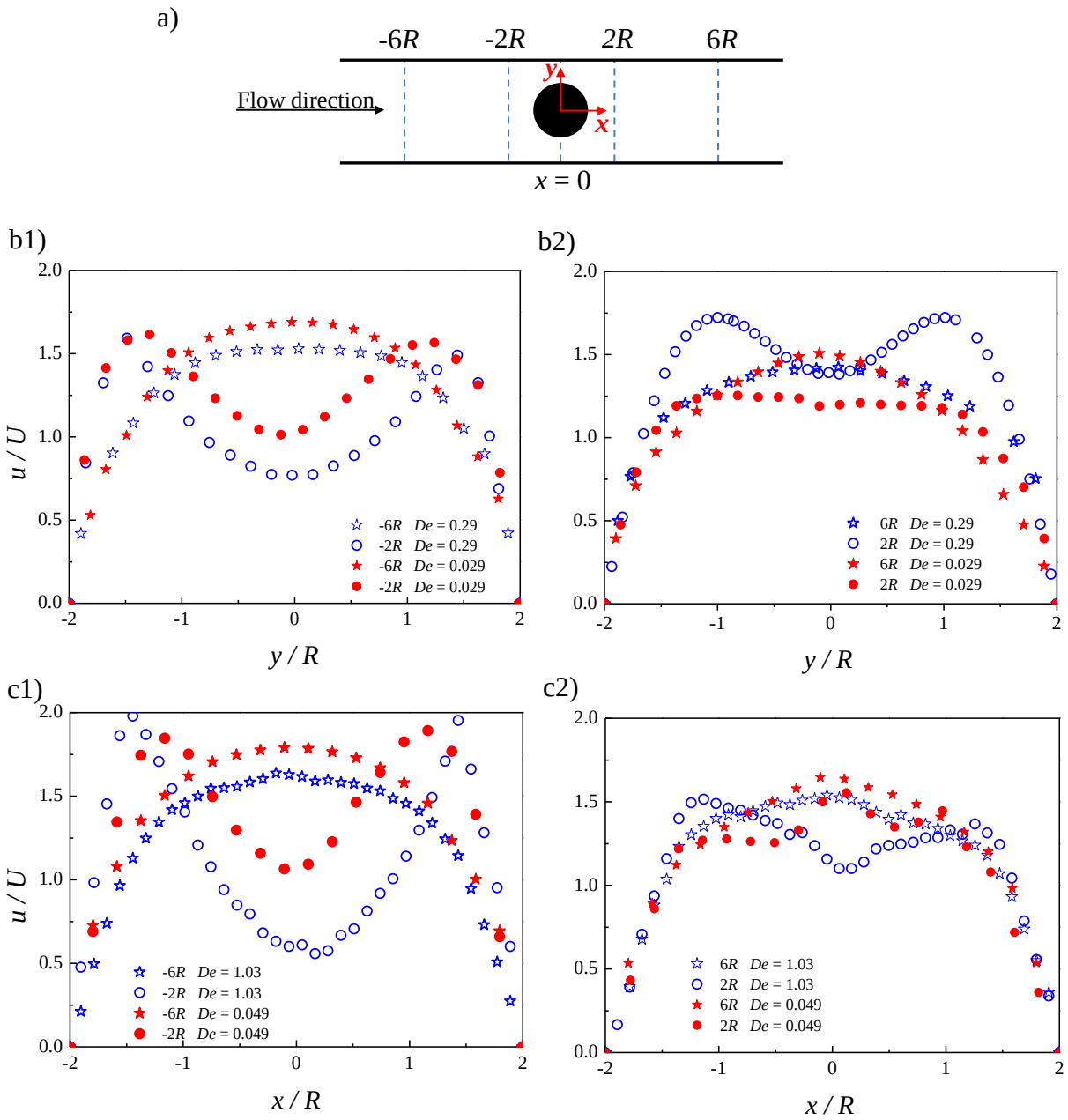

Figure 5.14. (a) Sketch of the location of the transverse profiles at symmetry plane (z/R = 0) of the streamwise velocity component under study both at the (b) macro-scale and at the (c) micro-scale.

Figures 5.14b2 and Figure 5.14c2 show that downstream of the cylinder, at x/R = 2, the flow is still influenced by the presence of the cylinder and the intensity of this influence is strongly dependent of *De*. At this location the velocities are significantly higher in the region $|y/R| \approx 1$ - 1.5 than near the side walls for the higher *De*, while for the lower *De* the flow is only slightly influenced by the cylinder at this downstream location. At the micro-scale and *De* = 1.03 (Figure 5.14c2) the flow is asymmetric, and at x/R = 2 the velocity profile is still

slightly asymmetric. Far downstream of the cylinder, at x/R = 6, the velocities are always higher on the centreline than near the side walls and are symmetric at both *De*. The redevelopment of the velocity profile downstream of the cylinder occurs further downstream for the higher *De*, in agreement with the profiles shown earlier in Figure 5.12 for the streamwise velocity along the centreline.

In Figure 5.15 we plot the velocity profiles show in Figure 5.14, but in a 3D view, which helps the reader to better visualize spatially the changes in the streamwise velocity profile along the channel, for the centreplane z/R = 0.

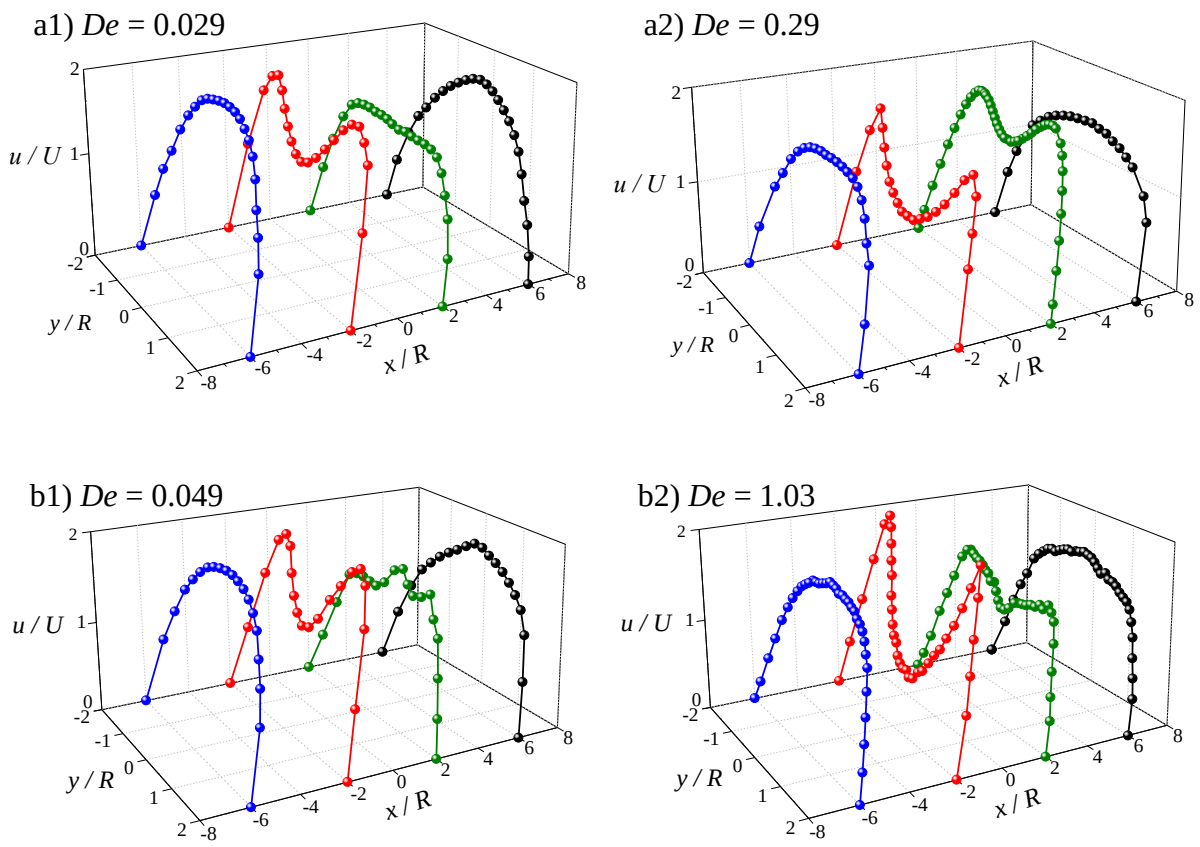

Figure 5.15. 3D representation of the streamwise variation of the transverse profiles of the streamwise velocity component at the z/R = 0: a) macro-scale; b) micro-scale.

5.6. Conclusions

An experimental and numerical investigation was carried out for the macro- and micro-scale flows of a Newtonian fluid and a shear-thinning viscoelastic fluid around a confined cylinder centred in a square duct with 50% blockage ratio. The flow conditions studied varied from creeping flow conditions up to the onset of time-dependent flow for the Newtonian fluid and varied from negligible elastic effects conditions (low *De*) up to the onset of unstable flow for the viscoelastic fluid. The experiments relied on flow visualizations, using long time exposure streak photography, and detailed velocity measurements using PIV and micro-PIV.

The numerical calculations were carried out with a finite volume numerical method and the predictions for the Newtonian fluid compare very well with the experimental results. For the shear-thinning viscoelastic fluid, the numerical calculations were performed using an inelastic shear-thinning GNF model, so that the differences between experimental and numerical results are due to elastic effects in the experiments. The inelastic fluid flow simulations were accurate far from the cylinder, where the steady shear flow properties are dominant.

For the Newtonian fluid flow there are no considerable changes as we move from macro- to micro-scale considering the same Reynolds number flow conditions. However, a distinct behaviour is observed for viscoelastic fluid flow where the elasticity number plays an important role. Through the flow visualizations taken for the viscoelastic fluid, a wide range on the *De-Re* map could be probed, allowing the identification of four different flow regimes: Newtonian-like flow; steady asymmetric flow; unsteady periodic flow; complex unstable flow. Despite the differences on the elasticity number, due to the different length scales, the critical Deborah number (De_c) for the onset of the first elastic instability upstream the cylinder was found to be $De_c \approx 0.4$ at the macro-scale and $De_c \approx 0.5$ for the micro-scale, thus inertial effects on this transition are still small at this *De* even at the macro-scale.

Regardless of the length scale, the deceleration of the velocity upstream of the cylinder and the required length for the fully-developed velocity downstream of the cylinder depend on *De*, which highlights the influence of viscoelasticity. Moreover, for the same Deborah number, the deceleration upstream is nearly independent on the length scale, but downstream of the cylinder the length required to achieve the fully-developed velocity increases as we move from the micro-scale to the macro-scale, due to the combination of elastic and inertial

effects at the macro-scale. The experimental results suggest that the *continuum* hypothesis is valid at the micro-scale, even for the long flexible polymer molecule used in this work.

References

Adrian, R.J., 2005. Twenty years of particle image velocimetry. Exp Fluids 39, 159-169.

Afonso, A., Oliveira, P.J., Pinho, F.T., Alves, M.A., 2009. The log-conformation tensor approach in the finite-volume method framework. J Non-Newton Fluid Mech 157, 55-65.

Alves, M.A., Oliveira, P.J., Pinho, F.T., 2003. A convergent and universally bounded interpolation scheme for the treatment of advection. Int J Numer Meth Fl 41, 47-75.

Bird, R.B., Armstrong, R.C., Hassanger, O., 1987. Dynamics of polymeric liquids. John Wiley and Sons, New York.

Brown, R.A., McKinley, G.H., 1994. Report on the VIIIth Int Workshop on numerical - methods in viscoelastic flows. J Non-Newton Fluid Mech 52, 407-413.

Carreau, P.J., 1972. Rheological Equations from Molecular Network Theories. Trans. Soc Rheol 16, 99-127.

Dealy, J., Plazek, D., 2009. Time-temperature superposition. Rheology Bulletin 18, 16-31.

deMello, A.J., 2006. Control and detection of chemical reactions in microfluidic systems. Nature 442, 394-402.

Entov, V.M., Hinch, E.J., 1997. Effect of a spectrum of relaxation times on the capillary thinning of a filament of elastic liquid. J Non-Newton Fluid Mech 72, 31-53.

Fiorini, G.S., Chiu, D.T., 2005. Disposable microfluidic devices: fabrication, function, and application. Biotechniques 38, 429-446.

Groisman, A., Steinberg, V., 2000. Elastic turbulence in a polymer solution flow. Nature 405, 53-55.

Jayaraj, S., Kang, S.M., Suh, Y.K., 2007. A review on the analysis and experiment of fluid flow and mixing in micro-channels. J Mech Sci Technol 21, 536-548.

Kenney, S., Poper, K., Chapagain, G., Christopher, G.F., 2013. Large Deborah number flows around confined microfluidic cylinders. Rheol Acta 52, 485-497.

Kim, S.M., Lee, S.H., Suh, K.Y., 2008. Cell research with physically modified microfluidic channels: A review. Lab Chip 8, 1015-1023.

Kumar, V., Paraschivoiu, M., Nigam, K.D.P., 2011. Single-phase fluid flow and mixing in microchannels. Chemical Engineering Science 66, 1329-1373.

Li, F.C., Kinoshita, H., Li, X.B., Oishi, M., Fujii, T., Oshima, M., 2010. Creation of very-low-Reynolds-number chaotic fluid motions in microchannels using viscoelastic surfactant solution. Exp Therm Fluid Sci 34, 20-27.

Li, X.B., Li, F.C., Cai, W.H., Zhang, H.N., Yang, J.C., 2012. Very-low-Re chaotic motions of viscoelastic fluid and its unique applications in microfluidic devices: A review. Exp Therm Fluid Sci 39, 1-16.

Lynn, N.S., Dandy, D.S., 2007. Geometrical optimization of helical flow in grooved micromixers. Lab Chip 7, 580-587.

Manero, O., Mena, B., 1981. On the Slow Flow of Viscoelastic Liquids Past a Circular-Cylinder. J Non-Newton Fluid Mech 9, 379-387.

McDonald, J.C., Duffy, D.C., Anderson, J.R., Chiu, D.T., Wu, H.K., Schueller, O.J.A., Whitesides, G.M., 2000. Fabrication of microfluidic systems in poly(dimethylsiloxane). Electrophoresis 21, 27-40.

McKinley, G.H., 1991. Nonlinear dynamics of viscoelastic flows in complex geometries, PhD Thesis. Department of Chemical Engineering. Massachusetts Institute of Technology, Cambridge.

McKinley, G.H., Armstrong, R.C., Brown, R.A., 1993. The Wake Instability in Viscoelastic Flow Past Confined Circular-Cylinders. Philos T Roy Soc A 344, 265-304.

Moss, G.R., Rothstein, J.P., 2010. Flow of wormlike micelle solutions past a confined circular cylinder. J Non-Newton Fluid 165, 1505-1515.

Nishimura, T., 1986. Flow across tube banks. In: Cheremisinoff, P. (Ed.), Encyclopedia of Fluid Mechanics. Gulf Publishing Company, pp. 763-785.

Oliveira, M.S.N., Alves, M.A., Pinho, F.T., 2012. Microfluidic flows of viscoelastic fluids. Chapter 6 in Transport and Mixing in Laminar Flows: From Microfluidics to Oceanic Currents. Wiley - VCH Verlag.

Oliveira, P.J., Pinho, F.T., Pinto, G.A., 1998. Numerical simulation of non-linear elastic flows with a general collocated finite-volume method. J Non-Newton Fluid Mech 79, 1-43.

Poole, R.J., Alves, M.A., Oliveira, P.J., 2007. Purely elastic flow asymmetries. Phys Rev Lett 99, 164503.

Ribeiro, V.M., Coelho, P.M., Pinho, F.T., Alves, M.A., 2012. Three-dimensional effects in laminar flow past a confined cylinder. Chem Eng Sci 84, 155-169.

Ribeiro, V.M., Coelho, P.M., Pinho, F.T., Alves, M.A., 2013. Viscoelastic fluid flow past a confined cylinder: three dimensional effects and stability Chem Eng Sci.

Sahin, M., Wilson, H.J., 2007. A semi-staggered dilation-free finite volume method for the numerical solution of viscoelastic fluid flows on all-hexahedral elements. J Non-Newton Fluid Mech 147, 79-91.

Shiang, A.H., Lin, J.C., Öztekin, A., Rockwell, D., 1997. Viscoelastic flow around a confined circular cylinder: measurements using high-image-density particle image velocimetry. J Non-Newton Fluid Mech 73, 29-49.

Wang, H.Z., 2004. Passive Mixing in Microchannels with Geometric Variations. Swinburne University of Technology, Australia.

Yue, P.T., Dooley, J., Feng, J.J., 2008. A general criterion for viscoelastic secondary flow in pipes of noncircular cross section. J Rheol 52, 315-332.

Chapter 6

Aspect ratio effect upon the viscoelastic fluid flow past a confined cylinder in microfluidic devices

Abstract

An experimental study of Newtonian and viscoelastic fluid flow around a confined cylinder in microfluidic devices was carried out to investigate the influence of the aspect ratio (AR), defined as the ratio between the microchannel depth and the cylinder diameter. The aspect ratio was varied between 0.55 and 2.0 for a blockage ratio (BR) of 50%, which is the ratio between the cylinder diameter and the microchannel width. The flow conditions varied in a wide range of flow rates up to the onset of time-dependent flow. The characterization of the complex 3D flow past the cylinder was carried out with flow visualizations using streak photography and detailed velocity measurements using micro-particle image velocimetry. The experimental results compared well with 3D numerical calculations, for Newtonian, Carreau and Oldroyd-B models, calculated with a finite volume code.

For the Newtonian fluid flow there is no dramatic change as we move from the macro- to the micro-scale for the same Reynolds number, AR and BR. For the Boger fluids the Newtonian-like and the steady divergent streamlines flow regimes were observed for all AR. For the shear-thinning fluid four flow regimes were identified with progressively increasing De. The critical conditions for the flow regime transitions were found to depend moderately on AR. The velocity profiles upstream and downstream of the cylinder are found to be dependent on the geometric confinement and on elasticity of the fluid.

6.1. Introduction

Recent progress in understanding fluid flow phenomena at the micro-scale, together with a significant cost reduction in microfabrication techniques led over the past decade to the development of complex lab-on-a-chip systems or micro total analysis systems (μTAS) and consequently to the scale-down of laboratory functions and processes with application in biological and chemical sciences, medicine and engineering. This miniaturization allows the implementation and integration of microfluidic devices with specific applications in the control and manipulation of systems (such as pumps, valves, filters, separators and mixers), detection techniques, micro chemical reactions, analysis of DNA molecules, or in cell sorting and manipulation (deMello, 2006). Microfluidic devices, with characteristic dimensions of the order of tens to hundreds of microns, have the advantages of a reduced consumption of materials and reagents, the reduction of the size of equipment, fast analysis, high sensitivity, short reaction times, and waste reduction, among others (Fiorini and Chiu, 2005).

Fluid flows of complex liquids, such as polymer solutions (Oliveira and McKinley, 2005), blood (Tovar-Lopez *et al.*, 2010; Sousa *et al.*, 2011) or saliva (Helton and Yager, 2007; Haward *et al.*, 2011) are also important applications fostering the development and optimization of microfluidic systems. The small size of microfluidic devices leads to a significant reduction in the Reynolds number (*Re*), but also originates a strong increase of the Deborah number (*De*), a measure of the importance of elastic effects in the flow of complex fluids. The Deborah number (*De*) is defined as the ratio between the relaxation time of the fluid and a characteristic time scale of the flow (Dealy, 2010; Poole, 2012). Reducing the scale of the geometry decreases the characteristic time scale of the flow, thus creating highly elastic flow conditions, difficult or even impossible to attain at macro scales, allowing the study of unexplored regions of the *De*-*Re* parameter space with polymer solution. Given the highly elastic flow conditions that naturally arise at the micro-scale using viscoelastic fluids, purely elastic instabilities often occur, which can be exploited in order to enhance mixing.

Several studies concerning microfluidic devices focus in micromixing, which is only one aspect on the vast landscape of microfluidics applications, as discussed in the recent review of Suh and Kang (2010). The micromixers can be categorized as passive or active mixers. Active mixing requires the use of an external source of energy such as electrokinetic, magnetic, acoustic, pressure disturbance or thermal (Kumar *et al.*, 2011). The disadvantages of active mixing are the higher energy consumption, the possible damage of the samples (e.g. long molecules, or biological samples), especially if the local rates of deformation are very

high (Nguyen *et al.*, 2008), the increased complexity of the devices since these systems often required active control and consequently a more difficult integration with other components (Asgar *et al.*, 2008). Several studies concerning active mixing refer to new techniques for microfluidic pumping and mixing using cylindrical obstacles (Bazant and Squires, 2004; Squires and Quake, 2005; Meisel and Ehrhard, 2006; Hsieh and Huang, 2008; Jeon and Shin, 2009).

In passive mixers, the fluid flow promotes mixing through chaotic advection, parallel lamination or injection, and subsequent molecular diffusion over much reduced scales. According to Jayaraj *et al*. (2007), chaotic advection is the best principle for efficient mixing in viscoelastic flows, and is a consequence of the increased contact surface area between fluid elements. This can be obtained with the use of abrupt contractions or solid obstacles placed in the microchannel, to create secondary transverse flows that eventually induce chaotic fluid motion, due to the onset of flow instabilities (Stroock *et al.*, 2002; Hessel *et al.*, 2005; Kumar *et al.*, 2011).

Gan *et al*. (2007) showed that flows in microfluidic devices with abrupt contractions lead to the appearance of flow instabilities, which are an effective platform for promoting mixing at the micro-scale. Improvements in mixing also depend strongly on the rheology of the liquids, in addition to the geometry topology and the number and arrangement of obstacles placed in the microchannels. Concerning the effect of the fluid rheology, large elastic normal stresses and stress gradients are generated with viscoelastic fluids, which can trigger flow instabilities and enhance mixing (Stone *et al.*, 2004). The studies concerning the development of micromixers with solid obstacles use different layouts as cylindrical obstacles (Wang *et al.*, 2001; Wang *et al.*, 2002b, a; Lin *et al.*, 2003; Wang *et al.*, 2003a, b; Wang, 2004), square obstacles (Asgar *et al.*, 2008; Nguyen *et al.*, 2008; Li *et al.*, 2010; Miranda *et al.*, 2010; Li *et al.*, 2012), triangular obstacles (Sheen *et al.*, 2007) or diamond-like obstacles (Bhagat *et al.*, 2007; Tseng *et al.*, 2011).

Highlighting the use of cylindrical obstacles in micromixers, the study of Wang *et al*. (2002b) states that staggered layouts of the cylindrical obstacles can enhance microfluidic mixing, while aligned layouts have little effect on mixing. According to Wang (2004), a properly designed microfluidic set-up using cylindrical obstacles can increase mixing performance without significantly increasing the pressure drop, which is very important to reduce energy consumption, prevent the degradation of the fluids and avoid damage of the microfluidic device. A common feature that is crucial to the development of elastic

instabilities is the presence of curvilinear streamlines (Pakdel and McKinley, 1996). Li *et al*. (2010) studied the chaotic motion of viscoelastic fluid in microchannels with three kinds of designs: a cylindrical pillar block, a disc cavity and a couple of interconnected part-rings. For the setup with a cylindrical pillar block, with a blockage ratio (*BR* – ratio between the cylinder diameter and the width of the rectangular channel) of 50% and an aspect ratio (*AR* - ratio between the length and diameter of the cylinder) of 0.4, an irregular vortex structure appears in the vicinity of the upstream stagnation point of the cylinder. According to the recent review of Li *et al.* (2012), the flow instabilities and subsequent chaotic flows that were observed at the macroscale indicated that the flexible macromolecular chains underwent unstable deformations in flow regions with streamline curvature. With the downscaling of devices, the elastic instabilities inherited from macroscale flows are amplified due to the significantly higher rates of deformation achieved, in combination with particular designs that induce streamline curvature. In addition, flow instabilities can appear with complex fluids due to properties other than elasticity, such as extreme shear thinning and shear banding in micellar solution. As these elastic instabilities becomes stronger they persist over a wide range of spacial and time scales, and the regime of elastic turbulence is observed, given the similarities with inertial instabilities (Groisman and Steinberg, 2000; Larson, 2000).

Cylindrical obstacles have also been used by Wang *et al.* (2011) to optimize the micromixing flow in microbial fuel cells. A rise in pressure drop with the Reynolds number was observed, and flow mixing was enhanced when a lower aspect ratio cylinder was used, i.e., the side walls and the resulting shear stress have a positive effect on mixing.

The flow past arrays of cylinders in channels has also been proposed for several applications at the microscale, providing a medium where the fluid elements experience a mixed shear and extensional flow, very much as occurs in porous media. It has been used to investigate the behaviour of DNA molecules (or other biomolecules) in such mixed flow kinematics by Teclemariam *et al.* (2007), since it can produce highly stretched DNA which may be used for on-chip sequencing applications (Chan *et al.*, 2004).

Microfluidic devices with arrays of cylindrical obstacles have also important applications in separation of particles by size (Huang *et al.*, 2004; Morton *et al.*, 2008; Inglis, 2009; Inglis *et al.*, 2011), in the separation of different types of blood cells (Davis *et al.*, 2006) and DNA separation, or in biological samples separation (Yi *et al.*, 2005; Eghbali *et al.*, 2009). In this context, recent studies about the microfluidic flow around non-porous and porous cylinders

have been useful in the development of applications for diagnosis of diseases and identification of viruses, such as HIV and cancer, among others (Fachin *et al.*, 2010; Chen *et al.*, 2011; Fachin *et al.*, 2011). Microfluidic devices with arrays of cylindrical obstacles can also be used in the miniaturization of chromatographic techniques (Fiorini and Chiu, 2005).

The complex interplay that arises between the viscoelasticity of complex fluids and the geometrical characteristics of the flow is a key for efficient mixing in microchannels with cylindrical obstacles. Understanding the flow dynamics in different aspect ratio devices with a cylinder placed in a rectangular duct with 50% blockage ratio is the main contribution from this work. This provides qualitative and quantitative data regarding 3D effects of the flow field. For that purpose, flow visualizations using streak photography and detailed velocity measurements using μPIV were carried out in micro-geometries having different aspect ratios for a Newtonian fluid, a shear-thinning fluid and a Boger fluid, from creeping flow conditions up to the onset of flow instabilities. In addition, complementing numerical simulations with a variety of fluid models are also presented.

The remainder of this chapter is organized as follows: the experimental set-up and techniques are described in section 6.2. The governing equations and a brief outline of the numerical method employed for the calculations of the Newtonian and non-Newtonian fluid flow are described in section 6.3. Section 6.4 presents the rheological characterization of the fluids used. Section 6.5 presents and discusses the experimental results and compares them with the corresponding numerical simulation results. In section 6.6 the main conclusions are summarized.

6.2. Experiments

6.2.1. Microchannels: fabrication and geometry

The microchannels used were fabricated in polydimethylsiloxane (PDMS) (Sylgard 184, Dow Corning), from an SU-8 reusable mould, using standard soft-lithography techniques (McDonald *et al.*, 2000). The final PDMS microchannels obtained by replication in the SU-8 mould were imaged in an inverted microscope.

The microgeometries with a confined cylinder placed at the centreplane of the microchannel are composed of one inlet and one outlet located at the extremes of the devices. The microchannel width (H) and the cylinder diameter (D) were kept constant and equal to

H = 212 µm and D = 105 µm, respectively, corresponding to a blockage ratio of 50% (D/H = 0.50), as shown in Figure 6.1a. The depth (h) of the microchannels was varied, taking the values of h = 213 µm, 105 µm and 58 µm to provide the following aspect ratios: $AR = h/D$ = 2.0, 1.0 and 0.55, respectively. The microchannel dimensions were measured using scanning electron microscopy (SEM). Figure 6.1b presents SEM images of the microchannel with AR = 0.55, illustrating the good manufacturing quality with well-defined vertical walls and a smooth well shaped cylinder.

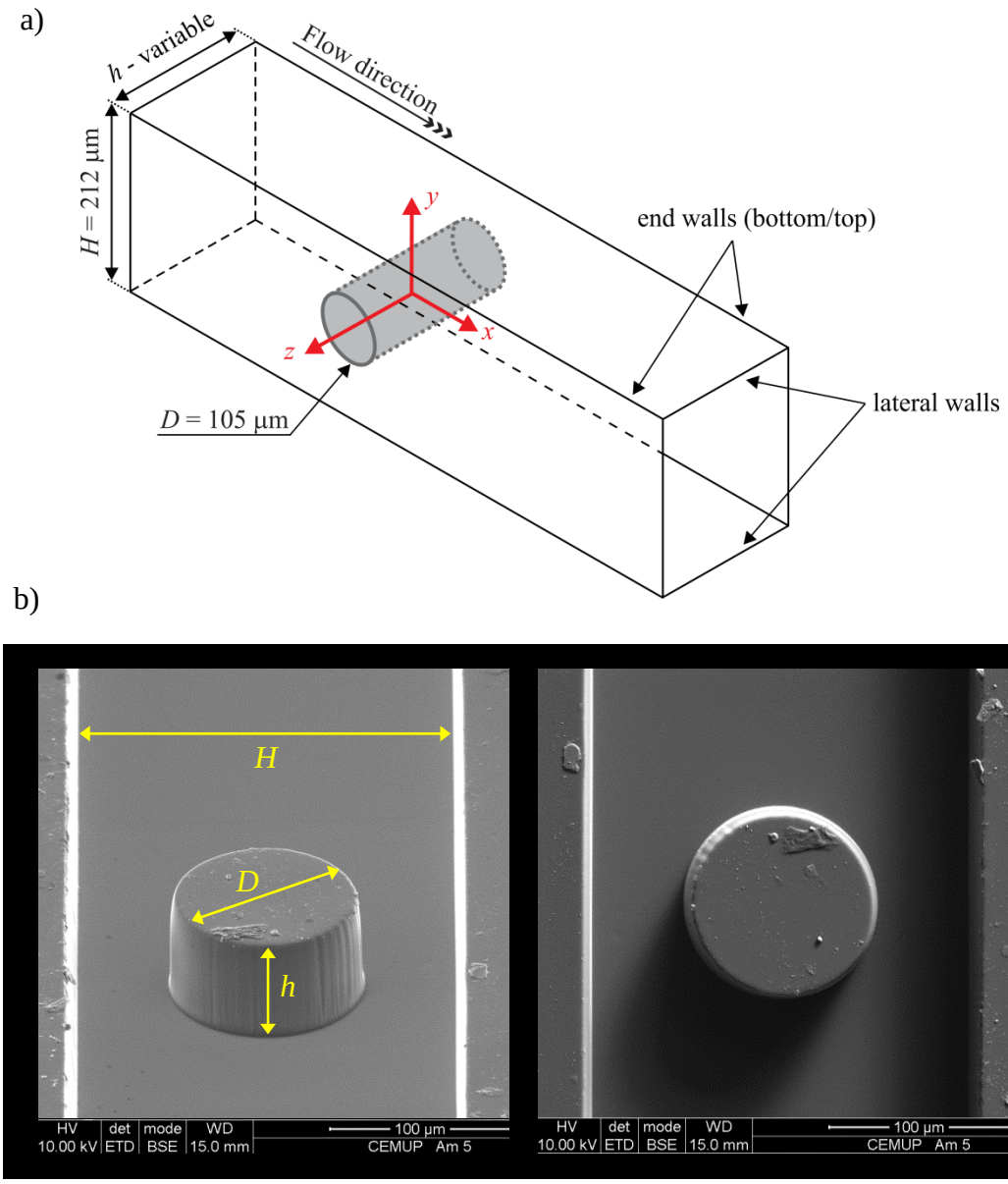

Figure 6.1. a) Illustration of the microfluidic device; b) SEM images of the microchannel with h = 58 µm (AR = 0.55).

The set-up with the microchannel included a syringe pump (Nemesys, Cetoni GmbH) which was used to inject the fluid and control the flow rate in the microchannels. Syringes (Hamilton) with different volumes (10 µl – 500 µl) were used, according to the desired flow rate, and were connected to the microgeometries using Tygon tubing with an internal diameter of 0.44 mm.

6.2.2. Experimental techniques

The flow around the confined cylinder in the microchannel was characterised using flow visualizations and microparticle image velocimetry (µPIV). The long time exposure streak photography allows the visualization of the flow patterns and the µPIV technique was used to measure in detail the velocity fields in different planes.

6.2.2.1. *Flow visualization*

Flow visualizations were carried out using *long* time exposure streak photography. The microgeometries were placed on an inverted epifluorescence microscope (DMI 5000M, Leica Microsystems GmbH) and were continuously illuminated by a 100 W mercury lamp. A filter cube (excitation filter band pass BP 545/30 nm, short pass dichroic at 565 nm, and barrier filter BP 605/75 nm) was used to filter the multichromatic light into the excitation light which reaches the microgeometries containing the seeded fluid via a microscope objective (20× magnification, numerical aperture NA = 0.4). The light emitted by the fluorescent tracer particles was imaged through the same objective onto the monochromatic camera (DFC350 FX, Leica Microsystems GmbH) in order to capture the particle trajectories. The fluids were seeded with 1.0 µm fluorescent polystyrene tracer particles at a concentration of 100 ppm (Nile Red, Molecular Probes, Invitrogen; Ex/Em: 535/575 nm; ρ: 1050 kg/m^3).

6.2.2.2. *Micro-particle image velocimetry*

For the µPIV measurements, the microgeometries were placed on the same microscope and were illuminated by a doubled pulsed Nd:YAG (neodymium-doped yttrium aluminum garnet) laser (Dual power 65-15, Dantec dynamics) working at a wavelength of 532 nm with a maximum energy emitted per pulse of 65 mJ at 15 Hz. The time between the two consecutive pulses of light was adjusted according to the flow rate, and varied in the range between Δt_{min} = 50 µs and Δt_{max} = 67 ms. A minimum of 150 pairs of images were acquired using a digital camera (Flow sense 4M, Dantec Dynamics) with a resolution of 2048x2048

pixels and running in double frame mode. The velocity fields were determined by processing the images using the Dynamic Studio V2.3 software (Dantec Dynamics) which generates a two-dimensional velocity vector map for each image pair. An objective with 20× magnification (NA = 0.4) was used to capture the displacement of the particles. The fluids were seeded with fluorescent polystyrene tracer particles with 0.5 µm in diameter at a concentration of 90 ppm (Nile Red, Molecular Probes, Invitrogen; Ex/Em: 535/575 nm; ρ: 1050 kg/m^3).

6.3. Governing equations and numerical method

The numerical results for the Newtonian and the viscoelastic fluids were obtained with a fully-implicit finite-volume method using a time marching pressure-correction algorithm (Oliveira *et al.*, 1998). The governing equations describing the isothermal laminar flow of an incompressible fluid are the mass conservation,

$$\nabla \cdot \mathbf{u} = 0, \tag{6.1}$$

and the momentum equations,

$$\rho\left(\frac{\partial \mathbf{u}}{\partial t} + \nabla \cdot \mathbf{uu}\right) = -\nabla p + \nabla \cdot \boldsymbol{\tau}, \tag{6.2}$$

where $\mathbf{u}$ represents the velocity vector, ρ the fluid density, t the time, p the pressure and $\boldsymbol{\tau}$ the extra-stress tensor. The extra-stress tensor is defined as the sum of a Newtonian solvent and a polymeric contribution $(\boldsymbol{\tau} = \boldsymbol{\tau}_s + \boldsymbol{\tau}_p)$. For Newtonian fluids, the polymeric contribution is neglected, $\boldsymbol{\tau}_p = \mathbf{0}$ and the Newtonian solvent component $\boldsymbol{\tau}_s$ is given by:

$$\boldsymbol{\tau}_s = \eta_s\,(\nabla \mathbf{u} + \nabla \mathbf{u}^T) = 2\eta_s\,\mathbf{D}\ , \tag{6.3}$$

where η_s is the constant solvent viscosity and $\mathbf{D}$ is the deformation rate tensor.

For the numerical calculations of the Boger fluid flow, the polymeric contribution is included and is described using the Oldroyd-B model:

$$\boldsymbol{\tau}_p + \lambda\left(\frac{\partial \boldsymbol{\tau}_p}{\partial t} + \nabla \cdot \mathbf{u}\boldsymbol{\tau}\right) = \eta_p(\nabla \mathbf{u} + \nabla \mathbf{u}^T) + \lambda(\boldsymbol{\tau}_p \cdot \nabla \mathbf{u} + \nabla \mathbf{u}^T \cdot \boldsymbol{\tau}_p), \tag{6.4}$$

where λ is the relaxation time of the fluid and η_P is the shear viscosity of the polymer.

For the shear-thinning fluid, the generalized Newtonian fluid (GNF) Carreau model was used to perform the numerical predictions for steady flow conditions. The numerical calculations with the inelastic GNF model do not describe adequately the flow near the cylinder, where the elastic extensional effects are dominant, but are able to predict with good accuracy the fully-developed velocity profiles far from the cylinder, where the shear viscosity is more relevant. The parameters used to fit the Carreau model to the shear viscosity master curve are presented in section 6.4.

In the simulations using the Carreau model, the polymeric contribution to the extra-stress tensor is neglected, $\boldsymbol{\tau}_p = \mathbf{0}$, and the shear-thinning viscosity function is introduced via the $\boldsymbol{\tau}_s$ term:

$$\boldsymbol{\tau}_s = 2\,\eta(\dot{\gamma})\,\mathbf{D}, \tag{6.5}$$

with the function $\eta(\dot{\gamma})$ given by the Carreau model described in section 6.4.

The numerical method is based on a time-marching version of the SIMPLEC pressure correction algorithm formulated for collocated variables (Oliveira *et al.*, 1998). The discretization of the governing equations is based on central-differences for diffusion terms and is based on the CUBISTA high-resolution scheme (Alves *et al.*, 2003) for the convective terms, both in the momentum and constitutive equations.

The computational domain was mapped using block-structured meshes. Extensive sets of calculations were carried out by Ferreira (2006) to estimate the numerical uncertainty and select an adequate mesh to provide mesh independent results. To generate the mesh the flow domain was divided into 24 blocks and within each block the cells were concentrated near the cylinder region. A zoomed view of the mesh used for aspect ratio *AR* = 2.0 is shown in Figure 6.2. For the other *AR* the meshes are similar, with only a change in the number of cells in the *z*-direction. The meshes have a large number of cells, ranging from 185850 cells for *AR* = 0.55 and *AR* = 1.0 to 255200 cells for *AR* = 2.0.

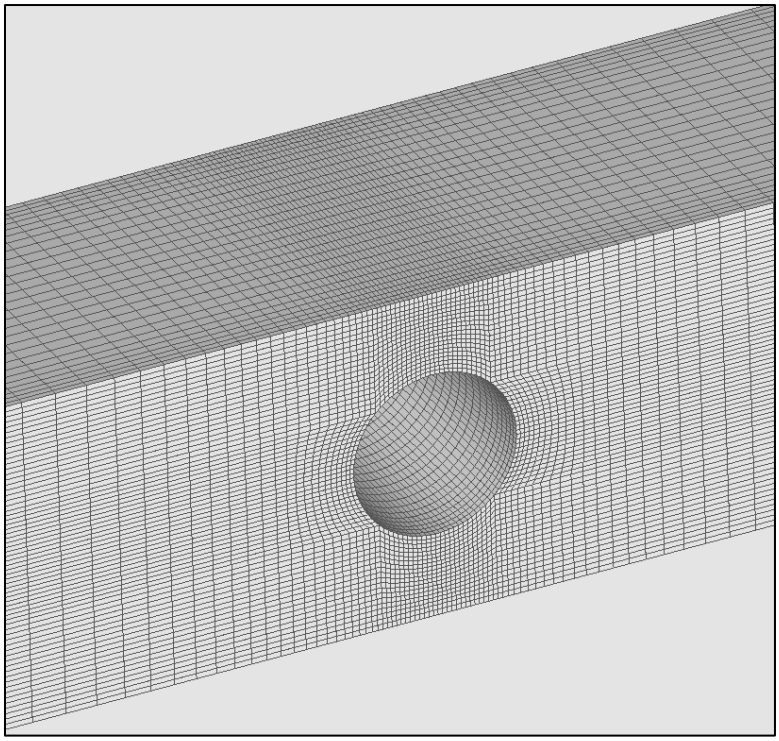

Figure 6.2. Zoomed view of the mesh used in the numerical simulations for AR = 2.0.

6.4. Fluid characterization

In this work, a Newtonian fluid, a Boger fluid and a shear-thinning viscoelastic fluid were used. The Newtonian fluid was de-ionized water, the Boger fluid was an aqueous solution of glycerine (85% w/w) and polyacrylamide (PAA) at a weight concentration of 200 ppm with 1% of NaCl, and the shear-thinning fluid was an aqueous solution of PAA at a weight concentration of 1000 ppm. All fluids were seeded with particles according the specifications described in section 6.2, for each experimental technique. The density (ρ) of the fluids was measured at 293.2 K using a pycnometer. The composition and the density of the fluids are presented in Table 6.1.

The rheological characterization of the fluids in shear flow conditions was done in a rotational rheometer (Physica MCR 301, Anton Paar) with a 75 mm cone-plate system with 1º angle to measure the steady-state shear viscosity. Additionally, another rotational rheometer (TA Instruments model, AR-G2) with higher torque sensitivity, equipped with a 40 mm cone-plate system with 2º angle was used to measure the material properties in small amplitude oscillatory shear flow (SAOS). A capillary break-up extensional rheometer (Haake CaBER 1, Thermo Scientific) was used to measure the relaxation time of the viscoelastic fluids under extensional flow.

Table 6.1. Composition (mass concentration) and properties of the fluids used.

Fluid	PAA (ppm)	Glycerine (%)	Water (%)	NaCl (%)	Kathon (ppm)	ρ (T = 293.2 K) (kg/m^3)
Newtonian	-	-	100	-	25	999.8
Shear-thinning PAA1000	1000	-	99.90	-	25	1001.5
Boger PAA200	200	85.05	13.91	1.02	25	1225.8

For the shear-thinning viscoelastic fluid (PAA1000), the flow curve was measured at different temperatures in the range between 283.2 and 303.2 K. The time-temperature superposition principle was used in order to obtain a master curve at the reference temperature, T_0 = 293.2 K. Figure 6.3 shows the steady-state shear viscosity master curve, together with the corresponding fit to a generalized Newtonian fluid (GNF) model. The Carreau model (1972) was used for the shear viscosity function, which is given by (Bird *et al.*, 1987):

$$\eta = \eta_s + \frac{\eta_0 - \eta_s}{\left[1 + (\Lambda\dot{\gamma})^2\right]^{(1-n)/2}} \tag{6.6}$$

where the fitted parameters are η_0 = 2.0 Pa.s, η_s = 0.004 Pa.s, Λ = 28 s and n = 0.38.

The time-temperature superposition principle was used in order to obtain the master curve at the reference temperature (T_0 = 293.2 K). The corresponding shift factor is defined as

$$a_T = \frac{\eta(T)}{\eta(T_0)}\frac{T_0}{T}\frac{\rho_0}{\rho}, \tag{6.7}$$

where η (T_0) is the shear viscosity at the reference temperature T_0, η (T) is the shear viscosity at a temperature T, ρ_0 is the density at the reference temperature and ρ is the density at temperature T. The temperature variation relative to the reference temperature is small for the range of measurements, thus the fluid density does not change significantly, and the shift factor further simplifies to (Dealy and Plazek, 2009):

$$a_T = \frac{\eta(T)}{\eta(T_0)}. \tag{6.8}$$

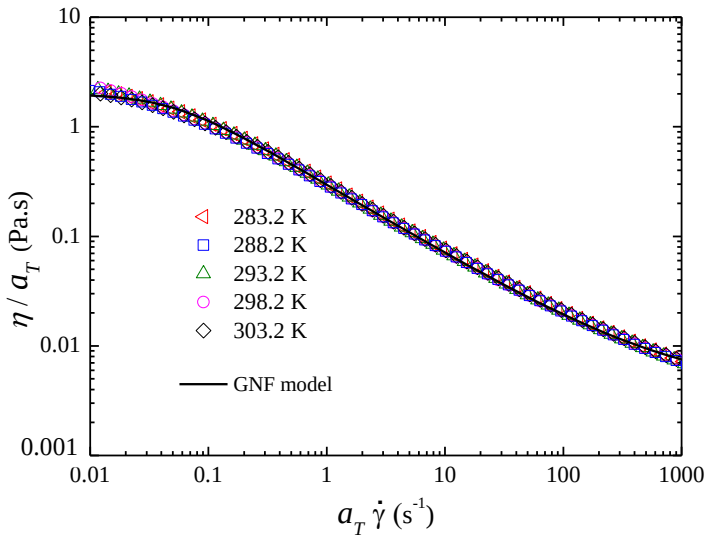

Figure 6.3. Steady shear viscosity master curve of the shear-thinning fluid (PAA1000). The symbols represent the experimental data measured at different temperatures and the solid line the GNF model fit.

Figure 6.4 shows the shear viscosity (η) as a function of shear rate ($\dot{\gamma}$) for the Boger fluid PAA 200 measured at different temperatures in the range between 288.5 and 298.5 K. The time-temperature superposition principle was used in order to obtain the master curve at the reference temperature T_0 = 293.2 K. Figure 6.4 shows a nearly constant viscosity of 0.152 Pa.s in a shear rate between 1 and 1000 s^{-1} (open symbols). This figure also shows the plot of the storage modulus G'/ω^2 vs. the angular frequency, ω (solid symbols), together with the corresponding fit using a two-mode Oldroyd-B model (line). This fit of the linear viscoelastic spectrum was determined at T_0 = 293.2 K and the two-mode model parameters are: λ_1 = 0.030 s and η_1 = 0.020 Pa.s; λ_2 = 0.38 s and η_2 = 0.0075 Pa.s; solvent viscosity, η_s = 0.126 Pa.s. Using the parameters of the multi-mode model, the average relaxation time can be calculated as a weighted average:

$$\lambda = \frac{1}{\eta_p} \sum_{k \neq solvent} \eta_k \lambda_k \ , \tag{6.9}$$

where $\eta_p = \sum_{k \neq solvent} \eta_k$, leading to λ = 125 ms for the Boger fluid.

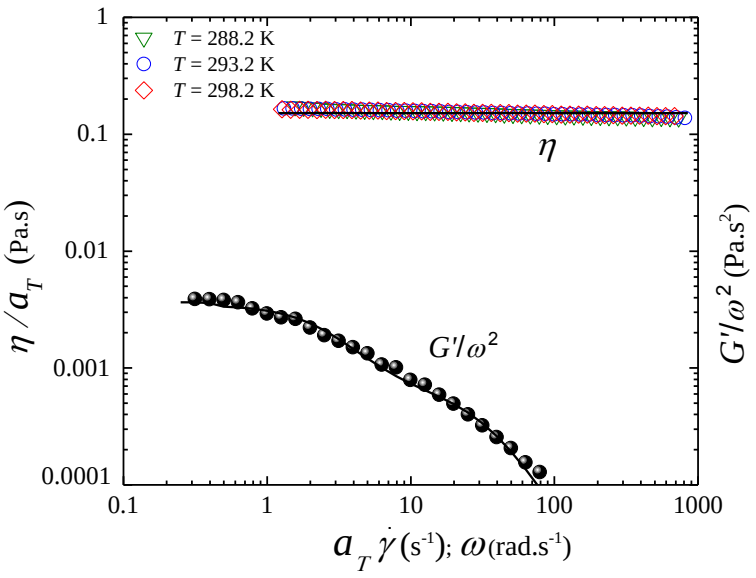

Figure 6.4. Material functions at reference temperature (T_0 = 293.2 K) in steady shear (open symbols) and storage modulus in small amplitude oscillatory shear flow (solid symbols) for PAA200 Boger fluid. The solid lines represent the fit of the multimode Oldroyd-B model.

The relaxation time in extensional flow was measured at the reference temperature (T_0 = 293.2 K) using the CaBER rheometer by fitting the experimental data in the elasto-capillary regime to the equation (Entov and Hinch, 1997):

$$\frac{D}{D_0} = e^{-\frac{t}{3\lambda}}, \tag{6.10}$$

where D_0 is the diameter of the filament at the reference time t = 0 and D is the diameter at time t. These measurements were performed using two circular plates with a diameter of 6 mm, an initial plate spacing of 3 mm, a final plate distance of 9 mm, with the step strain imposed during 50 ms.

As shown in Figure 6.5 the fit of Eq. (6.10) to the experimental data resulted in extensional flow relaxation time of λ = 104 ms for the shear-thinning fluid (PAA1000) and λ = 86.7 ms for the PAA200 Boger fluid.

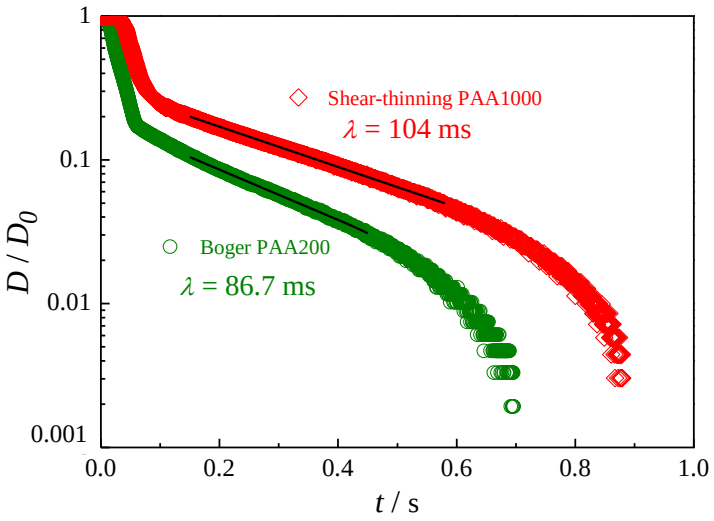

Figure 6.5. Time evolution of the filament diameter measured in the CaBER rheometer for the PAA1000 shear-thinning fluid and the PAA200 Boger fluid.

The two methods used to determine the relaxation time for the Boger fluid lead to slightly different values, as expected for the different canonical flows used in their determination. However, since the values obtained are of the same order of magnitude for both methods (due to the dilute concentration), this gives some reliability to the results obtained. The relaxation time determined in extensional flow is thought to be more appropriate for the flow around the cylinder, which is strongly dominated by the extensional stresses on the forward stagnation point and in the wake of the cylinder, and therefore the Deborah numbers will be calculated with the CaBER relaxation times. For the PAA1000 shear-thinning fluid, the relaxation time determined with the CaBER rheometer is much smaller than the relaxation time that could be estimated from the flow curve shown in Figure 6.3. The onset of shear-thinning usually starts to occur at a shear rate of $\dot{\gamma} \approx 0.05\ \mathrm{s}^{-1}$, which is approximately the inverse of the relaxation time. From Figure 6.3 the relaxation time can be estimated in the order of $\lambda \approx 20$ s, which is more than two orders of magnitude above the relaxation time in extension. Thus, the relaxation time used in the remaining calculations of this chapter should be viewed as a rough estimate, and the *De* values calculated are, most probably too small.

6.5. Results

The flow of the Newtonian and the two complex viscoelastic fluids around a confined cylinder in a microchannel was characterised through flow visualizations and detailed velocity measurements using μPIV to assess the effect of the geometrical aspect ratio upon the flow field for the benchmark case of 50% blockage ratio. The measurements were taken at the symmetry plane (z/R = 0), cf. Figure 6.1, and the flow rate was varied from creeping flow conditions up to the onset of time-dependent flow. The experimental results and numerical predictions for the Newtonian, Boger and shear-thinning fluids are presented in sections 6.5.1, 6.5.2 and 6.5.3, respectively. In addition to the study of the influence of the aspect ratio on the flow patterns, these measurements also provide the identification of the critical conditions for the onset of elastic instabilities observed in the vicinity of the cylinder.

Besides the geometrical dimensionless parameters (*AR* and *BR*), the Newtonian fluid flow also depends on the Reynolds number (*Re*):

$$Re = \frac{\rho U R}{\eta}, \tag{6.11}$$

where U is the bulk velocity of the approach flow, R is the radius of the cylinder and ρ and η are the density and shear viscosity of the fluid, respectively. For the shear-thinning fluid the shear viscosity is evaluated at a characteristic shear rate, $\dot{\gamma} = U / R$.

The flow of the viscoelastic fluids is also characterised by an additional dimensionless parameter that involves λ, such as the Deborah number, which represents the ratio between the characteristic times of the fluid (λ) and of the flow (R/U):

$$De = \frac{\lambda U}{R}. \tag{6.12}$$

Another alternative is the use of the Weissenberg number, which quantifies the nonlinear response of the fluid and is defined as the ratio between elastic (normal) stresses and viscous stresses, and can be written as (Dealy, 2010):

$$Wi = \lambda \dot{\gamma}\ , \tag{6.13}$$

with the shear rate being estimated as $\dot{\gamma} = U / R$, leading to a similar definition as *De*. The Weissenberg number (*Wi*) is used often in viscoelastic flows in which there is an important

elongation component of the flow. Although the *De* and *Wi* physically represent ratios of different quantities, their values sometimes are defined in a similar way, as in the flow around a confined cylinder.

Additionally, the flow of the viscoelastic fluids can be characterised by the elasticity number (*El*), which is a dimensionless parameter that quantifies the ratio between the elastic and inertial forces:

$$El = \frac{Wi}{Re} = \frac{\lambda \eta}{\rho R^2}, \tag{6.14}$$

6.5.1. Newtonian fluid

Figure 6.6 shows a typical flow visualization using streak photography (left hand side) and the corresponding numerical prediction (right hand side) of the flow patterns in the vicinity of the cylinder for the Newtonian fluid, for Re = 35.0 and AR = 1.0. The recirculation length (L_v) was measured at the symmetry plane, z/R = 0. Similar flow patterns are observed for AR = 2.0 and AR = 0.55, but are not shown for conciseness.

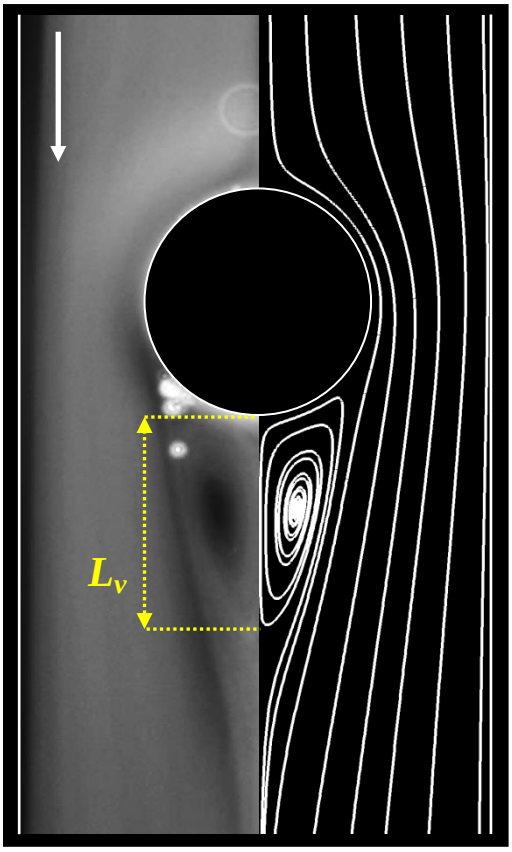

Figure 6.6. Experimental (left hand side) and numerical (right hand side) flow patterns at the symmetry plane (z/R = 0) for the Newtonian fluid at Re = 35.0 and AR = 1.0.

From the whole set of experimental data of Newtonian fluid flow visualizations for all AR (2.0, 1.0 and 0.55) and the corresponding numerical simulations, we were able to plot in Figure 6.7 the variation of the dimensionless recirculation length (L_v/R) with Re as a function of AR. Figure 6.7 also shows results for AR = 16, obtained in the previous macro-scale study of Ribeiro *et al*. (2012). Figure 6.7b is a zoom viewed of Figure 6.7a in the region of low Re. The comparison between the experimental data and the numerical predictions shows a good agreement and it is clear that, for all AR, the vortex length increases with Re and, as expected, there are no changes as we move from the macro- to the micro-scale. In fact, for Newtonian fluid flow only the Reynolds number and the geometric ratios, AR and BR, are important, and the results are independent of the scale, as long the *continuum* hypothesis holds. We can also observe in the zoom view of Figure 6.7b that the critical Re for the onset of flow separation increases as AR decrease. The onset of flow separation occurs at $Re \approx 6.5$ for AR = 16, $Re \approx 7$ for AR = 2.0, $Re \approx 8$ for AR = 1.0 and at $Re \approx 15$ for AR = 0.55. The time-dependent flow starts at $Re \approx 40$ for AR = 16, at $Re \approx 75$ for AR = 2.0, at $Re \approx 140$ for AR =

1.0 and at $Re \approx 150$ for $AR = 0.55$, i.e., the end walls (cf. Figure 6.1) have a stabilizing effect upon these two flow transitions.

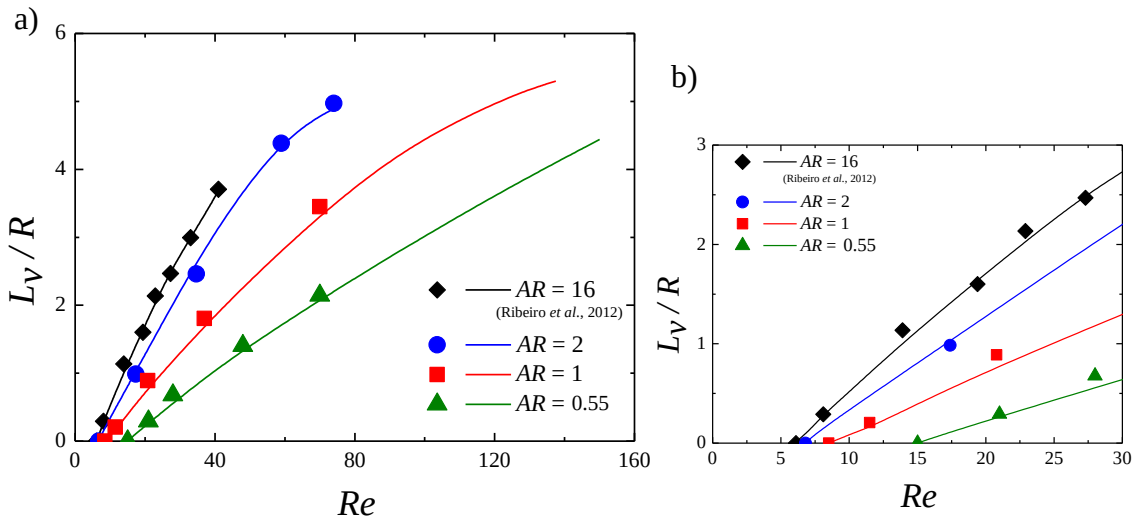

Figure 6.7. a) Variation of the separated flow length with the Reynolds number at the symmetry plane ($z/R = 0$) as a function of AR; b) Zoomed view of the Re range near the onset of flow separation. Comparison between experiments (symbols) and numerical predictions (lines).

6.5.2. Boger fluid

Flow visualizations

The effect of the Deborah number on the flow patterns of the PAA200 Boger fluid at the symmetry plane ($z/R = 0$) is illustrated in Figures 6.8-6.10. Regardless of the aspect ratio, the flow is always symmetric upstream and downstream of the cylinder at low De and low Re (cf. Figures 6.8a, 6.9a and 6.10a), but with increasing De diverging streamlines progressively appear upstream of the cylinder with the flow remaining symmetric relative to the $y = 0$ plane (cf. Figures 6.8b-d, 6.9b-d and 6.10b-d). The onset of the divergent streamlines occurs at a critical Deborah number (De_c), which depends on AR. The experimental pathlines provide only qualitative information and for that reason it is difficult to obtain accurate values of De_c. Still, careful visual inspection showed the critical value for the onset of the divergent streamlines to occur at $De_c \approx 8$ - 10 for $AR = 2.0$ and $AR = 1.0$ and at $De_c \approx 11$ - 13 for $AR = 0.55$. Diverging streamlines are typically observed in viscoelastic flows with an extensional nature (Poole and Alves, 2009) so it is not a surprise that the enhancement of shear effects induced by the closer end walls at lower AR leads to an increase of De_c.

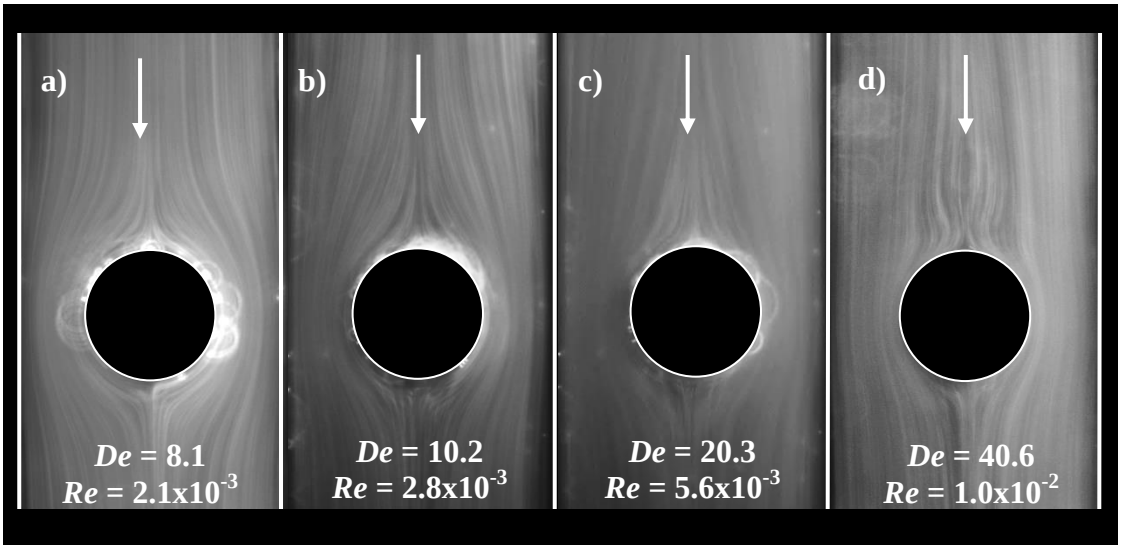

Figure 6.8. Flow patterns of the Boger fluid flow imaged at the centreplane $z/R = 0$ for $AR = 2.0$ and different Deborah numbers.

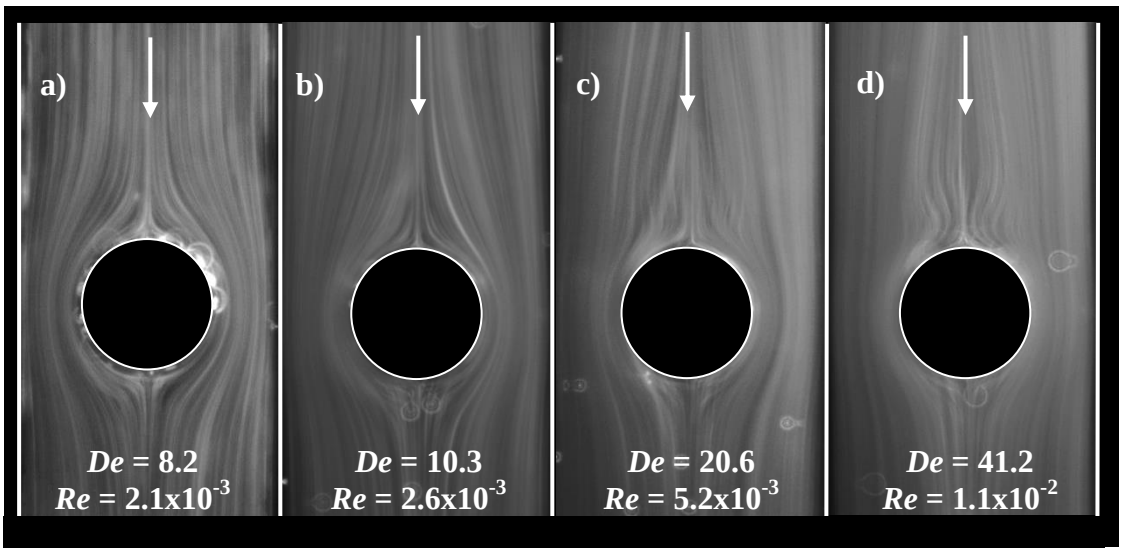

Figure 6.9. Flow patterns of the Boger fluid flow imaged at the centreplane $z/R = 0$ for $AR = 1.0$ and different Deborah numbers.

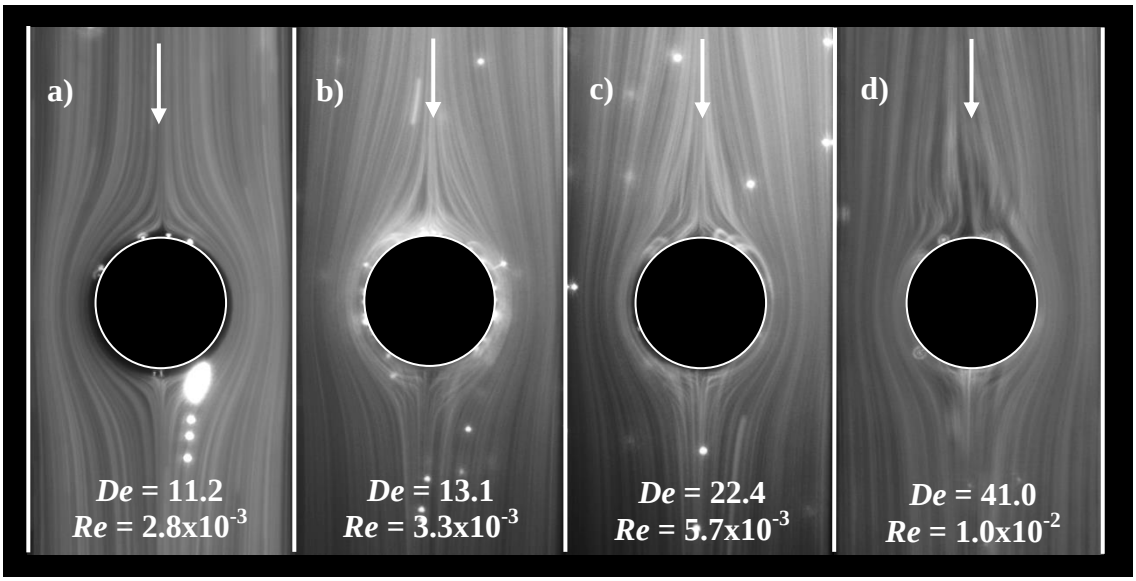

Figure 6.10. Flow patterns of the Boger fluid flow imaged at the centreplane $z/R = 0$ for $AR = 0.55$ and different Deborah numbers.

In summary, over the wide range of *De* achieved to characterize the flow of this Boger fluid, only the Newtonian-like and the steady divergent streamline flow regimes were observed regardless of the value of *AR* and no flow asymmetries or time dependencies were observed in contrast to what is reported in the next section for viscoelastic shear-thinning fluids. Further increase of the flow rate for the Boger fluids leads to a significant increase of the pressure drop and the PDMS channels are not able to sustain such high pressures leading to deformation and at higher flow rates to leakage.

Velocity field

Figure 6.11 shows the influences of *AR* and *De* on the measured streamwise dimensionless velocity profiles (u/U) taken along the centreline ($y/R = 0$; $z/R = 0$) using the Boger fluid. Figure 6.11 also includes numerical predictions for Newtonian fluid under creeping flow conditions and for the Oldroyd-B model at $De = 0.12$ and $De = 1.2$, which is the maximum *De* reached in the steady-state numerical calculations with this viscoelastic model. The fully-developed velocity in the duct axis with the Boger fluid is similar to that of the Newtonian fluid and is independent of *De*, due to the constant shear viscosity.

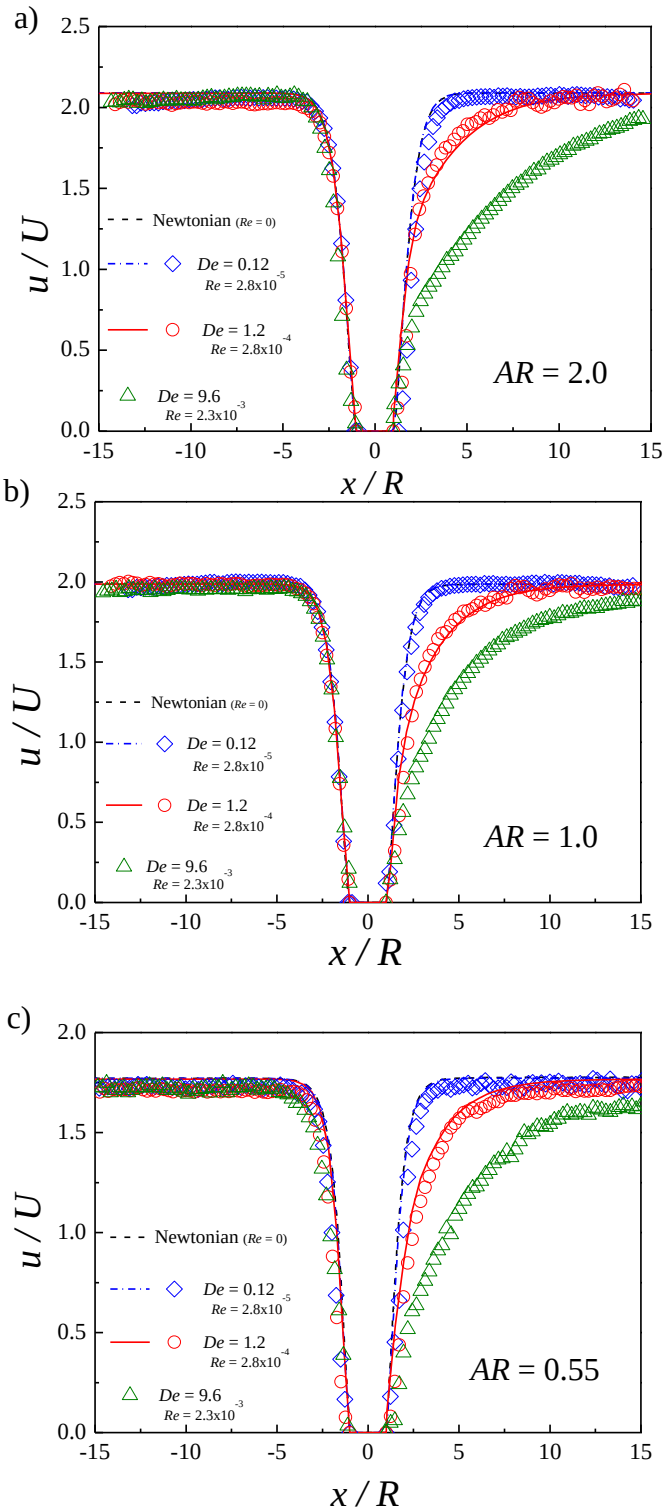

Figure 6.11. Streamwise velocity profiles measured along the centreline (y/R = 0, z/R = 0) for the Boger fluid as a function of *De*: a) *AR* = 2; b) *AR* = 1; c) *AR* = 0.55. The symbols represent the experimental results and the lines represent the numerical predictions.

Upstream of the cylinder, the flow deceleration up to the forward stagnation point is nearly independent of *De* and *AR*, and starts at $x/R \approx -4$. In contrast, downstream of the cylinder the required length to achieve fully-developed flow conditions increases significantly with *De*. The numerical predictions obtained with the Oldroyd-B model agree well with the corresponding experimental data, both upstream and downstream of the cylinder for all *AR* in the simulated *De* range. Predictions of this 3D flow at higher *De* are very costly due to the fine meshes and the large computational times due to the onset of time-dependent flows in the simulations.

Figure 6.12 shows transverse profiles of the normalized streamwise velocity, u/U, taken at the symmetry plane ($z/R = 0$) in several positions upstream (x/R = -12, -8, -6, -4, -3 and -2) and downstream (x/R = 2, 3, 4, 6, 8 and 12) of the cylinder for $De \approx 1$ and AR = 2.0, 1.0 and 0.55. The numerical solutions using the Oldroyd-B model are also presented (lines) and the comparison with the experimental results shows an overall good agreement.

Far upstream and downstream of the cylinder the profiles approach the expected parabolic shape for AR = 2.0 and 1.0. For AR = 0.55 the fully-developed velocity becomes flat, due to the geometric confinement (in this case the profiles are parabolic in the *z*-direction as shown in Figure 6.13).

Upstream of the cylinder, the flow deceleration is due to the combined effects of channel wall confinement and the presence of the cylindrical obstacle, until the flow eventually becomes exclusively dominated by the presence of the cylinder at $x/R \approx -2$, since there are no significant differences in the velocity profiles for all *AR*.

Downstream of the cylinder, from $x/R \approx 2$ up to $x/R \approx 4$, the velocities are higher at the jets formed between the cylinder and channel walls at $|y/R| \approx 1$, than at the centreline. The velocity peaks are slightly more intense for lower *AR*. At $x/R = 6$ the velocity profiles are already close the fully-developed shape but are still increasing progressively. At $x/R \approx 12$ the flow is fully-developed in the three *AR* shown.

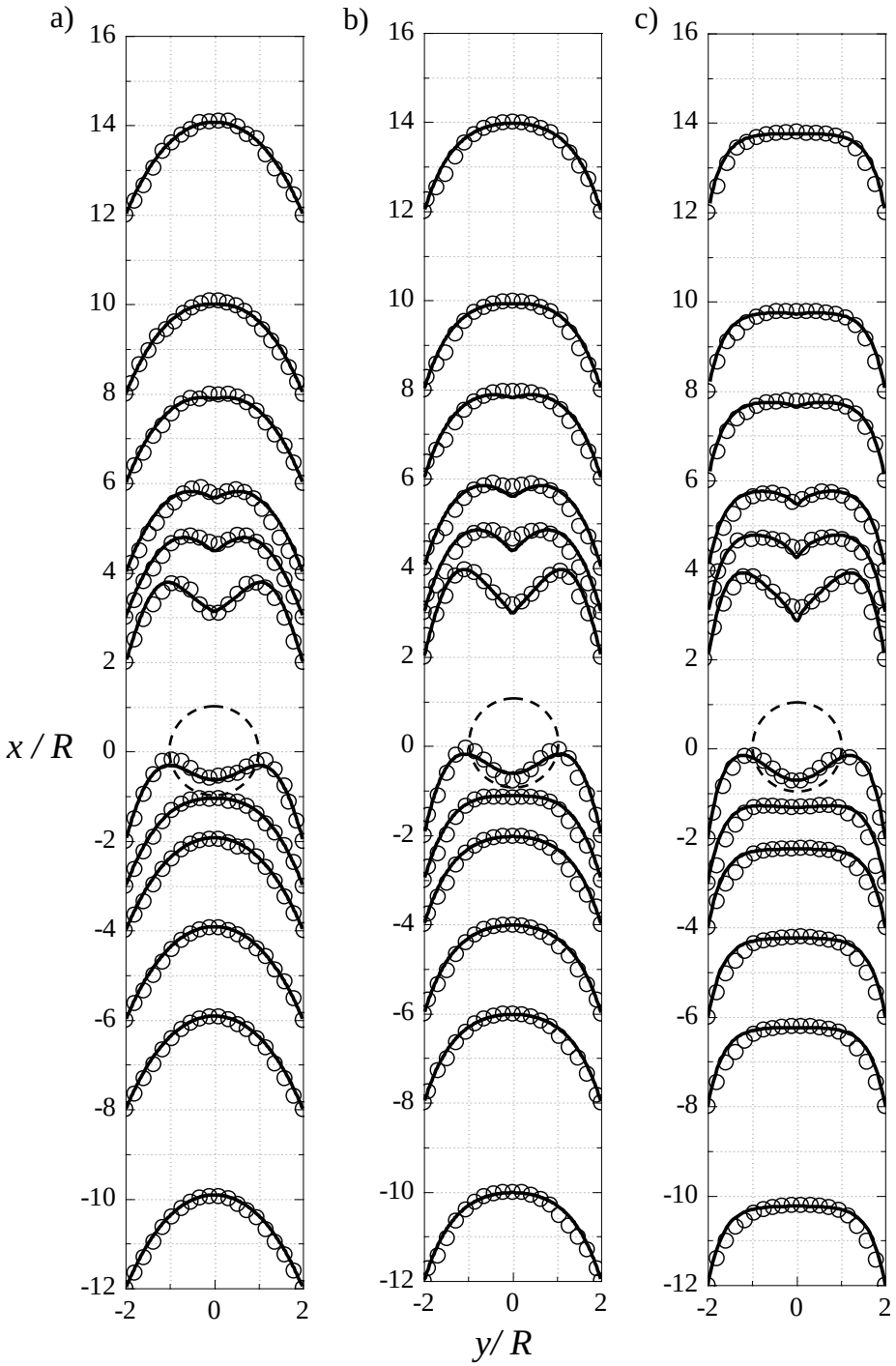

Figure 6.12. Transverse profiles of the streamwise velocity component for the Boger fluid at the symmetry plane, $z/R = 0$, and for multiple streamwise locations: a) $AR = 2.0$ ($De = 1.0$; $Re \approx 2.6\text{x}10^{-3}$); b) $AR = 1.0$ ($De = 1.0$; $Re \approx 2.6\text{x}10^{-3}$); c) $AR = 0.55$ ($De = 0.93$; $Re \approx 2.4\text{x}10^{-3}$). The symbols represent the experimental results and the lines numerical predictions using the Oldroyd-B model. The dashed circles indicate the location of the cylinder.

In order to better assess the complex flow field we present in Figure 6.13 the velocity profiles at different axial locations at the other centreplane, $y = 0$. In the z-direction, and for all AR, the upstream velocities are always higher in the centreline than close the lateral walls. Downstream of the cylinder the velocities are higher in the centreline except for $AR = 0.55$ and $x/R = 2$, where the velocities are slightly higher at $|z/R| \approx 0.125$. For $x/R > 2$ the velocity profiles progressively approach the fully-developed conditions, as expected.

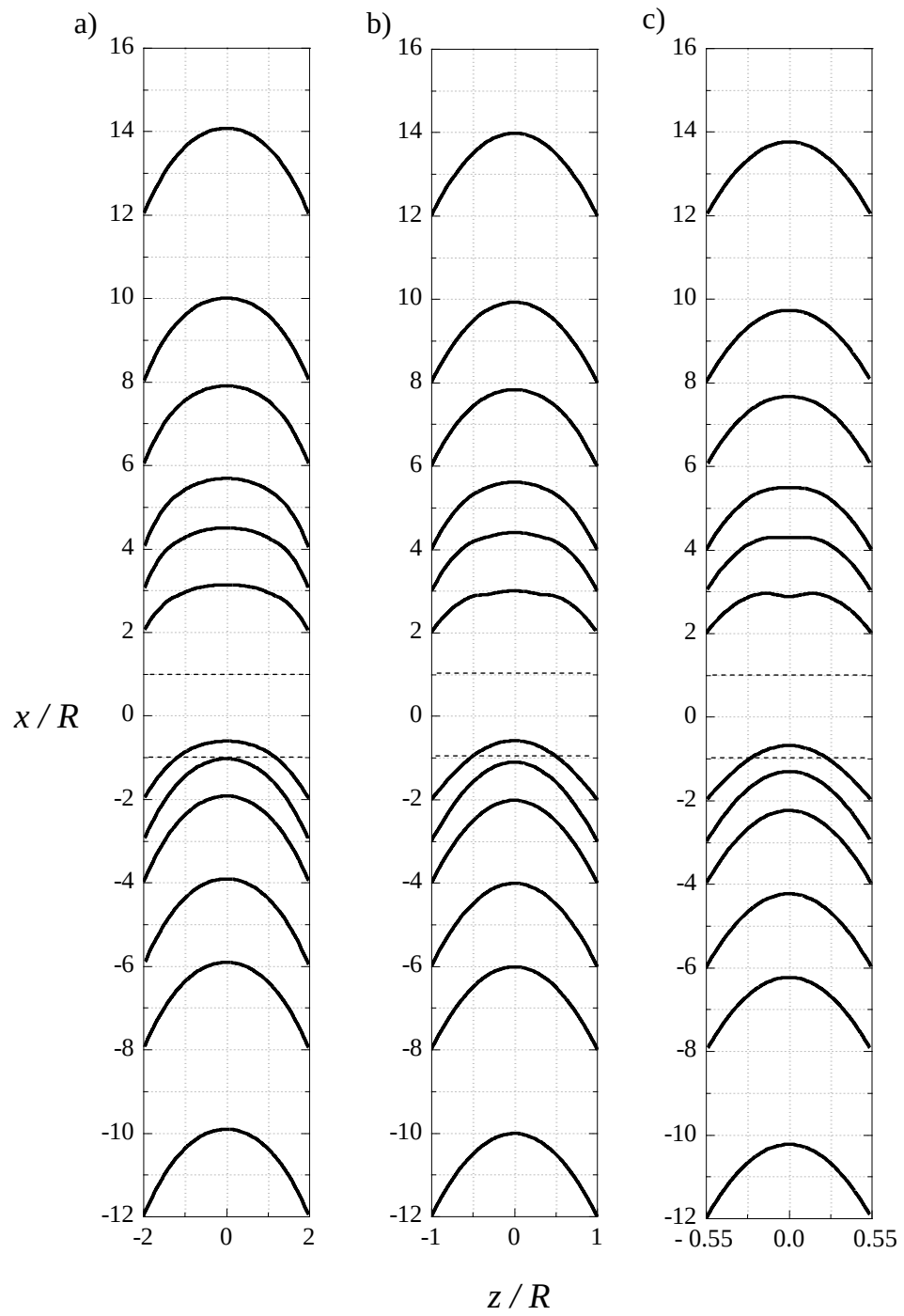

Figure 6.13. Computed transverse profiles of the streamwise velocity component for the Boger fluid at the symmetry plane, y/R = 0, and for multiple streamwise locations for De = 1.0 ($Re \approx 2.6 \times 10^{-3}$): a) AR = 2.0; b) AR = 1.0; c) AR = 0.55. The dashed lines indicate the location of the cylinder.

The μPIV measurements were done at the centreplane z = 0, but from the numerical simulations we can analyse the flow field in different planes, or the pressure and stress fields. Figures 6.14 and 6.15 show the influence of *De* on the normalized first-normal stress difference for the PAA200 Boger fluid at the centreplanes z/R = 0 and y/R = 0, respectively. The cases *De* = 0.1 and *De* = 1.0 were chosen in order to illustrate the influence of viscoelasticity on the first normal stress difference contour plots. As expected, at the higher *De* occurs the appearance of a birefringent strand in the cylinder wake, where the polymer molecules are highly extended and oriented and the first normal stress difference increases.

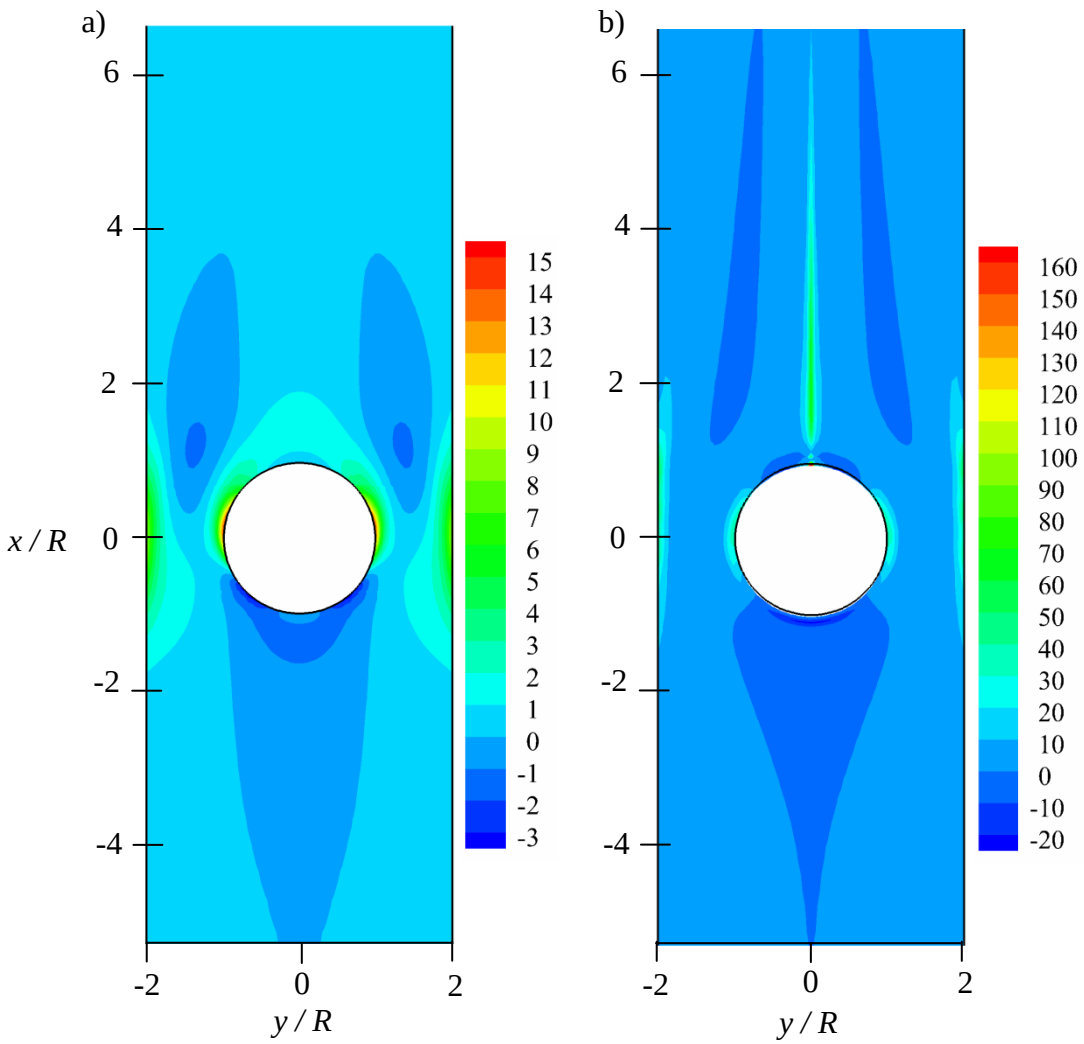

Figure 6.14. Normalized first normal stress difference $(\tau_{xx} - \tau_{yy})_{\text{polymer}} / (\eta_0 U / R)$ for the PAA200 Boger fluid at the centreplane z/R = 0 computed for AR = 1: a) *De* = 0.1; b) *De* = 1.0. Only the polymeric component of the first normal stress difference is shown, but the normalizing stress $(\eta_0 U / R)$ is based on the total shear viscosity, $\eta_0 = \eta_p + \eta_s$.

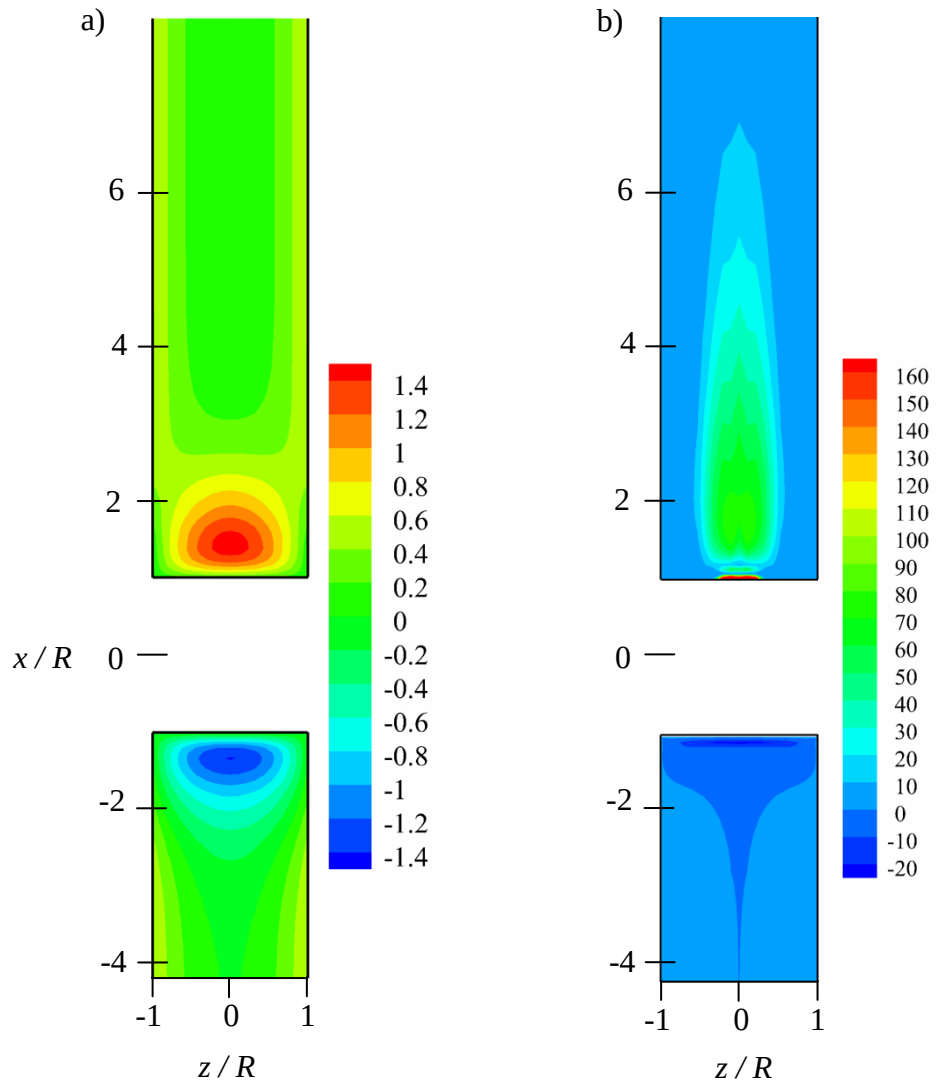

Figure 6.15. Normalized first normal stress difference $(\tau_{xx} - \tau_{yy})_{\text{polymer}} / (\eta_0 U / R)$ for the PAA200 Boger fluid at the centreplane $y/R = 0$ computed for $AR = 1$: a) $De = 0.1$; b) $De = 1.0$. Only the polymeric component of the first normal stress difference is shown, but the normalizing stress $(\eta_0 U / R)$ is based on the total shear viscosity, $\eta_0 = \eta_p + \eta_s$

6.5.3. Shear-thinning fluid

Flow visualizations

The effect of the Deborah number on the flow patterns of the shear-thinning fluid at the symmetry plane ($z/R = 0$) is illustrated in Figures 6.16-6.18. Regardless of the aspect ratio, and as also seen for Boger fluids, at low *De* the flow is symmetric upstream and downstream of the cylinder (cf. Figures 6.16a, 6.17a and 6.18a-b). However, as *De* increases an elastic instability arises upstream of the cylinder, near the forward stagnation point and the flow becomes asymmetric but still steady (cf. Figures 6.16b-c, 6.17b-d and 6.18c-d), a flow

feature that has also been observed at the macro-scale with the same fluid (see chapter 4). The critical Deborah number (De_c) for the onset of this elastic instability was found to occur between $De_c \approx 0.5$ for $AR = 2.0$, $De_c \approx 0.55$ for $AR = 1.0$ and $De_c \approx 0.6$ for $AR = 0.55$. Above De_c, the elastic instability becomes more intense as De increase until the flow eventually becomes time dependent, initially showing a periodic behaviour of oscillation. Then, as De is increased further, the elastic instability becomes more complex, showing chaotic-like behaviour as is illustrated in Figures 6.16d-f, 6.17e-f and 6.18e-f.

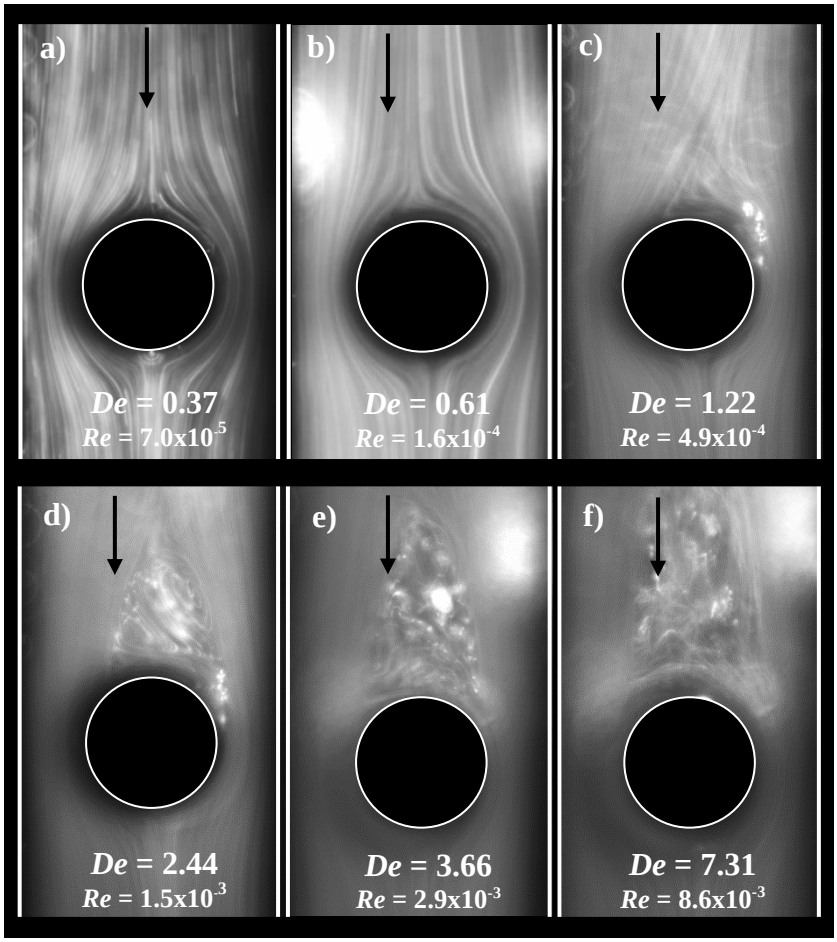

Figure 6.16. Influence of De on the flow patterns of the shear-thinning fluid at the symmetry plane ($z/R = 0$) for $AR = 2$.

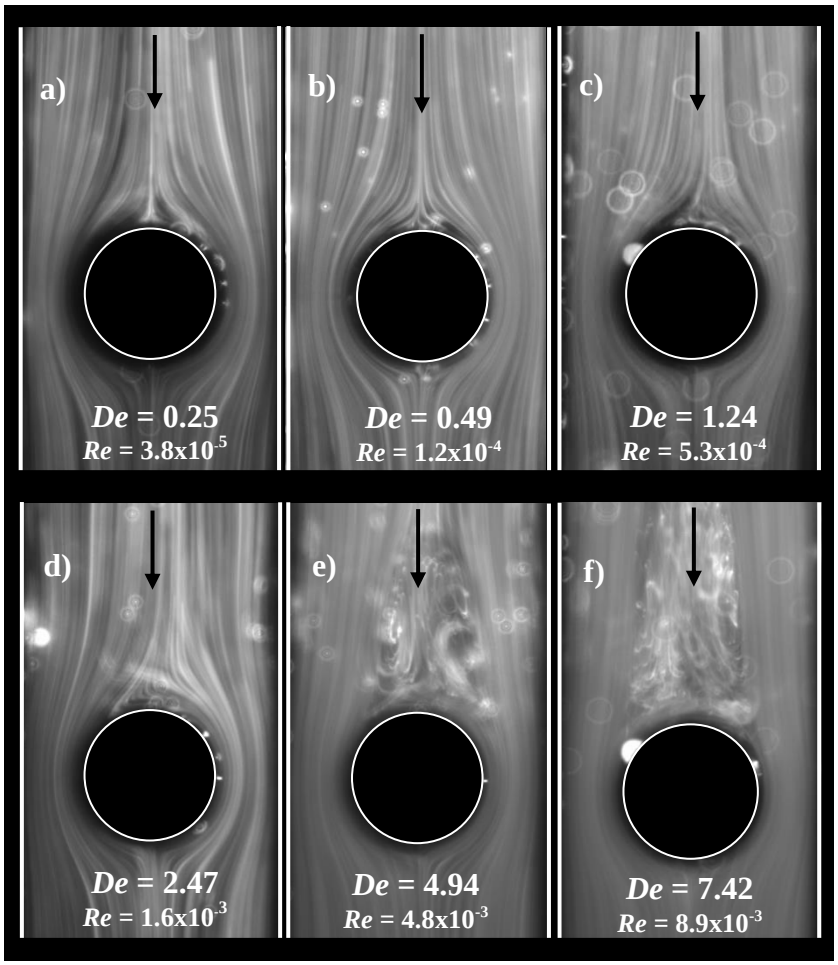

Figure 6.17. Influence of *De* on the flow patterns of the shear-thinning fluid at the symmetry plane ($z/R = 0$) for $AR = 1$.

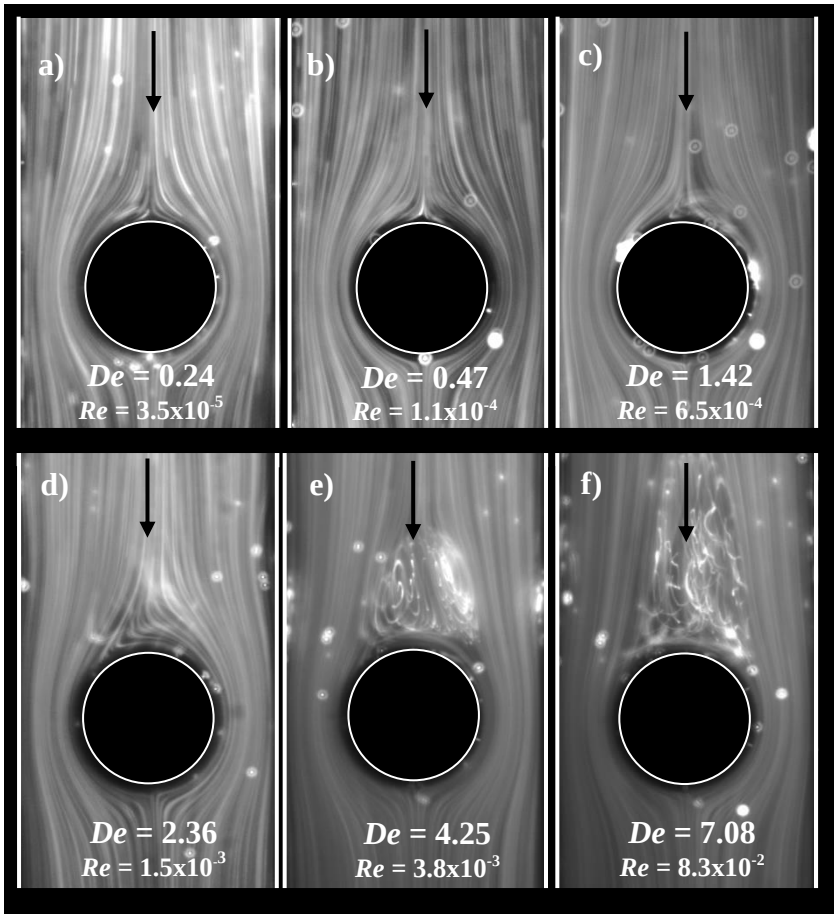

Figure 6.18. Influence of *De* on the flow patterns of the shear-thinning fluid at the symmetry plane ($z/R = 0$) for $AR = 0.55$.

Over the wide range of *De* achieved in the experiments with the shear-thinning fluid, the following four flow regimes were identified with progressively increasing *De*: Newtonian-like flow; steady asymmetric flow; unsteady periodic flow; unstable chaotic-like flow. In the Newtonian-like flow regime the flow is symmetric upstream and downstream of the cylinder, and elastic effects are negligible. In the steady asymmetric flow regime, a steady elastic instability is observed upstream of the cylinder. As *De* is further increased the flow asymmetry intensifies and the flow becomes unsteady, initially with periodic behaviour (unsteady periodic regime). As *De* increases even further the flow eventually becomes chaotic although this classification is only approximate since it was simply based on a qualitative observation of the time evolution of the flow patterns. The boundaries between these regimes depend slightly on *AR* and these flow transitions are summarized in Table 6.2.

Table 6.2. Range of *De* for each flow regime for the shear-thinning fluid.

Flow regime	***AR* = 2.0**	***AR* = 1.0**	***AR* = 0.55**
Newtonian-like	$De < 0.5$	$De < 0.55$	$De < 0.6$
steady asymmetric	$0.5 < De < 0.9$	$0.55 < De < 0.9$	$0.60 < De < 1.1$
unsteady periodic flow	$0.9 < De < 3.0$	$0.9 < De < 3.0$	$1.1 < De < 3.5$
chaotic-like	$De > 3.0$	$De > 3.0$	$De > 3.5$

Velocity field

To assess the effect of *AR* on the velocity field for the shear-thinning fluid, in Figures 6.19a-c we plot the dimensionless streamwise velocity component, *u/U*, measured along the centreline ($y/R = 0$; $z/R = 0$) for various *De* and *AR*. The experimental results are compared with the corresponding numerical predictions for the Newtonian creeping flow limit and for an inelastic Carreau model (GNF) with the parameters described in section 6.4.

The GNF model is used to analyse the effect of the shear-thinning viscosity in the flow field without the influence of viscoelasticity. The numerical calculations with the GNF model are unable to predict accurately the flow near the cylinder, where the elastic (memory) effects are important, but are able to predict the fully-developed velocity far from the cylinder, where the velocity field is essentially controlled by shear stresses and, except for the possibility of a weak secondary flow induced by normal stresses, the shear viscosity curve alone determines the fully-developed streamwise velocity profile. Comparing the Newtonian fluid case with the viscoelastic fluid data, we observe that the shear-thinning of the latter leads to a flatter velocity profile with a lower velocity on the centreline. Closer to the cylinder, comparing the predictions for the GNF and the Newtonian fluid models on one side with the experimental data for the viscoelastic shear-thinning fluid on the other shows that the fluid deceleration of the approach flow starts much earlier for the viscoelastic fluid than for the purely viscous fluid models, and this effect is stronger the higher the value of *De*. Far from the cylinder, on the downstream side, the flow is again dominated by viscous shear and consequently the GNF calculations agree well again with the experimental data, even though there is a slight

difference for AR = 0.55 on account of possible weak secondary flow effects induced by normal stresses not accounted for by the GNF model. The same deviation can be seen far upstream of the cylinder. Downstream of the cylinder there is also an effect of elasticity since the flow recovery takes longer the larger the value of De and this effect is enhanced as AR is reduced. Therefore, the development lengths required for the flow redevelopment increase with De and decrease with AR, as can be observed in Figure 6.19. Here, for example for De = 0.49 and AR = 2.0 (cf. Figure 6.19a) the fully-developed velocity on the centreline is achieved at $x/R \approx 7$ whereas for AR = 0.55 (cf. Figure 6.19c) it is achieved only at $x/R \approx 12$.

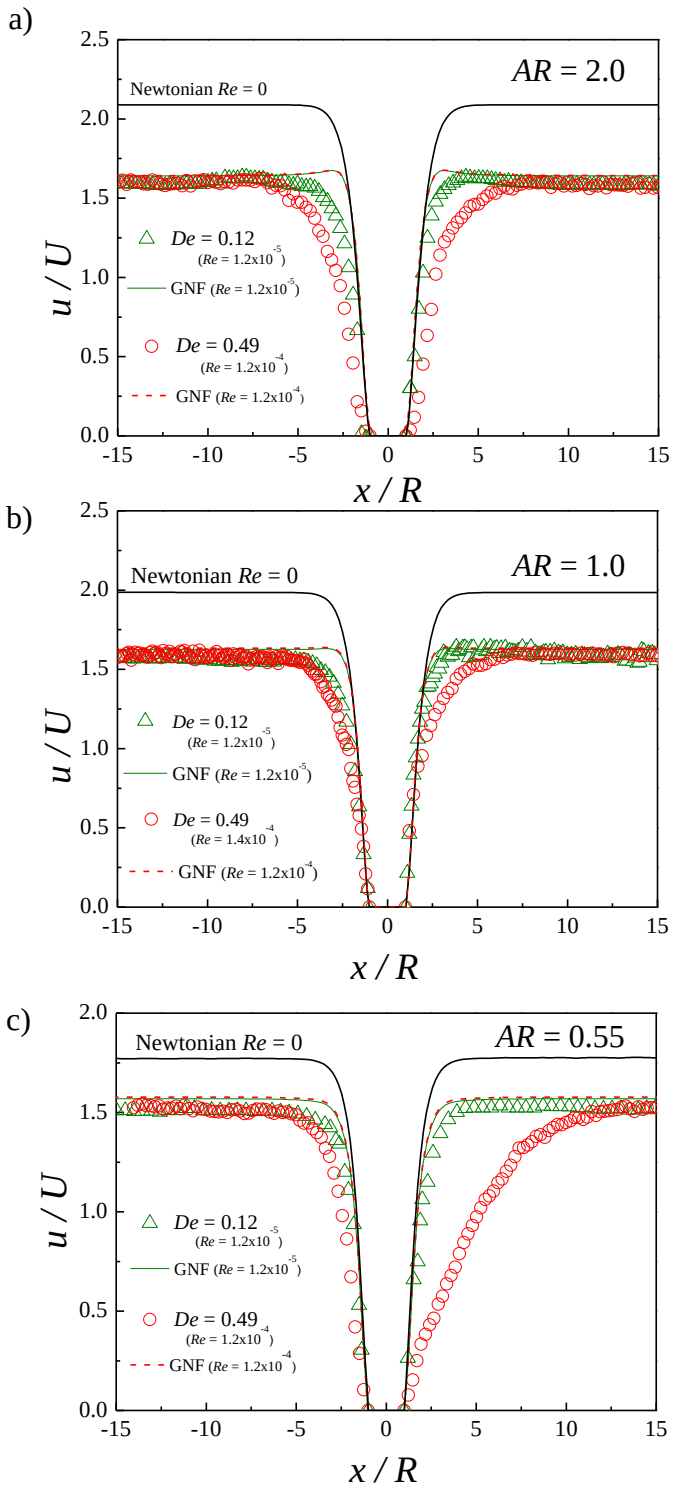

Figure 6.19. Streamwise velocity profiles measured along the centreline (y/R = 0, z/R = 0) for the shear-thinning fluid as a function of *De*: a) *AR* = 2; b) *AR* = 1; c) *AR* = 0.55. The symbols represent the experimental results and the lines represent the numerical predictions.

Figure 6.20 shows transverse profiles of the normalized streamwise velocity component at different positions upstream (x/R = -12, -8, -6, -4, -3 and -2) and downstream (x/R = 2, 3, 4, 6, 8 and 12) of the cylinder at the symmetry plane (z/R = 0) for $De \approx 0.49$ and for AR = 2.0, 1.0 and 0.55. At this De, there are no conclusive changes in regard to the velocity profiles upstream of the cylinder. Closer to the cylinder at $x/R \approx$ -3 and -2 the velocities are higher at $|y/R| \approx 1.5$ than at the duct centreline, as the fluid is forced to deviate towards the passages between the cylinder and the confinement walls. The deceleration observed upstream of the cylinder is essentially dominated by the presence of the cylinder, since there are no notorious differences between the profiles at the different AR cases.

In contrast, the flow redevelopment downstream of the cylinder is significantly dependent on the AR (cf. Figure 6.20). Changing from AR = 2 to AR = 0.55, the effect of the cylinder on the velocity profiles is progressively felt over longer distances from the cylinder. For AR = 2 the velocity is higher at $|y/R| \approx 1.5$ than at the centreline only up to $x/R \approx 2$. As the fluid moves further downstream to $x/R \approx 6$ the velocity profiles flatten, until the flow reaches the fully-developed shape at $x/R \approx 8$. For AR = 0.55, the velocities are higher near the walls than at the centreline up to $x/R \approx 8$, a mark of slower flow redevelopment. The velocity peaks move from near the walls to the centreline as the distance from the cylinder increases. For AR = 0.55 the flow reaches the fully-developed velocity at $x/R \approx 12$, in agreement with Figure 6.19c. The increasing effect of the elasticity as AR decreases is a direct consequence of the stronger velocity peaks formed downstream of the cylinder, and consequently larger stress gradients, which will require a longer development length for smearing out.

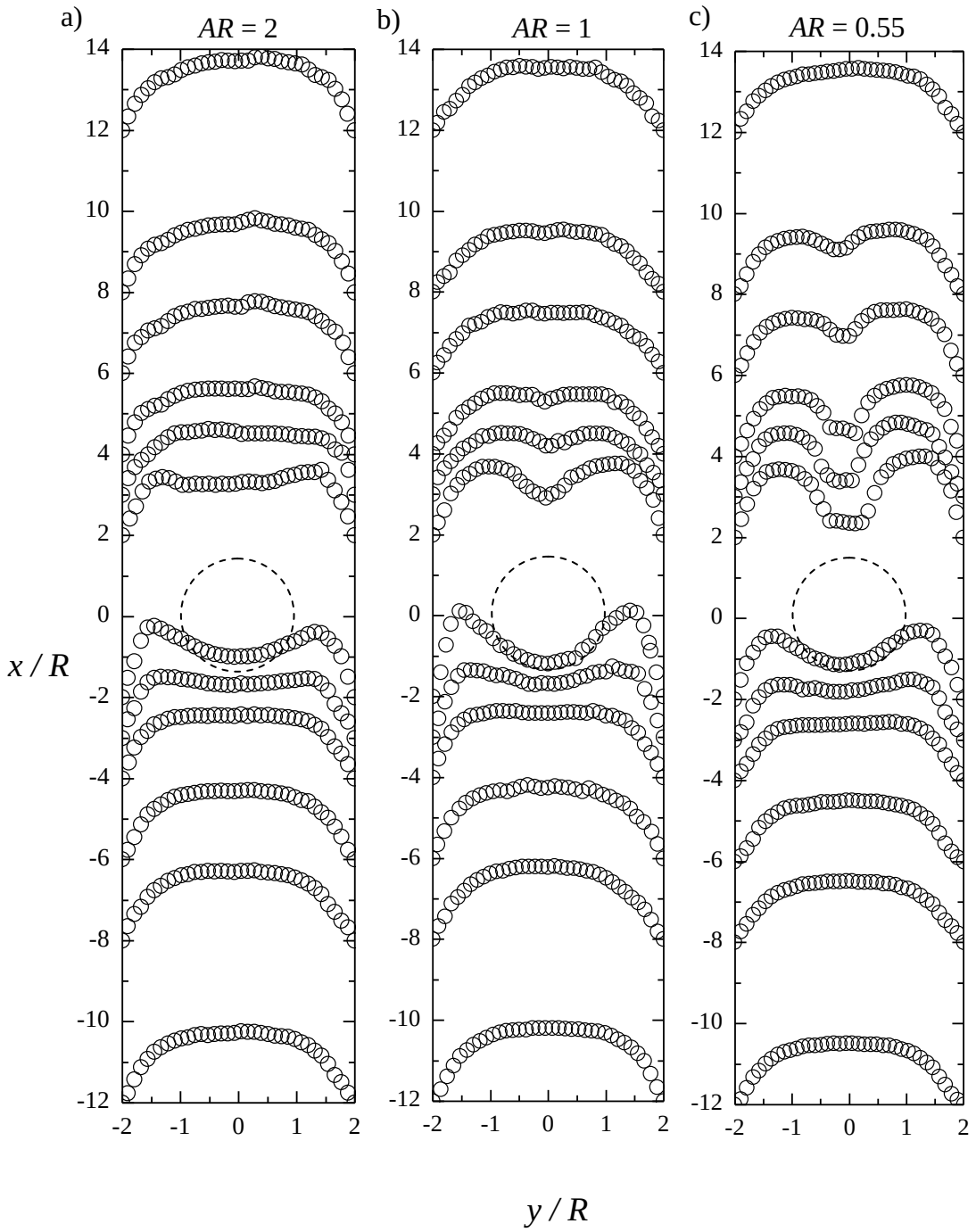

Figure 6.20. Transverse profiles of the streamwise velocity component for the shear-thinning fluid at the symmetry plane, z/R = 0, and for multiple streamwise locations: a) AR = 2.0 (De = 0.49, Re = 1.11x10^{-4}); b) AR = 1.0 (De = 0.49, Re = 1.13x10^{-4}); c) AR = 0.55 (De = 0.47, Re = 1.08x10^{-4}). The dashed circles indicate the location of the cylinder.

Figure 6.21 shows the transverse velocity profiles of the normalized streamwise velocity at different positions upstream (x/R = -12, -8, -6, -4, -3 and -2) and downstream (x/R = 2, 3, 4, 6, 8 and 12) of the cylinder at the symmetry plane (z/R = 0) for De = 0.12 and for AR = 1.0. Comparing this figure with the results shown in Figure 6.20b for De = 0.49 allows to infer the influence of De in the flow field when De decreases. For the lower De, the effect of flow deceleration upstream occurs closer to the cylinder and the flow-redevelopment occurs earlier in agreement with the results previously shown in Figure 6.19b. The intensity of the velocity peaks observed near the cylinder decrease for lower De, showing that elasticity enhances the velocity overshoots and increases the flow development length. A similar behaviour was observed for the AR = 2 and AR = 0.55 cases (not shown).

In an attempt to understand the differences observed in the flow patterns between the two types of viscoelastic fluids used, the elasticity number, $El = Wi/Re$, which is defined as the ratio between elastic and inertial forces, was calculated for both fluids, and is of order of $El = \mathcal{O}(10^3)$. Since the instabilities of the shear thinning fluid are in a more advanced stage than those observed for the Boger fluid, and knowing that lower elasticity numbers promotes the behaviour seen in here, as will also be shown in the next chapter, this can indicate that the estimated characteristic shear rate, used to calculate the Reynolds and elasticity numbers of the shear thinning fluid ($\dot{\gamma} = U/R$) is indeed much lower than it should. The same conclusion was obtained by Coelho and Pinho (2003) when they comment on the elasticity number used to correlate the data obtained from two different cylinder diameters, and state that "the elasticity number involves the viscosity calculated at a high characteristic shear rate typical of the boundary layer rather than the average value", this average value used in their work was $\dot{\gamma} = U/(2D)$. As already state in section 6.4, the relaxation time determined using the CaBER rheometer is probably too small for the shear-thinning viscoelastic fluid, thus explaining the much smaller De values found for the different flow regimes observed with the shear-thinning fluid.

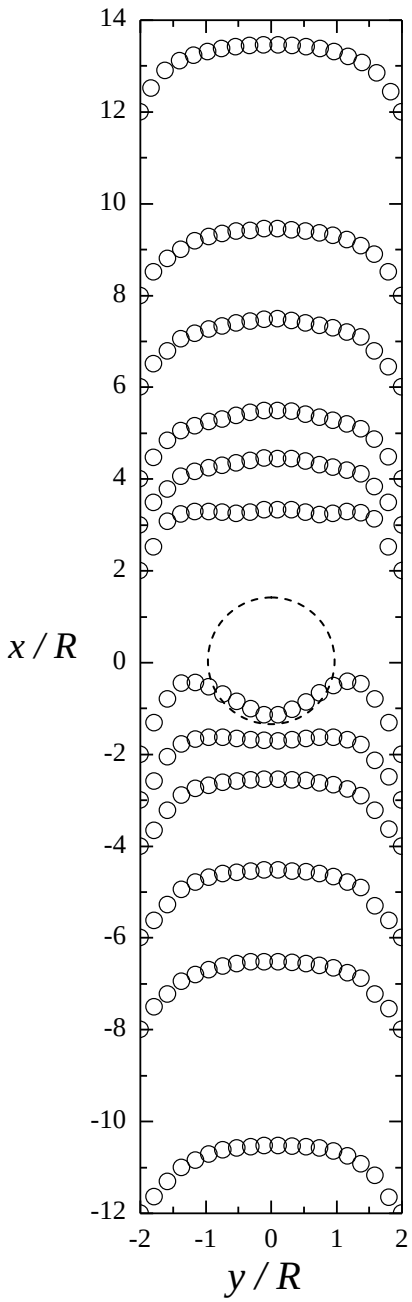

Figure 6.21. Transverse profiles of the streamwise velocity component for the shear-thinning fluid at the symmetry plane, z/R = 0, and for multiple streamwise locations for De = 0.12, Re = 1.20x10^{-5} and AR = 1.0. The dashed circle indicates the location of the cylinder.

6.6. Conclusions

The flow of a Newtonian fluid and two viscoelastic fluids past a confined cylinder in microfluidic devices was studied experimentally and numerically. The confined cylinder is placed in a rectangular duct with different aspect ratios, defining a 50% blockage ratio. The flow was characterised experimentally using streak photography and μPIV. The flow conditions ranged from Newtonian-like creeping flow conditions up to chaotic-like time-dependent flow, for aspect ratios of 2.0, 1.0 and 0.55.

The numerical calculations were carried out with a finite volume method. The numerical predictions for the Newtonian fluid flow and for the Boger fluid flow compare well with the experimental results. For the shear-thinning fluid flow, the GNF model used predicted with good accuracy the fully-developed velocity profiles, far from the cylinder, but near the cylinder is unable to predict the correct behaviour of the velocity profiles, where viscoelasticity plays a significant role.

For the Newtonian fluid flow, by comparing the present results with previous works at macro-scale, we conclude that there is no dramatic change as we move from the macro- to the micro-scale for the same Reynolds number, *AR* and *BR*. This allows us to conclude that the *continuum* hypothesis holds at the micro-scale.

Over the wide range of *De* achieved to characterize the flow of Boger fluid the Newtonian-like and the steady divergent streamlines flow regimes were observed regardless of the value of *AR*. No flow asymmetries or unsteady flow were observed in the limited range of operation of the PDMS microchannels used. For the shear-thinning fluid, a wider range of flow rates was available, due to the lower shear viscosity at higher shear rates, and the following four flow regimes were identified with progressively increasing *De*: Newtonian-like flow; steady asymmetric flow; unsteady periodic flow; chaotic-like flow. The critical conditions for the flow regime transitions were found to depend moderately on the *AR*, with the critical values of *De* slightly increasing for lower *AR*.

The velocity profiles upstream and downstream of the cylinder are dependent on the geometric confinement and on elasticity of the fluid. The flow deceleration upstream of the cylinder starts earlier when *De* and the confinement increase. Downstream of the cylinder, the length required for the flow redevelopment increases with *De* and when the geometric confinement increases.

References

Alves, M.A., Oliveira, P.J., Pinho, F.T., 2003. A convergent and universally bounded interpolation scheme for the treatment of advection. Int J Numer Meth Fl 41, 47-75.

Asgar, A., Bhagat, S., Papautsky, I., 2008. Enhancing particle dispersion in a passive planar micromixer using rectangular obstacles. J Micromech Microeng 18, 085005.

Bazant, M.Z., Squires, T.M., 2004. Induced-charge electrokinetic phenomena: Theory and microfluidic applications. Phys Rev Lett 92, 066101.

Bhagat, A.A.S., Peterson, E.T.K., Papautsky, I., 2007. A passive planar micromixer with obstructions for mixing at low Reynolds numbers. J Micromech Microeng 17, 1017-1024.

Bird, R.B., Armstrong, R.C., Hassanger, O., 1987. Dynamics of polymeric liquids. John Wiley and Sons, New York.

Carreau, P.J., 1972. Rheological Equations from Molecular Network Theories. Trans. Soc Rheol 16, 99-127.

Chan, E.Y., Gonçalves, N.M., Haeusler, R.A., Hatch, A.J., Larson, J.W., Maletta, A.M., Yantz, G.R., Carstea, E.D., Fuchs, M., Wong, G.G., Gullans, S.R., Gilmanshin, R., 2004. DNA mapping using microfluidic stretching and single-molecule detection of fluorescent site-specific tags. Genome Res 14, 1137-1146.

Chen, G.D., Fachin, F., Fernandez-Suarez, M., Wardle, B.L., Toner, M., 2011. Nanoporous Elements in Microfluidics for Multiscale Manipulation of Bioparticles. Small 7, 1061-1067.

Coelho, P.M., Pinho, F.T., 2003. Vortex shedding in cylinder flow of shear-thinning fluids II. Flow characteristics. J Non-Newton Fluid 110, 177-193.

Davis, J.A., Inglis, D.W., Morton, K.J., Lawrence, D.A., Huang, L.R., Chou, S.Y., Sturm, J.C., Austin, R.H., 2006. Deterministic hydrodynamics: Taking blood apart. P Natl Acad Sci USA 103, 14779-14784.

Dealy, J., Plazek, D., 2009. Time-temperature superposition - a user guide. Rheology Bulletin 78, 16-31.

Dealy, J.M., 2010. Weissenberg and Deborah numbers - Their definition and use. Rheology Bulletin, 14-18.

deMello, A.J., 2006. Control and detection of chemical reactions in microfluidic systems. Nature 442, 394-402.

Eghbali, H., Matthijs, S., Verdoold, V., Gardeniers, H., Cornelis, P., Desmet, G., 2009. Use of non-porous pillar array columns for the separation of Pseudomonas pyoverdine siderophores as an example of a real-world biological sample. J Chromatogr A 1216, 8603-8611.

Entov, V.M., Hinch, E.J., 1997. Effect of a spectrum of relaxation times on the capillary thinning of a filament of elastic liquid. J Non-Newton Fluid Mech 72, 31-53.

Fachin, F., Chen, G.D., Toner, M., Wardle, B.L., 2011. Integration of bulk nanoporous elements in microfluidic devices with application to biomedical diagnostics. Journal of Microelectromechanical systems 20, 1428-1438.

Fachin, F., Wardle, B.L., Chen, G.D., Toner, M., 2010. Integration of Vertically-Aligned Carbon Nanotube Forests in Microfluidic Devices for Multiscale Isolation of Bioparticles. Ieee Sensor, 47-51.

Ferreira, H.H., 2006. Escoamento de fluidos newtonianos e viscoelásticos em torno de um cilindro: estudo numérico de efeitos tridimensionais. MSc thesis. MSc on Fundamentals and Applications of Fluid Mechanics. Faculdade de Engenharia da Universidade do Porto.

Fiorini, G.S., Chiu, D.T., 2005. Disposable microfluidic devices: fabrication, function, and application. Biotechniques 38, 429-446.

Gan, H.Y., Lam, Y.C., Nguyen, N.T., Tam, K.C., Yang, C., 2007. Efficient mixing of viscoelastic fluids in a microchannel at low Reynolds number. Microfluid Nanofluid 3, 101-108.

Groisman, A., Steinberg, V., 2000. Elastic turbulence in a polymer solution flow. Nature 405, 53-55.

Haward, S.J., Odell, J.A., Berry, M., Hall, T., 2011. Extensional rheology of human saliva. Rheol Acta 50, 869-879.

Helton, K.L., Yager, P., 2007. Interfacial instabilities affect microfluidic extraction of small molecules from non-Newtonian fluids. Lab Chip 7, 1581-1588.

Hessel, V., Löwe, H., Schönfeld, F., 2005. Micromixers—a review on passive and active mixing principles. Chemical Engineering Science 60, 2479-2501.

Hsieh, S.S., Huang, Y.C., 2008. Passive mixing in micro-channels with geometric variations through mu PIV and mu LIF measurements. J Micromech Microeng 18, 065017.

Huang, L.R., Cox, E.C., Austin, R.H., Sturm, J.C., 2004. Continuous particle separation through deterministic lateral displacement. Science 304, 987-990.

Inglis, D.W., 2009. Efficient microfluidic particle separation arrays. Appl Phys Lett 94, 013510.

Inglis, D.W., Lord, M., Nordon, R.E., 2011. Scaling deterministic lateral displacement arrays for high throughput and dilution-free enrichment of leukocytes. J Micromech Microeng 21, 054024.

Jayaraj, S., Kang, S.M., Suh, Y.K., 2007. A review on the analysis and experiment of fluid flow and mixing in micro-channels. J Mech Sci Technol 21, 536-548.

Jeon, W., Shin, C.B., 2009. Design and simulation of passive mixing in microfluidic systems with geometric variations. Chem Eng J 152, 575-582.

Kumar, V., Paraschivoiu, M., Nigam, K.D.P., 2011. Single-phase fluid flow and mixing in microchannels. Chemical Engineering Science 66, 1329-1373.

Larson, R.G., 2000. Fluid dynamics - Turbulence without inertia. Nature 405, 27-28.

Li, F.C., Kinoshita, H., Li, X.B., Oishi, M., Fujii, T., Oshima, M., 2010. Creation of very-low-Reynolds-number chaotic fluid motions in microchannels using viscoelastic surfactant solution. Exp Therm Fluid Sci 34, 20-27.

Li, X.B., Li, F.C., Cai, W.H., Zhang, H.N., Yang, J.C., 2012. Very-low-Re chaotic motions of viscoelastic fluid and its unique applications in microfluidic devices: A review. Exp Therm Fluid Sci 39, 1-16.

Lin, Y., Gerfen, G.J., Rousseau, D.L., Yeh, S.R., 2003. Ultrafast microfluidic mixer and freeze-quenching device. Anal Chem 75, 5381-5386.

McDonald, J.C., Duffy, D.C., Anderson, J.R., Chiu, D.T., Wu, H.K., Schueller, O.J.A., Whitesides, G.M., 2000. Fabrication of microfluidic systems in poly(dimethylsiloxane). Electrophoresis 21, 27-40.

Meisel, I., Ehrhard, P., 2006. Electrically-excited (electroosmotic) flows in microchannels for mixing applications. Eur J Mech B-Fluid 25, 491-504.

Miranda, J.M., Oliveira, H., Teixeira, J.A., Vicente, A.A., Correia, J.H., Minas, G., 2010. Numerical study of micromixing combining alternate flow and obstacles. Int Commun Heat Mass 37, 581-586.

Morton, K.J., Loutherback, K., Inglis, D.W., Tsui, O.K., Sturm, J.C., Chou, S.Y., Austin, R.H., 2008. Hydrodynamic metamaterials: Microfabricated arrays to steer, refract, and focus streams of biomaterials. P Natl Acad Sci USA 105, 7434-7438.

Nguyen, T.N.T., Kim, M.C., Park, J.S., Lee, N.E., 2008. An effective passive microfluidic mixer utilizing chaotic advection. Sensor Actuat B-Chem 132, 172-181.

Oliveira, M.S.N., McKinley, G.H., 2005. Iterated stretching and multiple beads-on-a-string phenomena in dilute solutions of highly extensible flexible polymers. Phys Fluids 17, 071704.

Oliveira, P.J., Pinho, F.T., Pinto, G.A., 1998. Numerical simulation of non-linear elastic flows with a general collocated finite-volume method. J Non-Newton Fluid Mech 79, 1-43.

Pakdel, P., McKinley, G.H., 1996. Elastic instability and curved streamlines. Phys Rev Lett 77, 2459-2462.

Poole, R.J., 2012. The Deborah and Weissenberg numbers. Rheology Bulletin, 32-39.

Poole, R.J., Alves, M.A., 2009. Velocity overshoots in gradual contraction flows. J Non-Newton Fluid Mech 160, 47-54.

Ribeiro, V.M., Coelho, P.M., Pinho, F.T., Alves, M.A., 2012. Three-dimensional effects in laminar flow past a confined cylinder. Chem Eng Sci 84, 155-169.

Sheen, H.J., Hsu, C.J., Wu, T.H., Chu, H.C., Chang, C.C., Lei, U., 2007. Experimental study of flow characteristics and mixing performance in a PZT self-pumping micromixer. Sensor Actuat a-Phys 139, 237-244.

Sousa, P.C., Pinho, F.T., Oliveira, M.S.N., Alves, M.A., 2011. Extensional flow of blood analog solutions in microfluidic devices. Biomicrofluidics 5, 014108.

Squires, T.M., Quake, S.R., 2005. Microfluidics: Fluid physics at the nanoliter scale. Rev Mod Phys 77, 977-1026.

Stone, H.A., Stroock, A.D., Ajdari, A., 2004. Engineering flows in small devices: Microfluidics toward a lab-on-a-chip. Annu Rev Fluid Mech 36, 381-411.

Stroock, A.D., Dertinger, S.K.W., Ajdari, A., Mezic, I., Stone, H.A., Whitesides, G.M., 2002. Chaotic mixer for microchannels. Science 295, 647-651.

Suh, Y.K., Kang, S., 2010. A Review on Mixing in Microfluidics. Micromachines, 82-111.

Teclemariam, N.P., Beck, V.A., Shaqfeh, E.S.G., Muller, S.J., 2007. Dynamics of DNA polymers in post arrays: Comparison of single molecule experiments and simulations. Macromolecules 40, 3848-3859.

Tovar-Lopez, F.J., Rosengarten, G., Westein, E., Khoshmanesh, K., Jackson, S.P., Mitchell, A., Nesbitt, W.S., 2010. A microfluidics device to monitor platelet aggregation dynamics in response to strain rate micro-gradients in flowing blood. Lab Chip 10, 291-302.

Tseng, L.Y., Yang, A.S., Lee, C.Y., Hsieh, C.Y., 2011. Cfd-Based Optimization of a Diamond-Obstacles Inserted Micromixer with Boundary Protrusions. Eng Appl Comp Fluid 5, 210-222.

Wang, C.T., Shaw, C.K., Hu, T.Y., 2011. Optimization of Flow in Microbial Fuel Cells: An Investigation into Promoting Micro-Mixer Efficiency with Obstacle. Journal of Science and Engineering 14, 25 -31

Wang, H.Z., 2004. Passive Mixing in Microchannels with Geometric Variations. Swinburne University of Technology, Australia.

Wang, H.Z., Iovenitti, P., Harvey, E., Masood, S., 2002a. Mixing of two fluid streams in a microchannel using the Taylor-Aris dispersion effect. Biomedical Applications of Micro- and Nanoengineering 4937, 158-163.

Wang, H.Z., Iovenitti, P., Harvey, E., Masood, S., 2002b. Optimizing layout of obstacles for enhanced mixing m microchannels. Smart Mater Struct 11, 662-667.

Wang, H.Z., Iovenitti, P., Harvey, E., Masood, S., 2003a. Numerical investigation of mixing in microchannels with patterned grooves. J Micromech Microeng 13, 801-808.

Wang, H.Z., Iovenitti, P., Harvey, E., Masood, S., 2003b. Passive mixing in microchannels by applying geometric variations. Microfluidics, Biomems, and Medical Microsystems 4982, 282-289.

Wang, H.Z., Iovenitti, P., Harvey, E., Syed, M., Deam, R., 2001. Mixing of liquids using obstacles in microchannels. Biomems and Smart Nanostructures 4590, 204-212.

Yi, S., Seo, K.S., Cho, Y.H., 2005. Self-focusing chips for size-dependent DNA separation in nonuniformly distributed asymmetric electric fields. Transducers '05, Digest of Technical Papers, Vols 1 and 2, 1608-1611.

Chapter 7

Blockage ratio effect upon the Boger fluid flow past a confined cylinder in microfluidic devices

Abstract

This chapter presents an experimental study of Newtonian and viscoelastic Boger fluid flow around a confined cylinder in microfluidic devices to assess the influence of the blockage ratio, BR, defined as the ratio between the diameter of the cylinder and the width of the microchannel, from inertialess flow conditions up the onset of time-dependent flow. To achieve our goal, we characterize the complex 3D flow field through flow visualizations using streak photography and detailed velocity measurements using micro-particle image velocimetry. The experimental results are compared with numerical calculations, which were performed in 3D meshes using an in-house finite volume code. For the Newtonian fluid flow the numerical calculations showed a good agreement with experimental measurements. For the Boger fluids, the onset of divergent streamlines was observed near the forward stagnation point at a critical Deborah number, Wi^*, which develops into an elastic instability as Wi^* is increased further. In geometries with the same cross-section the aspect ratio of the cylinder and Wi^* are the dominant dimensionless parameters. The onset of divergent streamlines is enhanced by the large normal stresses and also by the lower elasticity numbers.

7.1. Introduction

Most of the studies concerning the complex viscoelastic fluid flows were driven by the emerging and rapid development of many industrial applications. Considering the diversity and the complexity of viscoelastic fluid flows that can be encountered in industrial applications, some simplified versions of these complex flows have been thoroughly investigated and were selected as benchmark flows to be studied independently by different research groups in order to obtain accurate results. The ubiquity of the flow around a circular cylinder in addition to the absence of geometrical singularities and the specificities of viscoelastic fluids, made the flow around a confined cylinder in a channel with as blockage ratio of 50% an established benchmark flow problem for the development of numerical methods (Brown and McKinley, 1994). Since the establishment as a benchmark case, several experimental and numerical studies have been conducted at the macro-scale (characteristic dimensions of order $10 - 10^3$ mm) and more recently also at the micro-scale (characteristic dimensions of order $10 - 10^3$ μm) (Oliveira *et al*., 2012). Given the extensive research of this benchmark case, the development of experimental studies for other blockage ratios, different from the 50% benchmark case, is also a relevant subject of interest which will be addressed in this chapter.

For Newtonian fluids, several studies at the macro-scale report a non-monotonic dependence of the critical Reynolds number for onset of vortex shedding on the blockage ratio (Chakraborty *et al.*, 2004; Sahin and Owens, 2004; Kumar and Mittal, 2006). The numerical study of Sahin and Owens (2004), investigates the flow around a cylinder for blockage ratios above 0.5. Numerical simulations (Camarri and Giannetti, 2010; Kanaris *et al.*, 2011) and also experimental studies (Rehimi *et al.*, 2008) of the two dimensional (2D) and three dimensional (3D) flow of Newtonian fluids around a circular cylinder in a duct have been performed for blockage ratios of 1/5 and 1/3, and for Reynolds number varying between 10 and 400. These studies show some differences in the critical conditions for the onset of vortex shedding between the 2D case and the 3D geometries with small blockage ratios. Bishop and Yarusevych (2011) studied the effect of the blockage ratio on the flow field past a circular cylinder at high Reynolds number (Re = 57 000) for different blockage ratios. The results show that the vortex shedding frequency increases with the blockage ratio, but such high Re flow conditions are clearly away from our range of interest (low to moderate Re up to the onset of flow instabilities).

For viscoelastic fluids, most of numerical studies were performed in 2D geometries (Huang and Feng, 1995; Tokpavi *et al.*, 2008; Mossaz *et al.*, 2012) while the existing 3D numerical studies focus primarily on the 50% blockage ratio benchmark case (Richter *et al.*, 2010; Sahin, 2011; Tenchev *et al.*, 2011).

The development of lab-on-a-chip systems or micro total analysis systems (μTAS) observed in recent years, leading to the scale-down of laboratory functions and processes, has generated a significant interest in investigating complex flows of viscoelastic fluids. The reduction in size of the microfluidic systems leads to a significant reduction in the Reynolds number (*Re*), but also originates a strong increase of the Deborah number (*De*), a measure of the importance of elastic effects, which is defined as the ratio between the relaxation time of the fluid and a characteristic time scale of the flow. Reducing the scale of the geometry leads to a significant decrease of the characteristic time scale of the flow, thus originating highly elastic flow conditions, difficult to attain at macro-scale, even for fluids with small relaxation times. It is expected that at highly elastic flow conditions, purely elastic instabilities will occur, even though *Re* is small.

For Newtonian fluids, there is no dramatic change as we move from macro to micro-scale (Deshmukh and Vlachos, 2005), as shown in Chapters 5 and 6. On the other hand, as we move from macro- to micro-scale using viscoelastic fluids, there are important differences on the flow behaviour as discussed in Chapter 5 due to the different inertial effects at both scales for similar *De*. The flow of viscoelastic fluids in microfluidic devices with cylindrical obstacles has important applications in the development of passive micromixers, where the obstacles are placed in the microchannels to create secondary transverse flows that induce chaotic fluid motions (Kumar *et al.*, 2011). When crossing the cylinder, the flexible macromolecules of the polymer solutions develop large elastic normal stresses that can trigger flow instabilities, which can be used to enhance mixing (Stone *et al.*, 2004). Several studies using viscoelastic fluids refer the development of micromixers with cylindrical obstacles in the flow using different layouts (Wang *et al.*, 2001; Wang *et al.*, 2002b, a; Lin *et al.*, 2003; Wang *et al.*, 2003a, b; Wang, 2004). It should be noted that none of the previous studies refer the blockage ratio effect in the viscoelastic flow around a confined cylinder, which is the main motivation for this work.

The previous studies concerning the viscoelastic fluid flow around a cylinder in microfluidic devices for a blockage ratio of 50% reported in chapters 5 and 6 have highlighted the

appearance of elastic instabilities upstream of the cylinder, near the forward stagnation point, and have shown the influence of the cylinder aspect ratio (*AR* - ratio between the cylinder length and the cylinder diameter) on the flow field. Motivated by these works and in an attempt to fill some gaps in our knowledge on the flow of complex fluids around a cylinder, the present work focus on the blockage ratio effect in the viscoelastic fluid flow around a confined cylinder in microfluidic devices.

To achieve these goals, the complex 3D flow past a cylinder is characterised through flow visualizations using streak photography and detailed velocity measurements using micro-particle image velocimetry (μPIV), to assess effect of the blockage ratio. For that purprose, a Newtonian and two Boger fluids were used from creeping flow conditions up the onset of time-dependent flow. The results are presented for BR = 25%, 50% and 75% to assess the BR effect for constant aspect ratio ($AR \approx 1$). Some of the experimental results are compared with numerical simulations for validation. The good agreement observed between the experimental and numerical results for the Newtonian fluid flow, allows the analysis of flow details and flow conditions not studied experimentally.

The remainder of this chapter is organized as follows: the experimental set-up and techniques are described in section 7.2. Section 7.3 presents the rheological characterization of the fluids used. The governing equations and a brief outline of the numerical method employed in the calculations are described in section 7.4. Section 7.5 presents and discusses the experimental results and compares them with the corresponding numerical simulations. Finally, in section 7.6 the main conclusions are summarized.

7.2. Experiments

7.2.1. Microchannels: fabrication and geometry

The microchannels were fabricated in polydimethylsiloxane, PDMS (Sylgard 184, Dow Corning), from an SU-8 photoresist reusable mould using standard soft lithography techniques (McDonald *et al.*, 2000). The microchannels with a confined cylinder placed at the centre include one inlet and one outlet located at the extremes of the microchannels. The microchannel width (H) is constant, H = 212 μm. The cylinder diameters' (D) used were D = 53 μm, 105 μm and 158 μm to provide the three different blockage ratios BR = 25%, 50% and 75%, respectively. The depth (h) of the microchannel, which is the same as the

length of the cylinder, is variable and takes the values h = 213 μm for BR = 75%, h = 105 μm for BR = 50% and h = 58 μm for BR = 25%, to keep $AR \approx 1$ (more precisely, AR = 1.3, 1.0 and 1.1, respectively, as can be observed in Figure 7.1. The origin of the coordinate system, represented in Figure 7.1, is located at the cylinder's geometric centre.

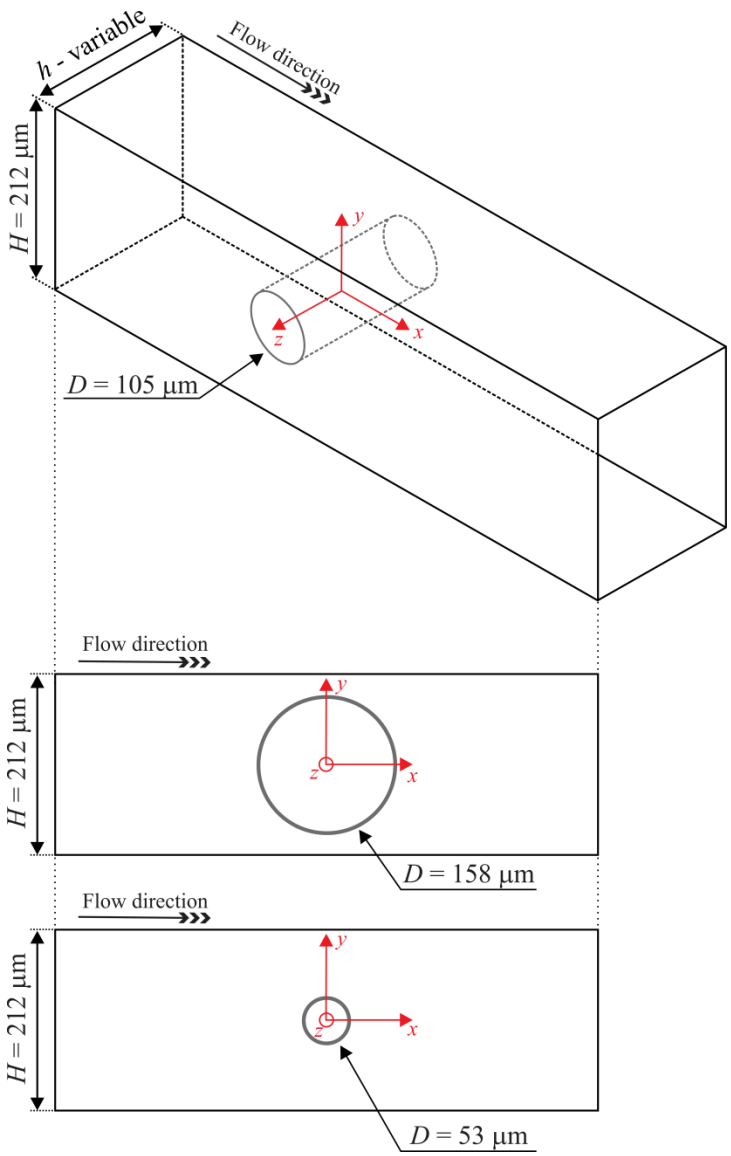

Figure 7.1. Illustration of the microchannels used.

Additionally, microchannels with a constant depth h = 213 μm, were also used to investigate the *AR* effect for the different blockage ratios under study. The microchannels dimensions used in the experiments are summarized on Table 7.1.

Table 7.1. Dimensions of the microgeometries.

Width - *H* (μm)	Cylinder Diameter - *D* (μm)	*BR = (D / H)*	Depth – *h* (μm)	*AR* = (*h / D*)
212	53	25%	58	1.1
			213	4.0
	105	50%	105	1.0
			213	2.0
	158	75%	213	1.3

A syringe pump (Nemesys, Cetoni GmbH) was used to inject the fluid in the microchannels and control the flow rate. Hamilton Syringes with different volumes (10 μl − 1 ml) were used, according to the desired flow rate, and were connected to the microgeometries using Tygon tubing with an internal diameter of 0.44 mm.

7.2.2. Experimental techniques

7.2.2.1. *Flow visualization*

The flow visualizations were carried out using streak photography, in an inverted epi-fluorescence microscope (DMI 5000M, Leica Microsystems GmbH) equipped with a CCD camera (DFC350 FX, Leica Microsystems GmbH), a 100 W mercury lamp (light source) and an appropriated filter cube (Leica Microsystems GmbH, excitation filter band pass BP 545/30 nm, short pass dichroic at 565 nm, and barrier filter BP 605/75 nm). The microgeometries containing the seeded fluid were continuously illuminated by the Hg light source and the light emitted by the fluorescent tracer particles was imaged through the

microscope objective (20×, NA = 0.4) onto the camera, with an exposure time that varied according to the flow rate, to capture the particles' pathlines.

The fluids were seeded with 1.0 μm fluorescent polystyrene tracer particles at a mass concentration of 100 ppm (Nile Red, Molecular Probes, Invitrogen; Ex/Em: 535/575 nm; density: 1.05 g/mL).

7.2.2.2. *Velocity field*

The velocity measurements were carried out using micro-particle image velocimetry (μPIV), in the same inverted epifluorescence microscope using a doubled pulsed Nd:YAG (neodymium-doped yttrium aluminum garnet) laser light source (Dual power 65-15, Dantec dynamics) operating at a wavelength of 532 nm. The time between the two consecutive pulses of light was adjusted according the flow rate in the range between 10 μs < Δt < 67 ms. At least 150 pairs of images were acquired using a CCD camera (Flow Sense 4M, Dantec Dynamics) running in double frame mode. The velocity fields were determined by processing the images using Dynamic Studio V2.3 software (Dantec Dynamics) which generates a two-dimensional velocity vector map for each image pair. A 20× objective (NA = 0.4) was used to capture the displacement of particles in a wide field of the microchannel. For PIV measurements, the fluids were seeded with fluorescent polystyrene tracer particles with 0.5 μm in diameter at a mass concentration of 90 ppm (Nile Red, Molecular Probes, Invitrogen; Ex/Em: 535/575 nm; density: ρ: 1050 kg/m^3).

7.3. Fluid characterization

One Newtonian and two Boger fluids were used in the experiments. The Newtonian fluid was de-ionized water and the Boger fluids were an aqueous solution of polyacrylamide (PAA) at a weight concentration of 125 ppm with 1% of NaCl (PAA125) and an aqueous solution of glycerine (85% w/w) with PAA at a weight concentration of 200 ppm with 1% of NaCl (PAA200). The composition and the density of the fluids are presented in Table 7.2. The density (ρ) of the fluids was measured using a pycnometer.

Table 7.2. Composition of the fluids and density measured at 293.2 K.

Fluid	PAA (ppm)	Glycerine (%)	Water (%)	NaCl (%)	Kathon (ppm)	ρ (kg/m^3)
Newtonian	-	-	100	-	25	999.8
Boger – PAA125	125	-	98.98	1.01	25	1001.1
Boger – PAA200	200	85.05	13.91	1.02	25	1225.8

The rheological characterization of the fluids in shear flow conditions was made in a rotational rheometer (Physica MCR 301, Anton Paar) with a 75 mm cone-plate system with 1º angle to measure the steady-state shear viscosity. In extensional flow conditions a capillary break-up extensional rheometer (Haake CaBER 1, Thermo Scientific) was used.

Figure 7.2 shows the shear viscosity (η) for the Boger fluids measured at different temperatures in the range between 288.2 K and 298.2 K. The time-temperature superposition principle was used in order to obtain the master curve at the reference temperature, T_0 = 293.2 K. The corresponding shift factor is defined as (Dealy and Plazek, 2009):

$$a_T = \frac{\eta(T)}{\eta(T_0)} \frac{T_0}{T} \frac{\rho_0}{\rho}, \tag{7.1}$$

where η (T_0) is the shear viscosity at the reference temperature T_0, η (T) is the shear viscosity at a given temperature T, ρ_0 is the density at the reference temperature and ρ is the density at temperature T. For the rheological measurements, the temperature variation is small, thus the fluid density does not change significantly and the shift factor simplifies to (Dealy and Plazek, 2009):

$$a_T = \frac{\eta(T)}{\eta(T_0)}. \tag{7.2}$$

Both the PAA200 and PAA125 Boger fluids have a nearly constant viscosity in the range of shear rates measured and the shear viscosities are 0.152 Pa s and 1.55 mPa s, respectively.

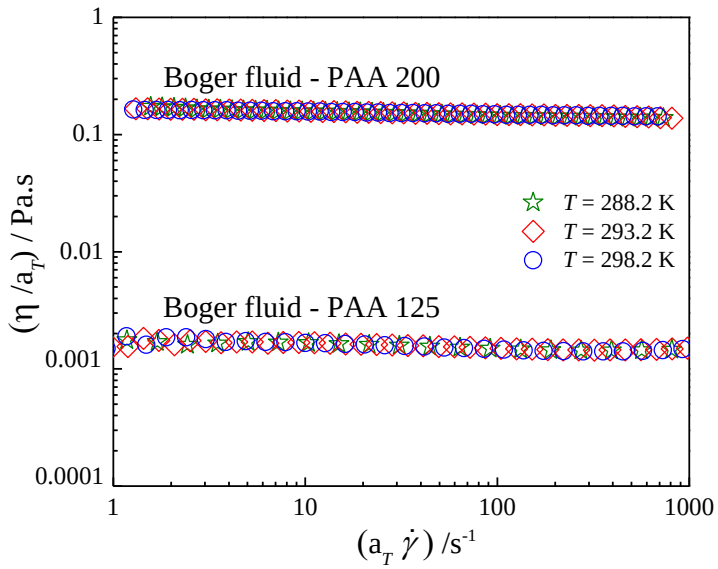

Figure 7.2. Steady shear viscosity of the Boger fluids PAA200 and PAA125.

Both Boger fluids were also characterised in extensional flow at the reference temperature (T_0 = 293.2 K) using the CaBER rheometer and the characteristic relaxation time in extensional flow was determined by fitting the experimental data of log [*D(t)*] *vs.* time in the linear region of Eq. (7.3) resulting from the elasto-capillary balance (Entov and Hinch, 1997):

$$\frac{D}{D_0} = e^{-\frac{t}{3\lambda}}, \tag{7.3}$$

where D_0 is the diameter of the filament at the reference time t = 0 and D is the diameter at time t. These measurements were performed using two circular plates with a diameter of 6 mm, an initial spacing of 3 mm and a final distance of 9 mm between the plates, with the strain step done in 50 ms.

As shown in Figure 7.3 the experimental data of log (D) vs. t was fitted using Eq. (7.3) and the relaxation time was determined from the slope, leading to λ = 86.7 ms for PAA200 Boger fluid and λ = 3.4 ms for the PAA125 Boger fluid. The relaxation time determined in extensional flow was used in the determination of *De*.

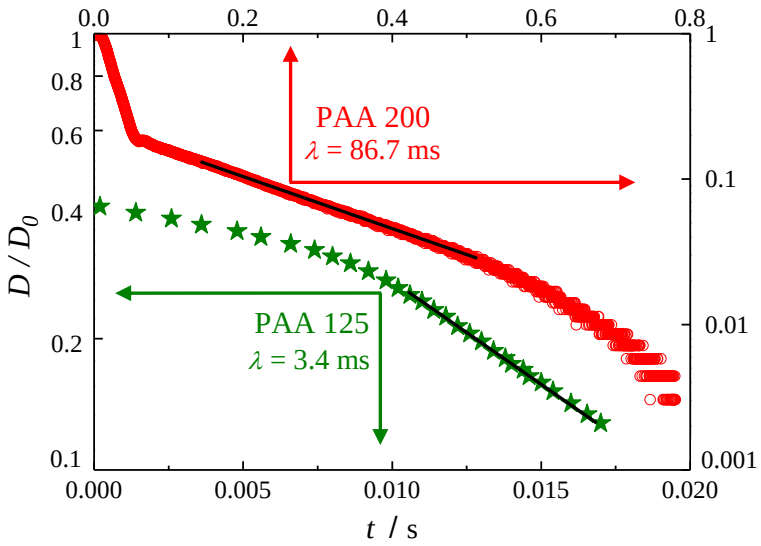

Figure 7.3. Diameter of the filament of the Boger fluids measured as a function of time using the CaBER rheometer.

7.4. Governing equations and numerical method

The numerical results for the flow of the Newtonian fluid and the Boger fluids were simulated using a fully-implicit finite-volume method algorithm (Oliveira *et al.*, 1998). The governing equations describing the isothermal laminar flow of an incompressible fluid are the mass conservation,

$$\nabla \cdot \mathbf{u} = 0, \tag{7.4}$$

and the momentum equations,

$$\rho\left(\frac{\partial \mathbf{u}}{\partial t} + \nabla \cdot \mathbf{uu}\right) = -\nabla p + \nabla \cdot \boldsymbol{\tau}, \tag{7.5}$$

where $\mathbf{u}$ represents the velocity vector, ρ the fluid density, t the time, p the pressure and $\boldsymbol{\tau}$ the extra-stress tensor. The extra-stress tensor is defined as the sum of a Newtonian solvent and a polymeric contribution $(\boldsymbol{\tau} = \boldsymbol{\tau}_s + \boldsymbol{\tau}_p)$. For Newtonian fluids, the polymeric contribution is neglected, $\boldsymbol{\tau}_p = \mathbf{0}$ and the Newtonian solvent component $\boldsymbol{\tau}_s$ is defined as:

$$\boldsymbol{\tau}_{\mathbf{s}} = \eta_s \left(\nabla \mathbf{u} + \nabla \mathbf{u}^{\mathrm{T}}\right) = 2\eta_s \mathbf{D} \ , \tag{7.6}$$

where η_s is the constant solvent viscosity and **D** is the deformation rate tensor.

For the numerical calculations of the non-Newtonian fluid flow, the polymeric contribution is included and is described using the Oldrody-B model:

$$\boldsymbol{\tau}_{\mathbf{p}} + \lambda\left(\frac{\partial \boldsymbol{\tau}_{\mathbf{p}}}{\partial \mathrm{t}} + \nabla \cdot \mathbf{u}\boldsymbol{\tau}\right) = \eta_{\mathrm{P}}\left(\nabla \mathbf{u} + \nabla \mathbf{u}^{\mathrm{T}}\right) + \lambda\left(\boldsymbol{\tau}_{\mathbf{p}} \cdot \nabla \mathbf{u} + \nabla \mathbf{u}^{\mathrm{T}} \cdot \boldsymbol{\tau}_{\mathbf{p}}\right) \tag{7.7}$$

where λ is the relaxation time of the fluid, η_{p} is the contribution of the polymer to the shear viscosity and $\boldsymbol{\tau}$ represents the polymer tensor.

The numerical method is based on the time-marching version of the SIMPLEC pressure correction algorithm formulated for collocated variables (Oliveira *et al.*, 1998). The discretization of the governing equations is based on central differences for diffusion terms and is based on the CUBISTA high-resolution scheme (Alves *et al.*, 2003) for the convective terms, both in the momentum and constitutive equations.

The computational domain was mapped using block-structured meshes. Extensive sets of calculations were carried out by Ferreira (2006) to estimate the numerical accuracy and select an adequate mesh to provide mesh independent results. To generate the mesh the flow domain was divided into 24 blocks and within each block the cells were concentrated near the cylinder region. A zoomed view of the meshes used for each aspect ratio under study is show in Figure 7.4.

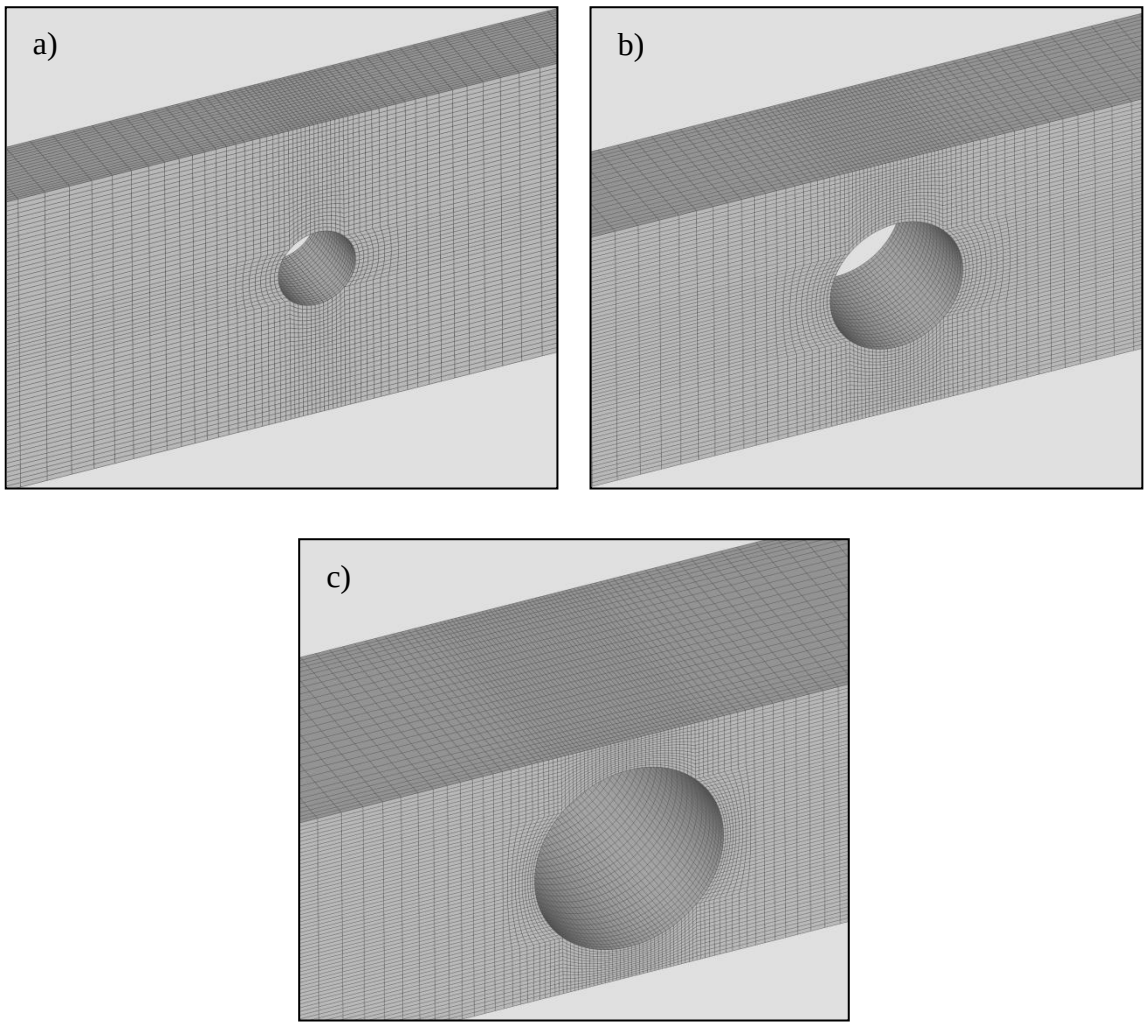

Figure 7.4. Zoomed view of the mesh used in the numerical simulations for: a) *BR* = 25% and *AR* = 1.1; b) *BR* = 50% and *AR* = 1.0; *BR* = 75% and *AR* = 1.3.

7.5. Results

A detailed discussion of the flow of the Newtonian fluid and the two Boger fluids around a confined cylinder in microfluidic devices are presented in this section to assess the influence of the blockage ratio (*BR*) in the critical conditions for the onset of elastic instabilities near the cylinder. The flow visualizations and velocity measurements were conducted at the centreplane ($z/R = 0$). The flow regimes studied varied from creeping flow conditions (negligible Reynolds number) up to the onset of time-dependent flow. The results are presented for *BR* = 25%, 50% and 75% for $AR \approx 1$, to isolate the *BR* effect (section 7.5.1). Additionally, the viscoelastic flow of the Boger fluids was studied in channels with the same cross-section but with varying cylinder diameters (D = 53, 105, 158 μm), thus at different *AR* and *BR* conditions, but at constant *AR* x *BR* and Wi^* (section 7.5.2).

The flow under study depends on two geometrical dimensionless numbers (e.g. *AR* and *BR*) and also on the Reynolds number (*Re*), here defined as:

$$Re = \frac{\rho U R}{\eta}, \tag{7.8}$$

where U is the bulk velocity in the channel, R is the cylinder radius and ρ and η are the density and shear viscosity of the fluid, respectively.

The flow of non-Newtonian fluids is also characterised using an additional dimensionless number involving the relaxation time of the fluid, such as the Deborah number, which represents the ratio of the relaxation time of the fluid (λ) and a characteristic time scale of the flow (*R/U*), and is here defined as (Reiner, 1964):

$$De = \frac{\lambda U}{R}. \tag{7.9}$$

The flow of non-Newtonian fluids can alternatively be characterised by the Weissenberg number which quantifies the ratio between elastic and the viscous stresses, and is defined as (Poole, 2012):

$$Wi = \frac{\eta \lambda \dot{\gamma}^2}{\eta \dot{\gamma}} = \lambda \dot{\gamma}, \tag{7.10}$$

where $\dot{\gamma}$ is a characteristic shear rate, which can be estimated as $\dot{\gamma} \approx U / R$, leading to a similar definition as the Deborah number, $Wi \approx \lambda U / R$.

Sometimes the ratio between the Weissenberg number and the Reynolds number is used, which represents the ratio between the elastic and inertial forces, and is known as the elasticity number (*El*):

$$El = \frac{Wi}{Re} = \frac{\eta \lambda}{\rho R^2}. \tag{7.11}$$

To establish a direct comparison between the results for the different *BR*, an alternative Weissenberg number (or Deborah number) can be defined as:

$$Wi^* = \frac{\lambda}{R/\left(U_L - U\right)} = \frac{\lambda U}{R} \frac{BR}{(1-BR)}, \tag{7.12}$$

where U_L is the bulk velocity of the flow between the wall and the cylinder shoulder. In Eq. (7.12) the characteristic time of the flow is taken as the inverse of the following elongational strain rate, $(U_L - U)/R$. Note that when BR = 0.5 the usual definition of De, Eq. (7.10), is recovered.

7.5.1. Blockage ratio effect

7.5.1.1. *Flow Visualizations*

For the Newtonian fluid the experiments were conducted for flow conditions in the range of $3.0 < Re < 70$. Figure 7.5 shows the experimental and numerical flow patterns within the separated flow region downstream the cylinder for the Newtonian fluid taken for the following cases at $AR \approx 1$: BR = 25%, Re = 30; BR = 50%, Re = 28; BR = 75%, Re = 18. The Newtonian fluid flow is characterised by the appearance of a steady separated flow in the cylinder wake above a critical Reynolds number and the comparison between the experimental and numerical results shows a good agreement.

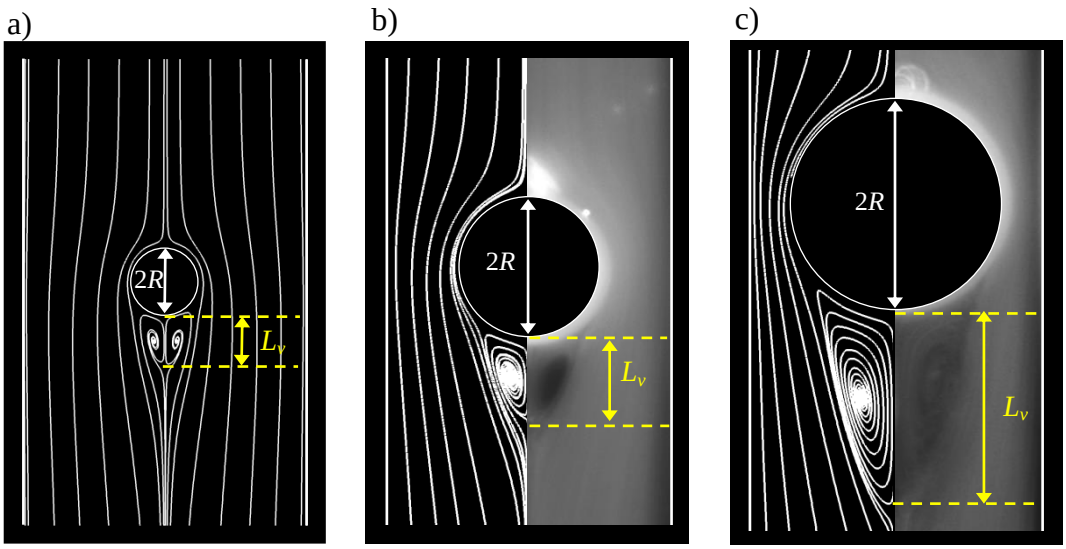

Figure 7.5. Numerical and experimental (right hand side b) and c)) flow patterns at the symmetry plane (z/R = 0) for the Newtonian fluid: a) Re = 30, AR = 1.1, BR = 25%; b) Re = 28, AR = 1.0, BR = 50%; c) Re = 18, AR = 1.3, BR = 75%.

Note the 3D nature of the flow which is clearly visible in the open nature of the recirculations, which is more visible in the lower *BR*. The fluid in the recirculation flows in a spiraling way, from the centre toward the periphery of the recirculation, and then the flows towards the exit direction.

From the whole set of experimental Newtonian fluid flow visualizations and the corresponding numerical simulations, it was possible to plot in Figure 7.6 the variation of the recirculation length (L_v/R) with *Re* for the different values of *BR* and for *AR* ≈ 1. The recirculation length (L_v) was measured at the symmetry plane (z/R = 0) and corresponding values were normalized with the cylinder radius. The symbols represent the experimental data and the lines represent the numerical predictions. The comparison between the experimental data and the numerical predictions shows a good agreement.

It is clear that L_v increases with *Re*. Comparing the different *BR* results, we can observe that the critical value of *Re* for the onset of flow separation decreases as *BR* increases, at least for the higher *BR* cases, showing that the blockage of the flow anticipates the onset of flow separation and the onset of the time dependent flow. The critical Reynolds number for the onset of flow separation was found to be *Re* ≈ 6.5 for *BR* = 75% and *Re* ≈ 8.0 for both *BR* = 50% and *BR* = 25%.

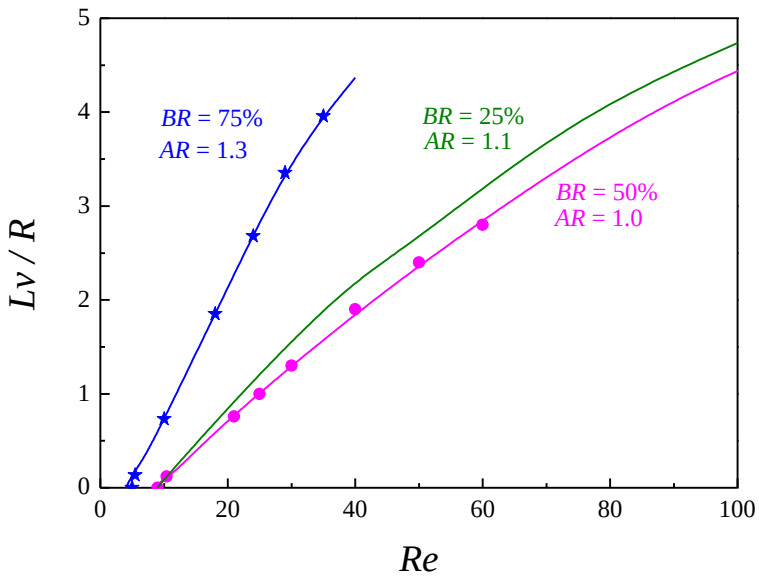

Figure 7.6. Variation of the normalized vortex length with *Re* for *BR* = 25% (*AR* = 1.1), *BR* = 50% (*AR* = 1.0) and *BR* = 75% (*AR* = 1.3). Comparison between experiments (symbols) and numerical predictions (lines). For *BR* = 25% only numerical predictions are shown.

For the Boger fluids the influence of the elasticity on the flow patterns was studied in the range of $0.1 < Wi^* < 70$ for the PAA200 Boger fluid and in the range of $0.05 < Wi^* < 11$ for the PAA125 Boger fluid. The effect of the modified Weissenberg number (Wi^*) on the flow patterns of the PAA200 Boger fluid was investigated at the symmetry plane ($z/R = 0$) as a function of *BR*, for $AR \approx 1.0$, and the resulting flow patterns are illustrated in Figures 7.7-7.9.

For lower Wi^*, the flow is symmetric upstream and downstream of the cylinder (cf. Figures 7.7a, 7.8a and 7.9a). As Wi^* increases we can observe the appearance of steady divergent streamlines, near the forward stagnation point, due to the increase of the normal stresses of the viscoelastic fluid (cf. Figures 7.7b-d, 7.8b-f and 7.9b-d). The onset of the divergent streamlines occurs at a critical Weissenberg number (Wi_c^*), in the range $Wi_c^* \approx 7$ - 10 for all *BR* under study, thus justifying the choice of Wi^* for reporting the results, instead of *De* (or *Wi*). As Wi^* increases further, at least up to $Wi^* \approx 40$, the divergent streamlines become progressively more pronounced, but remain steady for the *BR* = 25% and *BR* = 50% cases (cf. Figures 7.8f and 7.9d). For *BR* = 75%, the values of Wi^* achieved experimentally before the channels start leaking is higher and as Wi^* was increased further an elastic instability occurs upstream of the cylinder (cf. Figures 7.7e-f) leading to the onset of time-dependent flows at a critical Wi^* between 41 and 52.

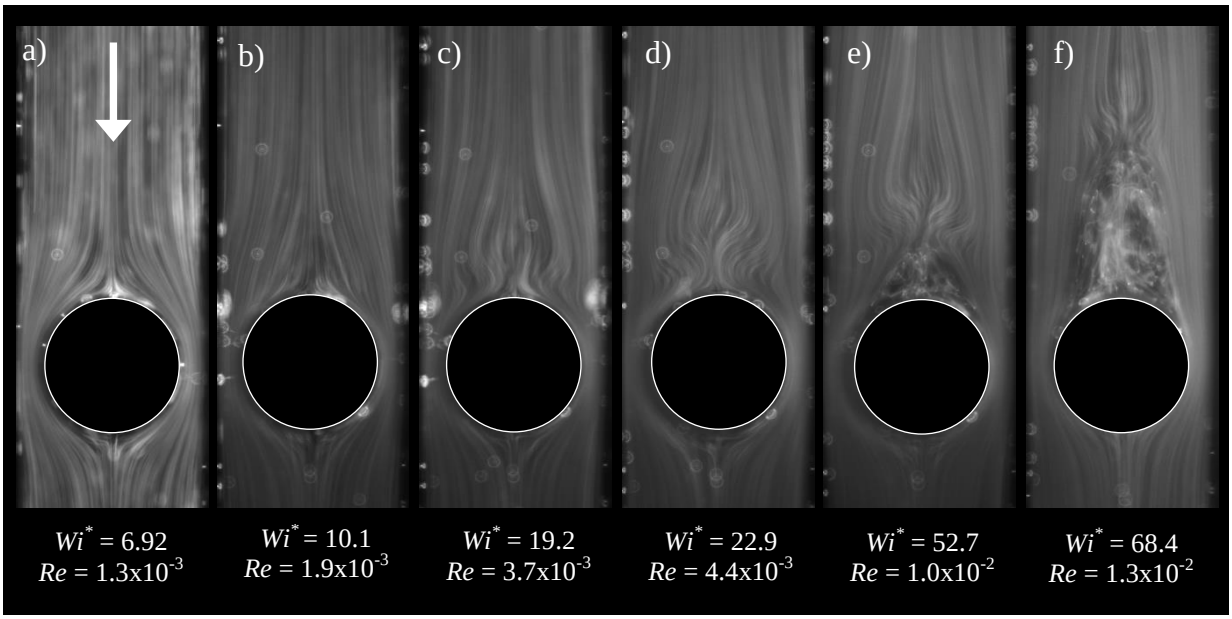

Figure 7.7. Influence of Wi^* on the flow patterns of the PAA200 Boger fluid at the symmetry plane ($z/R = 0$) for *BR* = 75 % and *AR* = 1.3.

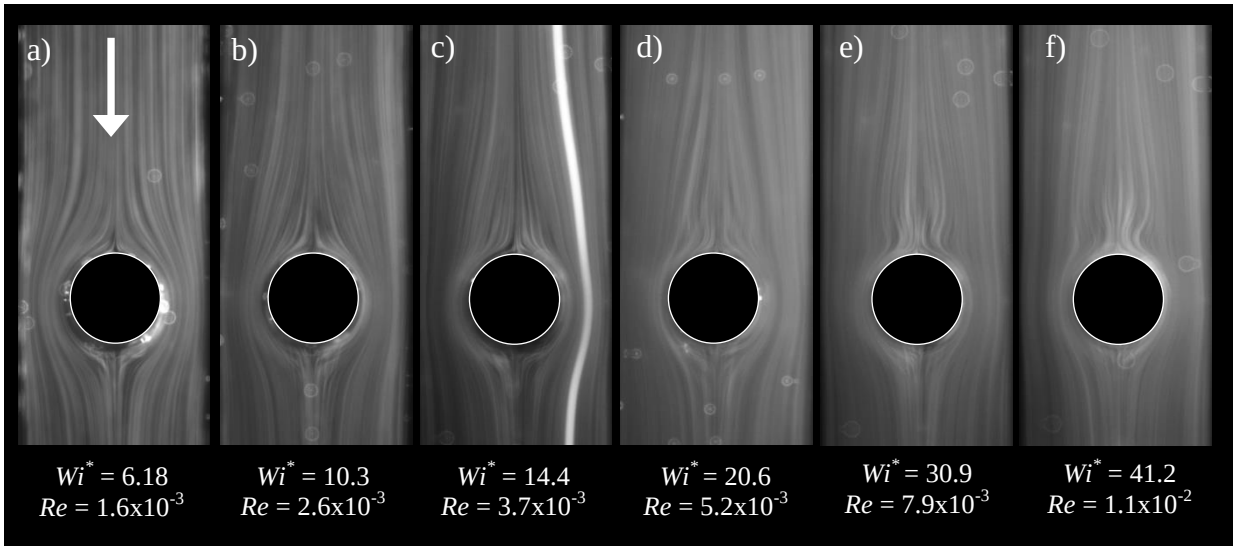

Figure 7.8. Influence of Wi^* on the flow patterns of the PAA200 Boger fluid at the symmetry plane (z/R = 0) for BR = 50 % and AR = 1.0.

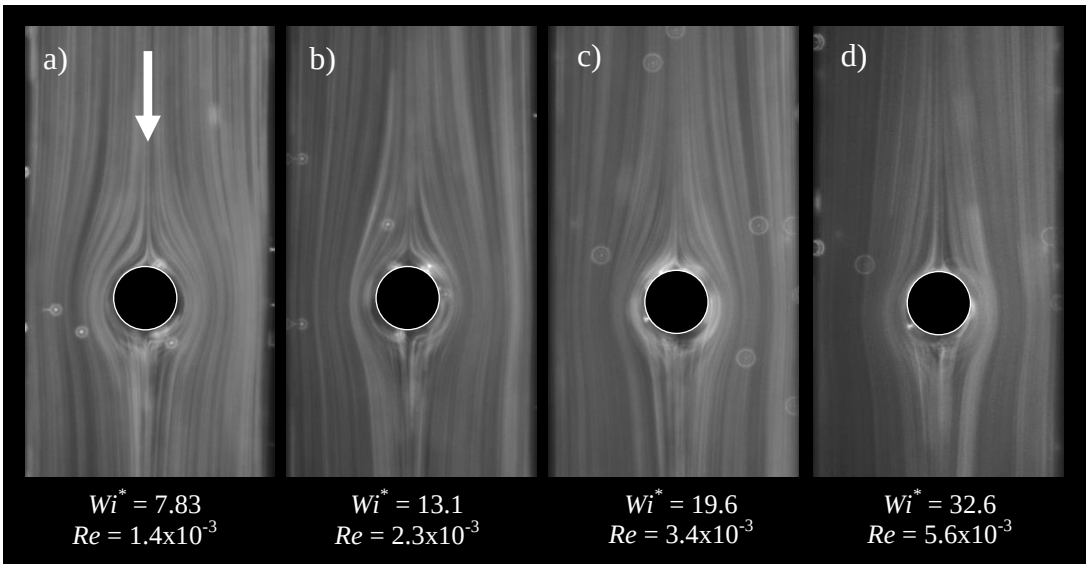

Figure 7.9. Influence of Wi^* on the flow patterns of the PAA200 Boger fluid at the symmetry plane (z/R = 0) for BR = 25 % and AR = 1.1.

The influence of the modified Weissenberg number Wi^* on the flow patterns of the PAA125 Boger fluid at the symmetry plane ($z/R = 0$) is illustrated in Figures 7.10-7.12 as a function of BR, for $AR \approx 1$.

As also found for the PAA200 Boger fluid, for lower Wi^* the flow is symmetric upstream and downstream the cylinder (cf. Figures 7.10a, 7.11a and 7.12a). As Wi^* increases steady divergent streamlines appear near the forward stagnation point (cf. Figures 7.10b-c, 7.11b-c and 7.12b-c), at a critical Weissenberg number (Wi_c^*), in the range $Wi_c^* \approx 1.1 - 1.5$ for all BR. As Wi^* increases further, the divergent streamlines becomes progressively more pronounced until an elastic instability arises upstream of the cylinder, near the forward stagnation point, leading to time-dependent flow for all BR, which occurs at $Wi^* \approx 3$ (cf. Figure 7.10d-f, 7.11d-f and 7.12-d).

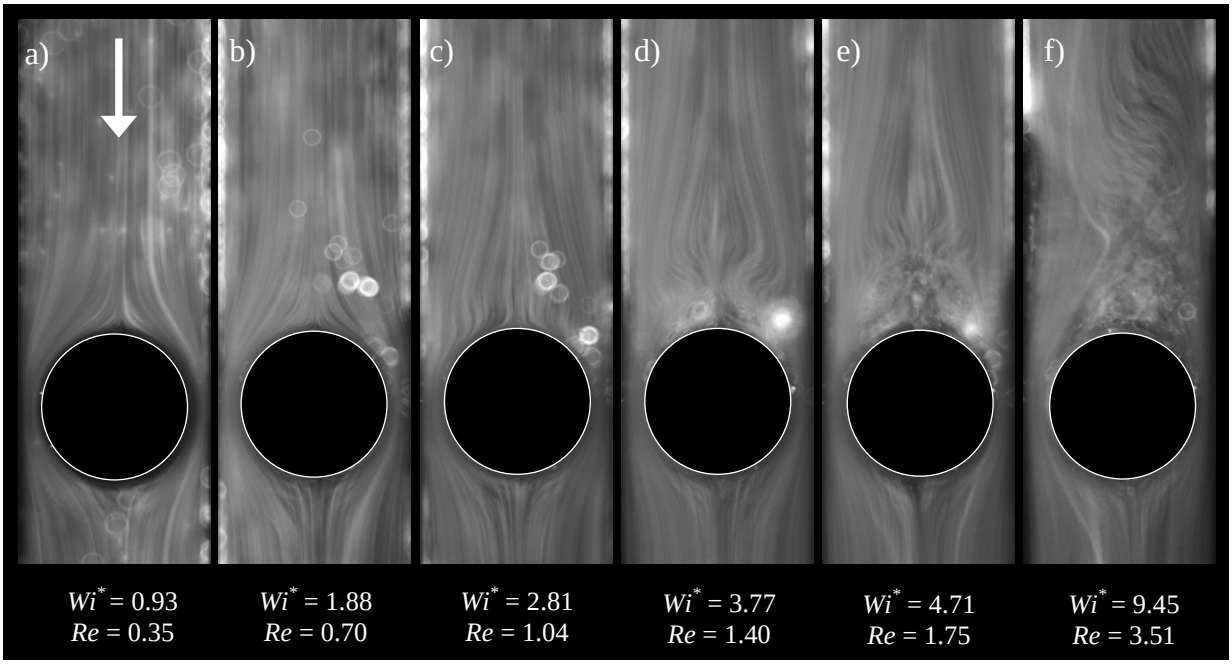

Figure 7.10. Influence of Wi^* on the flow patterns of the PAA125 Boger fluid at the symmetry plane ($z/R = 0$) for $BR = 75$ % and $AR = 1.3$.

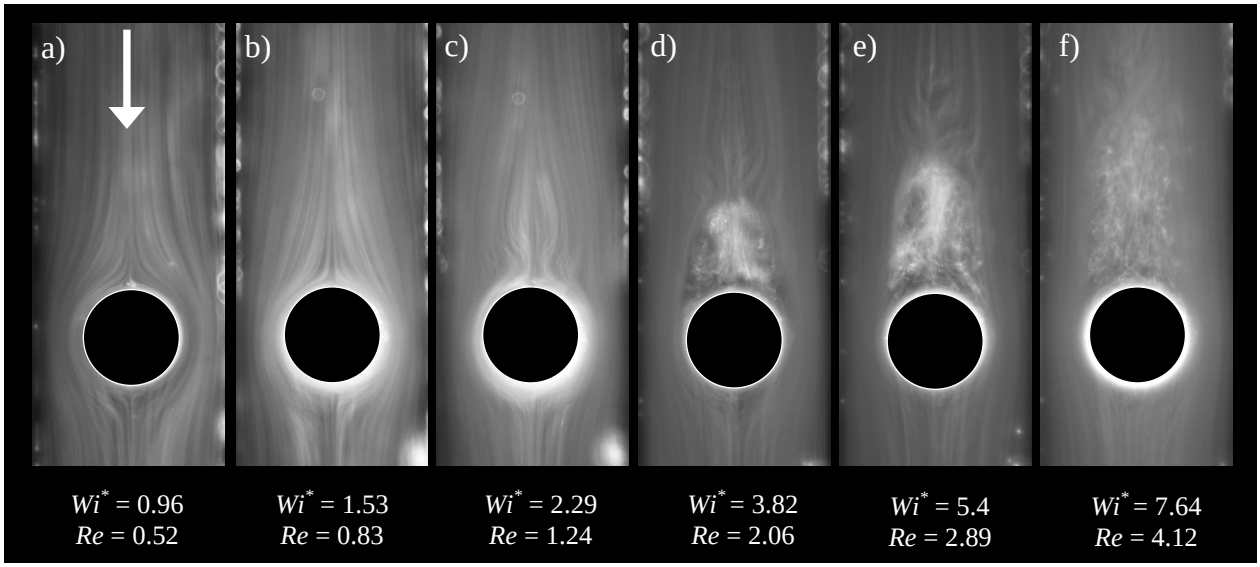

Figure 7.11. Influence of Wi^* on the flow patterns of the PAA125 Boger fluid at the centreline ($y/R = 0$; $z/R = 0$) for BR = 50 % and AR = 1.0.

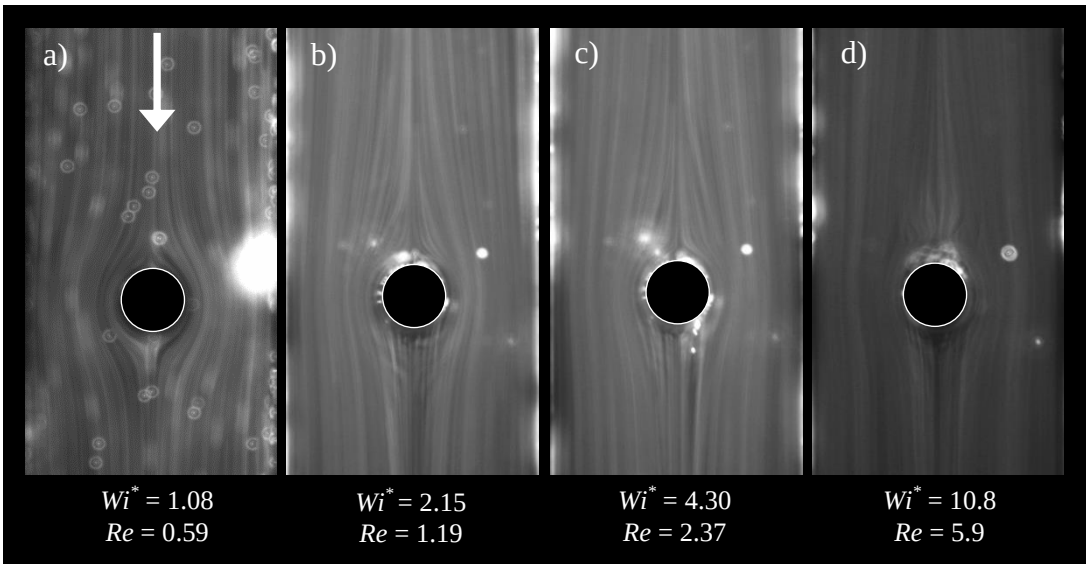

Figure 7.12. Influence of Wi^* on the flow patterns of the PAA125 Boger fluid at the centreline ($y/R = 0$; $z/R = 0$) for BR = 25 % and AR = 1.1.

For the PAA200 Boger fluid, the elasticity number Wi^*/Re is of order of 10^3, while for the PAA 125 Boger fluid Wi^*/Re takes values of the order of one, showing that the inertial forces are more significantly relevant for the PAA125 Boger fluid, as expected due to the smaller shear viscosity and smaller relaxation time. The flow of the PAA200 Boger fluid is clearly dominated by the elastic forces, while for the PAA125 Boger fluid viscous, inertial and elastic forces are of the same order of magnitude, and the interplay between inertia and elasticity makes the flow more prone to develop inertio-elastic flow instabilities.

7.5.1.2. *Velocity fields*

Figures 7.13 and 7.14 show the influence of fluid elasticity in the streamwise dimensionless velocity (u/U) along the centreline ($y/R = 0$; $z/R = 0$) for $AR \approx 1$ and for BR = 25%, 50% and 75% for both the Boger fluids. The solid lines represent the numerical predictions for a Newtonian fluid under creeping flow conditions ($Re \rightarrow 0$) and the dashed lines represent the numerical simulations obtained with the Oldroyd-B model for the PAA200 Boger fluid. The range of Deborah numbers reached in the numerical predictions is significantly smaller than in the experiments, as a consequence of the high-Weissenberg number problem (Fattal and Kupferman, 2004) and the limitations of the simplified constitutive model used, and for that reason the numerical predictions are only shown for the cases of $Wi^* \leq 1.0$ and are reported only for the PAA 200 Boger fluid.

Regardless of the BR, the far upstream and far downstream dimensionless streamwise velocity of the Boger fluids is similar to the Newtonian fluid and is independent of Wi^*, since the viscosity is constant and the shape of the velocity profile is exclusively determined by the shear stress under fully-developed flow conditions. For the PAA200 Boger fluid (cf. Figure 7.13), as the fluid elements approach the cylinder they are progressively influenced by the presence of the cylinder, and this effect is nearly independent on Wi^* for BR = 25%. For BR = 50 and 75% the upstream velocity profiles are significantly dependent of Wi^*, and the influence of the cylinder is felt farther away from the cylinder for the higher Wi^*. The change in the velocity profiles observed upstream of the cylinder for BR = 50% and 75% are due to the onset of the divergent streamlines, which occurs at $Wi_c^* \approx 7$ - 10. For lower Wi^* values there are no considerable changes in the velocity profiles.

Downstream of the cylinder, the required length to achieve the fully-developed flow conditions increases with Wi^* for all *BR* cases, and decreases with an increase of *BR* for a given Wi^*. The numerical predictions obtained for *BR* = 50% and Wi^* = 1.0 are in good agreement with the experimental results, but a significant deviation is found for *BR* = 25% and Wi^* = 0.31.

For the PAA125 Boger fluid (cf. Figure 7.14), the required length to achieve fully-developed flow conditions downstream of the cylinder also increases with Wi^* for all *BR* and decreases with *BR* for a given Wi^*. Upstream of the cylinder the deceleration is now nearly independent of Wi^* for all *BR* for the flow conditions analysed, which according to the flow visualizations correspond to conditions without the appearance of the steady divergent streamlines. Therefore, upstream of the cylinder the velocity profiles are influenced by viscoelasticity under the divergent streamlines flow regime.

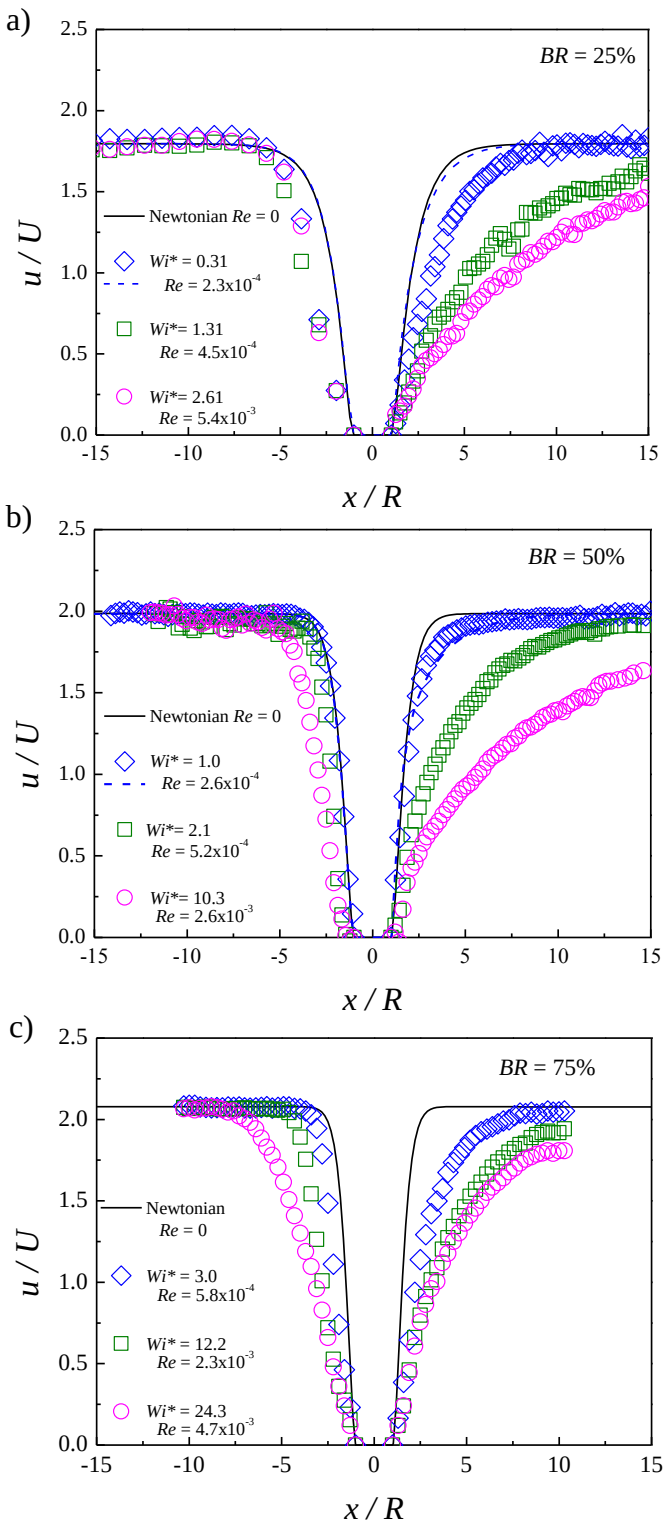

Figure 7.13. Streamwise velocity profiles along the centreline (y/R = 0, z/R = 0) of the PAA200 Boger fluid as a function of Wi^*: a) BR = 25% (AR = 1.1); b) BR = 50% (AR = 1.0); c) BR = 75% (AR = 1.3).

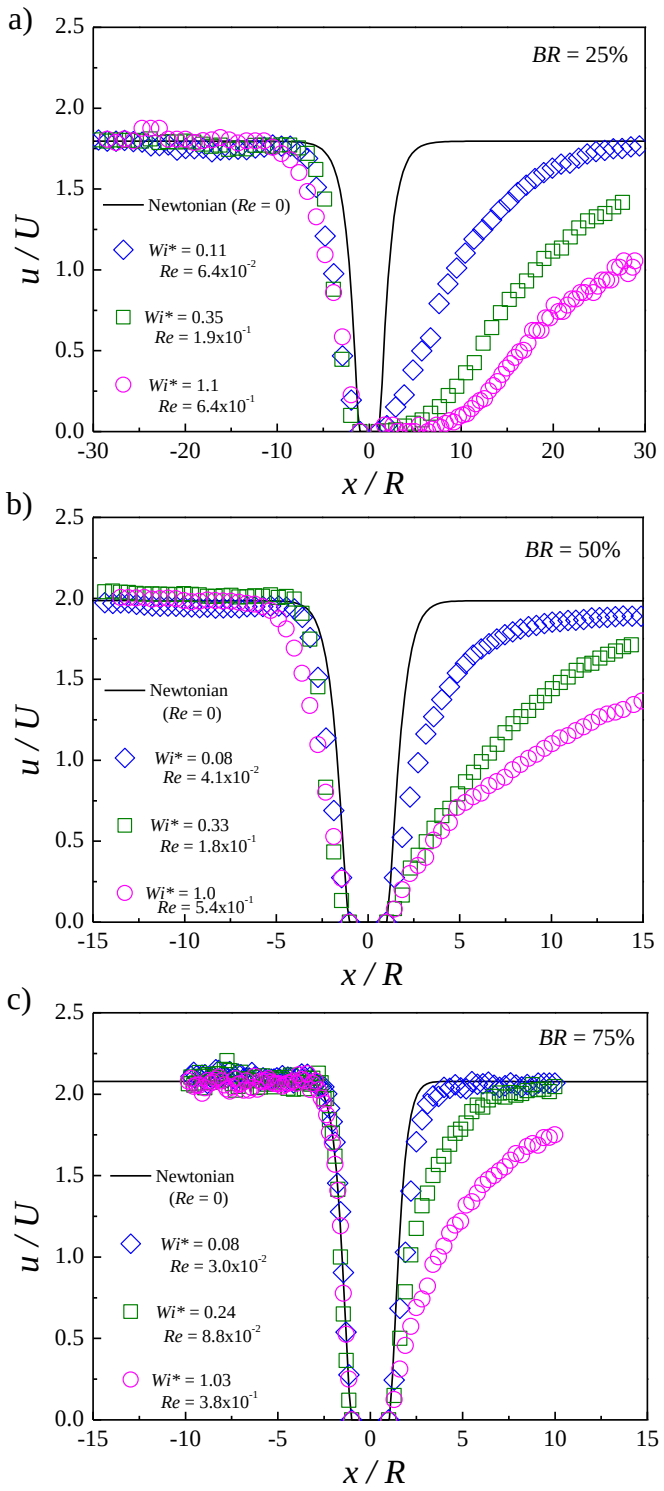

Figure 7.14. Streamwise velocity profiles along the centreline (y/R = 0, z/R = 0) of the PAA125 Boger fluid as a function of Wi^*: a) BR = 25% (AR = 1.1); b) BR = 50% (AR = 1.0); c) BR = 75% (AR = 1.3).

To better illustrate the influence created by the presence of the cylinder in the flow field, transverse profiles of the streamwise velocity component at multiple *x*-positions upstream and downstream of the cylinder were taken, in the locations illustrated in Figure 7.15. The upstream positions are not shown, but were taken at symmetric locations to the downstream positions illustrated.

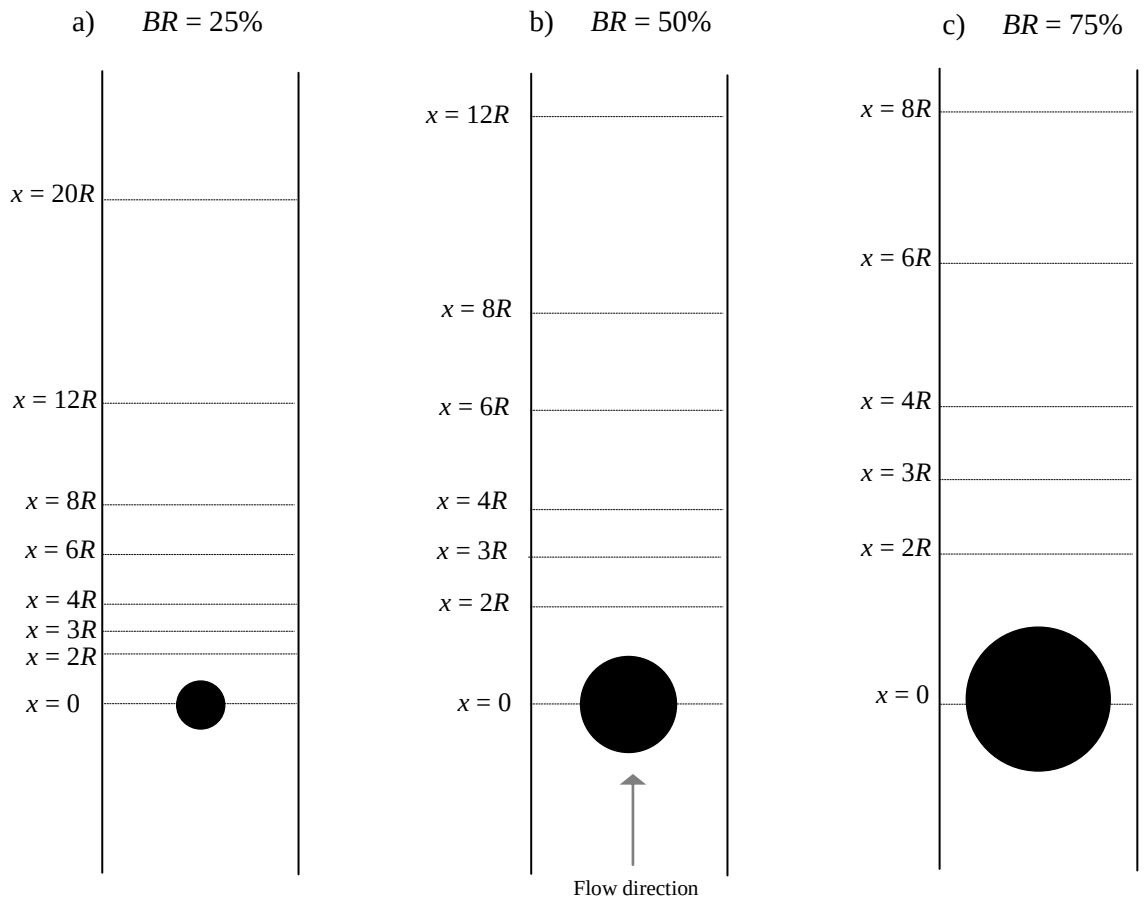

Figure 7.15. Downstream *x*-positions where the streamwise velocity profiles are presented in Figures 7.16 and 7.17: a) *BR* = 25%; b) *BR* = 50%; c) *BR* = 75%. The upstream locations (not shown) are symmetric to those shown downstream of the cylinder.

Figures 7.16 and 7.17 present the transverse profiles of the normalized streamwise velocity component at multiple *x*-positions, illustrated in Figure 7.15, along the flow direction as a function of *BR* for the PAA200 Boger fluid and for the PAA125 Boger fluid, respectively. The symbols represent the experimental results and the lines the analytical solutions for the

Newtonian fully-developed velocity profile (the comparison is only done far from the cylinder). The left axis represents the position along the flow direction, normalized with the cylinder radius, and the right axis represents the position along the flow direction normalized with half width of the microchannel ($H/2$).

For both fluids and far upstream of the cylinder at $x/(H/2) \approx -5$ the flow is nearly fully-developed, which is confirmed by the fully-developed flow analytical solutions (full lines). As the flow approaches the cylinder from $x/(H/2) \approx -5$ up to $x/(H/2) \approx -0.5$, the flow is strongly influenced by its presence due to the large axial normal stresses developed. The velocity profile loses the parabolic shape and two velocity peaks are formed near the cylinder, whose location depends on the *BR*, being more close to the side walls for the higher *BR*, due to the location of the open space between the cylinder and the wall, which becomes closer to the side wall as *BR* increases.

For the PAA200 Boger fluid, downstream of the cylinder up to $x/(H/2) \approx 5$ the velocity remains higher near the walls than at the centreline. As the fluid elements move away from the cylinder the fully-developed velocity is re-establish, which is confirmed by the comparison with the analytical solutions (full lines). For the PAA125 Boger fluid and due to the lower elasticity number (increased inertia) the recovery of the fully-developed velocity profiles occurs further away, in agreement with Figure 7.14.

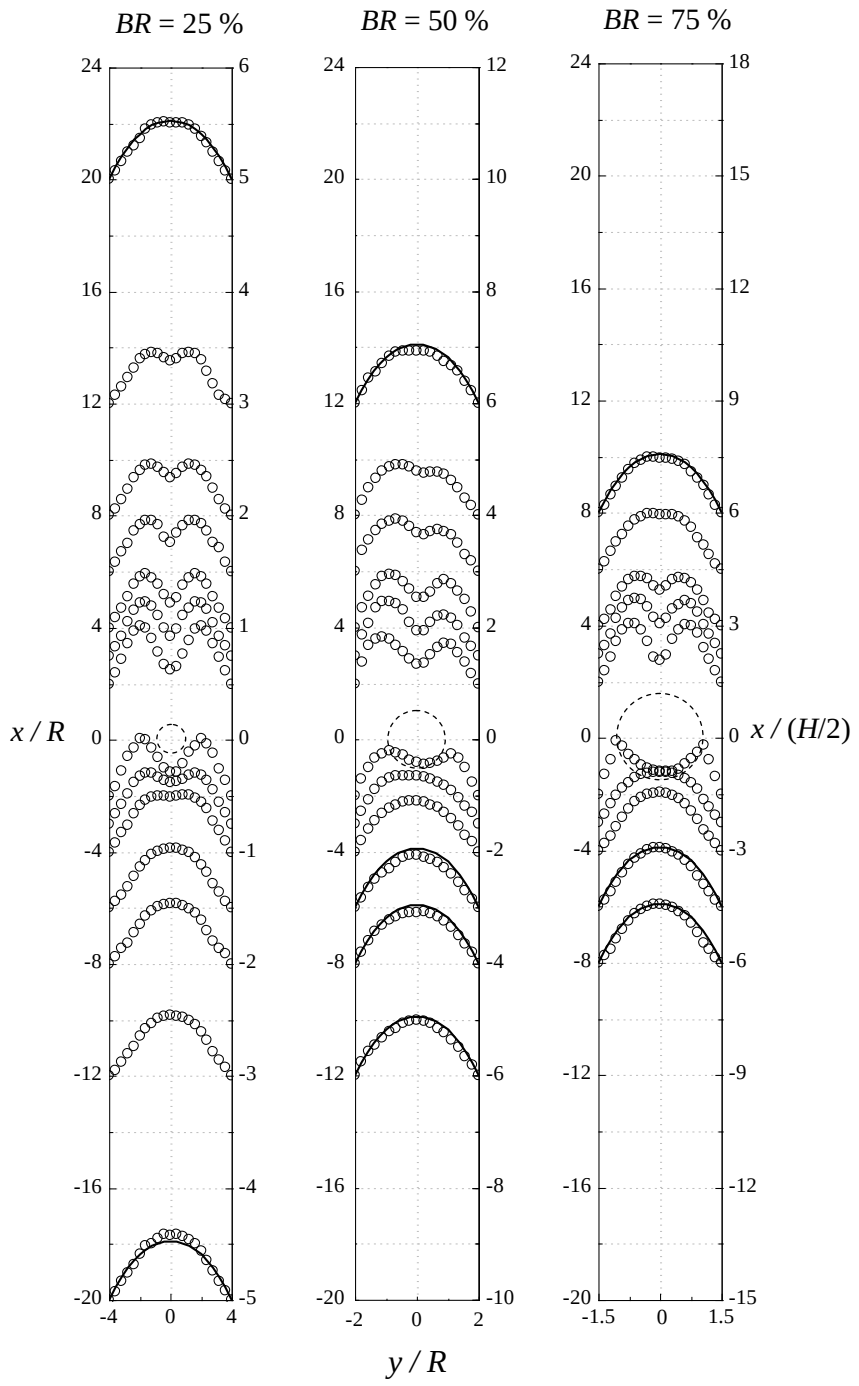

Figure 7.16. Transverse profiles of the normalized streamwise velocity at multiple *x*-positions along the flow direction as a function of *BR* for the PAA200 Boger fluid: *BR* = 25%, *AR* = 1.1, Wi^* = 4.1; *BR* = 50%, *AR* = 1.0 Wi^* = 4.1; *BR* = 75%, *AR* = 1.3, Wi^* = 4.2. The lines represent the analytical solutions for the Newtonian fully-developed velocity profile.

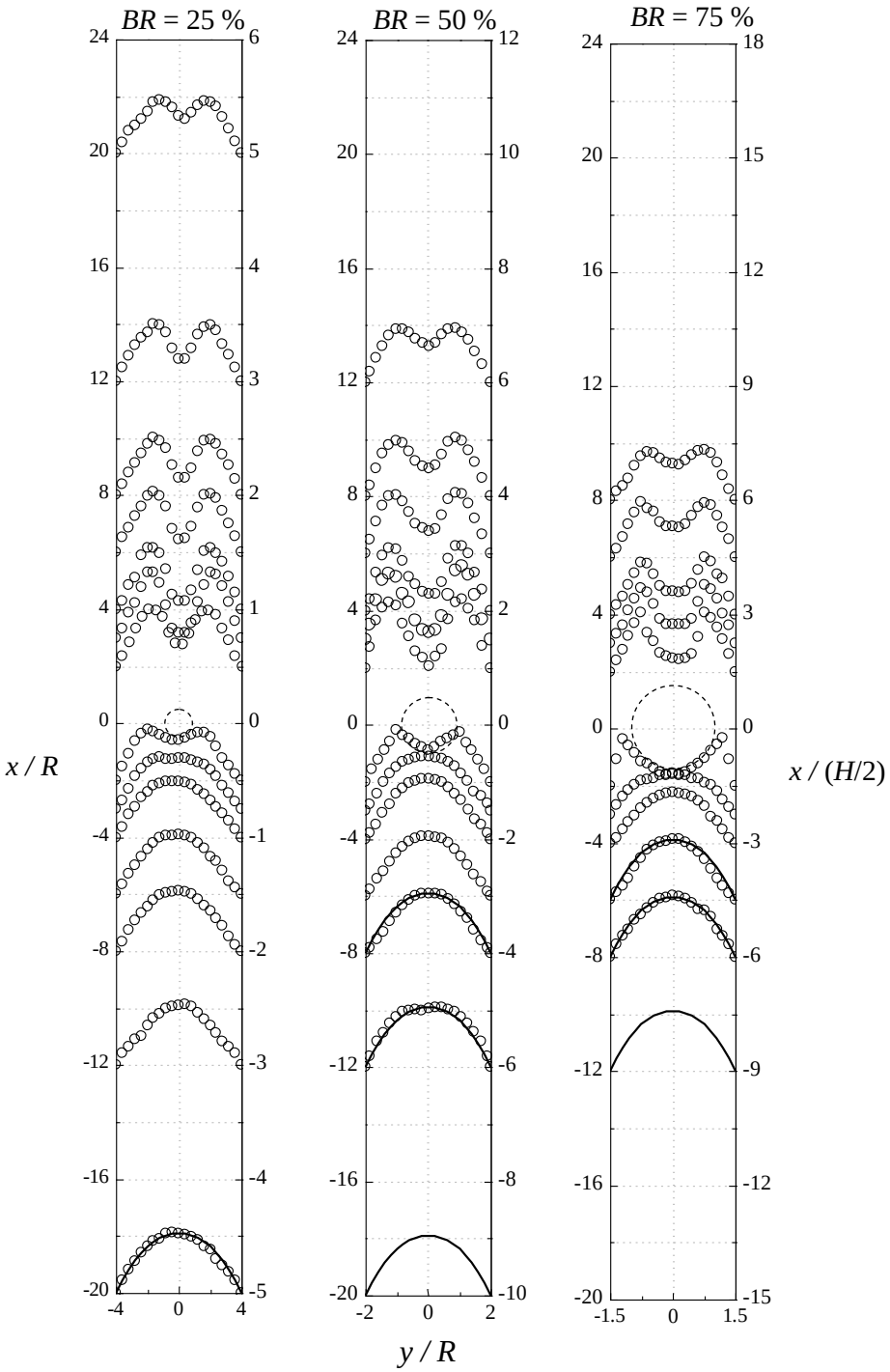

Figure 7.17. Transverse profiles of the normalized streamwise velocity at multiple *x*-positions along the flow direction as a function of *BR* for the PAA125 Boger fluid: *BR* = 25%, *AR* = 1.1, Wi^* = 0.98; *BR* = 50%, *AR* = 1.0 Wi^* = 1.0; *BR* = 75%, *AR* = 1.3, Wi^* = 0.96. The lines represent the analytical solutions for the Newtonian fully-developed velocity profile.

7.5.2. Microchannels with the same cross-section

In this section we investigate the flow in three different microchannels with the same cross-section (H = 212 μm, h = 213μm) but with cylinders with different diameters, D = 53 μm, 105 μm and 158 μm. The aspect ratio and the blockage ratio vary (AR = 4.0, BR = 25%; AR = 2.0, BR = 50%; AR = 1.3, BR = 75%), but AR x BR = h/H = 1.0 is constant and also Wi^* and Wi^*/Re values are kept almost constant.

The results in the previous section showed that the onset of divergent streamlines, and the onset of time-dependent flow occur at similar critical modified Weissenberg numbers (Wi^*) for the various BR geometries, keeping AR constant. In this section we analyse the flow patterns at constant Wi^* in geometries with the same cross-section, but with cylinders with different diameters.

Figure 7.18 illustrates the flow patterns of the PAA200 Boger fluid as a function of AR and BR, keeping Wi^* and the ratio Wi^*/Re approximately constant. As can be observed for the PAA200 Boger fluid and for $Wi^* \approx 10$, the divergent streamlines are observed only for AR = 1.3 and BR = 75% (cf. Figure 7.18a) while the flow is still symmetric for the remaining geometries. As Wi^* is increased, up to $Wi^* \approx 20$ (cf. Figure 7.18b) the divergent streamlines become more pronounced for AR = 1.3 and are already observable for the AR = 2.0 and 4.0 channels. However, the divergent streamlines are significantly more intense for AR = 2.0 than for AR = 4.0 (cf. Figure 7.18b).

Figure 7.19 illustrates the flow patterns of the PAA125 Boger fluids, in microchannels as a function of AR and BR, keeping Wi^* and Wi^*/Re approximately constant (and also the channel aspect ratio, h/H). For $Wi^* \approx 2$ the divergent streamlines are more pronounced for the lower AR cases as found previously for the PAA200 Boger fluid, but now due to the increase of inertia (lower values of Wi^*/Re), the effect is more pronounced and occurs at lower Wi^* (cf. Figure 7.19a). As Wi^* further increases to $Wi^* \approx 4$ (cf. Figure 7.19b) the divergent streamlines are clearly more pronounced.

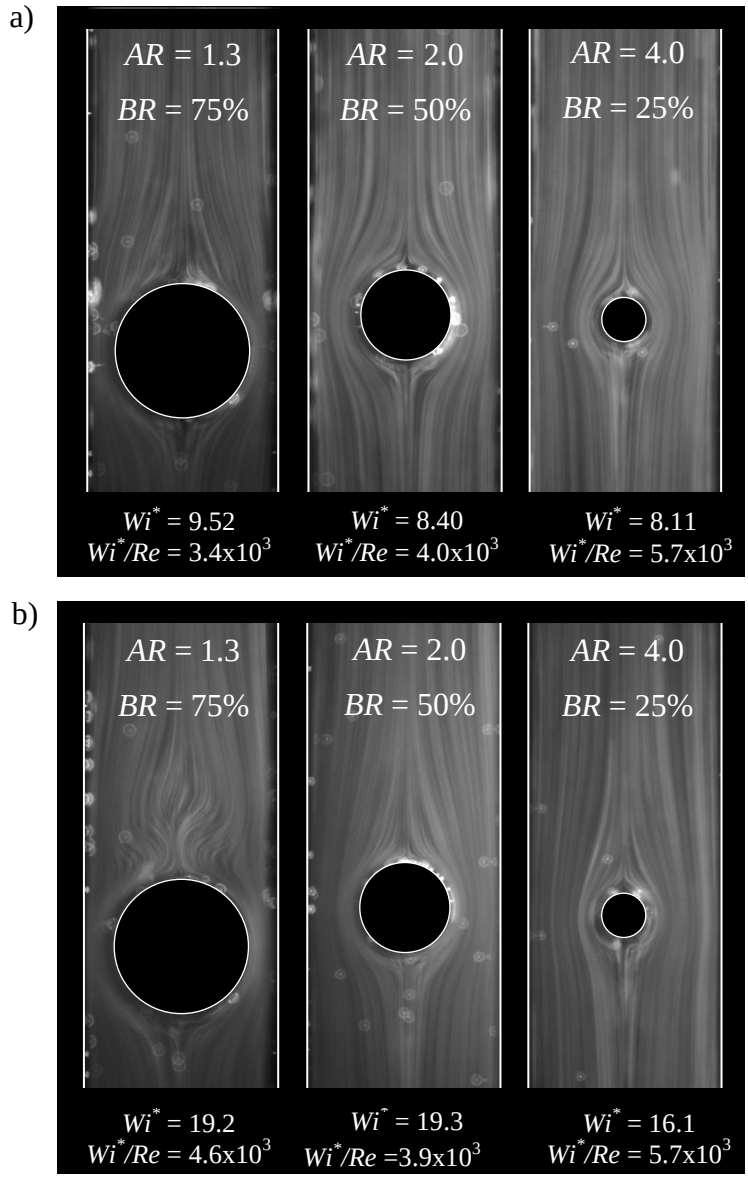

Figure 7.18. Flow patterns of the PAA200 Boger fluid at the symmetry plane ($z/R = 0$) for microchannels with the same cross-section (H = 212 μm, h = 213μm) with cylinders with different diameters (D = 158 μm, AR = 1.3, BR = 75%; D = 105 μm, AR = 2.0, BR = 50%; D = 53 μm, AR = 4.0, BR = 25%) and $Wi^*/Re \approx 5\times10^3$: a) $Wi^* \approx 10$; b) $Wi^* \approx 20$.

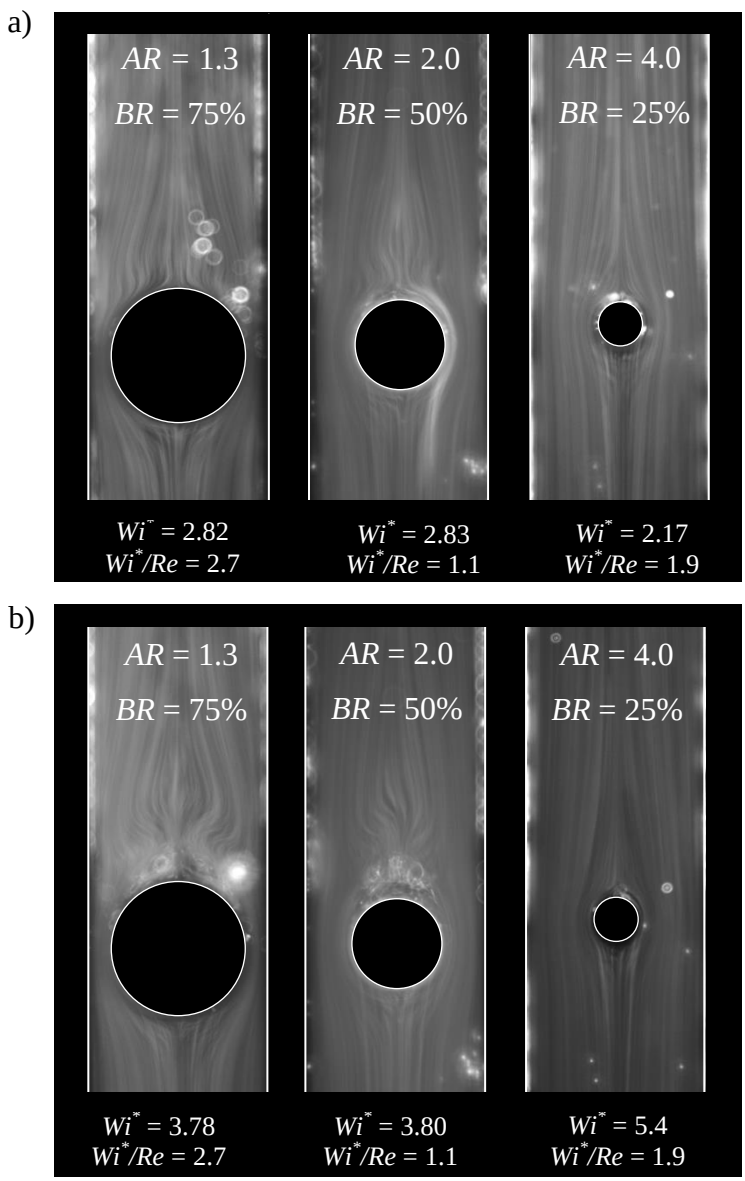

Figure 7.19. Flow patterns of the PAA125 Boger fluid at the symmetry plane ($z/R = 0$) for microchannels with the same cross-section (H = 212 μm, h = 213μm) with cylinders with different diameters (D = 158 μm, AR = 1.3, BR = 75%; D = 105 μm, AR = 2.0, BR = 50%; D = 53 μm, AR = 4.0, BR = 25%) and $Wi^*/Re \approx 2$: a) $Wi^* \approx 2$; b) $Wi^* \approx 4$.

Figure 7.20 compares the flow patterns of the PAA200 and PAA 125 Boger fluids at the same Wi^* and AR to once again illustrate that at lower elasticity numbers (Wi^*/Re) the divergent streamlines are more pronounced. A similar behaviour occurs in contraction flows, for which the onset of divergent flow is enhanced by the large normal stresses but also inertia has a key role, as discussed by Alves and Poole (2007). As can be observed, for the same Wi^* and AR, the flow is symmetric for the PAA200 Boger fluid, while for the PAA125 Boger fluid the flow is asymmetric, with a marked elastic instability upstream of the cylinder.

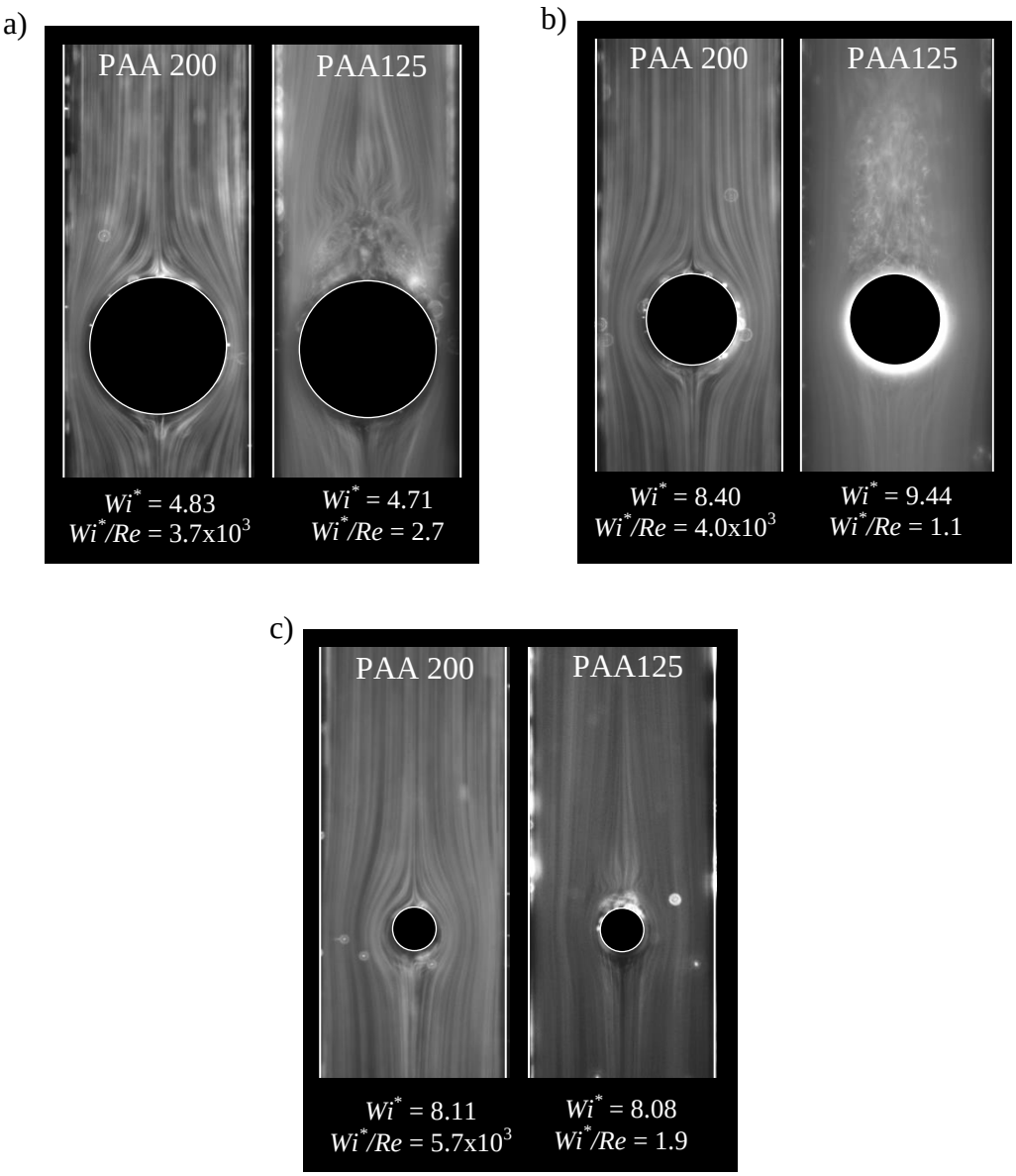

Figure 7.20. Effect of the fluid rheology at constant Wi^*: a) AR = 1.3, BR = 75%; b) AR = 2.0, BR = 50%; c) AR = 4.0, BR = 25%.

7.6. Conclusions

An experimental study was carried out on the microfluidic flow around a confined cylinder to assess the influence of the blockage ratio upon the flow field using a Newtonian and two Boger fluids. The flow was characterised using streak photography and μPIV. The Newtonian flow was simulated numerically to compare with the experimental results and in addition some low Wi^* flow conditions were also predicted numerically for the Boger fluids. The experimental flow conditions ranged from low *Re* and low Wi^* flow conditions up to the onset of time-dependent flow, for blockage ratios of 25%, 50% and 75%, and for an aspect ratio of $AR \approx 1$. Flow visualizations using microchannels with similar cross-section, but different cylinder diameters were also done at nearly constant Wi^* and Wi^*/Re was also carried out.

The measurements for the Newtonian fluid flow show the appearance of a recirculation downstream of the cylinder at a critical *Re* number, whose values increase as *BR* increases from 25% up to 75%, although the effect is more noticeable at high *BR*. At constant Wi^*/Re, the measurements for the Boger fluids at low Wi^* show that the flow is symmetric, but when Wi^* exceeds a critical value divergent streamlines are observed, becoming more intense with the increase of Wi^*. When the Wi^* is increased further, an elastic instability arises upstream of the cylinder leading to time-dependent flow. Comparing the two Boger fluids used, for the PAA200 Boger fluid the inertia contribution is negligible and for that reason the observed effects on the flow patterns are due to purely elastic effects. In contrast for the PAA125 Boger fluid the inertial effects are of the same order of elastic effects, and the onset of divergent streamlines and time-dependent flow occurs at lower Wi^*, and are more intense.

The experimental flow patterns at nearly constant Wi^* and Wi^*/Re in geometries with the same cross-section, but with cylinders with different diameters, show that the aspect ratio of the cylinder (*AR*) and the Wi^* are preferred dimensionless parameters to collapse the data, since the critical Wi^* is nearly independent of *AR* for all *BR* investigated.

It was also observed that at lower elasticity numbers (Wi^*/Re) the divergent streamlines are more pronounced and the onset of divergent flow is enhanced by the large normal stresses and also by inertia, which is more relevant for the PAA125 Boger fluid ($Wi^*/Re \approx 2$) than for the PAA200 Boger fluid ($Wi^*/Re \approx 5\times10^3$) and for that reason for the PAA125 Boger fluid the divergent streamlines are clearly more intense for similar Wi^*.

References

Alves, M.A., Oliveira, P.J., Pinho, F.T., 2003. A convergent and universally bounded interpolation scheme for the treatment of advection. Int J Numer Meth Fl 41, 47-75.

Alves, M.A., Poole, R.J., 2007. Divergent flow in contractions. J Non-Newton Fluid Mech 144, 140-148.

Bishop, M., Yarusevych, S., 2011. Mitigating Blockage Effects on Flow Over a Circular Cylinder in an Adaptive-Wall Wind Tunnel. Journal of Fluids Engineering 133, 081101-081107.

Brown, R.A., McKinley, G.H., 1994. Report on the VIIIth Int Workshop on numerical - methods in viscoelastic flows. J Non-Newton Fluid Mech 52, 407-413.

Camarri, S., Giannetti, F., 2010. Effect of confinement on three-dimensional stability in the wake of a circular cylinder. J Fluid Mech 642, 477-487.

Chakraborty, J., Verma, N., Chhabra, R.P., 2004. Wall effects in flow past a circular cylinder in a plane channel: a numerical study. Chem Eng Process 43, 1529-1537.

Dealy, J., Plazek, D., 2009. Time-temperature superposition - a user guide. Rheology Bulletin 78, 16-31.

Deshmukh, S.R., Vlachos, D.G., 2005. Novel micromixers driven by flow instabilities: Application to post-reactors. Aiche J 51, 3193-3204.

Entov, V.M., Hinch, E.J., 1997. Effect of a spectrum of relaxation times on the capillary thinning of a filament of elastic liquid. J Non-Newton Fluid Mech 72, 31-53.

Fattal, R., Kupferman, R., 2004. Constitutive laws for the matrix-logarithm of the conformation tensor. J Non-Newton Fluid Mech 123, 281-285.

Ferreira, H.H., 2006. Escoamento de fluidos newtonianos e viscoelásticos em torno de um cilindro: estudo numérico de efeitos tridimensionais. MSc thesis. MSc on Fundamentals and Applications of Fluid Mechanics. Faculdade de Engenharia da Universidade do Porto.

Huang, P.Y., Feng, J., 1995. Wall Effects on the Flow of Viscoelastic Fluids around a Circular-Cylinder. J Non-Newton Fluid Mech 60, 179-198.

Kanaris, N., Grigoriadis, D., Kassinos, S., 2011. Three dimensional flow around a circular cylinder confined in a plane channel. Phys Fluids 23, 064106-064114.

Kumar, B., Mittal, S., 2006. Effect of blockage on critical parameters for flow past a circular cylinder. Int J Numer Meth Fl 50, 987-1001.

Kumar, V., Paraschivoiu, M., Nigam, K.D.P., 2011. Single-phase fluid flow and mixing in microchannels. Chemical Engineering Science 66, 1329-1373.

Lin, Y., Gerfen, G.J., Rousseau, D.L., Yeh, S.R., 2003. Ultrafast microfluidic mixer and freeze-quenching device. Anal Chem 75, 5381-5386.

McDonald, J.C., Duffy, D.C., Anderson, J.R., Chiu, D.T., Wu, H.K., Schueller, O.J.A., Whitesides, G.M., 2000. Fabrication of microfluidic systems in poly(dimethylsiloxane). Electrophoresis 21, 27-40.

Mossaz, S., Jay, P., Magnin, A., 2012. Non-recirculating and recirculating inertial flows of a viscoplastic fluid around a cylinder. J Non-Newton Fluid Mech 177–178, 64-75.

Oliveira, M.S.N., Alves, M.A., Pinho, F.T., 2012. Microfluidic flows of viscoelastic fluids. Chapter 6 in Transport and Mixing in Laminar Flows: From Microfluidics to Oceanic Currents. Wiley - VCH Verlag.

Oliveira, P.J., Pinho, F.T., Pinto, G.A., 1998. Numerical simulation of non-linear elastic flows with a general collocated finite-volume method. J Non-Newton Fluid Mech 79, 1-43.

Poole, R.J., 2012. The Deborah and Weissenberg numbers. Rheology Bulletin, 32-39.

Rehimi, F., Aloui, F., Nasrallah, S.B., Doubliez, L., Legrand, J., 2008. Experimental investigation of a confined flow downstream of a circular cylinder centred between two parallel walls. J Fluid Struct 24, 855-882.

Reiner, M., 1964. The Deborah Number. Phys Today 17, 62.

Richter, D., Iaccarino, G., Shaqfeh, E.S.G., 2010. Simulations of three-dimensional viscoelastic flows past a circular cylinder at moderate Reynolds numbers. J Fluid Mech 651, 415-442.

Sahin, M., 2011. A stable unstructured finite volume method for parallel large-scale viscoelastic fluid flow calculations. J Non-Newton Fluid Mech 166, 779-791.

Sahin, M., Owens, R.G., 2004. A numerical investigation of wall effects up to high blockage ratios on two-dimensional flow past a confined circular cylinder. Phys Fluids 16, 1305-1320.

Stone, H.A., Stroock, A.D., Ajdari, A., 2004. Engineering flows in small devices: Microfluidics toward a lab-on-a-chip. Annu Rev Fluid Mech 36, 381-411.

Tenchev, R., Gough, T., Harlen, O.G., Jimack, P.K., Klein, D.H., Walkley, M.A., 2011. Three dimensional finite element analysis of the flow of polymer melts. J Non-Newton Fluid Mech 166, 307-320.

Tokpavi, D.L., Magnin, A., Jay, P., 2008. Very slow flow of Bingham viscoplastic fluid around a circular cylinder. J Non-Newton Fluid Mech 154, 65-76.

Wang, H.Z., 2004. Passive Mixing in Microchannels with Geometric Variations. Swinburne University of Technology, Australia.

Wang, H.Z., Iovenitti, P., Harvey, E., Masood, S., 2002a. Mixing of two fluid streams in a microchannel using the Taylor-Aris dispersion effect. Biomedical Applications of Micro- and Nanoengineering 4937, 158-163.

Wang, H.Z., Iovenitti, P., Harvey, E., Masood, S., 2002b. Optimizing layout of obstacles for enhanced mixing m microchannels. Smart Mater Struct 11, 662-667.

Wang, H.Z., Iovenitti, P., Harvey, E., Masood, S., 2003a. Numerical investigation of mixing in microchannels with patterned grooves. J Micromech Microeng 13, 801-808.

Wang, H.Z., Iovenitti, P., Harvey, E., Masood, S., 2003b. Passive mixing in microchannels by applying geometric variations. Microfluidics, Biomems, and Medical Microsystems 4982, 282-289.

Wang, H.Z., Iovenitti, P., Harvey, E., Syed, M., Deam, R., 2001. Mixing of liquids using obstacles in microchannels. Biomems and Smart Nanostructures 4590, 204-212.

Chapter 8

Viscoelastic fluid flow past an array of cylinders in a microfluidic channel

Abstract

This chapter presents an experimental study of the viscoelastic fluid flow through two different arrays of cylinders in a microfluidic channel, which can be considered as simplified two-dimensional porous media analogues. The viscoelastic fluids used were a Boger fluid and a wormlike micellar solution. Two cylinder arrangements were studied, namely a staggered and an aligned (or square) configuration. The complex 3D viscoelastic fluid flow patterns was characterized for different flow rates spanning from the Newtonian-like flow behaviour up to the onset of elastic instabilities, using flow visualizations and pressure drop measurements.

The pressure drop of the Newtonian fluid increases linearly with the flow rate for both arrangements. For the Boger fluid and for the wormlike micellar solution the pressure drop increases in a non-linear way with the flow rate, which is due to the onset of an elastic instability. The onset of these elastic instabilities indicates that an efficient mixing can be enhanced in porous media analogues.

8.1. Introduction

The viscoelastic fluid flow past a confined cylinder with 50% blockage ratio, which combines strong extensional and shear flow components, is an established benchmark since 1994 in computational rheology (Brown and McKinley, 1994) and has been the subject of several studies. To complement the studies of the flow around a confined cylinder, and taking into account the important practical applications, the studies concerning the flow past an array of cylinders, which can be thought as a two-dimensional (2D) analogue of a porous medium, has been of great interest considering its application in oil recovery or in the filtration of suspensions (Kozicki, 2001). A porous medium can be defined as a solid matrix with small interconnected cavities that allows fluid flow. The use of such porous media increases the surface area which allows the enhancement of mass and heat transfer rates (Sochi, 2010; Gunda *et al.*, 2013).

Viscoelastic flows through porous media formed by solid obstacles have been studied experimentally at the macro-scale (Khomami and Moreno, 1997; Anderson *et al.*, 2006; Rothstein, 2008; Moss and Rothstein, 2010; Yip *et al.*, 2011) and more recently, with the advances in microfluidics, have also been investigated at the micro-scale (Campo-Deano *et al.*, 2012; Gunda *et al.*, 2013). The scale-down of the flow geometry, typical in microfluidics, leads to a significant decrease of the characteristic time scale of the flow, originating highly elastic flow conditions, difficult to attain at macro-scales, especially for dilute polymer solutions.

The complexity of flow in porous media is due to the simultaneous importance of shear and extensional flow components, the typical anisotropy of the medium, with the added complexity created by inertial and elastic effects, inherent to viscoelastic flows. Viscoelastic fluids with constant viscosity, known as Boger fluids, have been used in several studies, to analyse the elastic effects isolated from the typical shear-thinning properties of most non-Newtonian fluids (Khomami and Moreno, 1997; Yip *et al.*, 2011; Campo-Deano *et al.*, 2012). Some studies analyse the influence of elastic effects using fluids with shear-thinning behaviour, such as wormlike micellar solutions (Moss and Rothstein, 2010).

Understanding the behaviour of wormlike micellar solutions is also important for the development of industrial applications such as jetting, spraying, enhanced oil recovery and turbulent drag reduction (Yang, 2002; Ober *et al.*, 2011). Micelles are formed through the

aggregation of surfactant molecules in solution and can form a variety of morphologies, such as spheres, ellipsoids, and long flexible cylindrical structures. The latter are commonly termed as wormlike micelles due to their shape. Wormlike micellar solutions display many of the properties observed in polymer solutions, such as viscoelasticity and shear-thinning, and usually lead to complex flows features (Yang, 2002). Despite the similar rheological properties with the so-called conventional polymer solutions, wormlike micelles are not covalently bonded along their backbone and consequently have the ability to break and reform dynamically during the flow, and for this reason the wormlike micelles are also known as "living" polymers (Larson, 1999). The break-up and reformation of wormlike micelles in strong shear and extensional flows can lead to variety of new and interesting phenomena and flow instabilities.

According to Khomami and Moreno (1997), the viscoelastic flow past a periodic array of cylinders can trigger the appearance of purely elastic flow instabilities, which can be exploited in order to promote mixing. The flow of viscoelastic fluids, carrying deformable macromolecules, in microchannels with solid obstacles generates large normal stresses which can trigger flow instabilities, and enhance mixing which is particularly useful at the micro-scale. According to Wang (2004), the use of cylindrical obstacles is an efficient method for mixing in microfluidic devices, that with properly designed geometric parameters, such as layout and number of obstacles, can improve the mixing performance without significantly increasing the pressure drop, which is important to prevent the degradation of the viscoelastic fluids.

Obtaining new insights on the complex flow of viscoelastic fluids through an array of cylinders in a microfluidic device, which can be considered as a simplified 2D porous medium analogue is the final goal of the present work. For that purpose, the flow of Newtonian and viscoelastic fluids past an array of cylinders is studied, which combines the elasticity enhancement through the scale-down of the microfluidic devices and the rheological specificities of the viscoelastic fluids used. One Boger fluid was used in order to isolate the elastic effects, and a wormlike micellar solution was also used in the experiments to explore the combined elastic and strong shear-thinning effects. Gunda *et al.* (2013) investigated the flow of a Newtonian fluid flow through microfluidic devices with cylindrical obstacles in aligned (square) and staggered arrangements to determine the pressure drop and flow resistance for both arrangements. This study can be used as a basis for comparison of the Newtonian fluid flow, since the arrangements under study in this work

are comparable. Two flow arrangements of porous media are investigated in this work, namely a staggered and an aligned (or square) configuration. The complex 3D viscoelastic fluid flow was characterized for a range of flow rates spanning from the Newtonian-like flow behaviour, up to the onset of elastic instabilities, using flow visualizations and pressure drop measurements.

The remainder of this chapter is organized as follows: the microchannels geometries, experimental techniques and the rheological characterization of the fluids are described in section 8.2. Section 8.3 presents and discusses the experimental results and the main conclusions are summarized in section 8.4.

8.2. Experimental

8.2.1. Fabrication techniques and geometry

The microchannels used in this study were fabricated in polydimethylsiloxane (PDMS) (Sylgard 184, Dow Corning), from an SU-8 reusable mould, using standard soft-lithography techniques (McDonald *et al.*, 2000). The final PDMS microchannels were obtained by replication in the SU-8 mould.

The flow through an array of cylinders was studied in two cylinder array configurations, namely staggered and aligned arrangements, as illustrated in Figure 8.1. The width (H) of the microchannels is 632 μm and 624 μm for the staggered and aligned configurations, respectively (cf. Figure 8.1). The depth of the microchannels, which coincides with the length of the cylinders is h = 158 μm, and the diameter of the cylinders is D = 105 μm. The cylinders were arranged to form interstitial spaces (e) of 50 μm for the staggered configuration and 14 μm for the aligned configuration, cf. Figures 8.1 b and c).

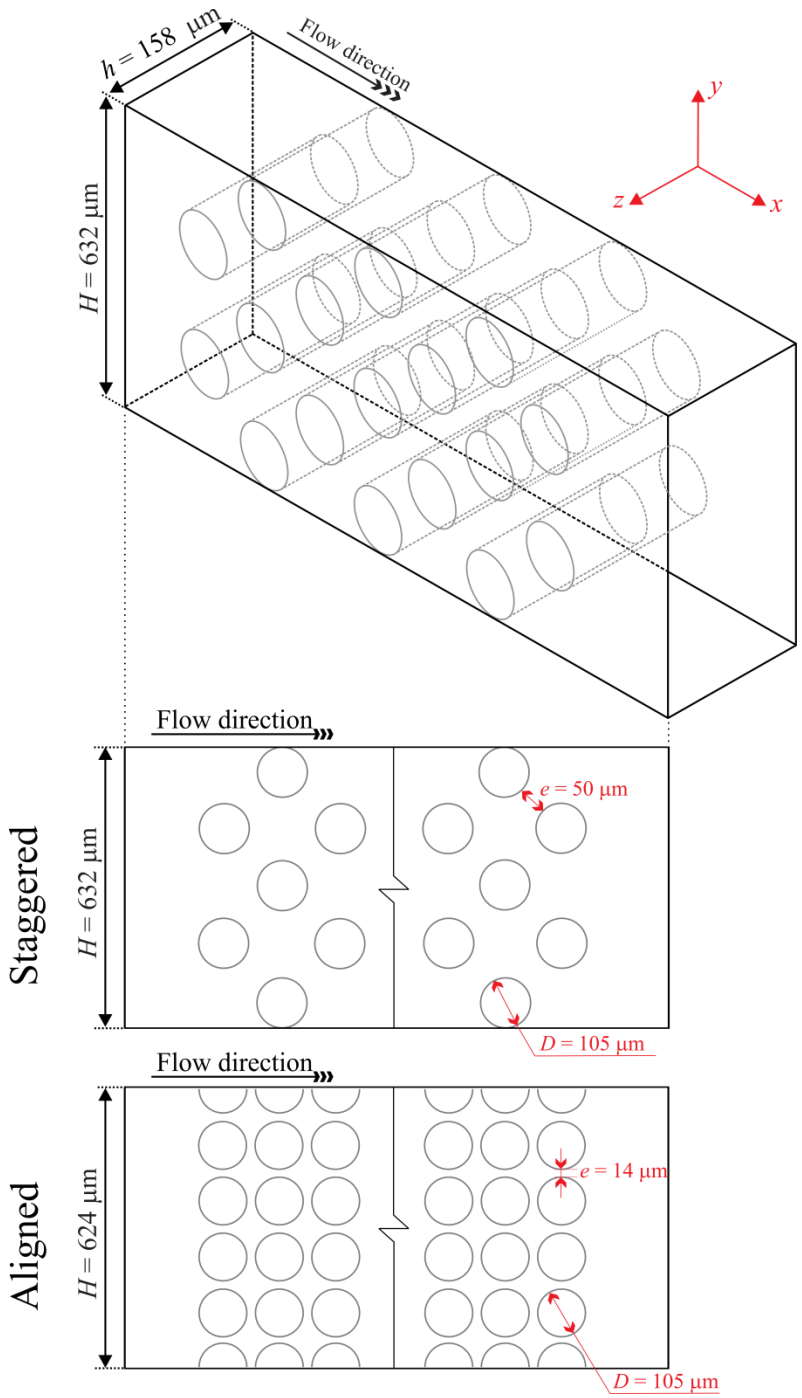

Figure 8.1. Sketch of the microfluidic devices with an array of cylinders: a) 3D view of the staggered configuration; b) front view of the staggered configuration; c) front view of the aligned configuration.

The dimensions of the microchannels were measured using a scanning electron microscope (SEM) FEG-ESEM/EDS/EBSD (FEI Quanta 400FEG ESEM/EDAX Genesis X4M), as illustrated in Figure 8.2.

a)

b)

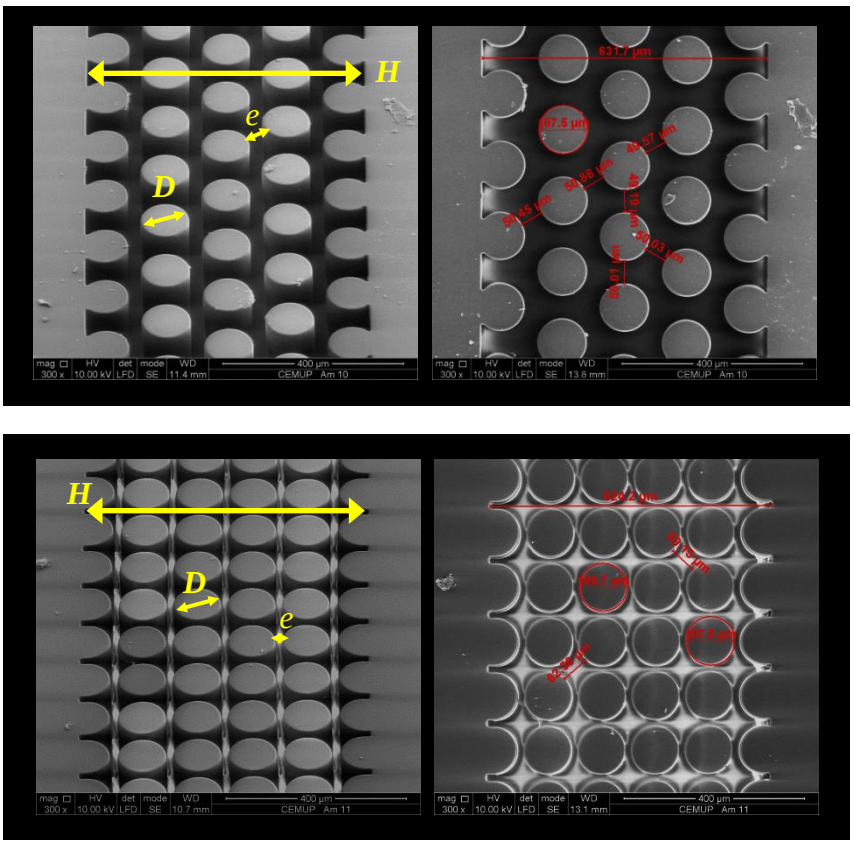

Figure 8.2. SEM images of the microfluidic devices with an array of cylinders: a) staggered configuration; b) aligned configuration. The dimensions of all elements are proportional to the microfluidic devices used.

The fluid flows in the microchannels, entering the device through one inlet and leaving through one outlet located at the ends of the microchannels, as illustrated in Figure 8.3. The pressure drop was measured using two pressure ports, which are positioned upstream (inlet) and downstream (outlet) of the region of interest. A syringe pump (Nemesys, Cetoni GmbH) was used to inject the fluid and control the flow rate in the microchannels. Hamilton syringes with different volumes (50 µl − 2 ml) were used, according to the desired flow rate, and were connected to the microgeometries using Tygon tubing with an internal diameter of 0.44 mm.

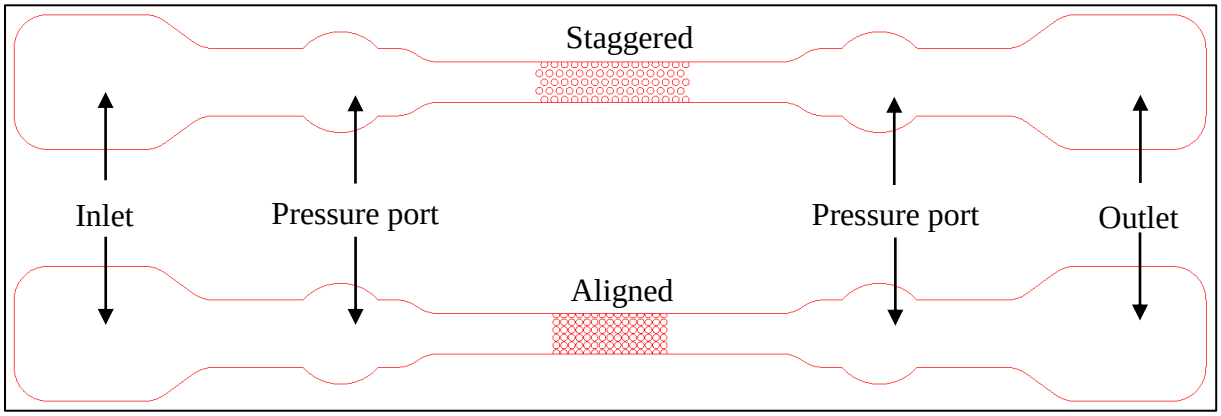

Figure 8.3. Drawings of the microfluidic devices for the staggered and aligned configurations.

8.2.2. Experimental techniques

8.2.2.1. Flow visualization

The microchannels were placed on an inverted epifluorescence microscope (DMI 5000M, Leica Microsystems GmbH) and were continuously illuminated by a 100 W mercury lamp. A filter cube (Leica Microsystems GmbH, excitation filter BP 545/30 nm, short pass dichroic at 565 nm, and barrier filter of 605/75 nm) was used to filter the polychromatic light allowing the excitation light to reach the microgeometries containing the fluid seeded with tracer particles via a 20× (NA = 0.4) microscope objective (Leica Microsystems GmbH). The light emitted by the fluorescent tracer particles was imaged through the same objective onto the CCD monochromatic camera (DFC350 FX, Leica Microsystems GmbH) in order to capture the particle trajectories using *long* time exposure times. The fluids were seeded with 1.0 μm fluorescent polystyrene tracer particles at a concentration of 100 ppm (Nile Red, Molecular Probes, Invitrogen; Ex/Em: 535/575 nm; density: 1050 kg/m^3).

8.2.2.2. Pressure drop measurements

Pressure drop measurements were performed using differential pressure sensors. The pressure drop was measured between two ports, which are positioned upstream and downstream of the array of cylinders as shown in Figure 8.3. These locations are far away from the array of cylinders in order to minimize the interference of the pressure taps on the flow. Three types of pressure sensors were used, which cover differential pressures up to 7 kPa, 34 kPa and 200 kPa, and were selected according the pressure drop to be measured,

which depends on the fluid, the flow rate and the geometrical arrangement under study. The pressure sensors were previously calibrated using a static column of water for the 7 kPa and 34 kPa ranges and using a compressed air line connected to a manometer (Wika Instrumental Corporation, model 332.50) for the 200 kPa pressure sensors. The pressure sensors were powered using a 12 V DC power supply (Lascar electronics, PSU 206) and the output signal was acquired using a data acquisition card (NI USB-6218, National Instruments), which was connected to the computer through an USB port. The output data was recorded and monitored using LabView v7.1 software.

8.2.3. Rheological characterization of the fluids

In the experiments, a Newtonian, a Boger fluid and a wormlike micellar solution were use. The Newtonian fluid was de-ionized water and the Boger fluid was an aqueous solution of polyacrylamide (PAA) at a weight concentration of 125 ppm with 1% of NaCl (PAA125). The density (ρ) of the fluids was measured using a pycnometer, taking the values of 999.8 kg/m^3 and 1001.1 kg/m^3 for the Newtonian fluid and for the Boger fluid, respectively. The wormlike micellar solution used in this study was an aqueous solution of 30 mM CTAB (cetyltrimethyl ammonium bromide) with 240 mM NaSal (sodium salicylate). In order to minimize bacteriological growth in the Boger fluid and prevent its degradation, a biocide was added at a weight concentration of 25 ppm (Kathon LXE, Rohm and Haas). The rheological characterization of the fluids in shear flow conditions was done in a rotational rheometer (Physica MCR 301, Anton Paar) with a 75 mm cone-plate system with 1º angle to measure the steady-state shear viscosity. A capillary break-up extensional rheometer (Haake CaBER 1, Thermo Scientific) was used to measure the relaxation time of the fluids in extensional flow.

Figure 8.4a shows the shear viscosity (η) of the Boger fluid measured in a wide the range of shear rates ($0.1 \leq \dot{\gamma}$ (s^{-1}) ≤ 1000) and at different temperatures in the range between 288.2 and 298.2 K.

The time-temperature superposition principle was used in order to obtain the master curve at the reference temperature (T_0 = 293.2 K). The corresponding shift factor is defined as (Dealy and Plazek, 2009):

$$a_T = \frac{\eta(T)}{\eta(T_0)} \frac{T_0}{T} \frac{\rho_0}{\rho} \ , \tag{8.1}$$

where η (T_0) is the shear viscosity at the reference temperature T_0, η (T) is the shear viscosity at a given temperature T, ρ_0 is the density at the reference temperature and ρ is the density at temperature T. Since the temperature variation in the rheological measurements was small, the fluid density does not change significantly and the shift factor, can be simplified to (Dealy and Plazek, 2009):

$$a_T = \frac{\eta(T)}{\eta(T_0)} \ . \tag{8.2}$$

The PAA125 Boger fluid is characterised by a nearly constant shear viscosity in the range of shear rates measured, and the average shear viscosity is 1.55 mPa.s.

The CaBER measurements were done at the reference temperature (T_0 = 293.2 K) and the relaxation time was determined by fitting the experimental data of log [*D(t)*] *vs.* time according to Eq. (8.3) that results from the elasto-capillary balance of the filament (Entov and Hinch, 1997):

$$\frac{D}{D_0} = e^{-\frac{t}{3\lambda}}, \tag{8.3}$$

where D_0 is the diameter of the filament at the reference time t = 0 and D is the diameter at the time t. These measurements were performed using two circular plates with a diameter of 6 mm, an initial spacing of 3 mm and a final gap of 9 mm between the plates, with the strain step done in 50 ms. As shown in Figure 8.4b the experimental data of log (D) vs t was fitted according Eq. (8.3) and the relaxation time was estimated to be λ = 3.4 ms for the PAA125 Boger fluid.

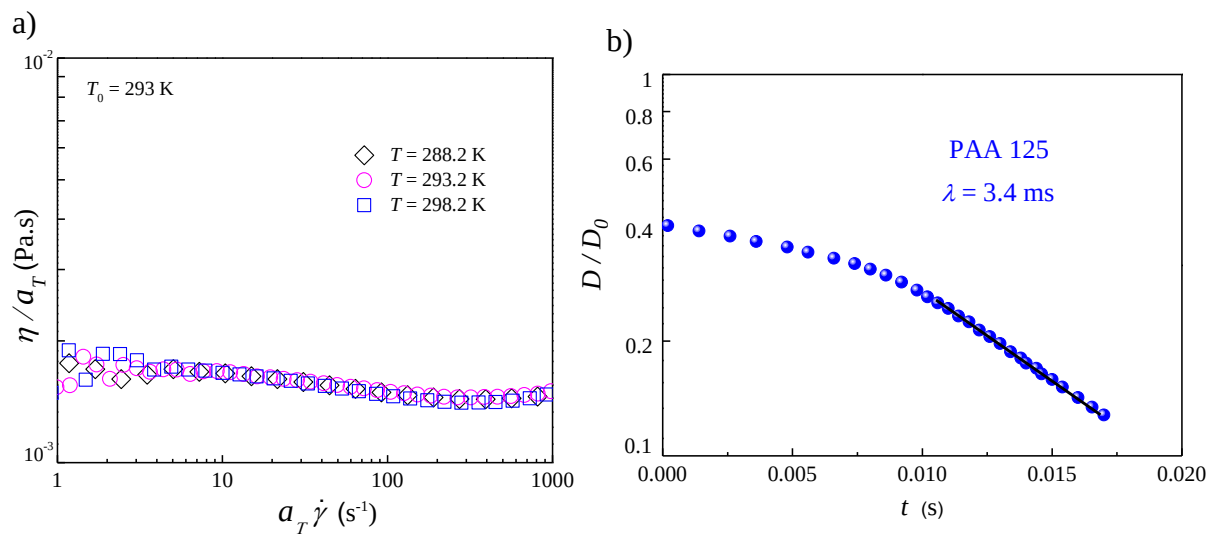

Figure 8.4. a) Steady shear viscosity of the PAA125 Boger fluid; b) Diameter of the filament measured as a function of time using Haake CaBER 1 extensional rheometer for the Boger fluid.

The results of steady and the dynamic shear flow, measured at 293 K (which is close to the average ambient laboratory temperature of the experiments), are presented in Figure 8.5 for the CTAB/NaSal micellar solution.

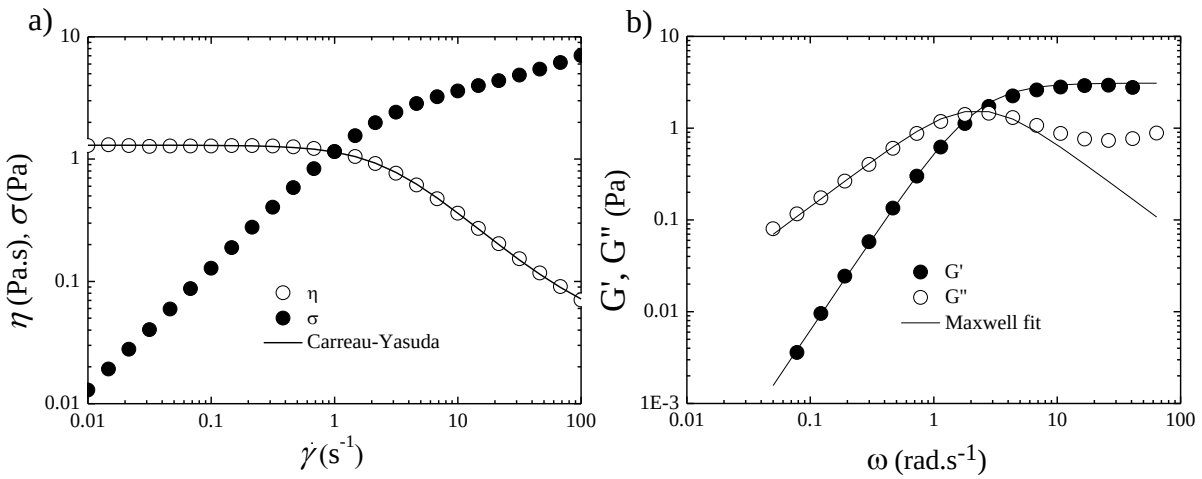

Figure 8.5. Shear rheology of the CTAB:NaSal (30:240 mM) solution: (a) Steady shear viscosity fitted with a Carreau-Yasuda model and shear stress as function of shear rate; (b) linear viscoelastic properties fitted with a single mode Maxwell model.

The steady shear viscosity results shown in Figure 8.5a, were fitted to the Carreau-Yasuda model (Bird *et al.*, 1987):

$$\eta = \eta_s + \frac{\eta_0 - \eta_s}{\left[1 + (\Lambda\dot{\gamma})^a\right]^{(1-n)/a}} \tag{8.4}$$

where the fitted parameters η_0, ηs, Λ, n and a are represented in Table 8.1.

The storage and loss moduli, G' and G'', measured in small amplitude oscillatory shear (SAOS) flow are presented in Figure 8.5b and were fitted using a single-mode Maxwell model, given by:

$$G'(\omega) = \frac{G_0(\lambda_M\omega)^2}{1 + (\lambda_M\omega)^2} \tag{8.5}$$

$$G''(\omega) = \frac{G_0\lambda_M\omega}{1 + (\lambda_M\omega)^2} \tag{8.6}$$

From the fitted parameters, the Maxwell relaxation time (λ_M) and the plateau modulus (G_0) were determined, which are represented in Table 8.1.

Table 8.1 – Fitted parameters of the rheology of the micellar solution.

Fluid	η_s (Pa.s)	η_0 (Pa.s)	Λ(s)	n	a	λ_M (s)	G_0 (Pa)
CTAB:NaSal (30:240 mM)	0.032	1.3	0.38	0.050	1.5	0.45	3.1

It should be noted that the Maxwell relaxation time determined in SAOS (λ_M) is similar to the relaxation time that could be inferred from the flow curve shown in Figure 8.5, since the shear-thinning behaviour starts at $\dot{\gamma} \approx 2\ \text{s}^{-1}$, leading to an estimate of $\lambda \approx 0.5\ \text{s}$ (inverse of $\dot{\gamma}$ at onset of shear-thinning).

8.3. Results

The flow past two different arrays of cylinders was studied using flow visualizations and pressure drop measurements. The experiments were conducted from low Reynolds and Deborah numbers flow conditions and over a wide range of Reynolds and Deborah numbers, up to the onset of elastic flow instabilities.

The Reynolds number (*Re*) that characterises the non-Newtonian fluid flow in the array of cylinders is here defined as:

$$Re = \frac{\rho U R}{\eta}, \tag{8.7}$$

where U is the superficial velocity in the porous medium ($U = Q / Hh$), R is the radius of the cylinders and ρ and η are the density and shear viscosity of the fluid, respectively. For the micellar solution the shear viscosity is evaluated at the following characteristic shear rate:

$$\dot{\gamma}_c = \frac{U_{interstitial}}{(e/2)}, \tag{8.8}$$

where $U_{interstitial}$ is the interstitial velocity, $U_{interstitial} = U / \varepsilon$ (ε is the porosity of the arrays), and e is a characteristic length scale, taken as the minimum interstitial distance between the cylinders. The porosity of the staggered and aligned arrays is $\varepsilon = 0.584$ and $\varepsilon = 0.389$, respectively.

In the definition of *Re* we use the cylinder radius instead of the diameter, as used in most works concerning the flow in porous media analogues, for consistency with the remaining chapters of this thesis.

The flow of viscoelastic fluids is also characterized through the Deborah number (*De*). In the classical definition, *De* represents the ratio between the relaxation time of the fluid (λ) and a characteristic time of the flow ($R/U_{interstitial}$):

$$De = \frac{\lambda U_{interstitial}}{R}. \tag{8.9}$$

For the micellar solution we use the Maxwell relaxation time λ_M in Eq. (8.9), while for the Boger fluid the value of λ determined in the CaBER was used.

The results are presented in section 8.3.1 for the Boger fluid and in section 8.3.2 for the wormlike micellar solution.

8.3.1. Boger fluid

The pressure drop measurements were carried out for a Newtonian fluid (de-ionized water) and a Boger fluid (PAA125) in the staggered and aligned array configurations. The range of flow rates, Q, under study in the staggered arrangement was $0.01 \leq Q \leq 50$ ml/h for the Newtonian fluid and the PAA125 Boger fluid. Typically, the PDMS microchannels used in the experiments can sustain pressure drops up to 100-150 kPa before starting to leak. We also note that at high pressure drops there is some compliance of the soft PDMS microchannels, and the cross section of the flow increases, thus the results around 100 kPa, and above, should be analysed with care. The range of flow rates used in the aligned arrangement was lower than for the staggered arrangement due to the smaller porosity.

Figure 8.7 shows the pressure drop measured in both array configurations, as a function of the flow rate. The pressure drop of the Newtonian fluid increases linearly with the flow rate for both arrangements as expected for a low *Re* flow. For the Boger fluid the pressure drop increases in a non-linear way with the flow rate, a manifestation of the nonlinear rheology of the Boger fluid.

Since the shear viscosity of the PAA125 Boger fluid is only around 50% higher than the dynamic viscosity of water, the pressure drop of the PAA125 fluid would be about 50% higher than the pressure drop measured with water if no elastic effects were important. However, the results shown in Figure 8.7 clearly illustrate that when the flow rate increases, the ratio between the measured pressure drop measured for the PAA125 Boger fluid and the pressure drop with water starts to increase, especially for the staggered arrangement, with pressure drop ratios of the order of 10 for the higher flow rates. This clearly indicates that when Q increases, or more correctly when *De* increases, the pressure drop observed with the Boger fluid increases nonlinearly due to the onset of an elastic instability, which is more intense in the staggered array, leading to pressure drops that can be more than 5 times higher than if only viscous effects would be relevant. The high flow deformation in the aligned configuration can promote the fluid degradation, which can explain the lowest increase of the pressure drop with the flow rate.

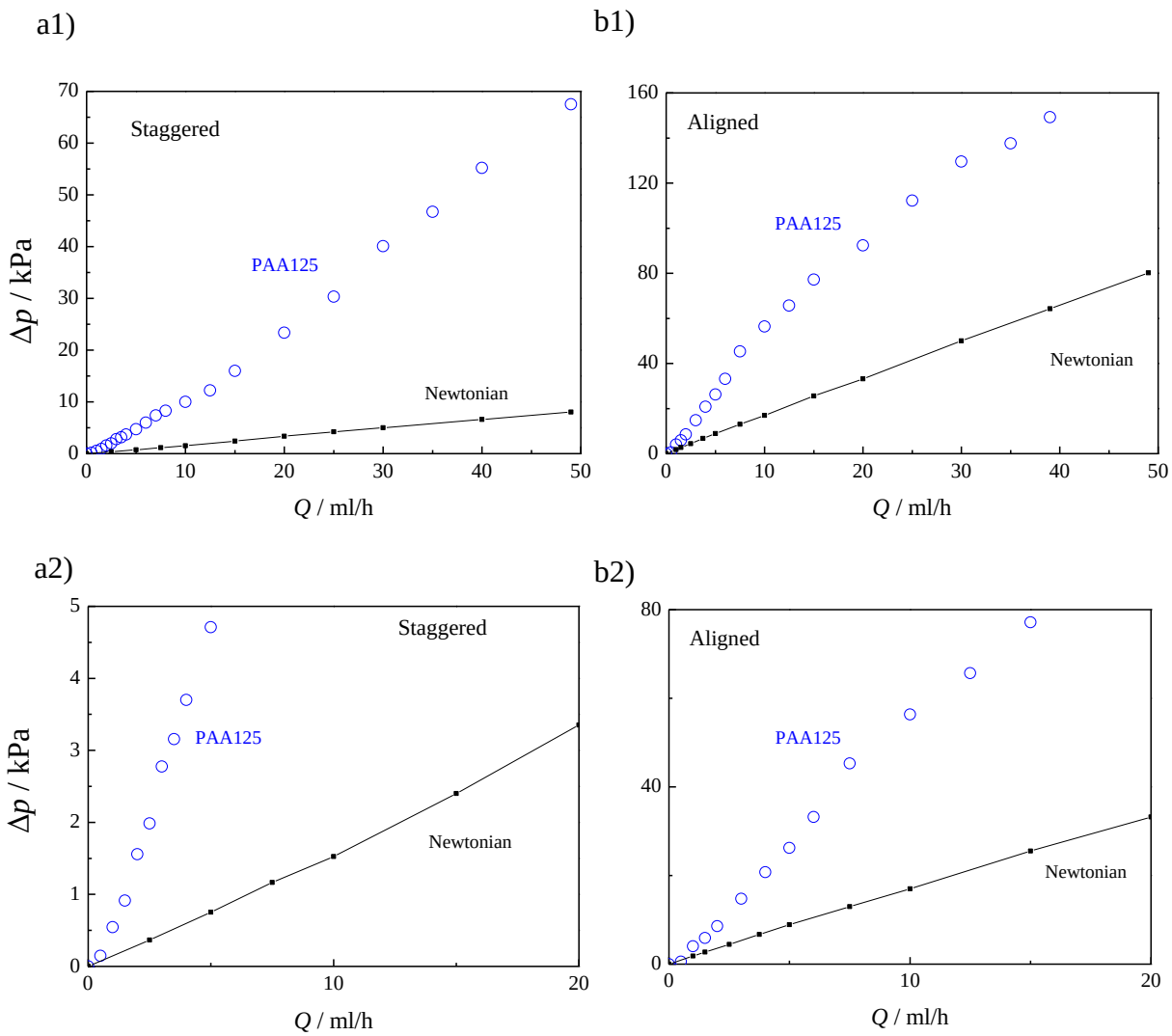

Figure 8.7. Pressure drop measurements as a function of flow rate for the Newtonian fluid and the PAA125 Boger fluid: a) staggered configuration; b) aligned configuration.

The flow of the PAA125 Boger fluid through the two arrays of cylinders were visualized in the range of $0.03 < De < 2.6$ for the staggered configuration and $0.08 < De < 3.4$ for the aligned configuration. The effect of the Deborah number on the flow patterns of the PAA125 Boger fluid, for the staggered and aligned configurations, is illustrated in Figures 8.8 and 8.9, respectively. Figure 8.8a was composed since in the visualizations (with the 20× objective) it was not possible to capture the entire cylinder array in a single image. Regardless of the flow conditions visualized and the cylinder array configuration, the flow is symmetric upstream and downstream of the array of cylinders, even for the higher *De* investigated. The flow in the interstices between the cylinders presents a symmetric structure, which becomes more

complex with the increase of *De*, due to the appearance of elastic instabilities. In the range of *De* studied and for both arrays configurations, we can observe what seems to be an elastic phenomenon similar to the extrudate swell (Bird *et al.*, 1987), as the fluid passes from a narrow to a wide section in-between the cylinders. A similar behaviour was predicted numerically in the flow in a planar expansion (Poole *et al.*, 2007).

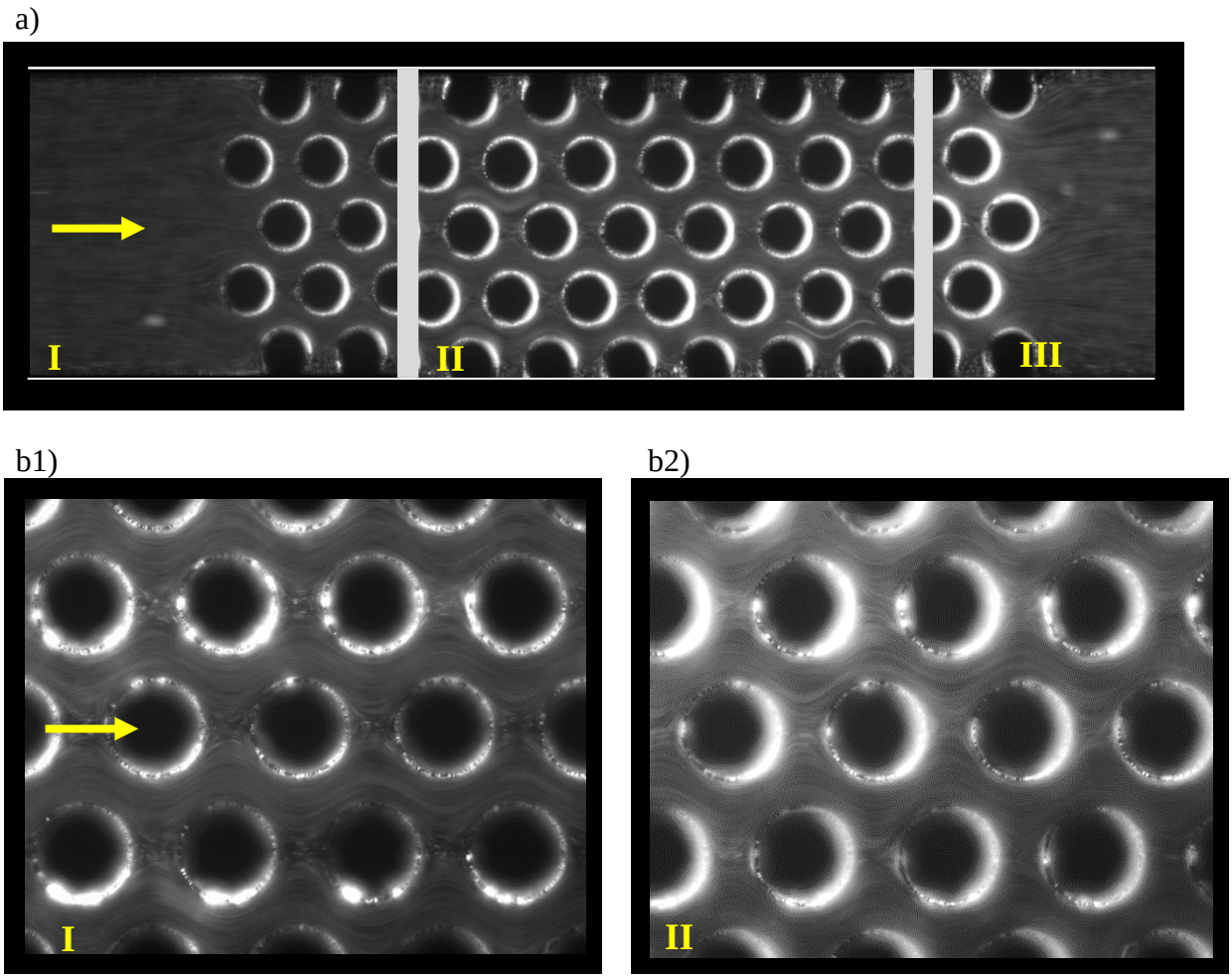

Figure 8.8. Flow patterns of the PAA125 Boger fluid in the staggered configuration: a) Overall view of the cylinder array at *De* = 2.3; b) Detailed view: b1) *De* = 0.19; b2) *De* = 2.3.

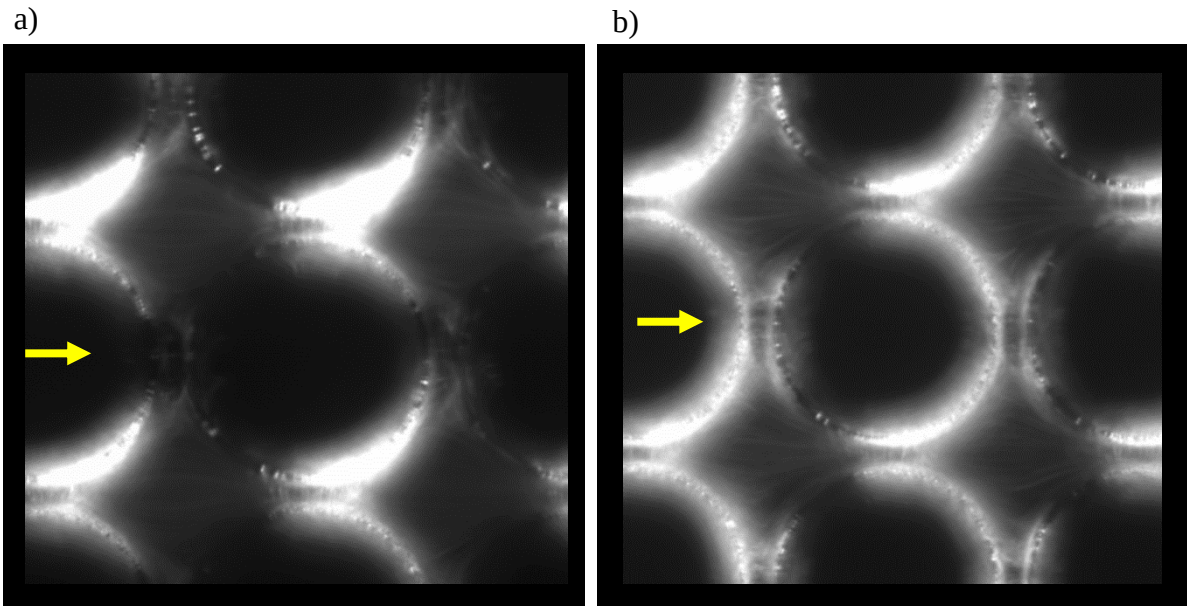

Figure 8.9. Flow patterns of the PAA125 Boger fluid in the aligned configuration: a) De = 0.49; b) De = 3.4.

8.3.2. Wormlike micellar solution

The pressure drop measurements were also carried out for the CTAB/NaSal wormlike micellar solution past the two arrays of cylinders in the flow rate range of $0.01 \leq Q \leq 0.5$ ml/h, which corresponds to $0.4 < De < 21$ for the staggered configuration and $0.6 < De < 31$ for the aligned configuration.

The variation of the pressure drop with flow rate can be observed in Figure 8.10 for the CTAB/NaSal micellar solution. In both flow arrangements there is an increase of the slope of the pressure drop variation with Q, despite all the measurements corresponding to characteristic shear rates clearly in the region of strong shear-thinning. Therefore, these pressure drop measurements indicate a significant pressure drop enhancement due to the elastic effects, which is clearly stronger than the shear-thinning effect of the micellar solution.

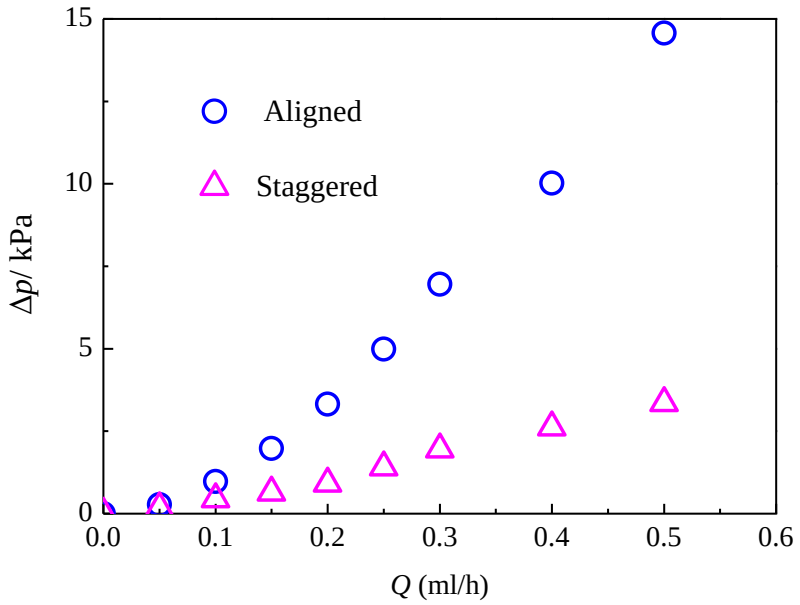

Figure 8.10. Pressure drop measurements as a function of flow rate, *Q*, for the CTAB/NaSal wormlike micellar solution.

Figures 8.11 and 8.12 show the flow patterns of the flow past the arrays of cylinders for two Deborah numbers for the staggered and aligned configurations, respectively. The images were composed by set of images taken at the same flow rates, since it was not possible to capture the entire array in a single image.

For the staggered configuration and at low *De* (cf. Figure 8.11a), the flow is symmetric, relative to the duct axis, upstream and downstream of the array of cylinders. As *De* increases (cf. Figure 8.11b) the appearance of elastic instabilities were clearly observed upstream of the array of cylinders. The critical Deborah number for the onset of such elastic instabilities was found to occur between $De_c \approx 0.5$ and 1.0. As expected, the intensity of the instability observed upstream of the cylinder array increases significantly with *De*. In the range of *De* studied the downstream flow patterns remained symmetric relative to the duct axis (cf. Figure 8.11b) indicating that the compressive flow at the entrance of the array is less stable than the expansion flow (stress relaxation) at the exit. As the fluid flows through the array of cylinders, we can observe elastic instabilities in the interstices between the cylinders, even for the lower *De*, and the instability magnitude increases with *De*.

a)

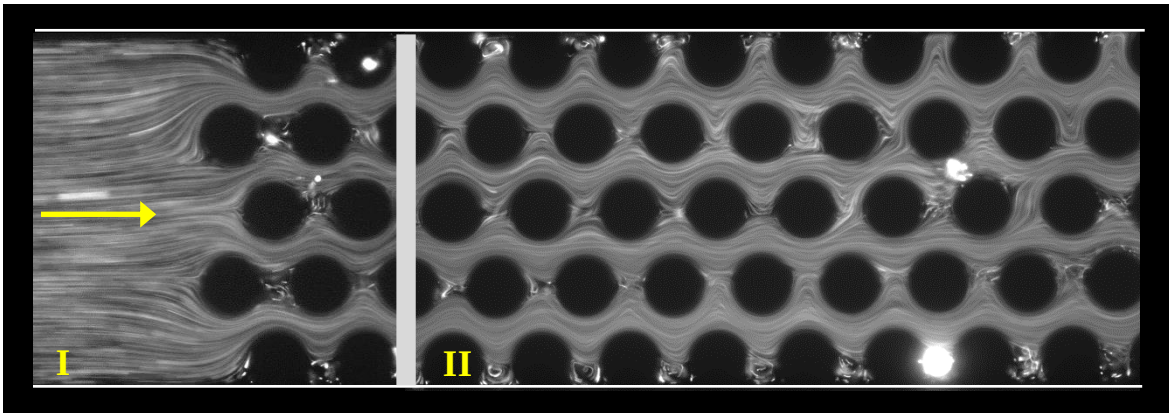

b)

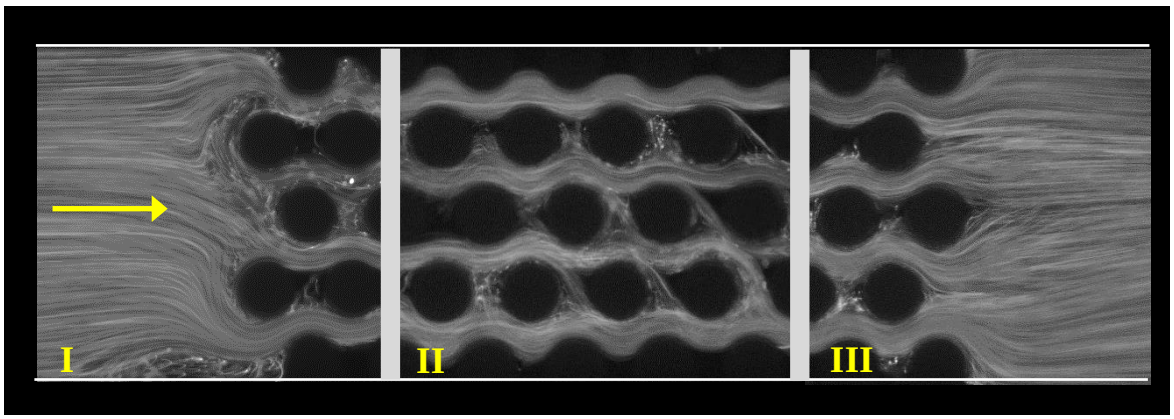

Figure 8.11. Effect of elasticity on the flow patterns of the CTAB/NaSal solution in the staggered array configuration: a) Q = 0.01 ml/h, De = 0.41; b) Q = 0.1 ml/h De = 4.1.

For the aligned configuration, we can also observe the appearance of elastic instabilities upstream of the array of cylinders above a critical Deborah number, which was found to be $De_c < 0.64$. As De increases further, the intensity of the elastic instabilities also increases, as expected. Regardless the De, elastic instabilities were observed in the interstices between the cylinders, and also upstream of the porous medium, as clearly shown in Figure 8.12b but now the instability is more pronounced than the similar effect observed in the staggered configuration, which partially explain the more pronounced pressure drop enhancement observed for the aligned array when the flow rate of the micellar solution is increased. In the range of flow rates investigated, flow patterns were always symmetric, relative to the duct axis, downstream of the array of cylinders.

a)

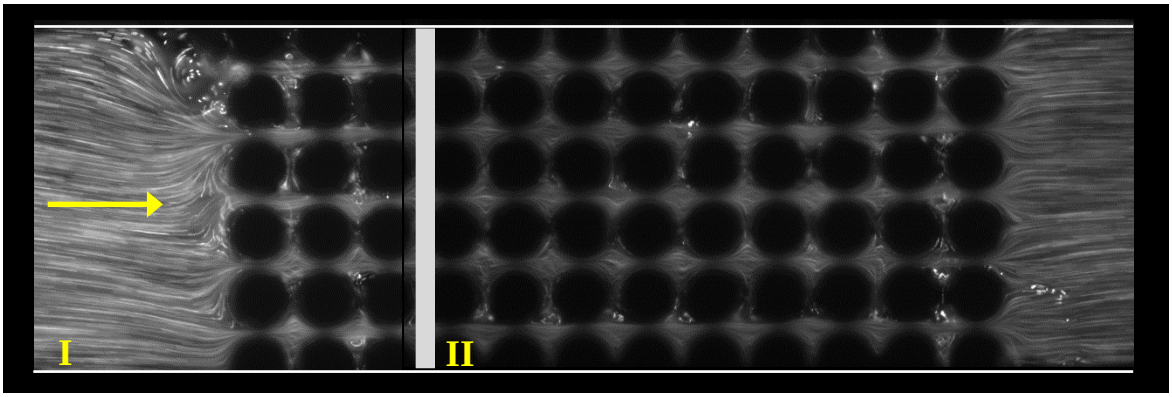

b)

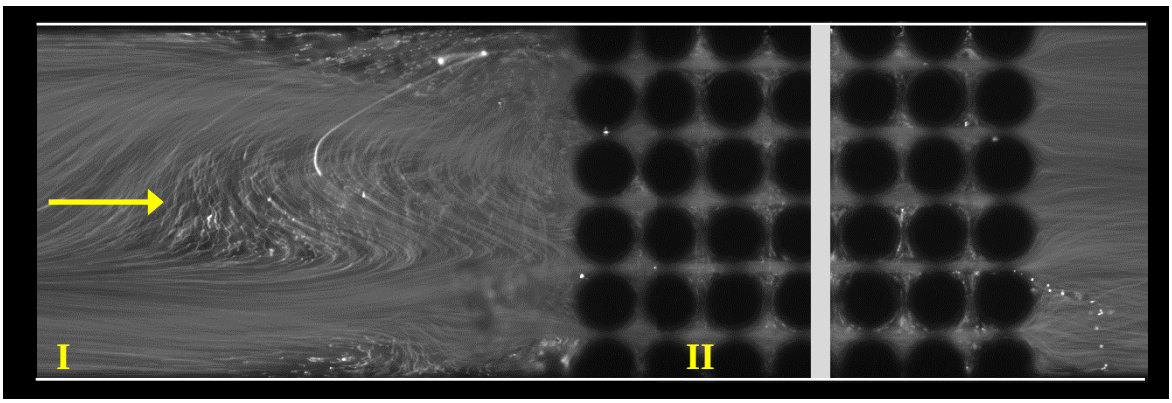

Figure 8.12. Effect of elasticity on the flow patterns of the CTAB/NaSal solution in the aligned array configuration: a) Q = 0.01 ml/h, De = 0.62; b) Q = 0.1 ml/h, De = 6.2.

Figure 8.13 shows the flow patterns of the CTAB/NaSal solution obtained at different instants for the staggered and aligned configuration, at constant flow rates. At these supercritical flow conditions, the elastic instabilities observed upstream of the arrays of cylinders presents a marked unstable flow, which puts in evidence the strong potential of using arrays of cylinders to promote efficient mixing at micro-scale.

a)

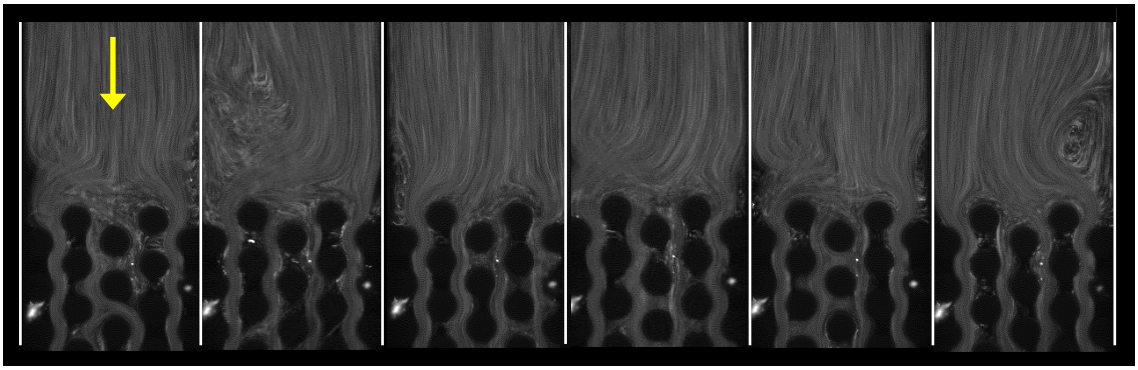

b)

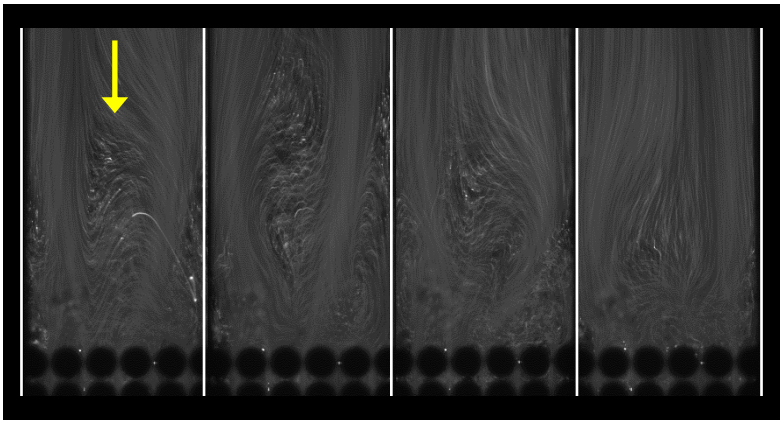

Figure 8.13. Flow patterns of the CTAB/NaSal solution visualized at different *instants*: a) staggered configuration, Q = 0.1 ml/h, De = 4.1; b) aligned configuration, Q = 0.1 ml/h, De = 6.2.

8.4. Conclusions

An experimental study of the viscoelastic fluid flow through arrays of cylinders, which can be considered as a simplified 2D porous media analogues, was carried out using microfluidic devices. The viscoelastic fluids used were a Boger fluid, to isolate the elastic effects, and a wormlike micellar solution to explore the combined elastic and shear-thinning effects. The effect of two cylinders arrangements were studied, namely staggered and aligned (or square) configuration. The complex 3D viscoelastic fluid flow was characterized as the flow rate is varied from the Newtonian-like flow up to the development of strong elastic instabilities, using flow visualizations and pressure drop measurements.

The pressure drop of the Newtonian fluid increases linearly with the flow rate for both arrangements. For the Boger fluid the pressure drop increases in a non-linear way with the flow rate, which is due to the onset of an elastic instability, which is more relevant in the staggered array.

For the wormlike micellar solutions, the pressure drop measurements indicate a significant pressure drop enhancement with the flow rate, specially for the aligned arrangement as expected, which is due to more pronounced elastic effects given the smaller interstitial distance between the cylinders and the corresponding higher shear rates. The intensity of the elastic instabilities increases as the interstitial space decreases which indicates that efficient mixing, promoted by the onset of strong elastic instabilities, is enhanced in cylinder arrays with smaller porosity.

References

Anderson, V.J., Pearson, J.R.A., Boek, E.S., 2006. The Rheology of Worm-Like Micellar Fluids. Rheology Reviews, D.M. Binding and K.Walters eds, 217-253.

Bird, R.B., Armstrong, R.C., Hassanger, O., 1987. Dynamics of polymeric liquids. John Wiley and Sons, New York.

Brown, R.A., McKinley, G.H., 1994. Report on the VIIIth Int Workshop on numerical - methods in viscoelastic flows. J Non-Newton Fluid Mech 52, 407-413.

Campo-Deano, L., Galindo-Rosales, F.J., Pinho, F.T., Alves, M.A., Oliveira, M.S.N., 2012. Nanogel formation of polymer solutions flowing through porous media. Soft Matter 8, 6445-6453.

Dealy, J., Plazek, D., 2009. Time-temperature superposition - a user guide. Rheology Bulletin 78, 16-31.

Entov, V.M., Hinch, E.J., 1997. Effect of a spectrum of relaxation times on the capillary thinning of a filament of elastic liquid. J Non-Newton Fluid Mech 72, 31-53.

Gunda, N.S.K., Joseph, J., Tamayol, A., Akbari, M., Mitra, S.K., 2013. Measurement of pressure drop and flow resistance in microchannels with integrated micropillars. Microfluid Nanofluid 14, 711-721.

Khomami, B., Moreno, L.D., 1997. Stability of viscoelastic flow around periodic arrays of cylinders. Rheol Acta 36, 367-383.

Kozicki, W., 2001. Viscoelastic flow in packed beds or porous media. Can J Chem Eng 79, 124-131.

Larson, R.G., 1999. The Structure and Rheology of Complex Fluids. Oxford University Press, New York.

McDonald, J.C., Duffy, D.C., Anderson, J.R., Chiu, D.T., Wu, H.K., Schueller, O.J.A., Whitesides, G.M., 2000. Fabrication of microfluidic systems in poly(dimethylsiloxane). Electrophoresis 21, 27-40.

Moss, G.R., Rothstein, J.P., 2010. Flow of wormlike micelle solutions through a periodic array of cylinders. J Non-Newton Fluid 165, 1-13.

Ober, T.J., Soulages, J., McKinley, G.H., 2011. Spatially resolved quantitative rheo-optics of complex fluids in a microfluidic device. J Rheol 55, 1127-1159.

Poole, R.J., Alves, M.A., Oliveira, P.J., Pinho, F.T., 2007. Plane sudden expansion flows of viscoelastic liquids. J Non-Newton Fluid 146, 79-91.

Rothstein, J.P., 2008. Strong flows of viscoelastic wormlike micelle solutions. Rheology Reviews, D.M. Binding and K.Walters eds, 1-46.

Sochi, T., 2010. Non-Newtonian flow in porous media. Polymer 51, 5007-5023.

Wang, H.Z., 2004. Passive Mixing in Microchannels with Geometric Variations. Swinburne University of Technology, Australia.

Yang, J., 2002. Viscoelastic wormlike micelles and their applications. Curr Opin Colloid In 7, 276-281.

Yip, R., James, D.F., Currie, I.G., 2011. PIV measurements of slow flow of a viscoelastic fluid within a porous medium. Exp Fluids 51, 801-809.

Chapter 9

Conclusions and Future work

This ending chapter summarizes the main conclusions of this thesis and presents relevant topics for future research.

9.1. Conclusions

The main goal of this thesis was the investigation of the flow of complex fluids past a confined cylinder, both at macro- and micro-scales, for different aspect ratios and blockage ratios. The work plan of this thesis was divided in two main parts: the first part was devoted to the study of the macro-scale flow past a confined cylinder, while the second part of the work included a similar investigation at the micro-scale, and also the investigation of the flow past a microfluidic array of cylinders. The comparison between the macro- and micro-scale results showed that the *continuum* hypothesis was still valid at the micro-scale, even for the large molecular weight polymer solutions used.

In the study at the macro-scale the flow of a Newtonian fluid, a shear-thinning viscoelastic fluid and two Boger fluids, were studied to explore the effect of the aspect ratio (AR = 16, 8 and 2) for the 50% blockage ratio (BR) case, in order to assess the influence of flow inertia and viscoelasticity in the complex three dimensional flow, up to the critical conditions for onset of inertial and elastic flow instabilities.

For the Newtonian fluid, it was found that the onset of flow separation occurs at a critical Reynolds number, which increases when the AR decreases. The numerical calculations agree very well with the experimental results, indicating that a more detailed study could be carried

out numerically to explore flow conditions not investigated experimentally and to help in the interpretation of the results obtained for the viscoelastic fluids, by comparing to the base case of Newtonian fluid flow.

For the viscoelastic fluid with shear-thinning behaviour, the flow visualizations showed the appearance of an elastic instability upstream of the cylinder, at a critical Deborah number (De_c), which increases when the *AR* decreases. The different types of flow observed can be categorized in the follow two flow regimes: Newtonian-like flow; steady asymmetric flow. For the Boger fluids, and over the limited range of *De* studied, the flow patterns were always symmetric and steady. The numerical predictions obtained using the Oldroyd-B model matched well with the experimental data. For all the viscoelastic fluids studied, the velocity measurements show that for lower *De* elastic effects are negligible (Newtonian-like flow), but when *De* increases the elasticity of the fluid influences the flow field, especially in the vicinity of the cylinder, and leads to an increase of the required development length downstream of the cylinder, also in agreement with the numerical simulations. The velocity development length is found to increase with an increase of the *AR*.

In the study at the micro-scale, Newtonian and viscoelastic fluids were used in the experiments, and the flow was investigated using in-house produced PDMS microfluidic devices. The effect of the aspect ratio (*AR* = 2.0, 1.0 and 0.55) and the blockage ratio (*BR* = 25%, 50% and 75%) on the flow around a confined cylinder was studied to assess the influence of elasticity in the flow field and also to determine the critical conditions for the onset the elastic instabilities that arise at highly elastic flow conditions, easily achieved in microfluidic devices, without inertial effects. Moreover, the viscoelastic fluid flow through an array of cylinders was also studied.

For the Newtonian fluid there were no significant changes as we move to smaller scales. The critical Reynolds number for the onset of flow separation increases as the aspect ratio decreases, in agreement with the observations at the macro-scale. The comparison between the numerical and experimental results showed a good agreement, validating the experimental techniques used at the micro-scale.

For the viscoelastic fluid with shear-thinning behaviour, we observed the appearance of an elastic instability upstream of the cylinder, at a critical *De*, which increases when the *AR* decreases. The different types of flow patterns were categorized in the follow four flow

regimes, as *De* increases: Newtonian-like flow; steady asymmetric flow; unsteady periodic flow; chaotic-like flow. In the Newtonian-like flow, the flow is symmetric upstream and downstream the cylinder, elastic effects are negligible and the flow is reversible at low *De* and low *Re*. In the following three regimes the flow is influenced by some type of elastic instability. First, in the steady asymmetric regime, the flow is asymmetric, but steady, upstream of the cylinder. As *De* further increases the elastic instability intensifies and the flow becomes unsteady and periodic, until eventually the flow loses periodicity at higher *De*.

Over the wide range of *De* achieved to characterize the flow of Boger fluids, the Newtonian-like, steady divergent streamlines and the unsteady chaotic-like flow regimes were observed upstream of the cylinder, which is propagated towards downstream as *De* increases. The critical conditions for the transition for the different flow regimes depend on the *AR* and also on the *BR*. It was found that for the same flow conditions the increase of the blockage anticipates the elastic flow regime transitions.

The flow of Newtonian and viscoelastic fluids, including a wormlike micellar solution, through a microfluidic array of cylinders, which can be considered as a two-dimensional porous media analogue, were investigated in staggered and aligned arrangements. Different flow patterns were found with different levels of instability, which can be used to efficiently promote mixing at micro-scale.

9.2. Future work

The experimental results obtained in the characterization of the viscoelastic fluid flow in simple geometries, such as the confined cylinder, or array of cylinders, provide a set of results that can be used for validation or comparison purposes in future works, with particular application in benchmarking of numerical codes.

The experimental characterization of the viscoelastic flow using other types of complex fluids is an important development, in order to explore other regions in the *De-Re* parameter space and obtain the critical flow conditions for the onset of elastic instabilities, which might be useful for theoreticians to understand the mechanisms involved in these fluid flow transitions. Additionally, the characterization of the viscoelastic fluid flow in microchannels with different geometrical confinement, and higher *AR*, from those covered in the present investigation is also an important contribution.

A more detailed study of the chaotic-like regime for viscoelastic flow past a confined cylinder and through an array of cylinders is an interesting topic for future research. The need of a time-resolved PIV system, coupled with a high speed camera, operating in the kHz frequency range would provide valuable data to probe this interesting flow regime, with useful applications in micro-mixing.

Single molecule studies of collision with a confined cylinder or an array of cylinders can be used to create conditions in which long molecules, such as DNA molecules or eventually other biopolymers, can be stretched significantly, allowing the study of molecular relaxation processes. This type of microfluidic devices can also be designed in order to promote the capture and elongation of biomolecules aiming the development of on-chip sequencing techniques.

Another interesting application for future work is the investigation of electro-osmotic driven flows of viscoelastic fluids in microchannels with a confined cylinder and an array of cylinders. Since most of the studies investigating viscoelastic fluid flow are based on pressure-driven flows, it would be of significant interest to perform electro-osmotic experiments to observe the effect of the application of an electric field to the viscoelastic behaviour of complex fluids and, in particular, to investigate the onset of electro-elastic flow instabilities.

Appendices

Appendix A. Microfluidic devices fabrication

The microfluidic devices fabrication process includes the following steps:

- Design of microgeometries using CAD software
- Manufacture of the chrome masks
- Manufacture the final moulds using photo-lithography
- Fabricate the PDMS microchannels using the moulds

The microchannel fabrication starts with the drawing of the intended design of the microchannel using CAD software. After the drawing, the CAD image is etched onto a chrome mask, which is obtained by sputtering a chrome layer onto a glass substrate. The combination between the hard resistant chrome and the good optical characteristic of the glass, allows the production of durable, robust and stable masks. The devices fabricated with chrome masks exhibit well defined features and sharp edges with a resolution around 1 – 5 μm. A cheaper alternative employs film masks, printed with high-resolution laser printers (20,000 dpi or higher), but the resolution of these masks is worse.

The moulds are fabricated using the chrome masks and are produced by photo-lithography technique. This technique uses a photoresist material (typically SU-8), which is used to create a positive-relief on the mould surface, with the inverse structure of the microchannels to be produced. Currently there are several foundries worldwide that provide the services of mould fabrication.

As a great advantage, the SU-8 moulds can be used to replicate the PDMS microchannels several times. An example of a SU-8 mould is presented in Figure A.1. The fabrication of the SU-8 moulds requires a clean-room facility with a controlled environment (temperature, humidity, pressure and air flow rate and direction). Due to the absence of clean room facilities in the host research group, the chrome masks and the SU-8 moulds necessary for the fabrications using soft-lithography were produced in Spain by the company Microliquid.

Figure A.1. Example of a SU-8 mould used in this work.

From the SU-8 moulds, the microfluidic devices were fabricated by replication using polydimethylsiloxane (PDMS), which is a soft polymer. PDMS has the advantages of being chemically inert with many fluids, non-toxic, and non-flammable, biocompatible, has good sealing properties, provides well-defined features and sizes and is optically transparent. Furthermore, PDMS is commercially available (sylgard 184), inexpensive and durable. The final microchannels were fabricated from the SU-8 moulds using soft-lithography according the following procedure, with a few steps also schematically represented in Figure A.2:

1. Silanization of the SU-8 mould

About 2-3 drops of trichlorosilane (tridecofluoro-1,1,2,2-tetrahydrooctyl-1-trochlorosilane, United Chemical Technologies) are placed on a petri dish with the SU-8 mould for 20 minutes (cf. Figure A.2-a). The silanization of the mould was done to facilitate the PDMS removal from the mould in the end of the process and must be repeated when the PDMS removal becomes difficult to minimize the risk of taking out small portions of the mould during the removal of the PDMS channel from the mould.

2. PDMS mixtures preparation

The mixtures of PDMS and oligomer cure agent, in the ratios 5:1 and 20:1 (PDMS: cure agent), are used for the substrate and to coat the glass slide respectively. After the preparation, the mixtures are homogenized in a vortex mixer and degassed with a vacuum pump.

3. PDMS 5:1 mixture over the SU:8 mould

The silanized mould is covered with the 5:1 PDMS mixture and degassed with a vacuum pump, as illustrated in Figure A.2-b).

4. Glass slides preparation

After cleaning the glass slide with ethanol, it is placed in a spin coater (Laurell WS-650S-6NPP). An adequate amount of 20:1 PDMS mixture is placed in the glass slide and spincoated using spin speeds of ω = 5000 rpm during 50 s to obtain a 30 μm thick layer of PDMS over the slide.

5. PDMS curing

Place the SU-8 mould and the PDMS mixture and the glass slide with the PDMS mixture in the oven for 20 minutes at 80 ºC to cure the PDMS (cf. Figure A.2-c). After curing, remove from the oven, allow some time to cool down and peel off the PDMS substrate from the mould after cutting the boundary with a sharp object.

6. Inlet and outlet access

Punch the inlet and outlet holes at the defined locations using a syringe tip with an appropriate size. The extracted PDMS resultant from punching the holes must be carefully removed.

7. Seal the microchannels

Seal the extracted PDMS substrate with the PDMS-covered glass slide and place in the oven at 80ºC for at least 12 hours. (cf. Figure A.2-d).

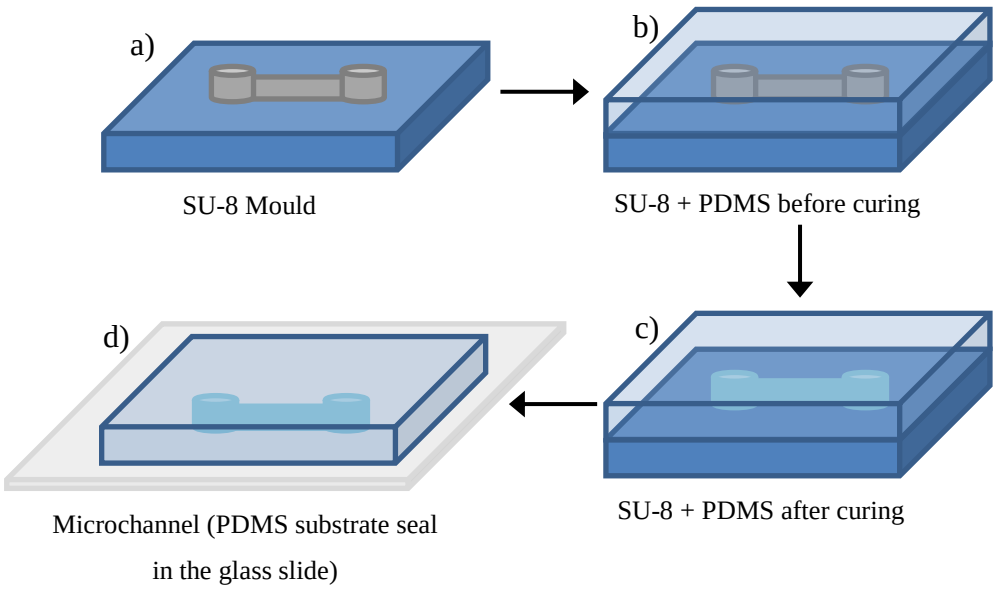

Figure A.2. Schematic overview of the microchannel fabrication using soft-lithography.

Appendix B. Procedure for particle image velocimetry

The procedure for measurements with the particle image velocimetry technique, from the image acquisition up to the final vector map, from which the velocity fields are exported, is described in detail for the macro-scale measurements. The images shown were obtained for the Newtonian fluid, as a typical example. The procedure followed to obtain the final vector map for the micro-particle image velocimetry is very similar and for that reason is not described.

1. Image acquisition

The seeding of the fluid should be done in order to have at least 5 -10 particles on each interrogation area and the particles diameter should be selected in order to occupy around 2 – 3 pixels (defocusing slightly the image can increase artificially the particle size imaged on the camera). Moreover, the displacement of particles between frames should be around 25% of the size of the interrogation area.

Verified all the necessary conditions, a minimum of 80 pairs of images were acquired for a constant flow rate. Figure B.1 shows the first frame of a pair of images acquired.

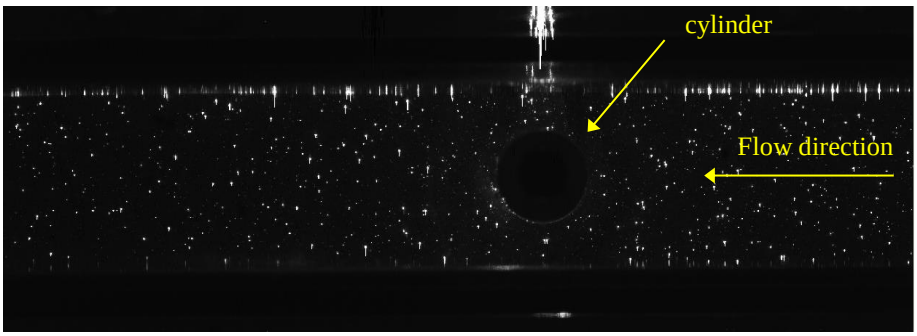

Figure B.1. Frame 1 of an image pair acquired.

2. Noise subtraction

For each image acquired, the background *noise* can be removed by the subtraction of the pixel mean resultant from averaging a significant number of images (typically we use 80 pairs of images). Figure B.2 illustrates a pixel mean image.

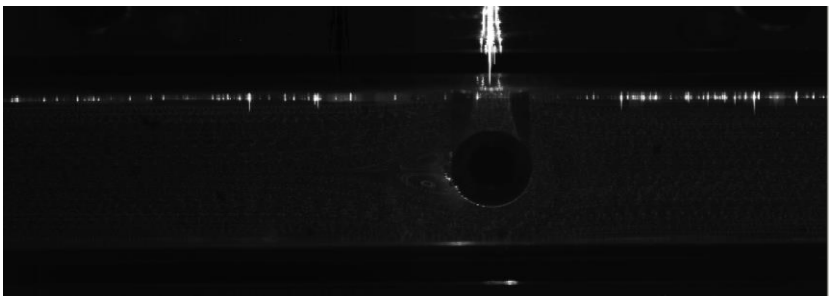

Figure B.2. Pixel Mean image.

Figure B.3 shows an image after the pixel mean subtraction. As can be clearly observed, the image of Figure B.1 has more noise than the image of Figure B.3. A much higher signal to noise ratio is obtained in the image shown in Figure B.3.

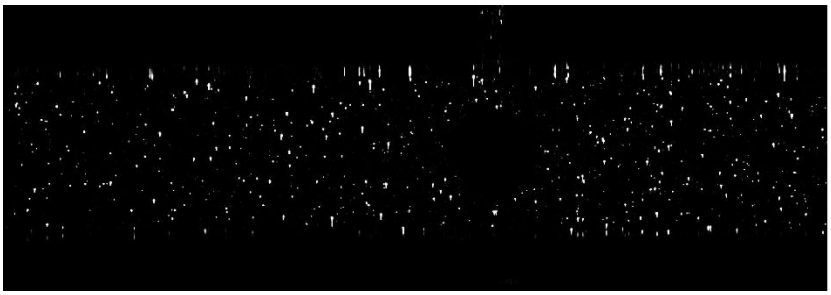

Figure B.3. Image obtained after the pixel mean subtraction.

3. Image masking

After the noise subtraction, all the images are masked with a mask, which defines the area to be rejected in the acquired images. Figure B.4 show the mask applied to an image, which includes the lateral walls, and the cylinder on the centre.

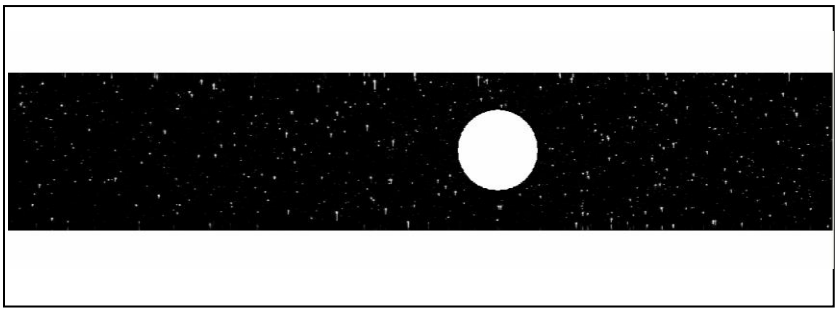

Figure B.4. Image obtained after the application of the image masking.

4. Correlation

An adaptive-correlation is applied to all masked images to obtain a two-dimensional velocity vector map for each image pair, as shown in Figure B.5, on interrogation windows of 32 by 32 pixels, with 50% overlap. The adaptive-correlation is an iterative process in which the interrogation area is successively refined, to determine the particle displacement between the two pulses and to reduce the loss of particles in the interrogation areas that occurs between the light pulses. In the calculations, a Gaussian window filter was applied, which reduces the problem of losing particles along the boundaries in the interrogation areas. The value of the parameter $1/k^2$ used was 0.75, where k is defined as the width of the window.

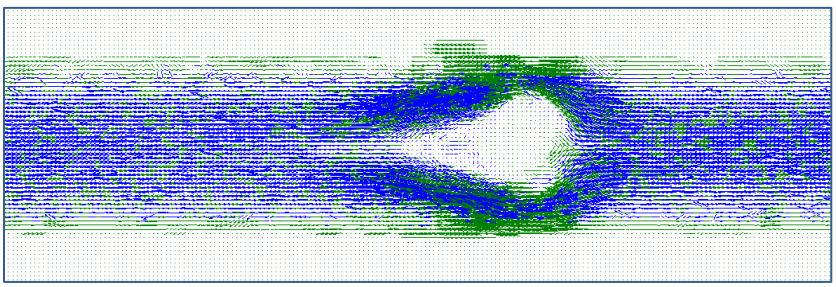

Figure B.5. Two-dimensional velocity vector map of an image pair.

In the two-dimensional velocity vector maps, the moving average validation is applied as a local neighbourhood validation method, in which validation is made by comparing each vector with their neighbours in an area of 3 x 3 pixels. After the comparison an average vector is calculated based on the comparison off all vectors of the neighbourhood, with an acceptance factor of 0.1. Figure B.6 show an image after the moving average validation, in

which the red vectors are the rejected vectors. After the moving average validation is performed, the created mask is applied again to remove the undesired vectors.

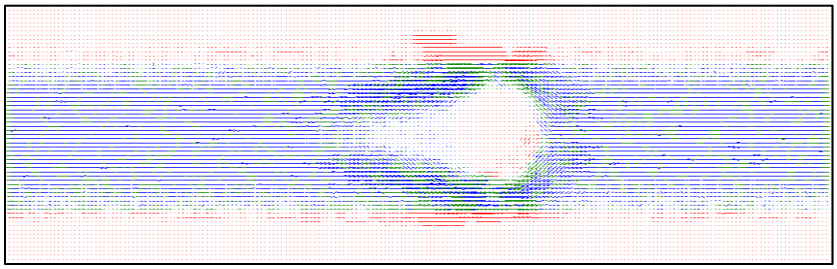

Figure B.6. Image after the moving average validation.

5. Final vector map

The average of the vector maps obtained from each pair of images provides the final vector map, as shown in Figure B.7.

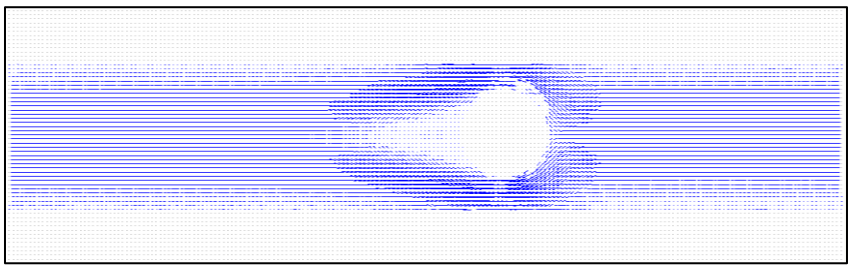

Figure B.7. Final vector map.

In the final vector map, the velocity fields can be taken in the desired locations, as represented in Figure B.8.

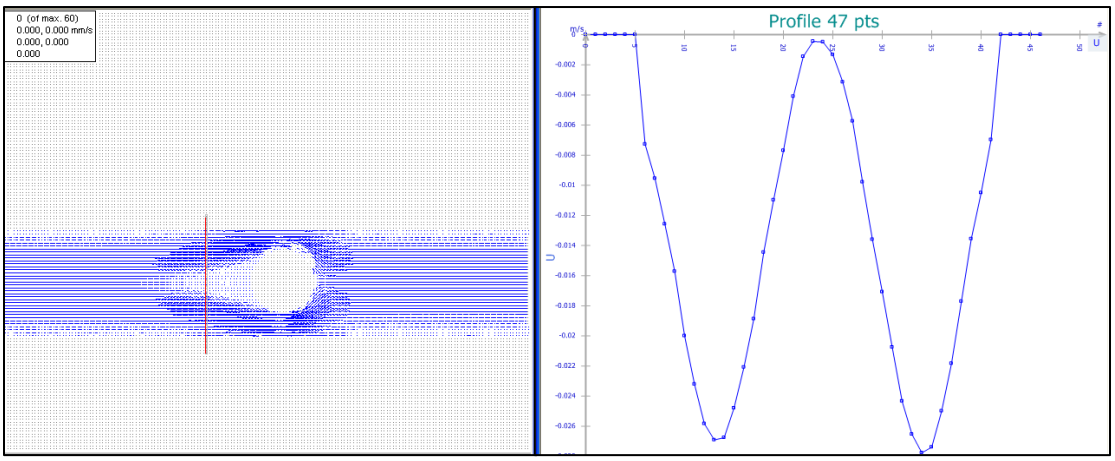

Figure B.8. Velocity field taken in a desired direction.